TECHNICAL UNIVERSITY OF MUNICH
DEPARTMENT OF PHYSICS

MAX-PLANCK-INSTITUT
FÜR CHEMISCHE PHYSIK FESTER STOFFE

Milli-Kelvin Thermal Transport in the Quasi-one-dimensional Quantum Magnet YbAlO₃

Parisa Mokhtari

TUM Uhrenturm

TUM School of Natural Sciences
Technische Universität München

Milli-Kelvin Thermal Transport in the Quasi-one-dimensional Quantum Magnet YbAlO₃

Parisa Mokhtari

Vollständiger Abdruck der von der TUM School of Natural Sciences der Technischen Universität München zur Erlangung des akademischen Grades einer

Doktorin der Naturwissenschaften (Dr. rer. nat.)

genehmigten Dissertation.

Vorsitz: Prof. Dr. Frank Pollmann

Prüfer*innen der Dissertation:
1. Prof. Dr. Elena Hassinger
2. Prof. Dr. Christian Hemker-Heß

Die Dissertation wurde am 18.09.2023 bei der Technischen Universität München eingereicht und durch die TUM School of Natural Sciences am 22.11.2023 angenommen.

Abstract

One-dimensional quantum systems are phenomenal because only collective excitations are present and strong influences of quantum fluctuations occur. Fractionalisation of the magnetic excitations in one-dimensional anti-ferromagnetic spin chains is a paradigmatic example in which low-energy excitations, known as spinons, carry fractional spin $\Delta S = 1/2$. Even though considerable progress has been made in the theoretical understanding of such quantum magnets, experimental realisations of this low-dimensional physics are relatively rare. In 2019, however, Wu *et al.* reported the realisation of a quantum $S = 1/2$ spin chain system in the rare-earth perovskite $YbAlO_3$, exhibiting both quantum critical Tomonaga-Luttinger liquid behaviour and spinon confinement-deconfinement transitions in different regions of the field-temperature phase diagram. At low-enough temperatures, Yb^{3+} Ising-like moments experience anti-ferromagnetic exchange interaction along the c-axis, namely the chain direction ($J_\parallel = 2.3\,\mathrm{K}$) and ferromagnetic coupling perpendicularly in the ab-plane ($J_\perp = 0.8\,\mathrm{K}$). In zero field, a three-dimensional anti-ferromagnetic order is established below $0.88\,\mathrm{K}$. For magnetic fields along the a-axis perpendicular to the spin chains, this order is suppressed and replaced by an incommensurate anti-ferromagnetic ground state until a full polarisation occurs above $1.5\,\mathrm{T}$.

In former works, magnetisation and specific heat capacity were measured to demonstrate various states of Tomonaga-Luttinger liquid, three-dimensional anti-ferromagnetic, incommensurate anti-ferromagnetic and fully-polarised. Moreover, the theory predicts that the incommensurate anti-ferromagnetic ground state comprises spin-density wave and transverse anti-ferromagnetic sub-phases. Inelastic neutron scattering confirmed the fractionalisation of the magnetic excitations in the Tomonaga-Luttinger liquid phase. Nonetheless, investigating the transport properties and the scattering effects in the different phases and across the transitions was missing. Hence, it was an open question whether magnetic excitations in this compound carry heat and how they interact with phonons.

In this research, I experimentally study the low-temperature thermal conductivity of $YbAlO_3$, measured down to $30\,\mathrm{mK}$ in fields up to $6\,\mathrm{T}$, with a focus on the contribution of the magnetic excitations to thermal transport within different phases and their interactions with lattice vibrations. A substantial enhancement of the thermal conductivity is observed in the proposed Tomonaga-Luttinger-liquid region. In addition, the large variation of the thermal conductivity throughout the phase diagram indicates strong magneto-elastic coupling. The phase diagram is successfully reproduced with pronounced anomalies in both temperature and field sweeps. Notably, my results agree with the previous reports, additionally providing complementary information to thermodynamics probes and theoretical predictions. An astonishing result is the high sensitivity of the thermal conductance to the phase transitions, especially the Tomonaga-Luttinger liquid to three-dimensional anti-ferromagnetic, and the commensurate to incommensurate ones. In addition, the diverse behaviour of the thermal conductivity within different phases is notable. A clear V-shaped anomaly in the field dependence at low temperatures is found at the crossover within the incommensurate phase, which was suggested before based only on a tiny plateau appearing in the magnetisation at $1/3$ of the saturation value. I detected an additional plateau-type anomaly via the delicate thermal-transport probe emerging in the field that the magnetisation is at $1/5$ of its saturation value. This feature is another outstanding result which was not observed before.

Zusammenfassung

Eindimensionale Quantensysteme sind phänomenal, weil nur kollektive Anregungen vorliegen und starke Einflüsse von Quantenfluktuationen auftreten. Die Fraktionalisierung der magnetischen Anregungen in eindimensionalen antiferromagnetischen Spinketten ist ein paradigmatisches Beispiel dafür, dass niederenergetische Anregungen, sogenannte Spinonen, einen fraktionierten Spin $\Delta S = 1/2$ tragen. Obwohl beim theoretischen Verständnis solcher Quantenmagnete erhebliche Fortschritte erzielt wurden, sind experimentelle Erkenntnisse im Hinblick auf diese niedrigdimensionalen Physik relativ selten. Im Jahr 2019 berichteten Wu *et al.* über die Realisierung eines Quanten-Spin 1/2-Spinkettensystems im das Seltenerd-Perovskit YbAlO$_3$, das sowohl quantenkritisches Tomonaga-Luttinger-Flüssigkeitsverhalten als auch 'confinement-deconfinement'-Übergänge von Spinonen in verschiedenen Bereichen des Feld-Temperatur-Phasendiagramms zeigt. Bei ausreichend tiefen Temperaturen erfahren Yb^{3+} Ising-ähnliche Momente eine antiferromagnetische Austauschwechselwirkung entlang der c-Achse, der sogenannten Kettenrichtung ($J_\parallel = 2{,}3\,\mathrm{K}$), und senkrechte ferromagnetische Kopplung in der ab-Ebene ($J_\perp = 0{,}8\,\mathrm{K}$). Im Nullfeld stellt sich unterhalb von 0,88 K eine dreidimensionale antiferromagnetische Anordnung ein. Für Magnetfelder entlang der a-Achse senkrecht zu den Spinketten wird diese Ordnung unterdrückt und durch einen inkommensurablen antiferromagnetischen Grundzustand ersetzt, bis oberhalb von 1,5 T eine vollständige Polarisation auftritt.

In früheren Arbeiten wurden Magnetisierungs- und spezifische Wärmekapazitätsmessungen durchgeführt, um verschiedene Zustände der Tomonaga-Luttinger-Flüssigkeit, dreidimensional antiferromagnetisch, inkommensurabel AFM, und vollständig polarisiert nachzuweisen. Darüber hinaus sagt die Theorie voraus, dass der inkommensurable antiferromagnetische Grundzustand Spindichtewellen und transversale antiferromagnetische Unterphasen umfasst. Inelastische Neutronenstreuung bestätigte die Fraktionalisierung der magnetischen Anregungen in der Tomonaga-Luttinger-Flüssigkeitsphase. Dennoch fehlte die Untersuchung der Transporteigenschaften und der Streueffekte in den verschiedenen Phasen und über Phasenübergänge hinweg. Daher war es eine offene Frage, ob magnetische Anregungen in dieser Verbindung Wärme transportieren und wie sie mit Phononen interagieren.

In dieser Arbeit untersuche ich experimentell die Wärmeleitfähigkeit von YbAlO$_3$ bei tiefen Temperaturen, gemessen bis zu 30 mK in Feldern bis zu 6 T. Der Schwerpunkt lag dabei auf dem Beitrag der magnetischen Anregungen zum Wärmetransport innerhalb verschiedener Phasen und ihre Wechselwirkungen mit Gitterschwingungen. In der vorgeschlagenen Region der Tomonaga-Luttinger-Flüssigkeit wird eine erhebliche Verstärkung der Wärmeleitfähigkeit beobachtet. Darüber hinaus deutet die große Variation der Wärmeleitfähigkeit im gesamten Phasendiagramm auf eine starke magnetoelastische Kopplung hin. Das Phasendiagramm wird erfolgreich mit ausgeprägten Anomalien sowohl als Funktion der Temperatur als auch des magnetischen Feldes reproduziert. Bemerkenswerterweise stimmen meine Ergebnisse mit den vorherigen Berichten überein und liefern ergänzende Informationen zu den Ergebnissen thermodynamischer Untersuchungen und theoretischen Vorhersagen. Ein erstaunliches Ergebnis ist die hohe Empfindlichkeit der Wärmeleitfähigkeit gegenüber den Phasenübergängen, insbesondere der Tomonaga-Luttinger-Flüssigkeit zu dreidimensional antiferromagnetisch und von kommensurablen zu inkommensurablen Zuständen. Darüber hinaus fällt das unterschiedliche Verhalten der Wärmeleitfähigkeit innerhalb verschiedener Phasen auf. Eine deutliche V-förmige Anom-

alie in der Feldabhängigkeit bei niedrigen Temperaturen findet sich am Übergang innerhalb der inkommensurablen Phase, die zuvor nur aufgrund eines winzigen Plateaus in der Magnetisierung bei 1/3 des Sättigungswerts vermutet wurde. Über die empfindliche Wärmetransportsonde habe ich eine zusätzliche Plateau-Anomalie entdeckt, die in dem Feld auftauchte, in dem die Magnetisierung 1/5 ihres Sättigungswerts beträgt. Dieses Merkmal ist ein weiteres herausragendes Ergebnis, das zuvor nicht beobachtet wurde.

Nomenclature

Here I present the abbreviations and the symbols I use in this text as a helping centre for the reader. Note that (i) bold and hat indicate the symbol is a vector and a tensor, respectively. Exceptionally, $\hat{\boldsymbol{\delta}}$ with $\delta \in \{x,y,z,a,b,c\}$ is the unit vector along the corresponding space coordinate or crystallographic direction. (ii) Indexed properties with $\delta \in \{x,y,z,a,b,c\}$ are along the corresponding direction. $\parallel$ and $\perp$ indexes are for along and perpendicular to the spin chains. (iii) The line over the symbols indicates the mean value of the property. (iv) x is often used as a mathematical variable, and i, j, k, l, n or p as counters or pointers to a site or a particle. ijk may follow a cyclic permutation. i is also for the imaginary number. (v) $\mathbb{Z}$ denotes the set of integers.

Acronyms

μSR	Muon spin spectroscopy
AC	Alternating current
AFM	Anti-ferromagnetic
BG	Background
CEF	Crystal electrical field
CF	Cold finger
CNC	Computer numerical control
CPT	Classical phase transition
D	Dimensional
DC	Direct current
DMRG	Density-matrix renormalisation group
ENS	Elastic neutron scattering
ESR	Electron spin resonance
F	Fermi
FFF	Fused filament fabrication
FFT	Fast Fourier transformation
FI	Field-induced
FL	Fermi liquid
FM	Ferromagnetic
FP	Fully-polarised
FS	Fermi surface
GS	Ground state
HAF	Heisenberg anti-ferromagnet
HAFC	Heisenberg anti-ferromagnetic chain
IC	Incommensurate
INS	Inelastic neutron scattering
LS	Lake Shore
LSDW	Longitudinal spin-density wave

MC	Mixing chamber
MPI-CPfS	Max-Planck-Institut für Chemische Physik fester Stoffe
MPS	Matrix product state
N	Normal
NMR	Nuclear magnetic resonance
PID	Proportionality-integral-derivative
PPMS	Physical property measurement system
PT	Phase transition
Q-1-D	Quasi-one-dimensional
QC	Quantum critical
QCP	Quantum critical point
QD	Quantum Design
QHE	Quantum Hall effect
QP	Quasi-particle
RC	Resistor-capacitor
RE	Rare-earth
RRR	Residual resistivity ratio
RT	Room temperature
SDW	Spin-density wave
SOC	Spin-orbit coupling
SP	Spin-Peierls
TAF	Transverse anti-ferromagnetic
TBA	Thermodynamics Bethe ansatz
TEBD	Time-evolving block decimation
TLL	Tomonaga-Luttinger liquid
TTO	Thermal transport option
U	Umkalpp
VSM	Vibrating sample magnetometer
WF	Wavefunction
YALO	$YAlO_3$
Yb:Y	Ratio between the values for $YbAlO_3$ and $YAlO_3$

Angles

$\angle\tilde{\delta}$	Angle between Yb^{3+} ions and the exemplary $\tilde{\delta}$-axis
θ	Sweeping angle of the applied external B from the a-axis
φ	Tilting angle of Ising moments of Yb^{3+} ions with respect to the a-axis

Fields and temperatures

$\Theta_{D(E)}$	Debye (Einstein) temperature
B	Magnetic field, also indexed $c1$ for critical field of 3-D to IC-AFM transition, $c2$ for critical field of SDW to TAF transition, s for saturation, mf for molecular field, $+(-)$ for spin up (down) of B_{mf}, and st for staggered

b	Field in Kelvin
B_c	Critical field of saturation; characteristic field
$B^{\mathrm{ON(OFF)}}$	Transition onset (offset) field
h	Reduced B in theoretical notations, also indexed corresponding as-defined B
h_z	Longitudinal external magnetic field
h_{ic}	Mean-field approximation of inter-chain incommensurate molecular field
T	Temperature, also indexed *mid* for $(T_\mathrm{C}+T_\mathrm{H})/2$, *avg* for average, and *int* for interpolated
t	Reduced T in theoretical notations
T_0	Constant T; Fit parameter
$T_\mathrm{C(H)}$	Temperature at the cold (hot) contact; Curie temperature
T_CF	Temperature of the cold finger
T_c	Superconducting critical temperature; magnetic ordering critical temperature
$T^{\mathrm{ON(OFF)}}$	Transition onset (offset) temperature
T_N	Néel ordering temperature

General: Lengths and areas

δl	Contact width
$\tilde\delta$	Expected δ-axis, $\delta \in \{a,b,c\}$, determined via Laue X-ray diffraction
a	Crystallographic axis; lattice constant
A_s	Cross-section of the sample
b	Crystallographic axis; lattice constant
c	Crystallographic axis; lattice constant
l	Minimum length of sample cross-section, also indexed C for Crimann length; distance between two arbitrary measuring points of T along the specimen; indexed $\delta \in \{a,b,c\}$ for sample length along the δ-axis
$l_{\mathrm{eff(av)}}$	Effective (Average) distance between T_C and T_H
V	Volume

General: Position, momenta, wave vectors and energies

Δ	Gap energy
δ	Shift of the IC ordering wave vector, i.e., $\boldsymbol{q} = (001 \pm \delta)$
ϵ	Energy, also indexed *max* for spin band maximum
$\hat{\mathcal{H}}$	Hamiltonian, also indexed *eff* for effective
$|n\rangle\,(|m\rangle)$	Eigenstate with the $E_n(E_m)$ eigenenergy
ψ_σ	Wavefunction of particle with spin σ, also indexed R *(L)* for right (left) movers
ε	Energy, also indexed z for tubes along the z-axis
$\boldsymbol{k}$	Angular wave vector, also indexed D for Debye; propagation vector
$\boldsymbol{p}$	Momentum
$\boldsymbol{Q}$	Wavevector transfer; scattering vector of neutrons
$\boldsymbol{q}$	Propagating wavevector
$\boldsymbol{r}$	Position vector

E	Energy, also indexed S *(T)* for singlet (triplet), *dip* for dipole-dipole, n *(m)* for the eigenenergy of the eigenstate $|n\rangle$ $(|m\rangle)$
k	Wavenumber; quantum number
L_δ	Length of the box along the $\delta \in \{x, y, z\}$ direction
m	Particle mass
r	Exemplary tuning parameter of the phase diagram
t	Hopping integral

Instrumentation: Electrical components and calibration procedure

α	Fit parameter in $R-T$ relation of RuO_2 chip resistors
ΔU	Voltage difference between terminals of gradient heater
A_n	Fit parameter in $R-T$ relation of RuO_2 chip resistors with $n \in [0, 2]$
C_{RC}	Capacitance of low-pass RC circuit
f	Frequency, also indexed c for cut-off frequency of low-pass RC circuit
g	geometrical factor of l/A_s
I	Electrical current
P_{Heater}	Heater power
R	Resistance, also indexed RC for low-pass RC circuit, *0* for nominal *or* a fit parameter in $R-T$ relation of RuO_2 chip resistors, C *(H)* for cold (hot) sensor and *int* for interpolated
R_{min}^{OFF}	Minimum measured R during OFF modes of a specific measurement
T_0	Fit parameter in $R-T$ relation of RuO_2 chip resistors
T_n	nth Chebyshev polynomial

Magnetism and Heisenberg model

χ	Magnetic susceptibility
ϵ	Spin anisotropy of the spin-chain coupling
$|\chi\rangle$	Spin wavefunction, also indexed S *(T)* for singlet (triplet)
$|\psi_i\rangle$	Spatial wavefunction of particle $i \in \{a, b\}$
$|\Psi\rangle$	Quantum state vector, also indexed S *(T)* for singlet (triplet)
$\uparrow (\downarrow)$	Spin up (down)
$\hat{\boldsymbol{S}}$	Spin operator, indexed $+(-)$ for raising (lowering)
$\boldsymbol{J}$	Total angular momentum
$\boldsymbol{L}$	Orbital angular momentum
$\boldsymbol{m}$	Magnetic moment
$\boldsymbol{S}$	Spin angular momentum
A	Amplitude of spin operator
a	Distance between the spins on the chain
B	Amplitude of spin operator
g	Landé factor, also indexed *eff* for effective
J	Exchange integral or exchange constant, also indexed *ab* for the *ab*-plane, *leg (rung)* for leg (rung) direction of spin ladders; total angular momentum

L	Number of the sites of the chain
M	Magnetisation, also indexed $+(-)$ for spin up (down), st for staggered, and s for saturation
m	Defined to be equal to M/M_s; Defined to be equal to $1/J_\parallel$
m_{ind}	Number of spins flipped in field
N	Number of the sites of the chain; number of sites with flipped spins
n	Number of legs of spin ladders
r	Deviation of field from the saturation value in Kelvin, $b - b_s$
S	Spin, also indexed tot for total; spin structural factor; entropy

Numeric: Thermal Drude weight

$\hat{j}_{\text{th}}$	Energy-current operator, also indexed th,i for the local operator at the site i
$|\Psi_t\rangle$	Quantum state vector $|\Psi_0\rangle = |\psi\rangle$ at time t
$|\sigma_1\sigma_2\ldots\sigma_L\rangle$	State vector of a spin chain with L sites with spin σ_i at site $i \in [1, L]$
$\tilde{\kappa}$	Defined to be equal to $2\pi D^{\text{th}}$
$c_{\sigma_1,\sigma_2,\ldots,\sigma_L}$	Normalisation coefficient
D^{th}	Thermal Drude weight
Z	Partition function

Physics constants

$\hbar$	Reduced Planck constant	$[1.054571817 \cdot 10^{-34}\,\text{J}\,\text{s}]$
μ_0	Vacuum magnetic permeability	$[1.25663706212 \cdot 10^{-6}\,\text{N}\,\text{A}^{-2}]$
μ_{B}	Bohr Magneton	$[9.2740100783 \cdot 10^{-24}\,\text{J}\,\text{T}^{-1}]$
h	Planck constant	$[6.62607015 \cdot 10^{-34}\,\text{J}\,\text{Hz}^{-1}]$
k_{B}	Boltzmann constant	$[1.380649 \cdot 10^{-23}\,\text{J}\,\text{K}^{-1}]$
N_{A}	Avogadro constant	$[6.022140 \cdot 10^{23}\,\text{mol}^{-1}]$
R	Molar gas constant	$[8.314462618\,\text{J}\,\text{K}^{-1}\text{mol}^{-1}]$

Quantum mechanics in one dimension and Tomonaga-Luttinger liquid theory

ϕ	Displacement operator
ϕ_l	Labelling field, indexed 0 for equilibrium condition
ψ	Annihilation operator
ρ	Density operator, indexed 0 for equilibrium condition
θ	Phase operator
C_i	Non-universal coefficients with $i \in [1, 4]$
d	Lattice spacing
g	Coupling constant
K	Luttinger parameter
u	Sound velocity of the propagating excitations

Transport, heat capacity and scattering processes

α	Thermal expansion coefficient; fit parameter in N-processes, also spin gap
β	Thermodynamic beta; fit parameter in U-processes, also spin gap
Γ	Grüneisen parameter

γ_{ss}	Fit parameter in spin-spin scattering describing the scattering probability
κ	Thermal conductivity, also indexed D for Debye, *ph* for phononic, *mag* for magnetic, *s* for spinon, *reg* for regular, *min* for minimum, and *0* for $\kappa(B=0)$
$\kappa_{\mathrm{ph,\,2T}}$	κ_{ph} determined from the 2 T results
$\kappa_{\mathrm{ph,\,cube}}$	κ_{ph} determined from the extrapolation of the cubic behaviour at the lowest T
$\kappa_{\mathrm{ph,\,perp}}$	κ_{ph} determined from the $\kappa_{\perp}$ results
$\kappa^{\mathrm{i\,(c)}}$	Initial (Corrected) values of κ from a field sweep
λ	Mean-free path
ω	Angular frequency, also indexed E for Einstein, D for Debye
ω_0	Fit parameter in resonance scattering describing *resonance frequency*
ρ	Mass density
τ	Relaxation time, also indexed c for combined, q for resistive, *bd* for boundaries, *pd* for point defects, *dis* for dislocations, and *res* for resonances
$\boldsymbol{j}_{\mathrm{Q}}$	Heat-current density
A	Fit parameter, no index in phonon-point-defect scattering and indexed *s-ph* for spin-phonon scattering
a_0	Bohr radius of a point-defect scattering centre
B	Bulk modulus; fit parameter in U-process scattering
b	Fit parameter in U-process scattering
C	Specific heat capacity, indexed *ph* for phonons, M for magnetic, and s for spinon; Total heat capacity; fit parameter in phonon-resonance scattering
c	Heat capacity per particle; indexed L for lattice constant along the ladder direction in spin-ladder systems; indexed *ii* with $i \in [1,6]$ for elastic constants
c_v	Specific heat capacity, also indexed E for Einstein, D for Debye
D	Fit parameter in phonon-dislocation scattering
d	Dimensionality
$F(X)$	Universal scaling function with dimensionless input X as in Relation 7.9
f	Characteristic function relating κ_{mag} and l_{mag} of a spin system
I	A locally-defined parameter carrying T and Θ_{D} functionality as in Relation 6.7
l	Mean-free path of magnetic excitations, indexed *mag* for total, *0* if being constant, *def* for defects and boundaries, *s-ph* for spin-phonon, and *ss* for spin-spin
M	Atomic mass
N	Number of atoms in a given volume; fit parameter in N-process scattering
n	Particle per unit volume; atomic number density; number of phonons in phonon-phonon processes, also indexed s for number of chains per unit area
P	Probability function of transport in a specific time with no collision
t	Time, also indexed *col* for the mean time between two collisions
T_{u}^*	Fit parameter in spin-phonon scattering
v	Velocity, also indexed s for spinon *or* shear, *l (t)* for longitudinal (transverse)
X_i	Dimensionless values at which $F(X_i)$ with $i \in \{1,2\}$ reaches maxima
Q	Heat flow, also Newton's dot notation is used for the rate of the heat flow

Contents

List of Tables

List of Figures

1 Introduction

The test of all knowledge is experiment.
Experiment is the sole judge of scientific truth. — Richard P. Feynman
Nevertheless, many times we observe what we never knew!

In this dissertation, I experimentally investigate an insulating quantum spin system under extreme conditions, particularly via thermal conductivity measurements at very low temperatures. Measuring a transport property is a standard technique which gives access to many principal quantities, such as the density, the velocity, and the heat capacity of the propagating particles and quasi-particles in a solid, in addition to their interaction with other particles. On the other hand, transport is also one of the most difficult properties to describe theoretically because it occurs only when the system is out of equilibrium though may be in a steady state. From a simple classical point of view, the old game of pinball machine is a basic model of transport: In the physical machine, the game plate has a non-zero slope, and the balls move along the gradient of gravitational potential energy from the top to the bottom. During the transport, the balls collide with little posts, the walls and other balls in the machine. One can classify the machines by their conductivity, i.e., how much time it takes on average for a ball to move from the top to the bottom of the same system. In a solid, the balls represent the quantum-mechanical particles and excitations such as electronic quasi-particles, phonons describing the vibrations of the crystal lattice or magnetic excitations via spin flips. If you opt for the *insulating quantum magnet* game machine, the last two sorts of quasi-particles are the balls in the game.

Transport stems from the gradient of potential energy: the gravitational potential gradient for the conductivity of the balls in pinball, the electrical potential gradient in electrical conductivity, the temperature gradient for thermal conductivity and thermopower. Propagating balls need non-zero mass to feel the force in the gravitational potential energy gradient in the pinball machine. In the solids, the propagating (quasi-)particles demand a non-zero charge to sense the electrical energy gradient in electrical conductivity. Nonetheless, any (quasi-) particle, regardless of its electrical charge, even insulating, can transport heat, making the thermal conductivity probe sensitive to all the emerging excitations. This responsiveness rocks the level of complexity not merely to predict the expected behaviour precisely on paper in theory but also to extract information from measured data in the laboratory. Furthermore, the particles and their interactions are highly quantum-mechanical in nature, and hence decoupling various types of quasi-particles with similar origins and studying them as individual propagating channels can get extremely complicated and challenging. Therefore, thermal transport is employed to answer specific physical questions in systems.

This thesis is on the milli-Kelvin thermal conductivity of the quasi-one-dimensional quantum magnet $YbAlO_3$. In Chapter 2, I provide general theoretical descriptions of spin systems with one-dimensional physics. Chapter 3 summarises the properties and previous works on the focused system $YbAlO_3$. Chapter 4 will introduce the concepts of transport in a more physical formalism. Moreover, I introduce the phononic thermal conductivity models as well as the magnetic thermal conduction in the spin systems with low dimensionality. In Chapter 5, I describe my experimental techniques for measuring thermal transport from room temperature down to sub-Kelvin temperatures, together with the computational

methods used throughout this research.

These chapters are followed by the main results and transport investigation performed on YbAlO$_3$ in the framework of this thesis in Chapter 6. In Chapter 7, I discuss more details on the magnetic thermal transport in YbAlO$_3$ and some remarks on the phase diagram reproduced by the thermal transport probe in this work.

In the appendix chapters, I give a general description of the Tomonaga-Luttinger liquid theory (Appendix A) and the magnetic structure of YbAlO$_3$ (Appendix B). From the experimental perspective, I present the influence of my modification to the contact between the sample and thermal bath on the measurements in Appendix C. New components and a sample holder for thermal conductivity and thermoelectricity measurements in the ^{3}He-^{4}He dilution refrigerator were designed in this research. The mechanical plans and descriptions are provided in Appendix D.

Even though this dissertation focuses on my main doctoral research, some side projects and experiences are also noteworthy.

Aiming for test and calibrations, I analysed de Haas-van Alphen quantum oscillations of two samples of the Weyl semimetal TaAs in magnetic fields up to 34 T measured by *Gabriel Seyfarth* from the *University of Grenoble* at the *Laboratoire National des Champs Magnétiques Intenses* using a new platform called *Antenna OK6* for magnetisation measurements based on the capacitance change. Accordingly, I analysed the obtained signal and compared the quantum oscillations frequencies with previous measurements performed in two different measuring systems by my colleagues at the *Max Planck Institute for Chemical Physics of Solids* (MPI-CPfS) as references. From the deviation of the periodicity of the quantum oscillations in the new setup in reversed field obtained, I derived the field shift caused by the gradient magnet of the measuring setup.

In another work, I developed a new probe for magnetometry using commercially available membrane-type surface stress sensors. This project was in collaboration with *Manuel Brando*, the group leader of *Physics of Quantum Materials: Novel States of Matter on the Border of Magnetism* at the MPI-CPfS. I successfully measured magnetisation and de Haas-van Alphen quantum oscillations of the Weyl semimetal TaAs via the developed setup. The instrument, however, was not sensitive enough for torque magnetometry in the presence of a magnetic field gradient. This work is unpublished yet.

By explaining the variations of the quantum oscillations frequencies measured by the former doctoral researcher of the group *Marcel Naumann* on CoSb$_3$ with the sample fabrication method as being due to antimony inclusions, I could complete the last piece of the puzzle and writing the article on these data as published in [1]. See [1] for more information.

In another study, I investigated electrical resistivity, thermal conductivity and thermopower of the non-oxide delafossite AgCrSe$_2$ as part of the big work published in [2]. Though the non-oxygen-based chromium delafossites were hardly investigated by the time, the oxygen-based delafossites had shown interesting features in electrical conductivity, e.g., evidence for hydrodynamic electron flow in PdCoO$_2$. Thermal transport measurements in AgCrSe$_2$ were suspended for the new batch of samples with higher quality.

As mentioned, this text reports only my work on the thermal conductivity of the quasi-one-dimensional quantum magnet YbAlO$_3$. The relevant publications are in preparation [3–5].

2 **Theoretical concepts**

2.1 Introduction

In this chapter, I will have a look on various theoretical concepts vital to comprehend this study. The outline of this chapter is as follows: I begin with a description of magnetic exchange interactions, the famous Heisenberg model and magnetic orderings in spin systems. I introduce the magnetic excitations in the frame work of spin wave theory. The possibility of fractionalisation of the magnetic excitations in quantum spin chains is explained afterwards.

This is followed by describing the one-dimensional (1-D) spin-chain model and the Tomonaga-Luttinger liquid (TLL) theory: I show briefly how Landau's Fermi liquid (FL) theory fails in 1-D systems, and a prominent phenomenon occurring in 1-D metallic compounds, namely spin-charge separation. I close the section by exemplary circumstances in which 1-D physics is experimentally feasible in the three-dimensional (3-D) world. A general description of the TLL theory is given in Appendix A. The chapter is closed with a recall on quantum criticality, where the quantum critical fluctuations affect a large range at finite temperatures (T) above a quantum critical point (QCP).

The most important references of this chapter are *Magnetism in Condensed Matter* [6] and *Quantum Physics in one dimension* [7], being the two main sources of the corresponding scopes in quantum many body physics. On all presented models a huge amount of literature exists, some of which is summarised in [8].

2.2 Exchange interaction, Heisenberg model & magnetic ordering

Magnet moments $\boldsymbol{m}$ of electrons along with their interactions in a crystalline material form the building blocks of magnetism. A famous example is spontaneous magnetic ordering in magnetic substances. The magnetic moment of an atom or an ion arises from a contribution of the orbital angular momentum L and the intrinsic spin angular momentum S of all electrons. While in filled electronic shells the angular and spin momenta sum up to zero, transition or rare-earth metals possess an incompletely-filled shell resulting in a net non-zero magnetic moment, as in the case of Yb^{3+} ions, which are the magnetic ions of interest for this research. For hypothetically isolated magnetic moments at finite T and in the absence of any external magnetic field (B), there is no special orientation due to thermal motions. In such a circumstance, the total $\boldsymbol{m}$ per unit volume defining *magnetisation* (M) of the compound equals zero. Application of the external B induces $\boldsymbol{m}$ to align parallel or anti-parallel to B, leading respectively to *paramagnetism* and *diamagnetism* phenomena. However, by tuning the interactions between the moments, different types of magnetic ground states (GS) can be produced even in the absence of the external B. *Ferromagnets* and *anti-ferromagnets* are the most famous ones. Magnetic configurations in the ferromagnets consist of individual $\boldsymbol{m}$ aligned in parallel, however, the adjacent $\boldsymbol{m}$ are in an anti-parallel alignment in the anti-ferromagnets. More complicated GSs though exist, e.g., spin density wave, etc.

In 1928-29, Heisenberg [9] and Dirac [10] studied the so-called quantum mechanical *exchange interaction* between the atoms of the crystal lattice, which brings about the non-spontaneous ordering of the moments. The main concept of the model is as follows: If

relativistic effects are not considered, then the electric interaction between particles does not depend on their spins. Thus, in the absence of B, the Hamiltonian $\hat{\mathcal{H}}$ of a system of particles with electric interaction does not contain spin operators ($\hat{\boldsymbol{S}}$). When it is applied to a wavefunction (WF), it does not affect the spinoidal variables. Hence, the WF of a system can be written as a product of the spin ($|\chi_i\rangle$) and spatial ($|\psi_i\rangle$) coordinates of its particles, where the Schrödinger equation leaves the former arbitrary and determines only the latter. One can motivate the origin of the exchange by just considering two independent electrons with orthogonal WF of $\left\langle \boldsymbol{r}_{1(2)} \big| \psi_{a(b)} \right\rangle$. Adding exchange symmetry to the product state of the two electrons gives $(\langle \boldsymbol{r}_1|\psi_a\rangle \langle \boldsymbol{r}_2|\psi_b\rangle \pm \langle \boldsymbol{r}_2|\psi_a\rangle \langle \boldsymbol{r}_1|\psi_b\rangle)/\sqrt{2}$. Considering a system of two identical particles, the $\hat{\mathcal{H}}$ of the system has to be invariant with respect to permutation of the particles (or carry antisymmetric WF). For a symmetric spatial state, this requires the spin wavefunction $|\chi\rangle$ to be in an antisymmetric singlet state of $|\chi_{\mathrm{S}}\rangle$ ($S=0$), or in a symmetric triplet state of $|\chi_{\mathrm{T}}\rangle$ ($S=1$). So the WF and the energy for singlet (triplet) $\left|\Psi_{\mathrm{S(T)}}\right\rangle$ may be written as

$$\left|\Psi_{\mathrm{S(T)}}\right\rangle = \frac{1}{\sqrt{2}}[\langle \boldsymbol{r}_1|\psi_a\rangle \langle \boldsymbol{r}_2|\psi_b\rangle \mp \langle \boldsymbol{r}_2|\psi_a\rangle \langle \boldsymbol{r}_1|\psi_b\rangle]\left|\Psi_{\mathrm{S(T)}}\right\rangle,$$

$$E_{\mathrm{S(T)}} = \int\int \left\langle \Psi_{\mathrm{S(T)}}\big|\boldsymbol{r}_1\right\rangle \langle \boldsymbol{r}_1|\hat{\mathcal{H}}|\boldsymbol{r}_2\rangle \left\langle \boldsymbol{r}_2\big|\Psi_{\mathrm{S(T)}}\right\rangle \mathrm{d}\boldsymbol{r}_1\mathrm{d}\boldsymbol{r}_2, \tag{2.1}$$

where it is assumed that the spin parts of the WF are normalised. Clearly, states like $|\uparrow\uparrow\rangle$ and $|\downarrow\downarrow\rangle$ are symmetric under the exchange of electrons; notwithstanding, the antisymmetric states can be achieved only via a linear combination of the asymmetric states of $|\uparrow\downarrow\rangle$ and $|\downarrow\uparrow\rangle$, e.g., $(|\uparrow\downarrow\rangle \pm |\downarrow\uparrow\rangle)/\sqrt{2}$. An effective spin Hamiltonian is shown to read

$$\hat{\mathcal{H}}^{\mathrm{eff}} = -(E_{\mathrm{S}} - E_{\mathrm{T}})\hat{\boldsymbol{S}}_1 \cdot \hat{\boldsymbol{S}}_2 = -2J\hat{\boldsymbol{S}}_1 \cdot \hat{\boldsymbol{S}}_2, \tag{2.2}$$

with the singlet and triplet states as eigenstates with eigenvalues of E_{S} and E_{T}, respectively. The spin interaction of the form of $S_i \cdot S_j$, is called an *exchange interaction*, and J is the so-called *exchange integral* or *exchange constant*, defined as

$$J = \frac{E_{\mathrm{S}} - E_{\mathrm{T}}}{2}. \tag{2.3}$$

Therefore, the ferromagnet GS with the symmetric triplet state of $|\uparrow\uparrow\rangle$ or $|\downarrow\downarrow\rangle$ results in $J < 0$. Accordingly, the interactions with $J < 0$ (> 0) favour (anti-)parallel alignment of the spins energetically, considering the interactions effective to nearest neighbouring spins. These interactions are called *ferromagnetic* or FM (*anti-ferromagnetic* or AFM) in short. Extending the effective spin Hamiltonian in Relation 2.2 to an isotropic many-body system leads to the so-called *Heisenberg model*

$$\hat{\mathcal{H}} = -J\sum\nolimits_{<i,j>} \hat{\boldsymbol{S}}_i \cdot \hat{\boldsymbol{S}}_j, \tag{2.4}$$

where i and j refer to neighbouring sites on a lattice. The lattice sites can form a 1-D array, a 2-D lattice, e.g., a hexagonal lattice, or a 3-D array, e.g., a cubic lattice. The dimensionality of spin space is independent of the lattice type. The spins can be Ising type when constrained to a (anti-)parallel configuration to a specific direction, XY type if restricted to a particular plane, or Heisenberg type if allowed to orient freely in a 3-D space. Whether the effective spin behaves as Ising, XY or Heisenberg, depends on the single-ion

anisotropies determined by the interactions between the orbital states of the magnetic ion and the surrounding crystal field. As mentioned, the individual $\boldsymbol{m}$ would be disordered at any T in the absence of B and any exchange interactions. However, including exchange interactions may produce a non-vanishing M below a critical temperature T_c, leading to spontaneous magnetic order[1]. T_c below which the magnetic ordering occurs is known as Curie temperature T_C in the ferromagnets, and Néel temperature T_N in anti-ferromagnets. In the ferromagnets, the spontaneous magnetisation rises up from zero once cooling below T_C while growing as cooled further. P. Weiss [13] explained this by defining an *effective molecular field* at the position of each spin responsible for the alignment of $\boldsymbol{m}$ as

$$\boldsymbol{B}_{\mathrm{mf}} = -\frac{2}{g\mu_B} \sum_j J_j \boldsymbol{S}_j, \tag{2.5}$$

where μ_B and g are the Bohr magneton and the Landé g-factor. He argued that at low T, the magnetic order is self-sustaining. Therefore, $\boldsymbol{m}$ can be aligned by the internal molecular field even in the absence of any external B. By rising T, thermal fluctuations progressively destroy the magnetisation, and the order will destroy entirely at T_c. This is known as the *Weiss model of ferromagnetism*. The concept of B_{mf} can be expanded to the anti-ferromagnets. In this case, the system is considered as two interpenetrating FM *sub-lattices* that point oppositely. One may define B_{mf}^+ (B_{mf}^-) and M^+ (M^-) as the molecular field and the magnetisation of the spin-up (spin-down) sub-lattices. In each of the FM sub-lattices and thus in the whole sample, $M(T)$ equals zero for T above the critical ordering temperature T_N. Despite the non-zero M_{mf} in each of the FM sub-lattices below T_c, the sample magnetisation $M = M^+ + M^- = 0$ as M^+ and M^- are in opposite directions. This means that $M(T) = 0$ for all T. In this case, application of the so-called *staggered field*, $B_{\mathrm{st}} = B_{\mathrm{mf}}^+ - B_{\mathrm{mf}}^-$, or the so-called *staggered magnetisation*, $M_{\mathrm{st}} = M^+ - M^-$, is practical. The staggered field and magnetisation then carry non-zero values below T_N.

The main focus of this work is on thermal conductivity of a material containing quasi-1-D Heisenberg spin chains. Perfect 1-D Heisenberg spin chains simply consist of 1-D lines with N equidistant sites, where on each site one particle is placed with an effective half-integer spin[2]. The 1-D spin chains are in fact, a result of strong exchange interaction along one particular direction in the system. In such circumstances usually, a spatial alignment of the orbitals results in a strong exchange interaction along one axis of the crystal, the so-called *chain direction*, while in the perpendicular direction the exchange interaction is very small due to a poor overlap of the corresponding orbitals. Notably, the 3-D character of these systems is usually recovered at low T. Generally, the anisotropic Heisenberg Hamiltonian reads

$$\hat{\mathcal{H}} = \sum_{i-1}^{N-1} \left(J_x \hat{S}_i^x \hat{S}_{i+1}^x + J_y \hat{S}_i^y \hat{S}_{i+1}^y + J_z \hat{S}_i^z \hat{S}_{i+1}^z \right). \tag{2.6}$$

The special cases of this Hamiltonian are the *XY*-model ($J_z = 0$), the *XXX* or isotropic Heisenberg model ($J_x = J_y = J_z$), the *XXZ* or anisotropic Heisenberg model ($J_x = J_y \neq J_z$) and the Ising model ($J_x = J_y = 0$). The material studied in this research, $YbAlO_3$, is well-described by weekly-coupled *XXZ* Heisenberg chains, i.e., $J_z \gg J_x, J_y$. The chains consist

---

[1]Spontaneous magnetic ordering as a spontaneous time-reversal symmetry breaking is deemed impossible in 1-D systems due to lack of long-range ordering. Though, spontaneous breaking of global continuous symmetry, e.g., rotational symmetry of the spins, can still lead to spontaneous magnetism [11]. In such cases, spontaneously-magnetised TLL occur with a dynamical origin [12]. That is beyond this thesis.

[2]The chains of integer spins are called *Haldane spin chains*. The fundamental difference is related to differences of ferminoic and bosonic interactions under exchange, and corresponding excitations.

of Yb^{3+} moments which exhibit an effective inter-chain exchange interaction of $\sim 20\%$ of the intra-chain one. More details are provided in Chapter 3. Lastly, I would like to mention that the term n-leg spin ladder ($n \in \mathbb{Z} \geq 2$) describes a system with n strongly coupled spin chains with the rungs being formed between the neighbouring spins of adjacent chains. J_{leg} and J_{rung} are commonly used to name the intra-chain and inter-chain exchange interactions in spin ladders.

2.3   Fractionalisation of magnetic excitations in quantum spin chains

One of the most famous theories of magnetism is the so-called *spin wave theory*, describing dynamics of magnetic excitations. In order to derive dispersion relations of these excitations one may look at a simple case of an Ising FM spin chain (some complexity arises in the AFM spin chains, as is discussed later in this section). An Ising FM GS consists of parallel spins all either up $\uparrow$ or down $\downarrow$. Considering the $|\text{P}\rangle = |\uparrow \cdots \uparrow\rangle$ GS, $|n\rangle = |\uparrow \cdots \downarrow \cdots \uparrow\rangle$ represents a $\Delta S = 1$ (triplon) excitation with one flipped spin at n^{th} position. The so-called *magnon* corresponds to a sum of all flip positions weighted with probability as $\sum_n \exp(i\boldsymbol{k} \cdot \boldsymbol{r}_n)|n\rangle$. Using the described spin Hamiltonian in Relation 2.6, time-dependent expectation values of $\langle \hat{\boldsymbol{S}}_j \rangle$ can be calculated. Supposing the spins aligned along the z-axis in the GS, it can be shown that $S_j^x = S_j^y = 0$ and $S_j^z = S$ for the GS, while for a small departure from the state, i.e., S_j^x, $S_j^y \to 0$ and $S_j^z \approx S$, $\boldsymbol{S}_j^x = Ae^{\mathrm{i}(qja - \omega t)}$ and $\boldsymbol{S}_j^y = Be^{\mathrm{i}(qja - \omega t)}$ with $A = \mathrm{i}B$, a as the distance between the spins on the chain, and q being a wave vector. The latter yields that the motions of the non-vanishing transverse components of the excited state, i.e., x and y, are $\pi/2$ out of phase on a spin wave. It is remarkable that the term *magnons* and *spin wave* refer to the same excitation but emphasise the particle and wave character, respectively. The general dispersion relation of the spin waves is found to be

$$E(\boldsymbol{q}) = \hbar\omega = 4JS(1 - \cos(\boldsymbol{q})). \tag{2.7}$$

The dispersion is ungapped. However, anisotropic terms in the spin Hamiltonian originating usually from strong spin-orbit coupling (SOC) or alternatively a dipole-dipole interaction can lead to a gap Δ as well.

The spin wave theory assumes the excitations being formed as a superposition of single spin deviations justifying the approach of linear superposition for the excitations. This situation applies to the described case of the FM spin chains with the GS consisting of all spins aligned in one direction and an excitation being composed of a single spin flip. This spin flip costs a finite energy allocated by the coupling constants, leading to a higher energy cost for two spin deviations pictured as two single spin flips compared to only one spin deviation validating the use of spin wave theory. While spin wave theory predicts fairly well the observed behaviour in high dimensions (≥ 2), discrepancies in the excitation spectrum arise in low dimensions where quantum effects dominate the behaviour. The $S = 1/2$ AFM Heisenberg chain serving as a model for the material studied in this research is an example of a low-D system, which fails to develop long-range order and to express the excitations as a superposition of single spin deviations, thus leading to the failure of the spin wave theory. This can be understood simply by investigating the free energy. The entropy gain due to the spin flips at N sites equals $S = k_{\text{B}}\ln(N)$ in an $S - 1/2$ AFM Ising chain. For a large chain $N \to \infty$ the energy cost remains the same but the entropy gain becomes infinite,

(a)

(c)

A pair of spinons (S = 2 x 1/2)

(b)

Individual magnon (S = 1)

(d)

Individual spinon (S = 1/2)
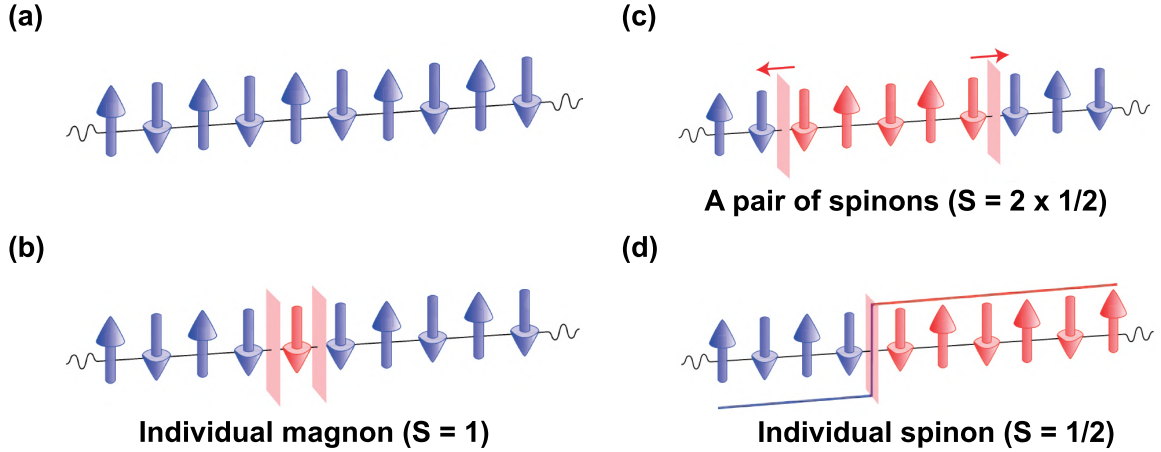
Figure 2.1: Fractionalisation of spin excitations in an AFM spin chain. **(a)**-**(b)** In high dimensions the minimal spin excitation on an AFM chain would be a magnon as marked in red, in which a single spin is flipped carrying an $\Delta S = 1$ excitation. **(c)** In one dimension, the magnon is not an individual excitation anymore. An individual magnon decomposes into a pair of $\Delta S = 1/2$ excitations, the so-called *spinons*, shown as the red walls propagating outwards. **(d)** An individual spinon, appears as the domain wall between the left and right AFM domains indicated in blue and red, respectively. Figure reproduced from [14].

and the free energy $F = E - TS$ stays negative for $T > 0$. So spins may spontaneously flip and long range order is not energetically favourable. Using symmetry considerations, this statement was rigorously proven by Mermin and Wagner for the isotropic Heisenberg model [15]. On the other hand, if an anisotropy of the exchange interaction is present, the extra energy cost associated with a spin deviating from the GS may dominate and enable long-range order. In 1991, Haldane [16] discussed the possibility of the magnetic excitations in 1-D interacting systems to fractionalise. He described such excitations using the so-called *fractional statistics* in 1-D as a generalisation of *anyons* for 2-D[3]. Figure 2.1 illustrates the concept of fractionalisation of the magnetic excitations on an AFM Ising spin chain schematically. Flipping one spin of the AFM Ising GS creates a $\Delta S = 1$ magnetic excitation, as illustrated in Figures 2.1 **(a)**-**(b)**. This creates a single magnon (tagged in red), similar to the minimal spin excitation in the FM Ising chain. The difference, however, rises up when flipping further spins. In the case of the FM Ising chain, flipping another single spin costs an energy of $E = J$, in line with the linear superposition approximation of the spin wave theory. In the case of the AFM Ising chain, the domain walls are delocalised and flipping the neighbouring spin costs no extra energy owing to the terms of the Heisenberg Hamiltonian. In such a circumstance, the initial individual magnon illustrated in Figure 2.1 **(b)** with the firmly bound walls (light red sheets between the blue and red domains) decomposes into two elementary excitations, each carrying a fractional quantum number $S = 1/2$, the so-called *spinons*. Therefore, the spinons can be visualised as two single walls propagating individually and independently (Figure 2.1 **(c)**). As indicated in Figure 2.1 **(d)**, each spinon separates two sections of the left and right AFM GS domains in an Ising chain. By raising the degree of freedom of the orientation of the spins from the Ising to

---

[3]Laughlin quasi-particle (QP) which is observable in the fractional quantum Hall effect (QHE), can carry a charge smaller than the one of the electron.

Heisenberg chains, the crossover of the spin-up to spin-down forms domain walls with non-zero thickness. In this case, the spinons decompose further into even numbers of spinons.

After the work of Haldane, both fractional [16, 17] and fermionic [18–22] statistics have been proposed for a spinon system. It is possible to derive the dispersion relation of the spinon excitations within the framework of the Bethe Ansatz [23–25]. Instead of a well-defined relation between the momentum $\boldsymbol{q}$ of the magnon and its energy E, there is a continuum. The two-spinon dispersion relation reads

$$E(\boldsymbol{q}_1, \boldsymbol{q}_2) = J\cos(\boldsymbol{q}_1) + J\cos(\boldsymbol{q}_2), \quad \boldsymbol{q} = \boldsymbol{q}_1 + \boldsymbol{q}_2 \qquad \text{where } \boldsymbol{q}_i \in [-\pi/2, \pi/2]. \tag{2.8}$$

Scattering measurements, in which the sample is bombarded by particles with non-zero spin, most commonly neutrons, can examine the derived dispersion relations. Elastically scattered neutrons in *elastic neutron scattering* (ENS) measurements produce strong Bragg reflections and are thus practical to determine the magnetic structures. *Inelastic neutron scattering* (INS) on the other hand, enables experimental determination of the dispersion relation of the spin excitations. More detail is available in related texts, e.g., [26–28]. Figure 2.2 compares intensity colour maps of the INS spectrum and theoretical calculation of the spinon dynamics structure factor on $CuSO_4 \cdot 5D_2O$ in zero B. In this compound, Cu^{2+} spins form a linear array of the interacting magnetic moments behaving as spin-1/2

Figure 2.2: Continuous spectrum of the dispersion relation of the spinons. Intensity colour maps of the Cu^{2+} AFM spin chains in the zero-B phase of $CuSO_4 \cdot 5D_2O$, obtained via the experimental INS measurements (left half) and theoretical calculations (right half). Figure from [14].

Heisenberg AFM chains. The experimental observations can be understood so that the neutron provokes an $\Delta S = 1$ excitation as a local spin flip surrounded by two domain walls, and thus the excitation spectrum is composed of spinon pairs with $S_{\text{tot}} = 1$ though each spinon has a discrete energy-momentum relation. Two crucial points can be extracted from Figure 2.2: (i) The spinons are gapless, and (ii) the characteristic continuous spectrum is observed both experimentally in INS and in exact calculations of the spinon dynamic structure factor. Another example for the experimental observation of the continuum spectrum of the spinons is the quasi 1-D quantum magnet $YbAlO_3$, which is studied in this work.

In the presence of B longitudinal to the magnetic spins, the vacuum and the GS are extremely affected [29]. In this case, the low-energy excitations of a cyclic AFM spin chain with N sites can be well explained in terms of spinon-like QP, the so-called *psinon*, as follows [30]: Defining m_{ind} as the number of the spins flipped in B, at $m_{\text{ind}} = 0$ $(N/2)$, the vacuum coincides with the spinon (magnon) vacuum. The GS and the low-lying excitations in B up to the saturation at B_s $(0 < m_{\text{ind}} < N/2)$ can be inferred neither from magnons nor spinons but rather as a mixed state with a new vacuum of $N/2 - m_{\text{ind}}$ magnons plus $2m_{\text{ind}}$ spinons [29]. Actually, we face a runaway of the QP population, namely a reduction (enhancement) for magnons (spinons), per decreasing B at B_s with the $|\uparrow \cdots \uparrow\rangle$ GS. In this circumstance, a

mixture of spectral properties from the magnons (Relation 2.7) and spinons (Relation 2.8) energy-momentum describes the dynamically relevant excitation spectrum [29].

To sum up, all spins are aligned in the GS of FM spin systems, and the excitations are superpositions of magnons with $S = 1$ (triplons) regardless of the dimensionality. The GS of the $S = 1/2$ AFM Heisenberg spin system is a Néel state, with spin waves as the elementary excitations in high dimensions. Reducing the number of dimensions to one invalidates the linear superposition of the excitations. The excitations of a $S = 1/2$ AFM Heisenberg chain in zero B are explained in terms of fractionalised magnetic excitations, the spinons. Various magnetic excitations such as magnons, spinons or psinons can be exhibited in B.

2.4 Haldane's Tomonaga-Luttinger liquid

In contrast to high dimensions (≥ 2) where it is possible for excitations to exist resembling individual particles, e.g., the famous Landau QP, this is not the case in one dimension where interactions turn any excitation into a collective one. Indeed, the low dimensionality amplifies the role of the quantum fluctuations and enhances correlations. In such a situation, these large quantum fluctuations result in anomalous quantum phenomena (distinct from those in three dimensions), and invalidate any chances for the FL theory to work[4] [7].

This fundamental point was addressed by Tomonaga in 1950, published as a pioneering paper on collective motion of interacting fermions in one spatial dimension [31]. Tomonaga elucidated that collective motion of electrons plays the key role in 1-D correlated electron systems instead of the individual electron motion. These collective excitations, characterised by a velocity u, are analogous to sound waves, i.e., density oscillations, though the oscillating density is the electronic or spin density [32]. From the other side, Luttinger, apparently unaware of Tomonaga's work, treated spin-less, mass-less fermions in one dimension [33]. It was found that the decay of all correlation functions and thermodynamic quantities of a system are controlled by a dimension-less parameter K, the so-called *Luttinger parameter*. Their approach, known as the *Tomonaga-Luttinger model*, has been proven to play a similar key role in one dimension as the FL in higher dimensions, describing the physical properties of most of the 1-D interacting systems (e.g., consisting of bosons, fermions, spins, etc.) as a universal concept. Later, the term *Tomonaga-Luttinger liquid* was coined by Haldane [34] in contrast to the FL, for the renewed theory describing the low-energy properties of 1-D quantum systems[5]. Note that the fractional statistics argued for fractionalised excitations in the spin chains in Section 2.3 is not confined to the low-energy properties of the system but a crucial characteristic of 1-D physics resting more on the 1-D nature.

Given the importance and universality of the TLL concept and the unusual 1-D physics, many experiments have sought to probe the 1-D systems. For more details see e.g. [7, 14, 35–37]. The fundamental interest originates from the fact that there is a fair number of exactly solvable models, allowing the research of non-perturbation effects. In this section, I will review the salient features of 1-D quantum systems widely based on [7, 14, 35, 38]. A brief description of the TLL theory can be found in Appendix A.

Where to look for 1-D physics? Discussing one dimension may seem rather esoteric when living in a 3-D world. A TLL state can develop in various types of situations, e.g., highly anisotropic systems. However, 1-D physics is not necessarily due to highly-anisotropic

---

[4]This ruins the urban legend that 1-D is a toy model to understand higher dimensions!

[5]Haldane received the Nobel prize in 2016 for *theoretical discoveries of topological phase transitions and topological phases of matter*; but many believe he could have gotten it for his TLL theory.

(a)

(b)
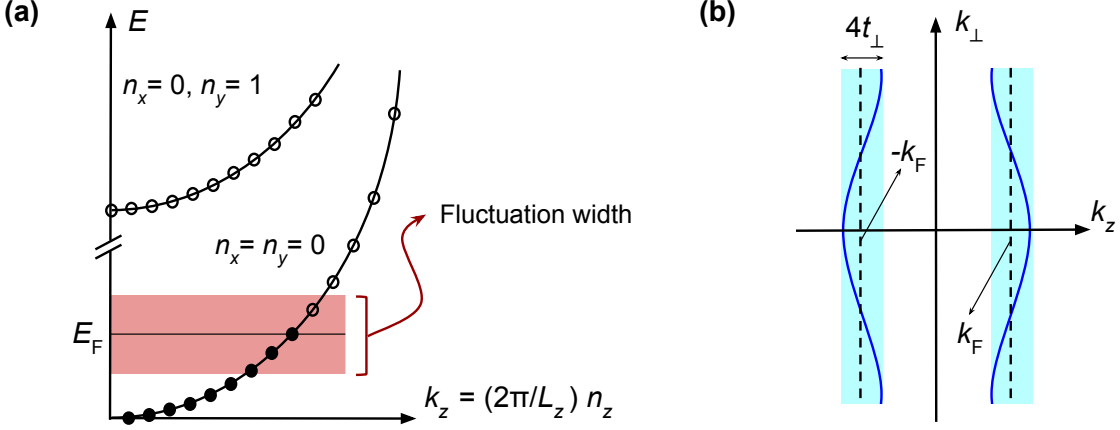
Figure 2.3: Examples of 1-D physics. **(a)** Total energy of non-interacting fermionic gas in a box as a function of the quantum number k_z, with $L_x < L_y \ll L_z$. $(n_x, n_y, n_z) = (0, 0, 1)$ and $(0, 1, 1)$ corresponding to the GS and the first excited state of the system, respectively. Scattering processes, thermal fluctuations, etc., introduce fluctuations to the system, whose width is marked in light red. **(b)** Iso-energy curve of tubes along the z-axis, connected with the hopping term of $t_\perp$ along the two remaining directions. Two dashed $k_\perp$-independent lines at $\pm k_F$ show no hopping is present. The lines distort due to the coherent inter-chain hoppings. For $T \gg 4t_\perp$, the hoppings are scattered by thermal excitations making the tubes independent and leading to a 1-D world. More discussion in the main text.

interactions. One simple alternative circumstance is a quantum mechanical confinement of non-interacting fermionic particles in a box along one direction. Supposing $L_x < L_y \ll L_z$ and a periodic boundary condition, one finds the momenta along the i-axis and the total energy as

$$k_i = \frac{2\pi}{L_i} \cdot n_i, \quad \text{and} \quad E_{\text{tot}} = \sum_{i \in \{x,y,z\}} \frac{\hbar^2 k_i^2}{2m} = \frac{(2\pi)^2 \hbar^2}{2m} \cdot \left(\frac{n_x^2}{L_x^2} + \frac{n_y^2}{L_y^2} + \frac{n_z^2}{L_z^2} \right), \quad (2.9)$$

with $n_i \in \mathbb{Z}^+$ and minimally one n_i non-zero. Tuning the quantum numbers n_i along the x- and/or y-direction will lead to a huge shift in the energy. Nonetheless, since L_z is so large, one can call the related variables along the z-axis roughly continuous variables. Dispersion relations for $(n_x, n_y, n_z) = (0, 0, 1)$ and $(0, 1, 1)$, corresponding to the ground and the first excited states of the system, are illustrated in Figure 2.3 **(a)**. The fermions occupy the states from the lowest energy up to the Fermi level depicted by the solid black line. Occupied and unoccupied states are marked as full and empty circles, respectively. However, the particles can get excited by various sources, e.g., scattering processes, thermal fluctuations, etc., within a band highlighted in light red. This band's width is a function of different parameters, e.g., T or the strength of the interactions. Narrow-enough widths of the bands compared to the seperation of the two bands [$n_x = n_y = 0$ and $n_x = 0, n_y = 1$] will proscribe any changes in the n_x or (and) n_y quantum number(s). This means that in any scattering process or despite thermal fluctuations, n_x and n_y are constant and the only quantum number that can change is n_z, associated with the longitudinal direction. Hence, the WF $\Psi(x, y, z)$ holds a transverse function fixed independent of x and y, and only the longitudinal
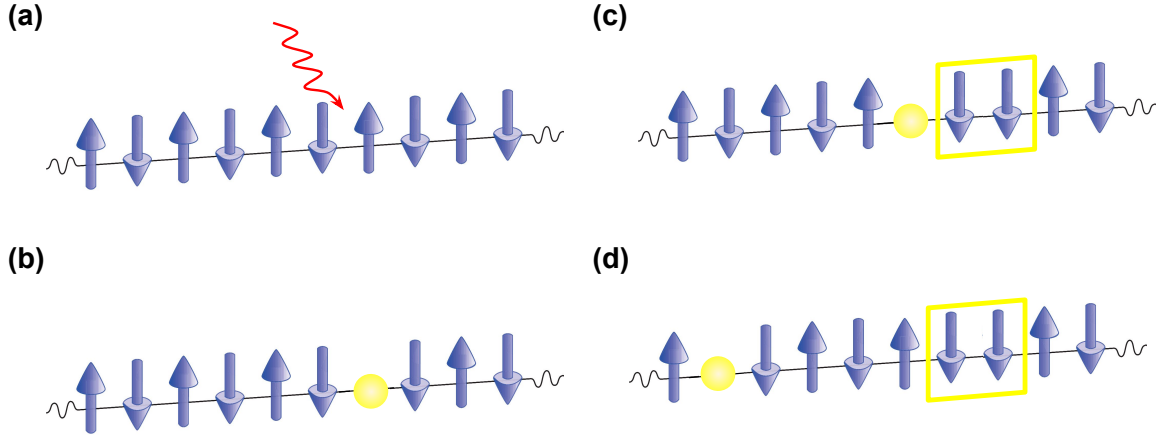
Figure 2.4: Cartoon of spin-charge separation in one dimension. **(a)** An electron is removed from the AFM Mott insulating state by a photon in a photo-emission experiment. **(b)** This leaves behind a disruption in both the spin and charge order. **(c)-(d)** As electrons move into the vacant site, the locations of the spin and charge disorder separate acting as distinct particles: (i) A spinon and (ii) a holon. Figures reproduced from [14, 35].

function $\Psi_Z(z)$ varies, i.e., $\Psi(x, y, z) = \Psi(z)$. In this case, all the quantum mechanical properties depend on the longitudinal quantum number.

Another instance is realised for a low probability of hopping in transverse directions: Suppose a system comprised of tubes along the z-direction (longitudinal) connected to each other by tunnelling terms of t_x and t_y in the transverses directions, namely $t_\perp$. The energy along the tubes ε_z, is modified by the tight-binding energy of hopping between the tubes, i.e., $-2t_\perp \cos(k_\perp)$. Figure 2.3 **(b)** represents the iso-energy curve for an exemplary energy of $\varepsilon_z = E_{\mathrm{F}}$. Two dashed lines at $\pm k_F$ illustrate *no-hopping*, in which $k_z = k_F = $ const. independent of the $k_\perp$. The tight-binding term of the dispersion from the other side, distorts the surface of the constant energy. The blue lines that are not flat reflect the coherent hopping of the particles between the various chains. If $T \gg 4t_\perp$, the thermal fluctuations will blur completely the surface (highlighted by light blue). Thus, one fails to distinguish the flat surface from the distorted one by the tunnelling. In principle, the hoppings are suppressed as scattered by thermal excitations, making the various chains a kind of independent collection with no possible coherent jumps between the chains. In closing, a certain crossover T would exist above which the system is 1-D, and 2(3)-D at lower T.

Experimentally, 1-D systems can be mainly detected in three cases [32]: (i) Cold atomic gases, in which interfering lasers are utilised to trap neutral atoms in an artificial lattice and control the hopping parameters, (ii) edge states, where the 1-D physics at the edge of the samples appear different from the bulk properties, and (iii) magnetic insulators, in which the two-state spin system of $S = 1/2$ can be mapped onto a hard core boson. In this circumstance, a spin-down is the absence of a boson on a site, and a spin-up can be mapped to the presence of the boson. A spin chain problem is thus strictly equivalent to mobile bosons hopping on a lattice. The magnetic insulator $YbAlO_3$ studied in this research shows the TLL state before its dimensional-crossover to 3-D at very low T (More in Chapter 3).

Spin-charge separation: An electron, carrying both spin and charge, cannot exist as a well-defined individual particle in the 1-D world. It instead dissolves into two separate

entities, moving independently and forming the spin and charge density eigenstates. In such a circumstance, the spin and charge excitations are known as *spinons* and *holons*, respectively. This effect cannot be described by FL theory. That is one of the basic properties of the TLL theory and the cornerstone of the description of 1-D materials, leading to the remarkable phenomenon of *spin-charge separation* [14, 39]. Figure 2.4 illustrates a simple picture of how this phenomenon occurs considering a single electron in a Mott insulator state, where the effect of the screened Coulomb interaction is irrelevant, and the physics of the $t-j$ model. Figure 2.4 **(a)** shows an AFM arrangement of the spins. The wave arrow shows symbolically that the spin chain is about to be hit by a photon in a photo-emission experiment. Once an electron is removed from the chain both the spin and the charged state are left behind. The vacant site is illustrated by a yellow ball in Figure 2.4 **(b)**. As the hole moves, the position of the hole and that of the spin structure perturbation (highlighted with a yellow box) are moved apart, leading to the so-called spin-charge separation. This effect is observable in Figures 2.4 **(c)**-**(d)**. In fact, the spin and charge of the original electron have separated and formed independent entities. These two branches show up in the dispersion of an infinite system with different propagation velocities. Finally yet importantly, per lowering the system dimensionality to one, the single sharp QP peak in the spectral function of the FL dissolves into two sharp features characterising the spin and charge parts of the electron moving with differing velocities (e.g., see [38]).

FL breakdown in one dimension:
Interactions among particles are what endows the 1-D world with its special properties. In Figure 2.5, cartoons of a free electron gas in the above-one and one dimension are given with purple (left) and yellow (right) balls. Landau QP as nearly-free excitations exist in high dimensions. An electron trying to propagate in one dimension, however, has to push its neighbour. That makes any individual motion forbidden and converts individual excitations into collective ones. Violating the existence
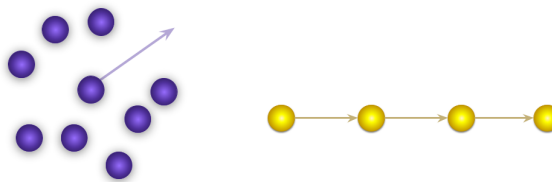
Figure 2.5: Free electron gas in high and one dimensions. Nearly-free QP excitations as individual particles are possible in high dimensions (purple). In 1-D world, single particle cannot move without pushing the others, and thus only *collective* excitations exist (yellow). Figure reproduced from [7].

of the Landau QP as the essence of the FL collapses the theory in 1-D and brings the need for a reborn one. Furthermore, the transformation of the motions from individual to collective leaves drastic consequences and makes it impossible to escape any interaction, no matter how weak. In such circumstances, strong effects of quantum fluctuations will emerge. Likewise, both the GS and excitations exhibit strong correlation effects. Tomonaga and Luttinger proceeded to construct an effective low-energy theory similar to what led to the FL by Landau; nevertheless, they found 1-D appearing quite different. Starting with the free fermionic system, instead of a Fermi surface (FS) we have two Fermi points at $\pm p_F$. The low-energy fermionic states have thus momenta $p \sim \pm p_F$ and single particle energies close to ε_F, and thus $\varepsilon(p) \simeq \varepsilon_F + (|p| - p_F)v_F + \cdots$. Considering the fermion operator with Fourier expansion in the thermodynamic limit, i.e., the length of an imaginary 1-D box goes to infinity, the WF in the position space $\psi_\sigma(x)$ yields to be $\psi_\sigma(x) = \int \frac{dp}{2\pi} \psi_\sigma(p)e^{ipx}$, with spin σ. Fourier components near $\pm p_F$ describe low-energy states. This suggests to stay restricted to the modes of the momentum expansion in a neighbourhood of $\pm p_F$ of width
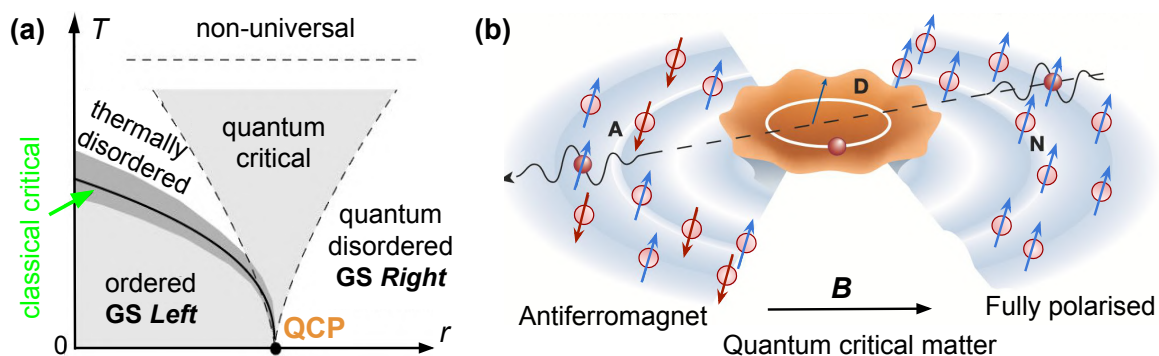
Figure 2.6: Generic phase diagram in the vicinity of a continuous QPT. **(a)** T-r phase diagram. **(b)** Moving across the QC regime at a fixed finite T with B as the tuning parameter. More argument in the text. Figures reproduced from [40, 41].

2Λ,

$$\psi_\sigma(x) \simeq \int_{-\Lambda}^{\Lambda} \frac{\mathrm{d}p}{2\pi} e^{i(p+p_F)x} \psi_\sigma(p+p_F) + \int_{-\Lambda}^{\Lambda} \frac{\mathrm{d}p}{2\pi} e^{i(p-p_F)x} \psi_\sigma(p-p_F). \tag{2.10}$$

At this point, one may define *right* and *left* moving fields $\psi_{\sigma,R}(x)$ and $\psi_{\sigma,L}(x)$ as

$$\psi_\sigma(x) \simeq e^{ip_F x} \psi_{\sigma,R}(x) + e^{-ip_F x} \psi_{\sigma,L}(x). \tag{2.11}$$

In Relation 2.11, we have split off the rapidly oscillating piece of the field and focus on the slow parts, i.e., $\psi_{\sigma,R}(x)$ and $\psi_{\sigma,L}(x)$, whose Fourier transforms are $\psi_{\sigma,R}(p) = \psi_\sigma(p+p_F)$ and $\psi_{\sigma,L}(p) = \psi_\sigma(p-p_F)$, respectively. In closing, following the effective low-energy theory in one dimension similar to the one for the FL ends up in collective excitations (right and left movers) instead of the standard fermionic excitation expected in the higher dimensions from the Landau's QP and thus demonstrates the failure of Landau's FL in 1-D systems.

2.5 Quantum critical phenomena

At high T, non-universal lattice physics occur as the correlation length is not as large as the microscopic length scale, namely the characteristic de Broglie wave-length of the excitations at the QCP [40, 42]. However, materials possessing distinct adjoining quantum phases at zero T can display universal behaviour insensitive to microscopic details, the so-called *quantum criticality*, in a certain region of the phase diagram [43]. Universality due to formation of small regions or *droplets* with nascent order close to a phase transition (PT) explains the continuity of the PT. The short-lived ordered droplets grow as the system is tuned to its critical point. At the critical point, the material is spanned by the ordered droplets of all sizes [41]. A generic phase diagram of T versus a relevant tuning parameter of r is sketched in Figure 2.6 **(a)**. r is usually accessible with hydrostatic pressure, chemical doping or magnetic field in experiments; the last is the case in this research.

Starting at the low extreme of the tuning parameter, there is a classical phase transition (CPT) from a high-T thermally-disordered state to a lower-T ordered state. The solid line is the finite-T boundary between the ordered and disordered phases. The term disordered in the latter refers to a phase without long-range order rather than a randomness in the Hamiltonian [44]. The critical behaviour across this transition is classical, i.e., the long-range

order is destroyed via the random thermal motion of molecules, ions or spins per increasing T across the PT [42, 45]. With increasing the tuning parameter r, the transition T of the quantum state *Left* is suppressed to zero T. In 1976, Hertz [46] discussed for the first time a CPT shifted to zero T by a non-thermal tuning parameter: The so-called *quantum phase transition* (QPT) can emerge at zero T due to quantum fluctuations associated with Heisenberg's uncertainly principle, and the point at which it occurs is a QCP. Hertz described the foreshadowing droplets with ordered states to be quantum mechanical rather than classical. Termination of the thermal motions at zero T leaves only the zero-point motions relevant for obeying the uncertainty principle of position and velocity. At the high extreme of r lies a quantum disordered state labelled as GS *Right*. Close to the QCP, both parent GSs are equally energetically favourable, and the requirement of a unique quantum GS is broken. Therefore, quantum fluctuations governed by Heisenberg's uncertainty principle can flip increasingly large regions of the system back and forth between the two. These quantum fluctuations between competing GSs get stronger as the GS energies approach one another, driving the QPT at the QCP [41, 42, 45].

At elevated T near the QCP, the system exists in a quantum critical (QC) regime, where physical properties are not derived from the quantum mechanical state of either *Left* or *Right* but instead dominated by the quantum fluctuations and exhibit behaviour different from both parent states. That is opposite to the conventional stable phases and develops around the precarious point of instability between the two stable *Left* and *Right* states of the matter. At non-zero T, thermal fluctuations increasingly mix with the quantum fluctuations, smearing out the energy scales involved and widening the QC regime. For a continuous QPT at $0\,\mathrm{K}$ from the AFM to field-polarised states per increasing B, the matter undergoes a quantum critical phase at $T > 0$. Figure 2.6 **(b)** illustrates the growth of the corresponding quantum critical matter at finite T in the vicinity of the QCP. The droplet with an ordered state faces with the impossible choice between the GS *Left* and *Right*. Instead, it settles into an entirely new state with its own unique GS, built upon the quantum fluctuations between the two competing parent GSs. This novel emergent state is usually confined to a small region of the phase diagram around the QCP, where quantum fluctuations are strong and thermal fluctuations are weak [41, 46].

2.6   Summary

Spontaneous (anti-)ferromagnetic ordering happens owing to exchange interactions between magnetic moments. However, a competition of the magnetic interactions of the neighbouring spins can inhibit ordering and result in frustration. Anisotropy of interactions can lower the effective dimensionality of a spin system to one, namely result in spin chains in a specific temperature (T) range. One-dimensionality has exotic consequences different from the ones of a Fermi liquid (FL). The most famous instances are the fractionalisation of the magnetic excitations, or the spin-charge separation. These non-FL behaviours are well-described by the Tomonaga-Luttinger liquid (TLL) theory.

A quantum phase transition (QPT) can occur at $0\,\mathrm{K}$ by tuning a non-thermal parameter, e.g., magnetic field. The point at which this QPT takes place at zero T is a quantum critical point (QCP), and the QPT at this point is another example where the FL behaviour is violated. In the absence of thermal fluctuations at $0\,\mathrm{K}$, the QPT is driven by the zero-point quantum fluctuations associated with Heisenberg's uncertainty principle.

3 Introduction to YbAlO$_3$

3.1 Introduction

From a theoretical point of view, one-dimensional (1-D) quantum magnets are among the best-understood quantum many-body systems. Such systems have been studied for long time as a simple model; however, the major progress has been achieved during the past decade [47–56]. Since 2019 that YbAlO$_3$ was found to be a quasi-1-D (Q-1-D) quantum anti-ferromagnet, it has been under both theoretical and experimental interest including the current research. This chapter gives an introduction to YbAlO$_3$. The crystal structure and single-ion anistropy are discussed initially. Then, I give a general introduction to the system being a Q-1-D quantum anti-ferromagnet. This is followed by a preliminary phase diagram obtained from thermodynamic-property measurements, including a summary on magnetisation (M) and specific heat (C) data. Then, I summarise some theoretical descriptions of how the single-ion anisotropy can influence the ground states (GS) in the incommensurate (IC) anti-ferromagnetic (AFM) sub-phases characterised by spin density wave (SDW) and putative canted transverse anti-ferromagnetic (TAF) orders. At this point, we can get the advantage of the theoretical calculations to adjoin the experimentally undetected GS of the IC region, i.e., most probably TAF, and improve the preliminary empirical phase diagram. I complete this with a summary on some theoretical studies on thermal conductivity (κ).

3.2 Crystal structure & single-ion anisotropy

YbAlO$_3$ crystallises in an orthorombically distorted perovskite structure, with room-temperature lattice parameters of $a = 5.126$ Å, $b = 5.331$ Å and $c = 7.313$ Å, using the conventional *Pbnm* notation [57, 58]. The special chemical environment leads to a distortion of the crystal structure and lowers the point symmetry of the rare-earth (RE) ion *Re* site from O_h ($m\bar{3}m$) in the perfect cubic perovskite structure (space group $Pm\bar{3}m$) to C_S (m) [59]. In such circumstances, the *Re* moments are either constrained along the *c*-axis as in the case of Er^{3+} or Tm^{3+} [60, 61], or are forced to lie in the *ab*-plane such as Dy^{3+}, Tb^{3+} and Yb^{3+} ions moments [62–65]. In this latter case, the point-group symmetry determines no high-symmetry directions, which may be favoured by the *Re* moments for alignment. Figure 3.1 **(a)** displays the YbAlO$_3$ crystal structure with the ytterbium ions surrounded by eight nearby distorted aluminium-oxygen (Al-O) octahedra. This local chemical environment pins the Yb^{3+} ions magnetic moments in the *ab*-plane and leads to a tilting with respect to the *a*-axis (see Figure 3.1 **(b)**). The tilting angle together with the RE crystalline-electric field (CEF) splitting are dictated by the relative distortion of the eight Al-O octahedra [59].

Calculations: Wu *et al.* used a point-charge model [67–70] to calculated the GS wavefunctions (WF) and the CEF configuration [59]. Similar to the case of the iso-structural compound DyScO$_3$ in a previous study [62], the first twelve nearest oxygen neighbours of the eight Al-O octahedra around each Yb^{3+} were considered to keep the correct local point-group symmetry (C_S) of the Yb site. The unpaired electron in the $4f^{13}$ shell of the Yb^{3+} ions defines the magnetic properties of the compound with $J = 7/2$ ($L \otimes S = 3 \otimes 1/2$). The low point symmetry of the local crystallographic surrounding splits the eight-fold degenerate multiplet of Yb^{3+} ($2J + 1 = 8$) into four Kramers doublet states [59]. It has been shown
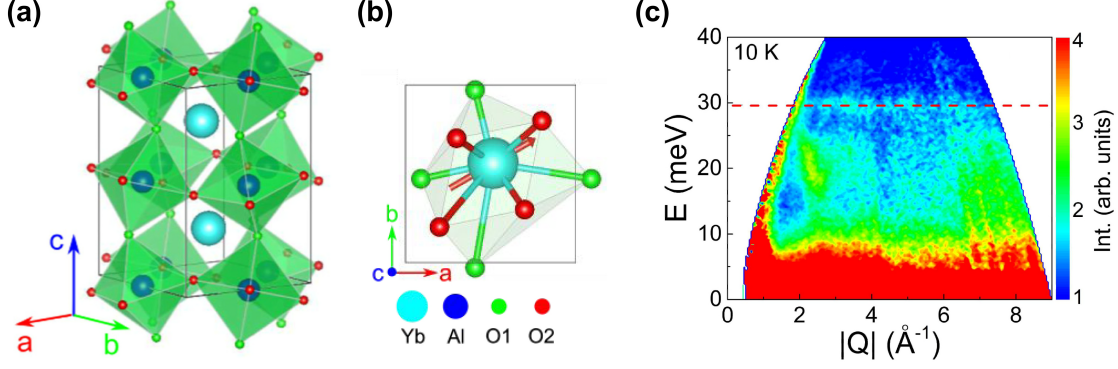
Figure 3.1: Crystal structure and crystalline-electrical field of YbAlO$_3$. **(a)** Sketch of the crystal structure of YbAlO$_3$. Cyan, dark blue and red+green balls represent Yb, Al and O ions, respectively. Yb ions are surrounded by eight nearby distorted Al-O octahedra as shown. **(b)** Local chemical environment of Yb^{3+} located at $c/4\, \hat{\boldsymbol{c}}$ ($\hat{\boldsymbol{c}}$ is a unit vector along the c-axis), considering twelve nearest oxygen neighbours: Four O1 (green) sites in the same $c/4$-plane, four O2 (red) sites above and four below. The red vector displays the magnetic moment of Yb^{3+}, lying in the ab-plane, with a tilting angle of 22° with respect to the a-axis. **(c)** Contour plot of the INS spectrum measured at 10 K. The flat CEF mode of the first-excited level is observed and indicated by the red dashed line. Figures from [59, 66].

theoretically that a local Ising-axis tilted from the a-axis at $\varphi = 22°$ diagonalises the four CEF doublet states the best (indicated by the red vector in Figure 3.1 **(b)**) [59]. By virtue of the tilting of the easy axis in the ab-plane, the coordinate system may be rotated to set the quantification z-axis parallel to it using the coordinate transformation, e.g., as

$$\hat{\boldsymbol{x}} = \hat{\boldsymbol{c}}, \quad \text{and} \quad \begin{pmatrix} \hat{\boldsymbol{y}} \\ \hat{\boldsymbol{z}} \end{pmatrix} = \begin{pmatrix} \sin\varphi & -\cos\varphi \\ \cos\varphi & \sin\varphi \end{pmatrix} \begin{pmatrix} \hat{\boldsymbol{a}} \\ \hat{\boldsymbol{b}} \end{pmatrix}. \tag{3.1}$$

For the z-axis along the easy-axis, the WF of the GS is calculated to be

$$|E_{0\pm}\rangle = +0.78\,|\pm 7/2\rangle - 0.03\,|\mp 5/2\rangle - 0.53\,|\pm 3/2\rangle \mp 0.14\,|\mp 3/2\rangle$$
$$\pm 0.18\,|\pm 1/2\rangle + 0.23\,|\mp 1/2\rangle, \tag{3.2}$$

with the excited levels separated with energies $\Delta = 6.7$ meV, 24.1 meV and 47 meV from the GS doublet [59]. Therefore, the calculations suggest qualitatively an Ising-like GS doublet with most contribution from $|\pm 7/2\rangle$, and well separated from the first excited CEF level.

Experiments: The single-crystal inelastic neutron scattering (INS) data at 10 K exhibit a flat wave-vector-independent mode (Figure 3.1 **(c)**), representing the excitation from the GS to the first excited CEF level. The energy dependence of the integrated intensity has a peak at $\Delta_{\mathrm{CEF}} \simeq 29.7 \pm 0.1$ meV (~ 345 K) suggesting a well-separated GS doublet dominating the low-T magnetic properties [59, 66]. M data versus field (B) at 2 K, along the two principal a- and b-axes are presented in Figure 3.2 **(a)** and **(b)**, respectively. The low-T magnetic properties are dominated by the GS doublet thanks to the relatively low experimental T and B, namely 2 K and < 5 T, compared to the energy scale of the first excited CEF level ($\Delta_1 = 29.7$ meV). In this case, the isolated GS doublet can be described as an effective $S = 1/2$ state, with $M = g_{\mathrm{eff}}\mu_{\mathrm{B}} \cdot S$. The saturation moments for different B directions are
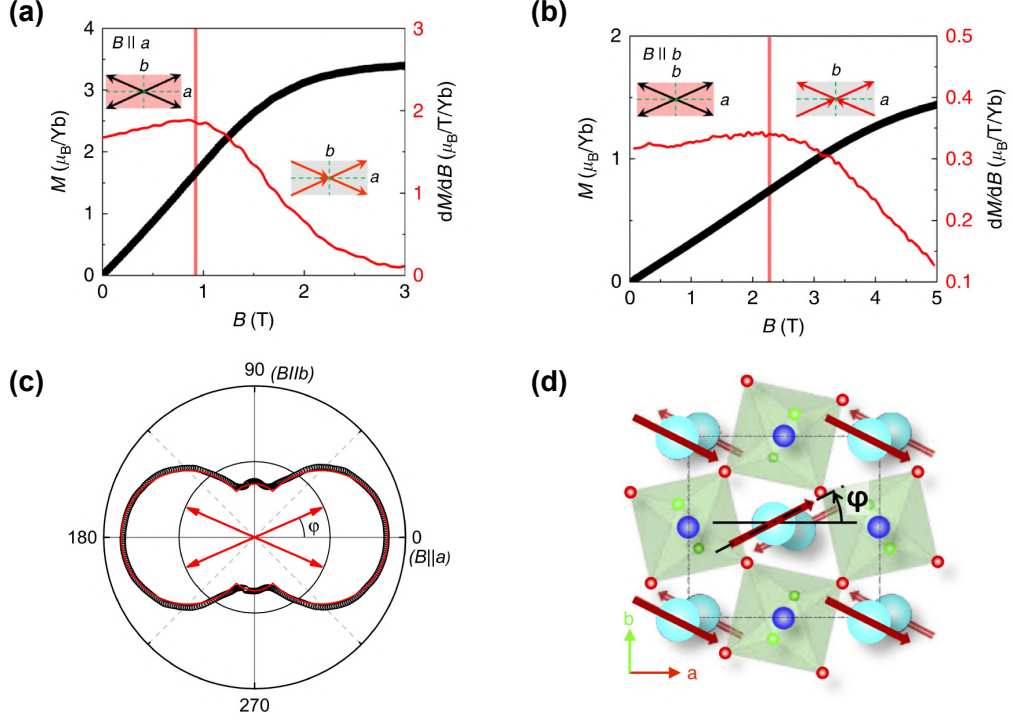
Figure 3.2: Single-ion anisotropy of YbAlO$_3$. **(a)-(b)** $M(B)$ (black circles) and magnetic susceptibility dM/dT (red line) at 2 K, with $B \parallel a$ and b as indicated. **(c)** Angular dependence of M measured in the *ab*-plane at $B = 5$ T and $T = 2$ K. Red arrows show schematically a moment configuration of Yb^{3+} at zero B with $\varphi = 23.5°$ between the *a*-axis and the Yb^{3+} moment. The solid line is the calculation as described in the text. **(d)** A possible configuration of the magnetic moments of the Yb^{3+} ions. Figures are reproduced from [59, 71].

reported as $M_s^a = M_s \cos\varphi \simeq 3.47 \mu_B/$Yb, $M_s^b = M_s \sin\varphi \simeq 1.54 \mu_B/$Yb, and $M_s^c \simeq 0.23 \mu_B/$Yb, indicating a significant anisotropy between the *ab*-plane and the *c*-axis [59]. The high-B saturation moments along the *a*- and *b*-directions are more than one order larger than the moment along the *c*-axis, confirming that the Yb^{3+} moments are locked to the *ab*-plane.

Figure 3.2 **(c)** depicts the angular dependency of M within the *ab*-plane at 5 T. Considering θ and φ being the angle between the applied B and the Ising moments both with respect to the *a*-axis, Figure 3.2 **(c)** shows two minima at $\theta = 90° \pm \varphi$, well-described by $M(\theta) = M_s \left(|\cos\varphi - \theta| + |\cos\varphi + \theta|\right)/2$. This suggests two different Yb^{3+} magnetic sites, with two easy axes, in the *ab*-plane spanning angles of $\pm\varphi$ to the *a*-axis. Substituting the saturation moment $M_s = 3.8 \mu_B/$Yb, the tilting angle of the local easy-axis relative to the *a*-axis φ is found to equal 23.5° [72]. In 2022, Ehlers *et al.* confirmed the two magnetic sites with their easy-axis tilting angles of $\pm23.5°$ via two separate signals detected in electron spin resonance (ESR) local probe [73]. A possible configuration of the Yb^{3+} magnetic moments fixed at the angle φ is given in Figure 3.2 **(d)**. In closing, the anisotropic $\hat{g}$-tensor can be calculated to be [59, 74]

$$M_s^z = M_s = 3.8 \mu_B/\text{Yb}, \qquad g_{\text{eff}}^{\parallel} = g_{\text{eff}}^{zz} = 7.6, \qquad (3.3)$$

$$M_\perp = M_{xy} = M_s^c = 0.23 \mu_B/\text{Yb}, \qquad g_{\text{eff}}^{\perp} = g_{\text{eff}}^{xx} = g_{\text{eff}}^{yy} = 0.46, \qquad (3.4)$$

17

with $M_s^z = g \langle E_{0\pm}|J_z|E_{0\pm}\rangle$ as the saturation magnetisation along the local-moment Ising easy-axis, $g = 8/7$ as the Landé factor of Yb^{3+}, and the x and y as the perpendicular directions. These values are in good agreement with $g_{\text{eff}}^{\parallel} = 7.01$ and $g_{\text{eff}}^{\perp} = 0.47$ found via ESR [73]. Similar effective g-factors were reported in earlier studies via Mössbauer effect and electron paramagnetic resonance as well [75, 76].

Discussion: Combining the results of paragraph § **Calculations** and § **Experiments**, (i) in agreement with the CEF calculations, M measurements reveal that the GS is well-separated from the excited levels [59]. (ii) B- and angular-dependent M plus the ESR results reveal a strong uni-axial (Ising-like) single-ion anisotropy of the Yb^{3+} ions, with the c-axis in the hard-plane and easy-axis in the ab-plane. The tilting angle of the local easy-axis relative to the a-axis φ was measured to be $23.5°$ in acceptable accordance with the computed value of $22°$ (see e.g. [59, 73, 74]). (iii) Despite of some discrepancies in the absolute values, the CEF calculations and the experimental results agree on the huge anisotropy predicting $g_{\text{eff}}^{xx} \approx g_{\text{eff}}^{yy} \ll g_{\text{eff}}^{zz}$ (see e.g. [59]). This brings the GS WF extracted from the measured M_s and the given symmetry, consistent with the one from the calculations. It is remarkable that the twelve-oxygen approximation of the nearest neighbours is practical in the point-charge CEF calculations; even though, it fails in quantitative predictions, e.g., (i) does not reproduce quantitatively the real WF of the GS. (ii) the energy scale of Δ_{CEF} was measured ($\sim 29.7\,\text{meV}$) to be way larger than that of the CEF calculation ($\sim 6.7\,\text{meV}$). Also not shown here, the measured $M(B)$ is lower than the calculated Brillouin function at fields before saturation [59]. This implies an additional AFM correlation, which is not taken into account in the calculations.

3.3   YbAlO₃ as a quasi one-dimensional spin system

In YbAlO₃ as one of the lately-found Q-1-D quantum magnets [66, 74], spin chains running along the crystallographic c-axis carry an effective inter-chain exchange interaction roughly $20\,\%$ of the intra-chain: $J_{ab}/J_c \simeq 0.04/0.21 \simeq 0.19$ (see Supplementary Materials of [74]). Wu *et al.* reported the zero-B spectrum of INS on single-crystal YbAlO₃ having gapless spinon excitations along the chain direction (00L) at $1\,\text{K}$ with a broad two-spinon continuum extending from 0 up to about $0.7\,\text{meV}$ in energy transfer (Figure 3.3 **(a)**) [74]. An effective spin-$1/2$ model, as *XXZ* spin chains with weak inter-chain dipole-dipole coupling under a longitudinal B with respect to the Yb^{3+} magnetic moments ($B \parallel a$), describes the system properly[1] [77, 78]. Above Néel orderings (discussed later), thermal fluctuations destroy any inter-chain ordering and weak dipole-dipole interactions become negligible. The Hamiltonian reads

$$H = J\sum\nolimits_{<i,j>}(S_i^x S_j^x + S_i^y S_j^y + \Delta \cdot S_i^z S_j^z) - g\mu_{\text{B}}B\sum\nolimits_i S_i^z, \qquad (3.5)$$

where J is the isotropic exchange interaction, i and j are nearest-neighbour sites, x, y, and z are defined as in Relation 3.1, $\boldsymbol{S}_{\text{i}} = \{S_i^x, S_i^y, S_i^z\}$ denotes a spin-$1/2$ operator defined at site i, Δ is the parameter of exchange anisotropy[2], g is the gyromagnetic factor, μ_{B} is the Bohr magneton and B is applied along the a-axis [74, 79]. In this 1-D chain picture, the elementary excitations are fractional spinon quasi-particles (QP) ($S = 1/2$) instead of the conventional magnons ($S = 1$) of a magnetically ordered state.

Below $T_{\text{N}} = 0.88\,\text{K}$, the dipole-dipole inter-chain interactions, despite being weak, bring a

---

[1]Similar physics is expected for $\parallel b$ though at higher B by a factor of $\cot\varphi \sim 2.4$ due to the moments' tilting.
[2]$\Delta J \to \infty$ yields the Ising model. $\Delta = 1$ and $\Delta = 0$ reproduce the *XXX* and *XX* Hamiltonians, respectively.
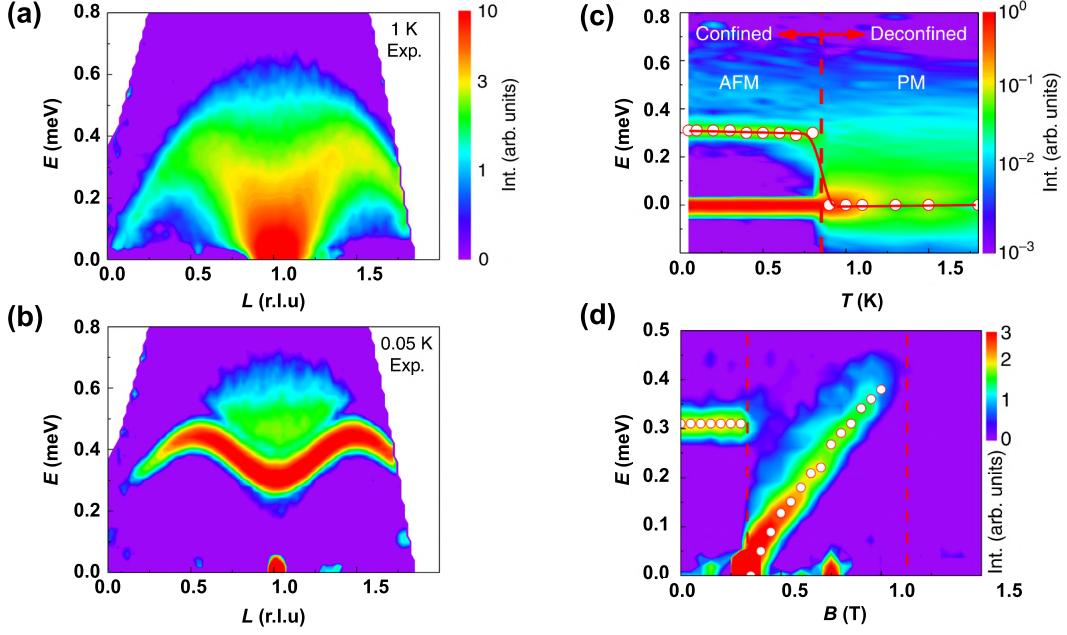
Figure 3.3: **(a)**-**(b)** Experimental INS results of YbAlO₃ in zero B. Spectra with background corrected measured at **(a)** 1 K and **(b)** 50 mK, above and below T_N, respectively. **(c)** T evolution of the energy-dependent neutron scattering spectrum integrated in window H = [-0.1, 0.1] r.l.u., K =[-0.1, 0.1] r.l.u., L = [0.9, 1.1] r.l.u. A gapless continuum is observed at high T, whereas a gap of about 0.3 meV (red circles) opens just at T_N, due to the appearance of B_{st}. **(d)** B evolution of the energy-dependent INS spectrum, at 50 mK, integrated over wavevector H = [-0.1, 0.1] r.l.u., K = [-0.6, 0.2] r.l.u., L = [0.9, 1.1] r.l.u.. The empty circles indicate the peak positions. Figures from [74].

three-dimensional (3-D) AFM ordering in the system (inter-chain interactions and magnetic orderings are discussed further in Appendix Section B.1). That is taken into account in the model by introducing an effective staggered molecular field B_{st} in the Hamiltonian (next paragraph). In agreement with the analytical result for the spin-1/2 Heisenberg model with a B_{st} [80], a significant gap is observed below T_N with a multi-spinon continuum extending from about 0.3 - 0.7 meV (Figure 3.3 **(b)**) [74]. Figure 3.3 **(c)** presents the T evolution of the energy-dependent scattering at the AFM zone centre $\boldsymbol{Q} = (001)$. The gap opens once entering the 3-D AFM ordered phase at T_N. It is noteworthy that application of a longitudinal B tunes the gap in the spectrum and induces phase transitions at lowest T [14, 81]. As depicted in Figure 3.3 **(d)**, at the critical field $B_{c1} = 0.32$ T, the spin excitation gap in the magnetic-zone centre $\boldsymbol{Q} = (001)$ closes abruptly as the static AFM is suppressed in favour of an IC ordering. Once entering the IC-AFM phase, the closed spin gap opens again and increases almost linearly till saturation at $B_c \sim 1.15$ T, where it gets gapless at (000).

Figure 3.4 **(a)** displays the zero-B magnetic structure below T_N. The ferromagnetic (FM) alignment of the Yb Ising moments in the ab-plane generates B_{st} (large red and blue arrows). This phenomenon is well explained via a two-magnetic-sub-lattices model, described further in Appendix Section B.2. Below T_N, B_{st} produces a confining potential that increases linearly with the distance between both spinons, leading to strong confinement of the two spinons [80]. That appears in the Hamiltonian as an extra term of $B_{st} \sum_{<i>} (-1)^i S_i^z$.
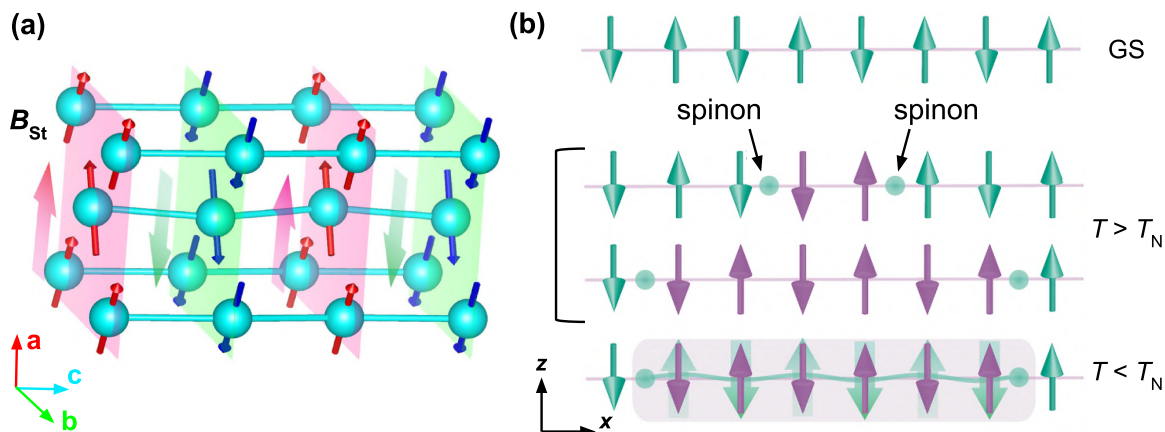
Figure 3.4: Magnetic structure and spinon confinement in YbAlO$_3$. **(a)** Zero-B magnetic structure below 0.88 K, where the AFM chains are coupled ferromagnetically, resulting in a net B_{st} indicated by the large red and blue arrows. **(b)** Sketch of the spinon generation, confinement and deconfinement in a 1-D AFM chain. Spinon excitations in a Heisenberg chain are created by the flip of two spins of the GS. In the two consecutive pictures, the excitations propagate outwards freely (deconfined) along the chain at $T > T_N$. Propagation of the spinons in the presence of B_{st} at $T < T_N$ costs energy by increasing the separation length (confinement), shown in last sketch as a grey box. Figures reproduced from [74].

Figure 3.4 **(b)** exemplifies the spinon QP generation and deconfinement in a 1-D AFM chain. The first picture displays one AFM chain in the GS. Since only longitudinal fluctuations of $\Delta S_z = 0$ are possible, even numbers of Yb^{3+} moments are flipped in the AFM GS, creating pairs of spinons. At $T > T_N$, the excitations propagate freely along the chain, being namely deconfined. Below T_N, the effective B_{st} confines the spinon excitations, since extra energy is required to part the AFM domain walls further as implying more spins anti-parallel to B_{st} with an energy cost increasing linearly with spinon seperation [74]. This effect is called *spinon confinement*, and gives rise to bound spinon states below T_N [82].

3.4 Phase diagram: Thermodynamic probes

Figure 3.5 shows a summary of the magnetisation and specific heat depending on T and B along the a-axis, taken from the PhD thesis of *S. E. Nikitin* [71]. Figure 3.5 **(a)** left axis depicts the B dependency of M normalised to the saturation value M_s, measured at $T = 50$ mK. In order to investigate the B dependency of the M behaviour, the derivative dM/dB is illustrated by a red curve in Figure 3.5 **(a)** right axis. The low-B M is almost zero, while by increasing B at $B_{c1} = 0.32$ T, $M(B)$ jumps to 0.1 of M_s, corresponding to a phase transition. There is a noticeable plateau emerging at $M_s/3$ at $B_{c2} \sim 0.75$ T, seen as a dip in dM/dB. A further increase of B changes the curvature of the $M(B)$ around $B_c \sim 1.15$ T, where it saturates. Figure 3.5 **(b)** shows vertically-shifted $M(B)$ curves for some selected T between 0.05 - 1 K, with arrows pointing to the two as-described features of the phase transition at B_{c1} and the plateau at B_{c2}. B_{c1} does not change considerably by increasing T up to 0.6 K and starts to decrease continuously only at higher T. The second characteristic field B_{c2}, however, gets unresolvable by increasing T already above 0.3 K (green curve). T-dependent M in selected B between 0.1 - 0.9 T are shown in Figure 3.5 **(c)**, with relative
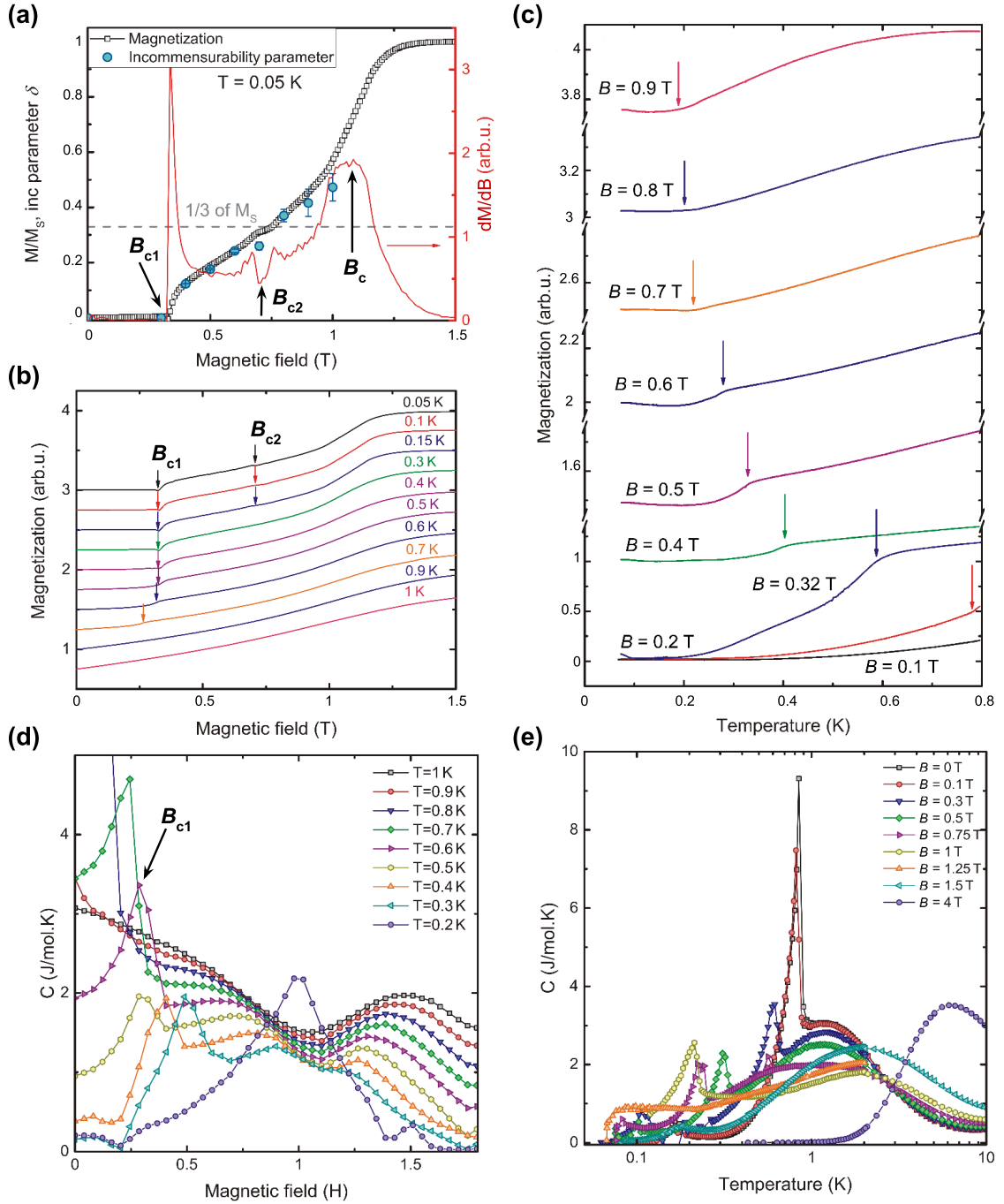
Figure 3.5: Summary of the low-T specific heat and magnetisation measurements taken from *S. E. Nikitin* PhD thesis [71]. Magnetic field are applied along the a-axis. **(a)** Field dependence of the magnetisation and its first derivative taken at $T = 50\,\text{mK}$ (Blue points shows the $\boldsymbol{q}$ position of the zero-energy mode obtained from the INS data). **(b)** Field and **(c)** temperature dependencies of the magnetisation. Arrows show the transition fields. Data on panel **(b)** are shifted for clarity. **(d)** Field and **(e)** temperature dependencies of the magnetic specific heat.

shifts for clarity. Anomalies due to the phase transition to the magnetically-ordered phase are detectable in all curves up to $0.9\,\mathrm{T}$ as marked by the arrows. In the work of S. E. Nikitin, this transition T was extracted as the inflection points of the $M(T)$ curves [71].

Figure 3.5 **(d)**-**(e)** show the B- and T-dependent specific heat results. Starting with the $C(B)$ results, curves at selected T from $0.2\,\mathrm{K}$ to $1\,\mathrm{K}$ are presented in Figure 3.5 **(d)**. All the curves except $T = 0.2\,\mathrm{K}$ exhibit similar behaviour and features: (i) a sharp maximum at low fields (B_{c1}), corresponding to the dip in $\mathrm{d}M/\mathrm{d}B$; (ii) a shoulder-like feature between $0.5\,\mathrm{T}$ and $0.9\,\mathrm{T}$, which gets more pronounced with decreasing T; (iii) a maximum above $1.1\,\mathrm{T}$. In contrast, the curve taken at $T = 0.2\,\mathrm{K}$ shows a single peak at $B_c = 1.05\,\mathrm{T}$ indicating a possible presence of a QPT which accumulates the magnetic entropy [71]. Next, we look at the T dependencies of C below $10\,\mathrm{K}$ for selected B along the a-axis up to $4\,\mathrm{T}$ (Figure 3.5 **(e)**). Two characteristic anomalies are seen at zero B: (i) a sharp peak at $0.88\,\mathrm{K}$; and (ii) a broad anomaly at $T^{*} \sim 2\,\mathrm{K}$ attributed to the inter-chain fluctuations. The former denoted by T_{N}, is a peak due to the phase transition into the long-range AFM order at lower T. By applying $B \parallel a$, this peak shifts to lower T while continuously broadening. It finally disappears at $B_c \sim 1 - 1.25\,\mathrm{T}$. With further increasing B, a typical Schottky-like anomaly is seen at highest T, indicating the presence of gapped excitations [71].

The critical and characteristic points determined from the magnetisation and specific heat data are summarised in Figure 3.6 to form a primary B-T phase diagram on a contour plot of C/T. Different phases of the phase diagram are described in detail in Section 3.5, though several main regions may be highlighted at this moment: (i) The 3-D AFM ordered phase in the low T-range $< T_{\mathrm{N}}$ and $B < B_{c1}$; (ii) A TLL phase, named as *Luttinger Liquid*, dominated by strong 1-D fluctuations above T_{N}. (iii) A field-induced (FI) ordered phase with an IC order parameter between $B_{c1} = 0.32\,\mathrm{T}$ and $B_c = 1.15\,\mathrm{T}$ at T below $\sim 0.25\,\mathrm{K}$; (iv) the field-polarised phase denoted by *Field-induced FM* at fields above B_c; and (v) the region close to B_c, dominated by quantum critical fluctuations.
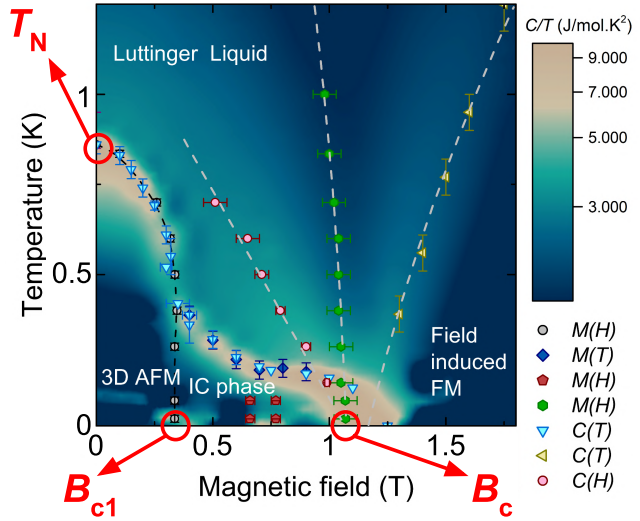
Figure 3.6: B-T phase diagram of YbAlO₃ from the thermodynamics probes. Magnetic phase boundaries are extracted from different measurements. Figure reproduced from [71].

3.5 Ground states of the incommensurate phase

Looking for the GS within the IC phase, Fan *et al.* [77, 78] theoretically described the system considering Heisenberg spin chains with Ising anisotropic inter-chain couplings. The Hamiltonian can be re-written as

$$\mathcal{H} = J_c \sum_i \boldsymbol{S}_i \cdot \boldsymbol{S}_{i+c} + J_{ab} \sum_{i,\delta=\{a,b\}} \left[\epsilon(S_i^x S_{i+\delta}^x + S_i^y S_{i+\delta}^y) + S_i^z S_{i+\delta}^z \right] - g\mu_{\mathrm{B}} B \sum_i S_i^z, \quad (3.6)$$
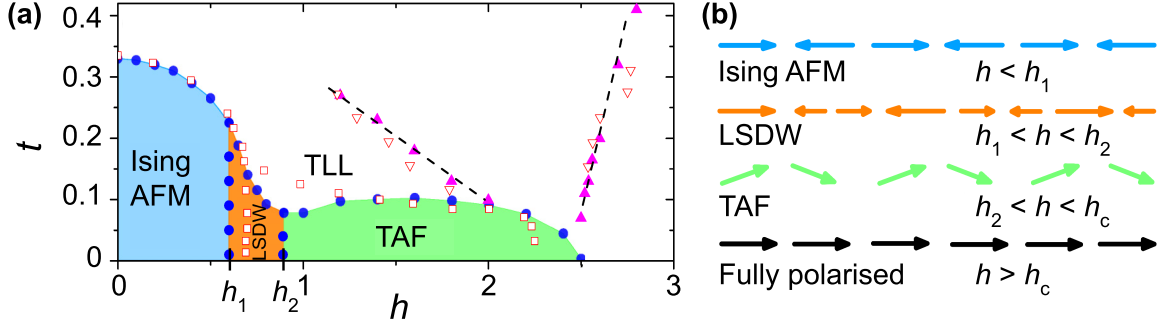
Figure 3.7: Theoretical phase diagram. **(a)** Reduced B-T phase diagram of the model. The calculated and adapted experimental phase boundary data from [74] are shown in filled and open markers, respectively. Filled circles denote the phase boundaries, with the order-disorder transitions determined by the specific heat, and the transitions between ordered phases determined by the change of ordering wavevectors in the spin structure factors. The triangles are the crossover T close to the QCP at h_c. Calculations on structure factor of the system, predict LSDW followed by TAF phases before full polarisation. **(b)** Spin patterns of one chain in Ising AFM, LSDW, TAF and FI-FM orders. Figures reproduced from [77].

where J_c (J_{ab}) is the intra-chain (inter-chain) exchange coupling between the nearest neigh-bouring spins, and ϵ is the spin anisotropy of the inter-chain coupling [77, 78]. Taking J_c as the energy unit, $J_{ab} \simeq -0.2$ for YbAlO$_3$, and reduced B and T may be defined as $h = gB/J_c$ and $t = k_B T/J_c$. Fan *et al.* investigated longitudinal and transverse spin structure factors, i.e., $S^{zz}(\boldsymbol{q})$ and $S^{xy}(\boldsymbol{q})$, and illustrated the GS phase diagram while spanning ϵ and h. They found the dominant spin correlation being always transverse consistent with the previous results of a Heisenberg chain [39], while for $\epsilon < \sim 0.49$ the IC longitudinal spin correlation dominates in certain B regions making longitudinal SDW (LSDW) the local GS. The ϵ-h GS phase diagram suggests LSDW stabilising over a broad ϵ range. That makes a rough guess of $\epsilon = 0.25$ an acceptable value to apply the model to YbAlO$_3$. Figures 3.7 **(a)**-**(b)** illustrate the theoretical phase diagram in the h-t plane and cartoons of GS spin patterns along one chain. At low T, the simulated magnetisation curve suggests a finite gap in the system for $h < h_1 = 0.5$. At $h = h_1$, $S^{zz}(\boldsymbol{q})$ changes from a single sharp peak of an Ising AFM ordered state to two peaks indicating an IC-AFM LSDW state, and vanishes at $h = h_2$. A curvature change arises in calculated $M(B)$ at $h_2 \simeq 0.8$, along with one peak in $S^{xy}(\boldsymbol{q})$ proposing the GS changing from the LSDW to the canted TAF state. This order persists up to a quantum critical point (QCP) at $h = h_c \simeq 1.7$, where M saturates and the system enters the spin polarised state. In YbAlO$_3$, h_1 and h_2 correspond to ~ 0.3 T and ~ 0.9 T, respectively, 6.25 % and 22 % away from the experimental values. The simplification of considering all inter-chain couplings to be FM, though a combination of both FM and AFM are present in real, seems to act as a secondary effect to tune the phase transition [77]. Another possibility is the existence of a third GS not determined in these calculations.

In theory, the propagation wavevector of the zero-B AFM phase is $\boldsymbol{q} = (001)$, changing to $(001 \pm \delta)$ and (001) in the case of the LSDW and TAF phases, respectively. Although experimental observation of SDW via INS are already reported (see, e.g., [74, 79]), the experimental detection of the TAF phase via normal neutron spectroscopy faces two obstacles: (i) The strong spin anisotropy of YbAlO$_3$ diminishes the cross-section of the transverse excitations (being $\propto g^2$) significantly. This makes the longitudinal excitations the main sig-
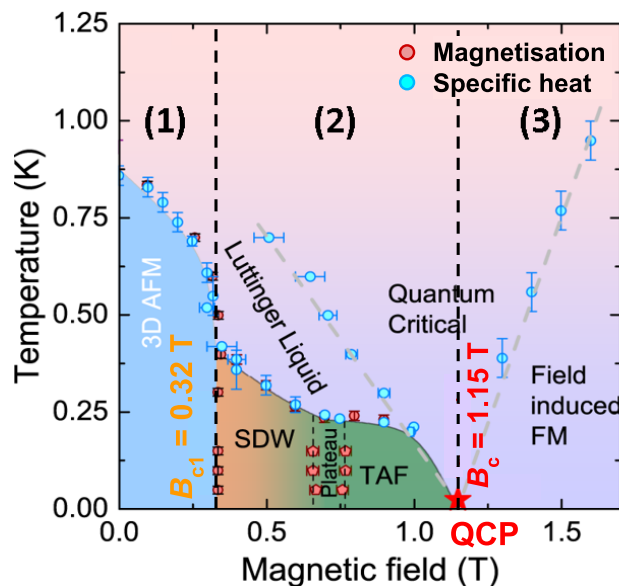
Figure 3.8: Up-to-date *B-T* phase diagram for $B \parallel a$. Coloured areas show three magnetically ordered phases; red points at low T and $B \sim 0.7\,\mathrm{T}$ mark the position of the $M_\mathrm{s}/3$ plateau. Gray dotted lines indicate crossovers between TLL, QC, and FI-FM regimes. Figure reproduced from [79].

nal, and the Bragg peak from the TAF phase as the transverse contribution too weak in the recorded spectrum $(g^{xx}/g^{zz})^2 \sim 1/273$ [83]. Considering that typically a minimum signal-to-background ratio of 1:10 - 15 is needed to distinguish both contributions [84], a huge effort would be required to resolve the TAF signal. This makes polarised neutron spectroscopy a better method rather than the normal neutron spectroscopy [85]. In fact, other local probes are recommended for experimental investigation of the TAF phase, which are not done as of August 2023 yet: (a) The best spectroscopy tool should be muon spin spectroscopy (µSR), where the incident beam carries intrinsically perpendicular polarisation and moments [86, 87]. (b) Nuclear magnetic resonance (NMR) spectroscopy is another proper tool to resolve the transverse excited moments according to their decay to equilibrium, namely spin-spin relaxations [86]. (ii) The measured sample has had a small twin ($\sim 5\,\%$), in which [100]- and [010]-axes are permuted, but the [001] direction is the same (see Supplementary Materials of [79]). The main sample goes to the SDW phase at $B(\parallel a) = 0.32\,\mathrm{T}$, but the twin remains in the AFM phase, appearing as a *B*-independent signal at $\boldsymbol{Q} = (001)$. Above $0.7\,\mathrm{T}$, the twin also goes to the SDW phase and the (001) signal gets *B* dependent till it disappears at $\sim 1.2\,\mathrm{T}$ [83] (in agreement with the phase diagram); however, it is not proved if this is associated with the twin or with the main crystallite [83]. In this circumstance, (a) theoretical investigation considering the twin sample, (b) experimental investigation of a twin-free sample or, (c) applying *B* along the *b*-axis should be helpful.

As discussed later in Chapter 6, the phase diagram of YbAlO₃ is suspected to be more complicated than what is known at the time of writing this text (as of August 2023). However, searching for an up-to-date magnetic phase diagram of this compound for *B* along the easy *a*-axis, one may combine the experimental results [71, 74] summarised in Section 3.4, and the theoretical predictions on the GS of the IC phases. Figure 3.8 provides an updated version of the phase diagram. Compared to the preliminary phase diagram of Figure 3.6,

Compound	v_l (km s^{-1})	v_s (km s^{-1})	$\overline{v}$ (km s^{-1})	Θ_D (K)	Γ	atomic weight (amu/atom)
YbAlO$_3$	6.41	3.51	3.91	538	1.69	49.6
YAlO$_3$	8.54	4.93	5.29	<u>760</u>	1.51	32.8

Table 3.1: Longitudinal, shear, and mean sound velocities, Debye temperature, Grüneisen parameter, and mean atomic weight of polycrystalline YbAlO$_3$ and YAlO$_3$ ceramics. The underlined value is obtained experimentally. Values from [88–90].

the IC-AFM phase comprises SDW and TAF sub-phases with a plateau phase emerging at the interface (close to $M = M_\mathrm{s}/3$). Decreasing T gives rise to different changes of the magnetic structure depending on the applied magnetic field: (1) For $B \leq 0.32$ T TLL to 3D-AFM ordering is observed. (2) For $0.32 \leq B \leq 1.15$ T a transition from TLL to IC-AFM takes place. (3) Above 1.15 T, the full polarisation of the spins, labelled FI-FM, is reached at the lowest T. Above T_N, the broad continuum of excitations seen in INS confirms the existence of spinon QP and the realisation of a TLL state. However, if T is high enough or one gets too close to the QCP, the fluctuations become strong, and the spinon description breaks down, meaning that spinons are not well-defined[3]. The change from the TLL to the QC regime is not a phase transition but rather a crossover, and the boundary is determined experimentally as a broad peak in $C(B)$ (indicated by a grey crossover line in Figure 3.8). In Chapter 6, I separated the description of my data for different B regimes determined from the behaviour at low T: In Chapter 6, I separated the description of my data for *Regime 1* covers the 3-D AFM GS ($B < 0.35$ T). *Regime 2-I*, *2-II* and *2-III* correspond to the SDW GS (0.35 T $\leq B \leq 0.75$ T), the TAF GS (0.75 T $\leq B \leq 1$ T) and the QC regime at low T (1 T $\leq B \leq 1.2$ T). *Regime 3* contains any field above ($B \geq 1.2$ T).

3.6 Previous studies of thermal conductivity

Although the fascinating low-T properties of YbAlO$_3$ were found only lately, the pure non-magnetic iso-structural compound YAlO$_3$ or Yb-doped YAlO$_3$ labelled as Yb:YAP (Yb-doped yttrium aluminium perovskite) are well-known as candidates for optical application and laser materials around room temperature. This may explain the absence of detailed studies on the thermal transport of YbAlO$_3$, particularly at low T. Aggarwal *et al.* [88] studied κ along with other thermo-optical properties of the doped laser crystals of Yb:YAP experimentally down to 80 K, the details of which are brought later in Chapter 6. In another work, Xiang *et al.* [89] theoretically investigated YbAlO$_3$ compared with YAlO$_3$ from the work of Zhan *et al.* [90]. They employed first-principle total energy calculations and chemical bond theory to investigate bonding characteristics, elastic stiffness, and κ_min[4] at T ranges well-above room temperature, i.e., 400 - 2200 K. At such high T, the dominant phonon scattering mechanism is via Umklapp processes, and heat transport is determined by all the

---

[3]Note that the existence of the spinons is not limited to the TLL state. The TLL phase may be defined as a state with (i) well-defined and (ii) deconfined spinon QP. In addition, satisfying (ii) the TLL should not be an ordered phase; otherwise the spinons would get confined.

[4]At very high T, e.g., ~2100 K for YbAlO$_3$, phonons are completely uncoupled and energy is transferred between neighbouring atoms. In that case, the phonon mean-free path decreases to the average atomic distance and κ approaches a minimum value κ_min. This T range, however, is irrelevant to this thesis.

acoustic and optical phonon branches and their interactions. The calculated κ of YbAlO$_3$ is very low, which indicates intense phonon scattering processes, the origin of which can be traced back to the characteristics of the crystal structure of YbAlO$_3$: Xiang *et al.* attributed this mainly to the special heterogeneous bonding. In the case of YAlO$_3$, softer Y-O polyhedra allow for thermal rattling, and provide *weak zones* that scatter phonons. These structural features are also applicable to YbAlO$_3$, where Yb-O polyhedra may provide weak zones.

The non-magnetic iso-structural compounds are often used to extract the phononic background of the magnetic compounds. Based on that, Wu *et al.* [74] used YAlO$_3$ to subtract the phononic contribution of the specific heat of YbAlO$_3$.

Calculated v_l, v_s, and $\overline{v}$ being average longitudinal, shear, and mean sound velocities, respectively, Θ_D being the Debye temperature and Γ being the Grüneisen parameter of YbAlO$_3$ together with those of YAlO$_3$ are listed in Table 3.1 [88–90]. The mean sound velocities of YbAlO$_3$ are significantly lower than those of YAlO$_3$, explained by smaller and higher values of elastic moduli and atomic weight, respectively [89]. The relatively low Θ_D of YbAlO$_3$ implies relatively weak atomic vibrations in the lattice. Finally, yet importantly, the Grüneisen parameter Γ was reported to be 1.69 and 1.51 for YbAlO$_3$ and YAlO$_3$, respectively. The 12 %-higher Grüneisen parameter of YbAlO$_3$ compared to that of YAlO$_3$ indicates stronger anharmonic phonon scattering in YbAlO$_3$. The mean-atomic weight of YbAlO$_3$ (49.6 amu/atom) is approximately 34 % larger than that of YAlO$_3$ (32.8 amu/atom), resulting in the lower calculated κ_{min} of YbAlO$_3$. Taking these differences into account, specifically in the mean sound velocities (elastic moduli) and the atomic weights, YAlO$_3$ is probably not a viable reference material for thermal transport measurements.

3.7 Summary

Quasi-1-D spin systems are among the both theoretically and experimentally interesting systems in quantum many-body physics, where various types of magnetic excitations, such as spinons in confined and deconfined states, magnons, psinons, etc., can arise. Despite the long-term history of studying YbAlO$_3$, it was only recently found to be a Q-1-D quantum anti-ferromagnet at low T [59, 71, 74]. At low T, Yb^{3+} Ising-like moments experience AFM exchange interaction along c, forming chains ($J_c = 2.3\,\mathrm{K}$). The dipole-dipole interaction between the Yb^{3+} moments is the lowest when they point in the same direction in each *ab*-plane, which leads to FM coupling in the *ab*-plane ($J_{ab} = 0.8\,\mathrm{K}$). This combination results in spin-1/2 AFM *XXZ* chains with weak 3-D interactions, and the effective spin model consists of Heisenberg chains weakly-coupled by dipole-dipole interactions [59, 71, 74].

A gapless continuous dispersion spectrum is reported at $B = 0\,\mathrm{T}$ and $T = 1\,\mathrm{K}$ in the TLL phase; though below $T_N = 0.88\,\mathrm{K}$, the ordered moments from neighbouring chains produce an effective staggered molecular field B_{st} to confine the spinons and give rise to a gap in the excitation spectrum [74]. Application of a longitudinal magnetic field ($B \parallel a$) for $T \to 0$ suppresses the commensurate ordering at low T in favour of an IC phase at $B_{c1} = 0.32\,\mathrm{T}$. Increasing B further drives the system to a QCP at $B_c = 1.15\,\mathrm{T}$ and the field-polarised state for $B > B_c$. Calculations predict LSDW and TAF sub-phases inside the IC-phase (0.35 - 1.15 T) [77, 78]; however, the TAF phase is not resolvable with the existing INS data.

Last but not least, the lower elastic moduli of YbAlO$_3$ produce a huge anharmonic phonon scattering compared to its non-magnetic iso-structural compound YAlO$_3$ [89]. This plays a significant role in the different thermal conductivities in these two compounds.

4 Thermal transport concepts

4.1 Introduction

In the current chapter, I focus on the most important concepts of thermal transport. I start with Fourier's law, kinetic model and Matthiessen's rule in the scope of the heat transport in solids. Then, I will give an introduction to the quantised lattice vibrations, the so-called *phonons*, harmonic and anharmonic oscillations, Debye model describing the phononic specific heat, and phonon-phonon interactions resulting in normal or Umklapp three-phonon (or higher-order) processes. Afterwards, I introduce the vastly used lattice thermal conductivity models, the Debye approximation and Callaway model. I close this section with an overview of different scattering mechanisms in the lattice thermal conductance. As the last section, I briefly summarise the essential points of studying heat transport by magnetic excitations in spin systems with low dimensionalities: Convenient methods to determine the magnetic contribution in thermal transport, fitting models, and the thermal Drude weight.

Basics of thermal conductivity are covered in most of the books of solid state [91–96], or extreme condition physics [97, 98]. More details of the theories are available in the specialised books [99–105], or related dissertations [106–108].

4.2 Heat transport in solids

Fourier's law: Thermal conductivity is a transport property of matter similar to electrical conductivity, viscosity, diffusion, damping of sound, etc. For thermal transport, one may start with a microscopic system characterised by a nonuniform temperature (T) profile $T(\boldsymbol{r})$, leading to a heat flow, i.e. an energy current. In general, the thermal conductivity tensor noted as $\hat{\kappa}$, describes the capability of a solid to conduct heat, and equals to the amount of the heat flowing through the material of unit cross sectional area under unit temperature gradient $\boldsymbol{\nabla} T(\boldsymbol{r})$ per unit time. In the sense of formula, the heat-current density $\boldsymbol{j}_Q$ for small $\boldsymbol{\nabla} T(\boldsymbol{r})$ within a framework of linear response is given by the so-called *Fourier's law*,

$$\boldsymbol{j}_Q = -\hat{\kappa}(T)\boldsymbol{\nabla} T(\boldsymbol{r}). \tag{4.1}$$

The negative sign yields that the heat current flows from the hot to the cold end. Generally, $\hat{\kappa}$ can contain non-zero off-diagonal elements, which Onsager has shown being symmetric using non-equilibrium statistical mechanics [109]. The off-diagonal elements raise interests of thermal Hall effect studies, where an orthogonal $\boldsymbol{\nabla} T$ is induced by application of a magnetic field (B); however, it is neither of the interest nor of the scope of this study. The 2nd-order tensor $\hat{\kappa}$ for $\boldsymbol{\nabla} T \parallel \boldsymbol{j}_Q$, i.e., longitudinal cases, reduces to a scalar κ along the given direction.

Kinetic model: Heat carriers usually do not fly ballistically from the hot to the cold region. They are scattered by lattice, electrons, etc., performing a diffusion process. To compute transport quantities in a semi-classical picture, one must know how far (quasi-)particles travel without collision and how far they transport the relevant physical quantity[1]. Assuming that the probability of a scattering event in the travel time $\mathrm{d}t$ is $\mathrm{d}t/\tau$, it follows

---

[1]Relevant quantities can be just the particles themselves (diffusion), the kinetic energy (thermal conductivity) or the momentum (viscosity).

for the probability of a travel of time t with no collision $P(t)$ that $\mathrm{d}P/\mathrm{d}t = -P/\tau$, which is solved by $P(t) = \frac{1}{\tau} \cdot \exp\left(\frac{-t}{\tau}\right)$; and the mean time between the collisions equals

$$\langle t_{col} \rangle = \int_0^\infty t \, P(t) \, \mathrm{d}t = \tau. \tag{4.2}$$

The relaxation time τ appearing is frequently identified with the so-called *scattering, collision, relaxation* or *mean-free time*. Related to the scattering time, the average distance a particle travels before being scattered is the so-called *mean-free path*, as

$$\lambda = \tau|\boldsymbol{v}| = \tau v, \tag{4.3}$$

where $\boldsymbol{v}$ is the mean velocity of the considered propagating (quasi-) particles. To study the energy transport rate, I label the heat capacity of each particle as c, and its energy as E. In the kinetic model formalisation, it can be shown that the rate of change of the particle energy in the presence of a temperature gradient $\boldsymbol{\nabla}T$ is

$$\partial E/\partial t = c\boldsymbol{v} \cdot \boldsymbol{\nabla}T. \tag{4.4}$$

Assuming n being the concentration of the particles, i.e., particles per unit volume, the average of total heat flow rate per unit area summing over all particles is

$$\boldsymbol{j}_Q = -nc\tau\langle\boldsymbol{v} \cdot \boldsymbol{v}\rangle\boldsymbol{\nabla}T = -\frac{1}{d}nc\tau v^2\boldsymbol{\nabla}T, \tag{4.5}$$

where the brackets represent an average over all particles, and d is the dimensionality of transport (usually $d = 3$). Substituting nc by the total heat capacity C, thermal conductivity κ by means of kinetic gas theory can be found to be

$$\kappa = \frac{1}{d}nc\tau v^2 = \frac{1}{d}C|\boldsymbol{v}|\lambda. \tag{4.6}$$

Therefore, κ is a product of the specific heat, the velocity, and the mean-free path of the heat carriers. In other words, the type of carriers performing the transport, their velocity, and how far the carriers fly before getting scattered again. The factor $1/d$ comes from the fact that the heat flows in one direction whereas the motion of the carriers is d-dimensional. In a simple model, one can consider the total thermal conductivity in the solid as a summation over different conduction channels, i.e., $\kappa_{\mathrm{net}} = \Sigma_i\kappa_i$. In the present study, the compound YbAlO$_3$ is electrically insulating but magnetic excitations are present. This makes the lattice excitations along with the magnetic excitations the two main heat carriers. We have

$$\kappa_{\mathrm{net}} = \kappa_{\mathrm{lattice}} + \kappa_{\mathrm{magnetic}}. \tag{4.7}$$

The lattice thermal conductivity is due to a single type of excitations, namely phonons. By contrast, many different magnetic excitations exist, leading to a more diverse behaviour of $\kappa_{\mathrm{magnetic}}$ compared to $\kappa_{\mathrm{lattice}}$. In the next sections, I give a recap on the lattice thermal conductivity and a summary on the thermal conductivity behaviour in different spin systems. **Matthiessen's rule:** As derived in paragraph § **Kinetic model**, the three parameters of specific heat, mean-free path and velocity of the heat carriers determine the thermal conductance in the solids. Thus, it is crucial to identify the heat carriers in the solid, e.g., lattice vibrations, electrons, magnetic excitations, etc., and to investigate different

scattering processes present in the lattice, respectively. An empirical rule described by Matthiessen in 1862 [110], asserts that in case of a single channel where several distinct scattering mechanisms are at play, the overall resistivity is simply the sum of the resistivities one would obtain if each scattering mechanism was present alone. This leads to a reciprocal summation of the relaxation times, i.e.,

$$\tau_{\text{net}}^{-1} = \Sigma_i \tau_i^{-1}. \tag{4.8}$$

Different scattering rates can be found in the literature. The most important scattering mechanisms related to this work will be mentioned later in this chapter.

4.3 Phonons and lattice vibrations

In the presence of a temperature gradient, lattice thermal energy is considered to propagate by means of wave packets with various normal modes. Crystal vibrational fields, the so-called *phonons*, are the quanta of vibrational energy. The phonons can be thought of as quantised sound waves, thus quasi-particles carrying the heat through the crystal. The energy of a phonon equals $E = \hbar\omega_s(\boldsymbol{k})$, with $\omega_s(\boldsymbol{k})$ as the phononic angular frequency of the normal mode of type s with the wave vector $\boldsymbol{k}$. Different kinds of vibration modes involving different frequencies and thus phonon energies are classified as: (i) *Acoustic phonons* associated with neighboured particles oscillating nearly in phase (long wavelength). (ii) *Optical phonons* associated with neighboured particles oscillating nearly in anti-phase (short wavelength). Derivation of phonon dispersion curves can be found in standard solid-state books, e.g., [91]. Normally, optical phonons themselves are not effective in transporting heat energy due to their small group velocity $\partial\omega_s(\boldsymbol{k})/\partial\boldsymbol{k}$ but may affect heat conduction by interacting with the phonons of the acoustic branch as the main heat conductors.

Harmonic and anharmonic oscillations: Harmonicity and anharmonicity correspond to quadratic and higher-order terms, respectively, in terms of the lattice potential energy. Properties like the lattice specific heat, thermal diffuse scattering, etc., can be very well interpreted in terms of the harmonic theory of the crystal lattice, and the anharmonic corrections are only significant at high T; nevertheless, the effects on thermal expansion and thermal conductivity are observable at all T ranges. Although the latter is of the direct interest of this research, it is useful to have first a short look at the thermal expansion and the so-called *Grüneisen parameter*. The thermal expansion coefficient α is a good tool to examine the anharmonic oscillations in the compound. If the lattice potential is harmonic, the phonon frequencies are volume-independent and α is zero at all T. Consequently, it is necessary to go beyond the harmonic approximation to explain thermal expansion. The relative oscillation frequency change $\partial\omega_s(\boldsymbol{k})/\omega_s(\boldsymbol{k})$ of a phonon of a certain momentum depends linearly on the relative volume expansion $\partial V/V$. The so-called *partial Grüneisen parameter* related to the anharmonicity of individual phonons is defined as $\partial\ln\omega_s(\boldsymbol{k}) = -\Gamma_{\boldsymbol{k}s} \cdot (\partial\ln V)$. The thermodynamic overall Grüneisen parameter is

$$\Gamma = \frac{3B\alpha}{c_v}, \tag{4.9}$$

where B is the bulk modulus and c_v is the specific heat capacity at constant volume.

Phononic specific heat (Einstein and Debye models): The constant-volume lattice specific heat in the quantum theory of harmonic solids depends on the frequency spectrum
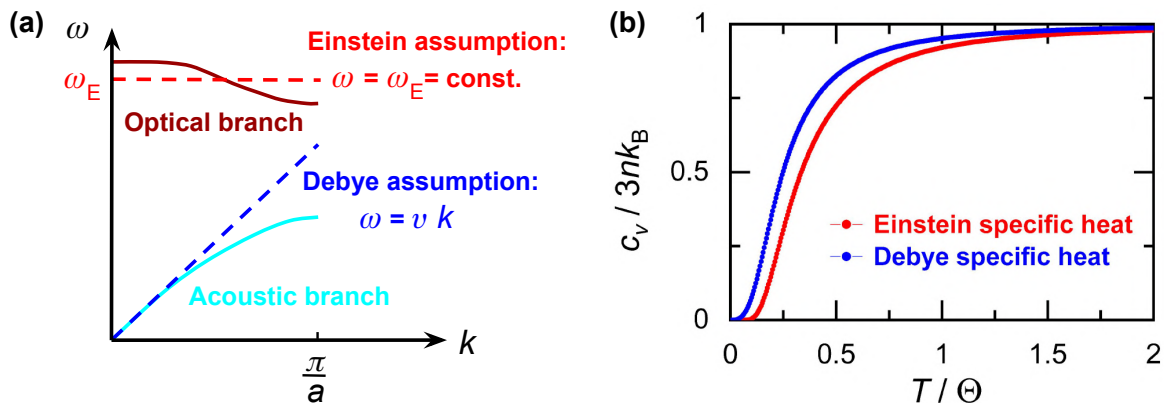
Figure 4.1: Einstein versus Debye model of phononic specific heat. **(a)** Debye (Einstein) approximation for the acoustic (optical) branch. The acoustic (optical) branch is replaced by a linear (constant) branch. **(b)** A comparison of the specific heat within the Debye and Einstein approximations of an insulating crystal. Θ is either the Debye or the Einstein temperature, depending on which curve is being examined. Both curves are normalised to approach the Dulong-Petit value at high T.

of the normal modes as

$$c_v = \frac{1}{V}\Sigma_{k,s}\frac{\partial}{\partial T}\frac{\hbar\omega_s(\boldsymbol{k})}{e^{\beta\hbar\omega_s(\boldsymbol{k})}-1}, \tag{4.10}$$

where $\beta = 1/k_{\mathrm{B}}T$. The sum can be replaced by an integral over the first Brillouin zone satisfying the so-called *Born-von-Karman boundary* conditions

$$c_v = \frac{\partial}{\partial T}\Sigma_s\int\frac{\mathrm{d}^3\boldsymbol{k}}{(2\pi)^3}\frac{\hbar\omega_s(\boldsymbol{k})}{e^{\beta\hbar\omega_s(\boldsymbol{k})}-1}. \tag{4.11}$$

As is evident, modes with $\hbar\omega_s(\boldsymbol{k})\gg k_{\mathrm{B}}T$ will contribute negligibly since the integrand will vanish exponentially. In this circumstance, the only modes that can continue to contribute appreciably to the specific heat are the ones from the acoustic branches of sufficiently long wavelength for the reason that $\omega_s(\boldsymbol{k})\to 0$ as $k\to 0$, no matter how low the temperature.

At the high T limit, the exponential term gets small as any normal mode is in a highly excited state. This gives the classical so-called *Dulong-Petit law*, that $c_v\to 3nk_{\mathrm{B}}$ for $k_{\mathrm{B}}T\gg\hbar\omega_s(\boldsymbol{k})$ with $n = N/V$ being the atomic density per volume. In real systems additional terms of quantum corrections have to be incorporated. Deviations from the Dulong-Petit law kick off by decreasing T once the thermal energy $k_{\mathrm{B}}T$ is no longer large compared to all phonon frequencies, i.e., $T\approx\hbar\omega/k_{\mathrm{B}}$; this limiting T is typically of the order of a few $100\,\mathrm{K}$.

The theory of the specific heat of solids proposed by Einstein in 1906 [111], simplifies all the vibrations to a constant frequency namely the *Einstein frequency* ω_{E}. This describes the optical branch well. The specific heat within the *Einstein model* is

$$c_v^{\mathrm{E}} = nk_{\mathrm{B}}\frac{e^{\hbar\omega_E/k_{\mathrm{B}}T}(\hbar\omega_E/k_{\mathrm{B}}T)^2}{(e^{\hbar\omega_E/k_{\mathrm{B}}T}-1)^2}. \tag{4.12}$$

The so-called *Einstein temperature* is defined as $\Theta_{\mathrm{E}} = (\hbar/k_{\mathrm{B}})\,\omega_{\mathrm{E}}$. For $T\gg\Theta_{\mathrm{E}}$, each optical mode simply contributes the constant k_{B} to the specific heat, as required by the classical law of Dulong and Petit. At $T\ll\Theta_{\mathrm{E}}$, the contribution of the optical modes drops exponentially,

reflecting the difficulty in thermally exciting any optical modes at low T. Under certain conditions, usually associated with an imminent change in the crystal structure, an optional branch may dip down almost to zero frequency, acquiring what is known as a *soft mode*, and there will be an additional contribution to the low-T c_v from that optical branch.

In contrast to Einstein's theory of specific heat, Debye replaced all the branches of the vibrational spectrum with three branches, each of which having the same linear dispersion relation $\omega = v|\boldsymbol{k}|$ [112], where the mean sound velocity can be estimated via $\overline{v} = \Theta_{\mathrm{D}}\left(\frac{k_{\mathrm{B}}}{\hbar}\right)(6\pi^2 n)^{-1/3}$. Debye postulated that there is a continuous range of frequencies that cuts off at a maximum frequency, the so-called *Debye frequency* ω_{D}. He defined $\omega_{\mathrm{D}} = vk_{\mathrm{D}}$, where k_{D} is determined via the volume of the first Brillouin zone, and is characteristic of a particular solid. The differential lattice specific heat calculated under the assumptions of the *Debye model* is expressed as

$$c_v^{\mathrm{D}}(x)\,\mathrm{d}x = \left(\frac{3k_{\mathrm{B}}}{2\pi^2\overline{v}^3}\right)\left(\frac{k_{\mathrm{B}}}{\hbar}\right)^3 T^3 \frac{e^x x^4}{(e^x - 1)^2}\,\mathrm{d}x = 9nk_{\mathrm{B}}\left(\frac{T}{\Theta_{\mathrm{D}}}\right)^3 \frac{e^x x^4}{(e^x - 1)^2}\,\mathrm{d}x, \qquad (4.13)$$

where $x = (\hbar\omega)/(k_{\mathrm{B}}T)$. Relation 4.13 expresses the specific heat at all T in terms of a single empirical parameter, the so-called *Debye temperature* defined as $\Theta_{\mathrm{D}} = (\hbar/k_{\mathrm{B}})\,\omega_{\mathrm{D}}$. ω_{D} and Θ_{D} are in fact measures of the maximum phonon frequency and the temperature, above which all modes are excited, and below which modes begin to *freeze out*. Θ_{D} is extensively used as a scale of the phonon energy scale since it is proportional to the maximum frequency of the atomic vibrations. Considering a simple harmonic system, higher Θ_{D} represents stronger atomic forces and/or lighter atoms. For instance, the diamond with strong atomic bindings and low atomic weight has $\Theta_{\mathrm{D}} \simeq 2000\,\mathrm{K}$, while the lead with heavy atoms and weak atomic forces $\Theta_{\mathrm{D}} \simeq 100\,\mathrm{K}$. Eventually, the Debye model predicts a cubic T dependency of c_v at low T. Debye's approach works for the case where the acoustic phonons are dominating. In case the anharmonicity of the optical branch plays a role, e.g., near phase transitions, where part of the optical branch goes soft, one may employ the Einstein model.

Phonon-phonon interactions: Intrinsic phonon scattering is caused by the lattice anharmonicity [115]. In an *n-phonon process*, the incoming phonon combines $i \in [0, n-2]$ other phonons to form $n-i-1$ phonons. The n-phonon scattering rates for each phonon mode are calculated by summing up the probabilities of all possible scattering events involving the given mode. Each transition probability is calculated by the so-called *Fermi's golden rule* from density functional theory [114]. Figure 4.2 illustrates first-order three- and four-phonon processes, in which an incident phonon carrying wave vector $\boldsymbol{q}$ (displayed in black) undergoes various types of phonon-phonon processes. Figure 4.2 **(a)** depicts lowest-order anharmonic couplings involving three phonons in splitting (left column) and combination (right column) processes. In the case of four-phonon processes (panel **(b)**), redistribution (middle column) is another possibility along with the splitting (left column) and combination (right column). In all these processes, energy and momentum need to be conserved. Though, the resultant phonon may lie inside or outside the first Brillouin zone shown by grey boxes based on the initial $\boldsymbol{q_i}$ wavevectors. In the former, the conservation laws read

$$\hbar\omega + \hbar\omega_1 = \hbar\omega_2, \qquad (4.14)$$

$$\hbar\boldsymbol{q} + \hbar\boldsymbol{q_1} = \hbar\boldsymbol{q_2}. \qquad (4.15)$$

In the case of the latter, however, the final phonon has such a high wave vector that it is knocked out of the Brillouin zone. By mapping it back into the Brillouin zone using the

(a)
$q = q_1 + q_2$ $q + q_1 = q_2$

(b)
$q = q_1 + q_2 + q_3$ $q + q_1 = q_2 + q_3$ $q + q_1 + q_2 = q_3$

$q = q_1 + q_2 + R$ $q + q_1 = q_2 + R$ $q = q_1 + q_2 + q_3 + R$ $q + q_1 = q_2 + q_3 + R$ $q + q_1 + q_2 = q_3 + R$
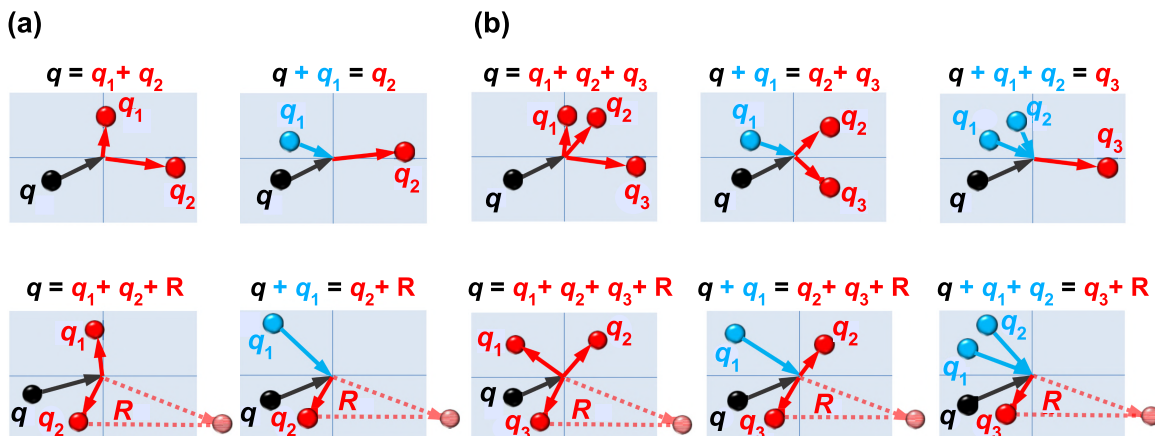
Figure 4.2: Three- and four-phonon processes. **(a)** Three-phonon splitting and combination processes. **(b)** Four-phonon splitting, redistribution, and combination processes. In each mode, the incoming phonon with a momentum of $\hbar q$ (black) may combine other phonons (blue) to form the resultant phonons (red). The top and bottom rows depict processes with momentum conserved (*normal* or *N-process*), and non-conserved (*Umklapp* or *U-process*), respectively. The resultant phonon in the U-process is folded back by reciprocal lattice vector R to the first Brillouin zone (shaded rectangle). Figures reproduced from [113, 114].

reciprocal lattice vector R, the momentum conservation follows

$$\hbar q + \hbar q_1 = \hbar q_2 + \hbar R. \tag{4.16}$$

These processes are classified into the so-called *normal* and *Umklapp* processes, labelled as N- and U-processes, respectively. In fact, in U-processes real momentum is transferred to the crystal as a whole. However, because of the large mass of the crystal, real momentum transfer to the whole crystal implies essentially no energy transfer. In Figure 4.2 **(a)-(b)**, the N- and U-processes for different scattering events are plotted in top and bottom rows of each column, respectively.

In the sense of the thermal transport, both N- and U-processes are capable to take part in the heat conduction: Unlike the U-processes, the N-processes do not impede the heat flow in favour of non-diffusive and non-resistive heat transport, the so-called *ballistic* transport. Nonetheless, a phonon created by two N-processes may gain enough energy to take part in an U-process. That means the N-processes can redistribute the overall phonon population, which can further participate in U-processes and indirectly contribute to thermal conductance. This indirect influence is only important in a small T range. Scattering rates of the processes and numerical approaches to κ_{lattice} are given in details in Section 4.4.

It is noteworthy that the most significant phonon-phonon processes are usually the three-phonon ones; however, Feng *et al.* demonstrated that four-phonon scattering resistance can reduce the predicted thermal conductivities and optical phonon lifetimes significantly in the T range above $200\,\text{K}$, manifesting the general impact of four-phonon scattering in solids [113]. Additionally to this type of scattering, second-order anharmonicity may give rise to four-phonon processes. Compared to three-phonon scattering, four-phonon scattering is more relevant at higher T and for higher-energy phonons as the phonon population increases with T [114].

4.4 Lattice thermal conductivity

The lattice thermal conduction is the standard mechanism of heat transport in solids and the prime source in insulators, if not the only one. The heat flux due to a phonon mode is the product of the average phonon energy and the group velocity. Considering τ_q being the phonon scattering time via resistive processes, and using the Debye model of specific heat, κ can be calculated to be

$$\kappa_{\mathrm{D}} = \frac{1}{3}\int_0^{\Theta_{\mathrm{D}}/T}\mathrm{d}x\; c_v^{\mathrm{D}}(x)\overline{v}^2\tau_q(x) = \frac{k_{\mathrm{B}}}{2\pi^2\overline{v}}\left(\frac{k_{\mathrm{B}}}{\hbar}\right)^3 T^3\int_0^{\Theta_{\mathrm{D}}/T}\mathrm{d}x\;\frac{e^x x^4}{(e^x-1)^2}\tau_q(x). \qquad (4.17)$$

Relation 4.17 is called the Debye approximation for the lattice thermal conductivity. It is adequate for analysing a lot of the experimental data, in particular, if an appreciable concentration of lattice defects or isotopes prevails in the solid. The phonon scattering processes considered in the Debye approximation are resistive; however, there exist the non-resistive N-processes, which still have a profound indirect influence on the lattice thermal conductivity of solids. They lead to energy transfer between the phonon modes. The Callaway model is the most widely used model in analysing the effects of both the resistive scatterings and N-processes on $\kappa_{\mathrm{lattice}}$ [100].

Callaway Model: Callaway's model assumes that N-processes tend to restore a non-equilibrium phonon distribution to a displaced phonon distribution of a particular form [116]. The combined relaxation time τ_{c} is defined as $\tau_{\mathrm{c}}^{-1} = \tau_q^{-1} + \tau_{\mathrm{N}}^{-1}$, i.e., as a combination of the phonon scattering time via resistive processes τ_q and the relaxation time of the N-processes τ_{N}. The Callaway model predicts the lattice thermal conductivity consisting of two parts:

$$\kappa_1 = \frac{k_{\mathrm{B}}}{2\pi^2\overline{v}}\left(\frac{k_{\mathrm{B}}}{\hbar}\right)^3 T^3\int_0^{\Theta_{\mathrm{D}}/T}\mathrm{d}x\;\frac{e^x x^4}{(e^x-1)^2}\tau_{\mathrm{c}}(x), \qquad (4.18)$$

$$\kappa_2 = \frac{k_{\mathrm{B}}}{2\pi^2\overline{v}}\left(\frac{k_{\mathrm{B}}}{\hbar}\right)^3 T^3\frac{\left(\displaystyle\int_0^{\Theta_{\mathrm{D}}/T}\mathrm{d}x\;\frac{e^x x^4}{(e^x-1)^2}\cdot\frac{\tau_{\mathrm{c}}}{\tau_{\mathrm{N}}}\right)^2}{\displaystyle\int_0^{\Theta_{\mathrm{D}}/T}\mathrm{d}x\;\frac{e^x x^4}{(e^x-1)^2}\cdot\frac{\tau_{\mathrm{c}}}{\tau_{\mathrm{N}}\tau_q}}. \qquad (4.19)$$

Hence, the total lattice thermal conductivity is $\kappa_{\mathrm{ph}} = \kappa_1 + \kappa_2$. When the phonon modes are strongly scattered by the resistive processes and the N-processes are negligible, then $\tau_{\mathrm{N}} \gg \tau_q$ and $\tau_{\mathrm{c}} \approx \tau_q$. Thus $\kappa_1 \gg \kappa_2$, and $\kappa_{\mathrm{ph}} \approx \kappa_1 \approx \kappa_{\mathrm{D}}$. For instance, the addition of a small amount of defects will rapidly suppress κ_2, though the decrease of κ_1 is much slower. In the opposite extreme, when N-processes are the only effective phonon scattering mechanism, $\tau_{\mathrm{N}} \ll \tau_q$ and $\tau_{\mathrm{c}} \approx \tau_{\mathrm{N}}$. The denominator of κ_2 then approaches 0 leading to an infinitive κ_{ph}.

Scattering mechanisms: Different scattering mechanisms in phononic conductivity dominate in different T regions, the most important of which are summarised here. I start with the non-resistive phonon-phonon N-processes.

- **Normal processes:** Considering ω as the frequency of the lattice vibrations, the scattering rate for an N-process is experimentally suggested to be (see e.g. [117])

$$\tau_{\mathrm{N}}^{-1} = N\cdot\omega^\alpha\cdot T^{5-\alpha}. \qquad (4.20)$$

The exponent α is dependent on the crystal symmetry and the types of phonons and usually around 1 - 4, and N is a fit parameter.

Continuing with resistive scattering processes, no electron-phonon scattering takes place in an insulator. At low T, the phonons can only be scattered via crystal imperfections, i.e., defects and ultimately the surface of the crystal, and magnetic excitations. In both cases, real momentum is transferred between the phonons and the crystal as a whole.

- **Boundaries:** At very low T, the mean-free path of the heat carriers may be limited by the crystal dimensions only to conduct heat. Obviously, the larger the sample, the lower the probability of boundary scattering. Supposing a constant mean-free path related to the sample size, one may write the phonon-boundaries scattering rate as

$$\tau_{\mathrm{bd}}^{-1} = \overline{v}/l. \tag{4.21}$$

  Here, l is the minimum length of the cross-section of a single-crystalline sample. One can use the so-called *Crimann length* $l_{\mathrm{C}} = \sqrt{4A_{\mathrm{s}}/\pi}$ as well, with A_{s} as the sample cross-section. The Crimann length represents an average of the cross-section dimensions, by mapping the sample to an imaginary collision cylinder. Finally, it is outstanding that grain boundaries scatter likewise independent of frequency [118].
- **Point defects:** Point imperfections work as barriers against the propagation of the heat carriers and the relaxation rate depends on their size: Scattering from molecules and very tiny particles, i.e., $< 1/10$ of the phonon wavelength (λ_{ph}), is predominantly Rayleigh type. In such a case, the scattering mechanism may be modelled as

$$\text{Probability} \propto \lambda^{-4} \approx (T/\Theta_{\mathrm{D}} a_0)^4, \tag{4.22}$$

  with a_0 as the Bohr radius of the scattering centre. For low-ω lattice vibrations, i.e., $\lambda_{\mathrm{ph}} \gg a_0$, the scattering rate is very small, T independent and instead strongly ω-dependent. Klemens [118] calculated the scattering rate of low-ω lattice waves by the static imperfection, namely the phonon-point-defect scattering rate, to be

$$\tau_{\mathrm{pd}}^{-1} = A\omega^4. \tag{4.23}$$

  Here, A is the free parameter of the model.
  For high-ω lattice vibrations, where the linear dimensions of the defects are larger than λ_{ph}, the ω-independent Mie scattering predominates the Rayleigh approximation and thus is more relevant for modelling the phonon-imperfection scattering mechanism.
- **Dislocations:** Phonon-dislocation scattering varies with the type of the dislocations [118, 119]. The most common is caused by the surrounding strain field with

$$\tau_{\mathrm{dis}}^{-1} = D\omega \tag{4.24}$$

  as the scattering rate, where D is the free parameter of the model.
- **Resonances:** An empirical nonmagnetic phonon-resonance scattering was investigate by Pohl [120], revealing a relaxation rate of

$$\tau_{\mathrm{res}}^{-1} = C\frac{\omega^2}{(\omega^2 - \omega_0^2)^2}, \tag{4.25}$$

  where ω_0 is the resonance frequency and C is a free parameter.

As described in Section 4.3, phonons interact with each other via the N- and U- processes. The latter influences the scattering rates more efficiently with increasing T.

- **Umklapp processes:** The U-processes impede phonon momentum and thereby the heat flow. The scattering rate τ_U^{-1} is proportional to the probability of phonons with adequate energy to participate in an U-processes based on the Bose-Einstein statistics. Thus, Peierls [121] suggested that the scattering rate has to contain an additional exponential T dependence as

$$\tau_U^{-1} = B\,T^\beta \cdot \exp\left(-\frac{\Theta_D}{bT}\right).\tag{4.26}$$

β and b are of the order of 1, and together with B the free parameters.

A typical behaviour of κ_{ph} in T is shown in Figure 4.3. The circles and the lines represent the experimental data and a theoretical fit to the Debye model, respectively. At very-low T, $\ll \Theta_D$, only a small number of phonons are excited. In a highly pure sample, they can travel vast distances with the crystal boundaries limiting the mean-free path only. In such a case, one should have $\kappa_{ph} \propto T^3$ at low T. Inclusions of impurities, grain boundaries or different phases, particularly defects of various types and concentrations, are found in every real crystal. Compared to a pure crystal, the defects reduce the overall κ. Around the peak region, defect scattering is the foremost process in limiting the mean-free path and, therefore, κ_{ph}. Reducing purity reduces κ significantly in the region of the peak, e.g., [123, 124]. The reduction by the defects for low and high T is much smaller since other scattering

Figure 4.3: The lattice thermal conductivity versus T of CoSb$_3$. Circles show the experimental data. Dashed curves are the theoretical limits imposed by boundary, boundary together with point-defect, and Umklapp scatterings. Figure from [122].

mechanisms govern in these regimes. At T above the peak, the U-processes dominate the scattering. Though c_v saturates at high T according to the Dulong-petit law, κ decreases as $\propto T^{-x}$, where usually $1 \leq x \leq 2$. This confirms experimentally that not all the phonon-phonon scattering processes are equally effective in reducing the mean-free path for entropy transfer: Only U-processes can bring about the release of entropy and attainment of thermal equilibrium. That is since the phonons transferring entropy should carry a net momentum whereas phonons in thermal equilibrium will have a net momentum of zero.

As a final point, I must clarify that κ_{ph} discussed till now was for an electrically insulating non-magnetic lattice with a single mechanism of heat conduction, namely phonons. However, presence of any other lanes of transport influences κ_{ph} by introducing new scattering processes. In this case, the net scattering rate of the phonons includes additional term(s) describing the scattering rate of the phonons with the other channel(s) of heat conduction. The compound under study YbAlO$_3$ is electrically insulating but magnetic, and thus the net relaxation time of phonons includes the phonon-spin scattering mechanisms as well.

Spin system		Compound	$J_\parallel/k_B$(K)	T_N(K)	$J_\perp/J_\parallel$
	S=1/2 HAFC	$Cu(C_6H_5COO)_2.3H_2O$	18	0.0008	$\sim 10^{-5}$
		Yb_4As_3	25		10^{-4}
		$SrCuO_2$	~ 2400	1.5 - 2	$7 \cdot 10^{-4}$
		Sr_2CuO_3	~ 2650	5.4	$2 \cdot 10^{-3}$
Q-1-D *S=1/2* HAFC		$BaCu_2Si_2O_7$	280	9.2	0.015
		$KCuF_3$	190	39	0.027
		$CaCu_2O_3$	2000	25	0.05
		$Sr_2V_3O_9$	82	5	0.061
		$CuGeO_3$	120	~ 10	0.1
		YbAlO$_3$	2.3	0.88	0.19
two-leg ladder		$(La,Sr,Ca)_{14}Cu_{24}O_{41}$	1500 - 2000	100	0.05
2-D HAF		La_2CuO_4	~ 1800		$\sim 0.5/1$?

Table 4.1: Overview on selected low-D spin systems of spin chains [126–132], two-leg ladders [133–135], and 2-D lattices [136], of which thermal transport is studied. $J_\perp/J_\parallel$ (or $k_B T_N/J_\parallel$) represents the inter- to intra-chain interaction strength ratio. HAFC stands for Heisenberg anti-ferromagnetic chains, and HAF is Heisenberg anti-ferromagnet.

Figure 4.4 illustrates the relaxation time of phonons in an imaginary spin system. Blue, pink and green curves depict the typical qualitative behaviour of $\tau_{\text{phonon-phonon}}$, $\tau_{\text{phonon-impurity}}$, and $\tau_{\text{phonon-magnon}}$ [125]. τ_{phonon} shown in red is the net relaxation time and a reciprocal summation of the relaxation times following the Matthiessen rule. It is prominent that phonons get scattered via the spin excitations with a similar rate as the spin excitations are scattered via the phonons. The spin-phonon scattering mechanism will be discussed in the next section.
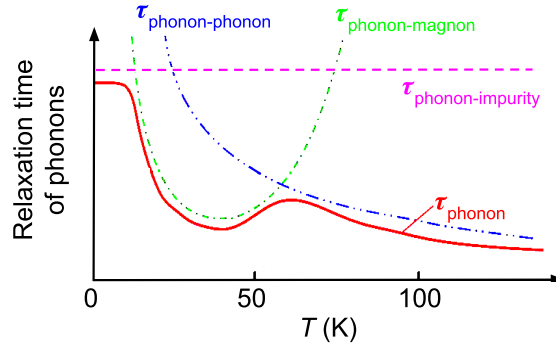
Figure 4.4: Relaxation time of phonons in an imaginary spin system. Figure reproduced from [125].

4.5 Thermal conductivity of spin systems

Considering the fact that any particle and/or quasi-particle with a specific heat and a non-vanishing group velocity can carry heat, magnetic excitations of spin systems may contribute to the thermal conductivity. The main focus of this thesis is the thermal transport via the magnetic excitations in the quasi-one-dimensional (Q-1-D) quantum magnet YbAlO$_3$. Analysis of κ_{magnetic} (or κ_{mag} for short) provides information about the excitation and scattering (by, e.g., phonons, sample boundaries, defects) of magnons similar to the case of κ_{ph}. In 1936, Fröhlich and Heitler predicted theoretically a possible contribution of spin-waves to κ [137]. However, it took almost 30 years until the first convincing experimental

evidence for magnetic heat transport by classical spin waves was found in ferrimagnetic YIG [138]. To date, numerous materials have been found with magnetic heat conductivity. Here, I give a summary for low-D spin systems with anti-ferromagnetic (AFM) coupling, namely similar magnetic properties as YbAlO$_3$. A more detailed introduction to the heat transport by the magnetic excitations can be found elsewhere, e.g., [139–141]. Table 4.1 shows an overview of selected low-D spin systems on which the magnetic thermal conductivity has been studied, including their exchange interactions along the spin chains $J_\parallel$, Néel ordering temperature T_N, and the inter- to intra-chain interaction strength ratio $J_\perp/J_\parallel$ (or $k_B T_N/J_\parallel$). Realisation of $S = 1/2$ Heisenberg anti-ferromagnetic (AFM) chains (or HAFC for short) usually demands $J_\perp/J_\parallel < 10^{-3}$. For the case of the spin ladders, $J_\parallel = J_{leg}$ and $J_\perp = J_{rung}$.

Copper-oxide (cuprate) compounds are the most prominent materials realising a magnetic heat transport, though not the only ones [139]. One major advantage of these compounds is that 3-D magnetic ordering occurs only at relatively low T due to the moderately weak inter-chain interactions, thus providing a large T range for modelling. Moreover, the fact that these materials are electrically insulating eliminates the contribution of electrons in conducting the heat. KCuF$_3$, BaCu$_2$Si$_2$O$_7$, CaCu$_2$O$_3$, SrCuO$_2$ and Sr$_2$CuO$_3$ are among our best realisations of the $S = 1/2$ Heisenberg AFM chains [126–130]. Studies on the ladder materials are mostly done on the $S = 1/2$ two-leg ladder (Sr,Ca,La)$_{14}$Cu$_{24}$O$_{41}$ family, the so-called *telephone number* series of compounds [133–135]. The ladder structures with more legs can in principle be created by coupling more chains to the structure in an infinite limit; eventually this would lead to a 2-D Heisenberg anti-ferromagnet on a square lattice (2-D HAF). A good realisation of a 2-D HAF with $S = 1/2$ is given by La$_2$CuO$_4$ [136].

YbAlO$_3$, which is the focus of this research, is included in Table 4.1 and highlighted in green. However, no literature data on the low-T thermal conductivity of YbAlO$_3$ has been published up to now. The smallest $J_\parallel$ value and the narrow T range between $J_\parallel$ and T_N of YbAlO$_3$ compared to the other compounds are remarkable. Therefore, compared to the other spin chain materials: (i) Very-low T ($< 2\,\mathrm{K}$) is required to detect the magnetic heat transport in YbAlO$_3$. (ii) The system is in the 1-D state only in a very limited T range, as the crossover to the 3-D one occurs at around $0.38 J_\parallel$.

Separation of phonon and magnetic contributions: The magnetic excitations show various types of behaviour depending on the origin and sort of excitation, e.g., magnon, spinon, gapped or gapless, and so on. Since κ_{ph} is an integral part of any system, the initial and indeed essential step in studying κ_{mag} is a clear separation of the phononic and magnetic contributions. Nevertheless, one of the severe difficulties in studying magnetic heat conduction is the robust determination of κ_{mag}. That is particularly difficult if κ_{ph} is dominating or if κ_{ph} and κ_{mag} have a similar T dependence. An example is 3-D AFM magnons with linear dispersion, which are expected to have $\kappa_{mag} \propto T^3$ at low T, i.e. the same T dependence as κ_{ph} [142]. One widely used approach for establishing experimental κ_{mag} in low-D magnets exploits the fact that the spin contribution to the transport perpendicular to the chains is usually negligible due to the very-weak inter-chain interactions, i.e., $\kappa_\perp = \kappa_{ph,\perp}$. By contrast, $\kappa_\parallel$ can be considered a summation of two channels: The phonons along the chains $\kappa_{ph,\parallel}$ and the magnetic excitations κ_{mag}. Hence, $\kappa_\parallel = \kappa_{ph,\parallel} + \kappa_{mag}$. In a first approximation, one may assume that $\kappa_{ph,\parallel} = \kappa_{ph,\perp}$ or that $\kappa_{ph,\parallel}/\kappa_{ph,\perp} = \mathrm{const}$. In that case, κ_{mag} can be estimated by measuring both $\kappa_\parallel$ and $\kappa_\perp$.

Another simple situation is realised for strong phonon-disorder scattering, where κ_{ph} may be approximated by a constant value. In the following, I present some examples from literature for κ_{mag} estimations. Figure 4.5 shows experimental results on the thermal
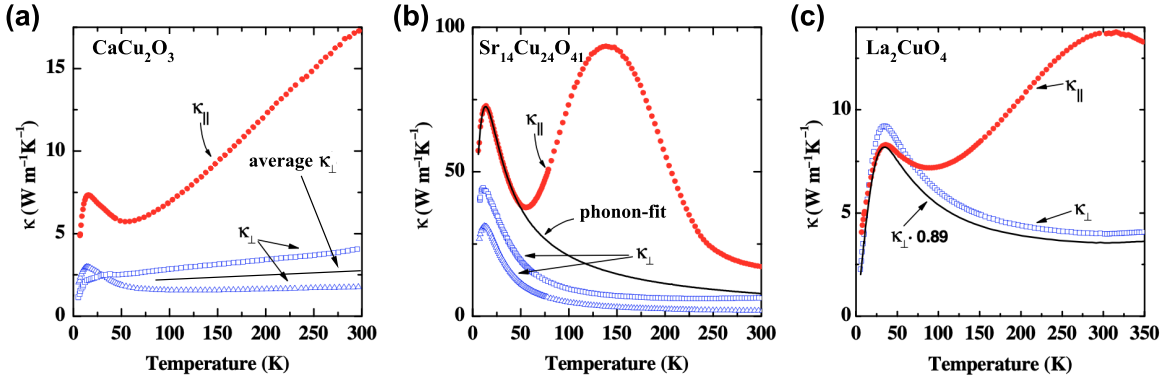
Figure 4.5: Measured $\kappa(T)$ of selected low-D spin structures. **(a)** A spin chain, **(b)** a two-leg spin ladder, and **(c)** a 2-D square lattice. Figure reproduced from [140].

conductivity of $CaCu_2O_3$, $Sr_{14}Cu_{24}O_{41}$ and La_2CuO_4 as representatives of the spin chains, the spin ladders and the 2-D lattice in zero B. In each panel, the thermal conductivity measured parallel to the chains $\kappa_\parallel$ is displayed in red, and the one perpendicular to the chains $\kappa_\perp$ in blue markers. In the spin chain compound $CaCu_2O_3$ (Figure 4.5 **(a)**), disorder leads to a strong suppression of κ_{ph}, evidenced by the weak T dependence of $\kappa_\perp$ and the absence of a pronounced phonon maximum. At elevated T ($>100\,\mathrm{K}$), κ_{mag} was therefore estimated by subtracting a constant mean value assuming that $\kappa_{ph,\parallel} \simeq \kappa_\perp \simeq$ const. Another well-known example is the spin ladder system $Sr_{14}Cu_{24}O_{41}$, shown in Figure 4.5 **(b)**. In this material, $\kappa_\perp$ has a typical lattice thermal conductivity and was fitted by the Debye model. For estimating $\kappa_{ph,\parallel}$, it was assumed that the ratio $\kappa_{ph,\parallel}/\kappa_\perp$ is T-independent and that κ at lowest $T \to 0$ is only due to phonons. A similar method was applied for the 2-D spin lattice La_2CuO_4 shown in Figure 4.5. Instead of subtracting a fit however, $\kappa_{mag,\parallel}$ was determined using directly the measured $\kappa_\perp$ scaled by a suitable factor to match the data at low T. Thus

$$\kappa_{mag} = \kappa_\parallel - \kappa_\perp \cdot \left(\frac{\kappa_\parallel}{\kappa_\perp}\right)_{T\to 0}. \tag{4.27}$$

In general, investigating the heat-transport anisotropy is a beneficial method to determine κ_{mag}. Even though, that is not always practical. For instance, if the existence of a well-defined anisotropy of the phononic heat transport is violated, e.g., in the vicinity of phase transitions, where the phonon scattering by critical fluctuations is often very strong or not necessarily following the lattice anisotropy, one can hardly avoid substantial uncertainties in the evaluation of $\kappa_{mag}(T)$ [142]. Another case is when a crystal has a strong spin-phonon coupling. A famous example is a family of (Q-) 1-D HAFC compounds in which huge spin coupling of the chains to the lattice excitations can lead to a periodic deformation of the lattice, and hence a 3-D structural phase transition, the formation of so-called *Spin-Peierls* (SP) chains [143–145]. The $S = 1/2$ chain $CuGeO_3$ is among the first and the mostly studied SP systems [143, 144]. The SP transition of $CuGeO_3$ occurs exactly between the two peaks of the phononic and magnetic contributions at $T_{s-ph} \approx 14\,\mathrm{K}$. In such circumstances, the two-peak feature can get dissolved in a broadened single peak *OR* may be attributed to phonon transport with enhanced scattering close to the transition (see, e.g., [146]), and thus a precise determination of κ_{mag} and κ_{ph} is precluded. On the other side, though $\kappa_\perp$ is expected to be negligible by virtue of the one-dimensionality of the system, the same
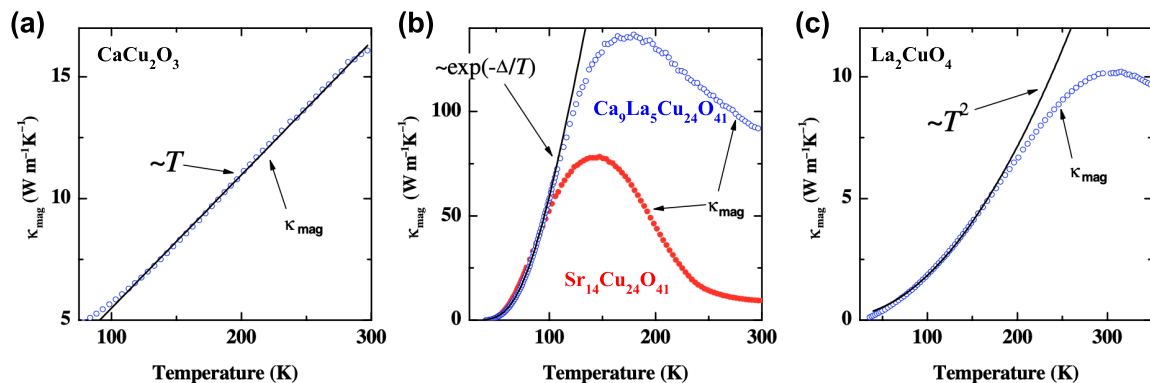
Figure 4.6: Magnetic thermal conductivity of low-D spin structures. **(a)** A spin chain, **(b)** a two-leg spin ladder, and **(c)** a 2-D square lattice. Figure from [140].

features observed in $\kappa_\parallel$ can appear in $\kappa_\perp$ thanks to the remarkable spin-phonon coupling. Thus, despite the large amount of experimental work on thermal transport in the $S = 1/2$ SP chain $CuGeO_3$, the identification of spin-carried heat conduction has not been established unequivocally [145]. Eventually, determining κ_{ph} and thus extracting κ_{mag} is conclusively not feasible/trivial in all the spin systems.

Magnetic contribution in thermal transport: Figure 4.6 displays κ_{mag} of different representative compounds of the low-D spin systems. In the case of the gapless spin chain $CaCu_2O_3$ in which fractional spinon excitations are expected, κ_{mag} is almost linear in T (Figure 4.6 **(a)**) [126]. The linear T-dependence of the spinons is predicted and reported in other spin-chain compounds, e.g., $Cu(C_6H_5COO)_2.3H_2O$ [131]. However, $\kappa_{mag} \propto T$ is not observed in all spin chains, e.g., Sr_2CuO_3 and $SrCuO_2$ [128, 129, 142], or some $S = 1$ Haldane spin chains [147]. Although the *cleanness* of the chains is effective in the non-linear behaviour observed in Sr_2CuO_3 and $SrCuO_2$ [139, 142], the so-called *bypassing mechanism* is argued to change a linear-T dependency in the $S = 1$ Haldane spin compound $Ni(C_2H_8N_2)_2NO_2(ClO_4)$ [147]: The spinon can bypass the strong impurities by hopping to the neighbouring chains.

The gapped spin ladders, however, show an exponentially activated behaviour of κ_{mag} at low T, as depicted in Figure 4.6 **(b)** [133–135]. It must be noted that regardless of the dimensionality, a factor of the form of $\propto \exp(-\Delta/k_B T)$ appears in κ_{mag} of the spin-gapped systems at $k_B T \ll \Delta < J$ [135]. The exponential term comes from the thermal population.

Lastly, Figure 4.6 **(c)** represents κ_{mag} of the 2-D HAF La_2CuO_4, which shows a T^2 behaviour at low T. A similar dependence of T^2 is also predicted and observed in other 2-D square lattices, e.g., the 2-D ferromagnet $C_{12}(CH_3NH_3Cl)$ [136].

In-field thermal transport: Application of an external B can influence the measured κ. Possible emergence of different magnetic phases is the first and most clear benefit of studying thermal transport of spin systems in B. If tuning B can induce/suppress orderings, the magnetic scattering rates can be tuned accordingly. Another effect is a change in the type and/or number of the magnetic heat carriers within the same magnetic state, and consequently, a change in magnetic scattering rates may occur. On the other side, the lattice thermal conductivity can be affected not in a direct process but via the spin-phonon magnetic scatterings. Another beneficial case of studying $\kappa(B)$ is at high B, where a B-induced spin-polarised state can be achieved so that all the magnetic excitations are frozen out, and thus a pure phononic state is expected. Particularly, a spin gap opens, which

increases linearly with B above the saturation point. Notably, observing the effect of B on κ in spin systems requires B comparable with $J/g\mu_B$ with g as the g-factor and μ_B the Bohr magneton. For this reason, B up to $14\,\mathrm{T}$ has hardly an influence on the measured κ of the cuprate quantum magnets [132].

An instance of in-B studies of spin systems is the HAFC with low $J_\parallel$, in which B suppress κ only along the spin chains, though $\kappa_\perp$ hardly changes [132]. In this environment, psinons introduced by B behave as scatters of the other psinons rather than operate to carry heat. In the case of the SP chain CuGeO$_3$, two effects are remarkable: (i) The higher-T peak is almost unchanged in B, though the lower-T peak gets strongly suppressed [143]. That is explained as a strong phonon-magnon scattering of the mobile magnetic excitations in the SP phase. (ii) Increasing B closes the spin gap at $\sim 12.5\,\mathrm{T}$ in favour of an incommensurate state [148]. The suppression of the SP order is manifested as a sharp drop in $\kappa(B)$ [143]. The largest decrease, namely by a factor of 30 at $5\,\mathrm{K}$ and $30\,\mathrm{T}$, was observed in the frustrated two-leg ladder BiCu$_2$PO$_6$ [125, 146]. Resonant scattering of the phonons with magnetic excitation levels plus the conventional magnetic fluctuations were argued to be the dominant scattering source, both susceptible to B changes [146]. Notable, this shows the potential of the quantum magnets as candidates for B-tunable thermal insulators in high-B, complementary to superconductors known in low B below their upper critical B [146]. The quantum spin liquid α-RuCl$_3$ in which the spins emerge fluctuating rather than long-range ordered shows the primarily phononic origin of κ in zero-B. External B, however, can tune quantum fluctuations, and the strong enhancement of κ in B was attributed to a radical change in the low-energy magnetic excitations [149, 150]. $\kappa(B)$ of the candidate Kitaev material Na$_2$Co$_2$TeO$_6$ behaves similarly to α-RuCl$_3$: B induces a striking extra peak, described as a suppression of magnetic scattering in B, and thus an increase of κ_{ph} [151].

Within the framework of this thesis, I measured κ of YbAlO$_3$ up to $6\,\mathrm{T}$ to evaluate if a magnetic contribution κ_{mag} is observable at lower T, get information on the B-T phase diagram, heat carriers and scattering mechanisms.

Models of magnetic thermal conductivity: After a successful quantification of the magnetic contribution to $\kappa(T)$, one can employ the existing models to fit κ_{mag} based on the type of magnetic excitations. Within the Kinetic model, Relation 4.6 for the low-D magnetic systems results in

$$\kappa_{\mathrm{mag}}(T) \propto f(T) \cdot l_{\mathrm{mag}}(T), \tag{4.28}$$

where $f(T)$ has a characteristic of the considered spin system. Calculations for a gapless $S = 1/2$ Heisenberg chain and a gapped spin-ladder yield [139]

$$f(T) = \frac{2n_s k_B^2}{\pi \hbar}\, T \int_0^{\pi J_\parallel / 2 k_B T} \mathrm{d}x\, \frac{e^x x^2}{(e^x + 1)^2} \tag{4.29}$$

and

$$f^\Delta(T) = \frac{3n_s k_B^2}{\pi \hbar}\, T \int_{\Delta / k_B T}^{\epsilon_{\mathrm{max}} / k_B T} \mathrm{d}x\, \frac{e^x x^2}{(e^x + 3)^2}, \tag{4.30}$$

where n_s is a geometrical factor that counts the number of chains per unit area. ϵ_{max} and Δ in Relation 4.30 are the spin band maximum and gap, respectively.

For $k_B T \ll J_\parallel$, the integral in Relation 4.29 reaches the constant $\pi^2/6$. The low-T κ approximation of the magnetic excitations of a gapless $S = 1/2$ Heisenberg chain, the spinons, is

$$\kappa_s(T) = \left(\frac{2n_s k_B^2}{\pi \hbar}\, T \cdot \frac{\pi^2}{6}\right) \cdot l_{\mathrm{mag}}(T) = \left(\frac{n_s k_B^2 \pi}{3 \hbar} T\right) \cdot l_{\mathrm{mag}}(T). \tag{4.31}$$

The same can be derived with a product of the specific heat and velocity of the spinons, i.e., C_s and v_s, multiplied by the mean-free path of the magnetic excitation l_{mag}. $C_s = 2N_s k_B^2\, T/3J_\parallel$, and $v_s = J_\parallel a\pi/2\hbar$ in a first approximation of the spin model [126]. Thus, $\kappa_s = C_s v_s \cdot l_{mag} = \left(n_s k_B^2 \pi/3\hbar\right) T \cdot l_{mag}$. That is observable at $T \lesssim 0.15 J_\parallel$ (see, e.g., [152, 153]), meaning that it never appears in YbAlO$_3$ as $J_\parallel$ is not much larger than T_N (Table 4.1).

Magnetic scatterings: The variety of magnetic excitations is one of the reasons that magnetic scattering mechanisms are so complicated. In what follows, the most significant scattering mechanisms in the spin systems are mentioned.

- **Boundaries and defects:** l_{def}, describing the mean-free path limited by static defects, spin defects and spin-boundary scattering, is considered T-independent [139]. Thus,

$$l_{def}^{-1} = l_0^{-1} = \text{const.} \tag{4.32}$$

- **Spin-phonon:** The mean-free path of the spin-phonon scattering, typically denoted as $l_{s\text{-}ph}$, can be considered as an Umklapp process according to Relation 4.26 with a characteristic energy scale of T_u^* of the order of $\Theta_D/2$ [154] as

$$l_{s\text{-}ph}^{-1} = A_{s\text{-}ph}^{-1}\ T^{-1}\ \exp(-T_u^*/T). \tag{4.33}$$

  $A_{s\text{-}ph}$ and T_u^* are the free parameters of the model; though the former, describes the spin-phonon coupling. It is worth recalling that the phonons get scattered via the spin excitations in the same rate; to wit, $\tau_{phonon\text{-}spin} = \tau_{spin\text{-}phonon}$.

- **Spin-spin:** Spin-spin scattering mechanisms have more empirical relations and are still under study [106]. In the case of the gapless spin chains, the integrability of the Hamiltonian results in non-dispersive conduction, and thus, no intrinsic spin-spin scattering exists; albeit, the dirtiness of the real materials explains holding a finite l_{mag}, see, e.g., [155, 156]. Further explanation is provided in paragraph § **Thermal Drude weight**. In case of the spin-gapped ladders,

$$l_{ss}^{-1} = \frac{\gamma_{ss}}{\pi c_L} \int_0^\pi \mathrm{d}k\ 3\left(3 + (\exp(\epsilon_k/k_B T))^{-1}\right), \tag{4.34}$$

  where c_L is the lattice constant along the ladder and $\epsilon_k(\pi) = \Delta$ (see, e.g., [139]). γ_{ss} is the free parameter of the model describing the probability of the spin-spin scattering.

Experimentally, $\kappa_{mag}(T)$ is usually known, and the mean-free path of the magnetic excitations $l_{mag}(T)$ is derived following Relation 4.28. From the other side, the total mean-free path of the magnetic excitations can be estimated using Matthiessen's rule as

$$l_{mag}^{-1} = l_0^{-1} + l_{s\text{-}ph}^{-1} + l_{ss}^{-1}. \tag{4.35}$$

In the next step, different scattering rates are investigated considering the type of spin systems and their typical behaviour: In the case of the 2-D spin planes, the spin-spin scattering is neglected as the spin-defect one is dominating [136]. In the spin-ladder family (Sr,Ca,La)$_{14}$Cu$_{24}$O$_{41}$, a description of l_{mag} via scattering on non-dispersive optical phonons along the ladders was found to be sufficient without the necessity to invoke the spin-spin scattering additionally [157]. Moreover, the spin-hole scattering is reported to be crucial to be considered in case of the ladder compounds, see, e.g. [133–135].

Despite the complexity of the magnetic scattering mechanisms, different processes dominate in different T regions, similar to the case of pure phonon thermal conductivity. $l_{s\text{-}ph}$

dictates the overall mean-free path for high T. Close to zero T, $l_{\text{s-ph}}$ and l_{ss} are usually subdominant compared to the spin-defect scattering, hence $l_{\text{mag}} \to l_0$.

Thermal Drude weight: Energy transport in the 1-D spin systems is addressed either by employing the Boltzmann transport equation formalism or the linear-response formalism. The former approach relies on the notion of quasi-particle modes with associated velocities and relaxation times, which is not always applicable to quantum many-body systems [158]. Thus, the most widely used approach to study the spin systems is the calculation of transport coefficients via time-dependent current-current correlation functions [158]. Kubo [159, 160] showed that using the linear-response theory for κ at a finite frequency ω, one can write

$$\kappa(\omega) = \frac{1}{T} \int_0^\infty \mathrm{d}t \; e^{-i\omega t} \int_0^{1/T} \mathrm{d}\tau \langle \hat{j}_{\text{th}}(-t-i\tau)\hat{j}_{\text{th}} \rangle, \tag{4.36}$$

with $\hat{j}_{\text{th}}$ being the energy-current operator. The real part of the conductivity can be decomposed into singular and regular terms as $Re \, \kappa(\omega) = 2\pi D^{\text{th}}\delta(\omega) + \kappa_{\text{reg}}(\omega)$ [161, 162]. The weight of the δ-peak singularity at $\omega = 0$ noted by D^{th} is the so-called *thermal Drude weight*. The thermal Drude weight can be computed to be [152]

$$D^{\text{th}}(T) = \frac{\pi\beta^2}{N} \sum_{\substack{m,n \\ E_m=E_n}} \frac{e^{-\beta E_m}}{Z} \left| \langle m| \hat{j}_{\text{th}} |n\rangle \right|^2, \tag{4.37}$$

where $\beta = 1/k_{\text{B}}T$, N is the number of the lattice sites, $|n\rangle$ ($|m\rangle$) refers to the eigenstate of the Hamiltonian $\hat{\mathcal{H}}$ with the eigenenergy of E_n (E_m), and Z is the partition function.

In the case of the anisotropic Heisenberg spin chains studied in this work, the Hamiltonian reads

$$\hat{\mathcal{H}} = J_x \sum_{i-1}^{N-1} \boldsymbol{S}_i^x \cdot \boldsymbol{S}_{i+1}^x + J_y \boldsymbol{S}_i^y \cdot \boldsymbol{S}_{i+1}^y + J_z \boldsymbol{S}_i^z \cdot \boldsymbol{S}_{i+1}^z, \tag{4.38}$$

as defined in Relation 2.6. $\hat{j}_{\text{th},i}$ as the local energy-current operator at site i is [161]

$$\hat{j}_{\text{th},i} = J_x J_y (\boldsymbol{S}_{i-1}^x \cdot \boldsymbol{S}_i^z \cdot \boldsymbol{S}_{i+1}^y - \boldsymbol{S}_{i-1}^x \cdot \boldsymbol{S}_i^z \cdot \boldsymbol{S}_{i+1}^y) + \text{ cyclic permutations of } (x,y,z). \tag{4.39}$$

It can be readily shown that the total energy-current operator $\hat{j}_{\text{th}}$ commutes with the anisotropic Heisenberg Hamiltonian, i.e., $[\hat{\mathcal{H}}, \hat{j}_{\text{th}}] = 0$, implying that the energy-current time correlations are time-independent [161]. In this case, (i) the non-decaying of the energy current leads to a diverging $\kappa(\omega)$ related to the $\langle \hat{j}_{\text{th}}(t)\hat{j}_{\text{th}} \rangle$ correlation [161], (ii) Relation 4.37 simplifies to

$$D^{\text{th}} = \pi\beta^2/N \, \langle \hat{j}_{\text{th}}^2 \rangle, \tag{4.40}$$

and (iii) the regular term κ_{reg} becomes negligible reducing the total conductivity to [152]

$$\kappa(\omega) = 2\pi D^{\text{th}}(T)\delta\omega. \tag{4.41}$$

A non-zero/finite D^{th} involves a non-decaying thermal current and, thereby, a non-dissipative thermal transport, the so-called *ballistic* heat transport. Since the energy current is one of the conserved quantities, the existence of the non-zero Drude weight is often linked with the integrability of the system [161–164]. As evident, the property of a non-decaying thermal current is a feature of the 1-D integrable systems, see [165] for more discussion.

$D^{\text{th}}(T)$ of the integrable anisotropic XXZ Heisenberg spin chains has been widely studied and calculated exactly using the Bethe-ansatz method by Zotos *et al.* [161–164]. Around
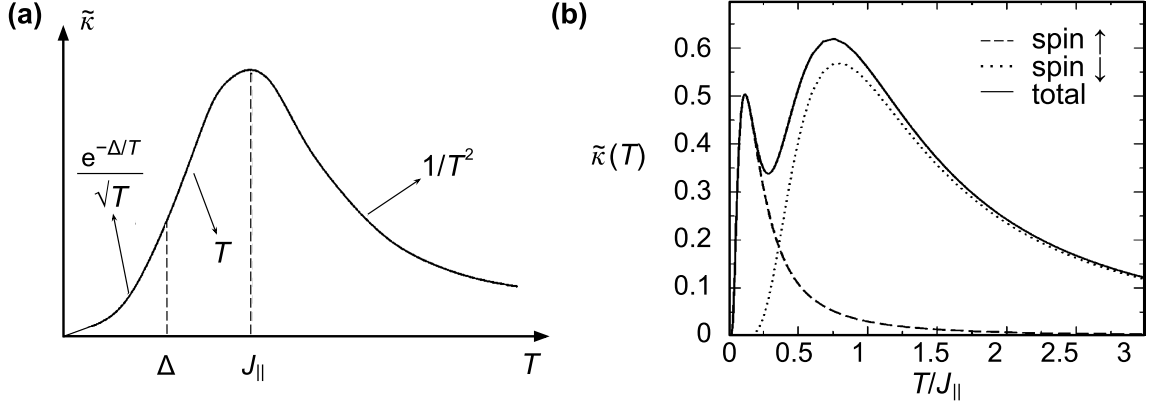
Figure 4.7: Theoretical thermal Drude weight for Heisenberg spin chains. **(a)** Schematic representation of $\tilde{\kappa}(T) := 2\pi D^{\text{th}}(T)$ in a spin gap system without impurities. **(b)** A double-peak structure of $D^{\text{th}}(T)$ is predicted for high B due to separation of the maximum of the up-spin and the down-spin contributions in B. Figures reproduced from [170].

2002 and 2003, several groups including Zotos *et al.* [165, 166], Klümper and Sakai [155, 156], Alvarez *et al.* [167–169], Heidrich-Meisner *et al.* [152, 153], and Orignac *et al.* [170] did analytical and numerical works on $D^{\text{th}}(T)$ of the $S = 1/2$ 1-D spin systems. The results of the $S = 1/2$ gap-less XXZ Heisenberg chains and the two-leg ladders are given in the subsequent paragraph. Remarkably, for the 1-D $S = 1/2$ spin systems described by the Heisenberg AFM XXZ Hamiltonian, different numerical approaches and mathematical techniques of mean-field theory, exact diagonalisation and bosonisation (based on Tomonaga-Luttinger liquid theory) gave consistent values of $D^{\text{th}}(T)$, see, e.g., [152, 153, 155, 167–169].

- **$S = 1/2$ XXZ chains:** T dependence of Dth of the Heisenberg XXZ spin chains is

$$D^{\text{th}}(T) = \begin{cases} \left(\pi^2 k_{\text{B}}^2/3\hbar\right) vT \ \propto T, & \text{low-}T \text{ limit.} \\ \left(3J_{\parallel}^4/2\hbar\right) T^{-2} \propto T^{-2}, & T \gg J_{\parallel}. \end{cases} \qquad (4.42)$$

- **$S = 1/2$ ladders:** Three main regimes are expected for the $D^{\text{th}}(T)$ behaviour of the 1-D two-leg spin ladders with very weak inter-chain coupling ($J_{\perp} \ll J_{\parallel}$): (i) At $T \ll \Delta$,

$$D^{\text{th}}(T) = 3v\sqrt{\pi\Delta^2/2T} \cdot \exp(-\Delta/T), \qquad (4.43)$$

where Δ is the gap energy. (ii) For intermediate T range of $\Delta \ll T \ll J_{\parallel}$, $D^{\text{th}}(T) \propto T$. That is since the rung exchange gets irrelevant and $D^{\text{th}}(T)$ is simply akin to the case of two independent $S = 1/2$ chains. (iii) $D^{\text{th}}(T)$ recovers to $\propto T^{-2}$ at $T \gg J_{\parallel}$.

In the both cases, $D^{\text{th}}(T \to 0) = 0$ and $D^{\text{th}}(T \gg J_{\parallel}) \propto T^{-2}$. Therefore, at least one maximum in $D^{\text{th}}(T)$ at a finite T is expected. Figure 4.7 **(a)** schematically represents the T dependence of $\tilde{\kappa} := 2\pi D^{\text{th}}$ in a *clean* spin-gapped system in the as-described T regimes showing a peak in the vicinity of $T \sim J_{\parallel}$.

Theoretically, the application of an external B can alter the dispersion of the magnetic excitations. For high B (longitudinal to the magnetic moments/spins), the maximum contributions of the spins up (parallel to B) move to lower T, while for the spins down, to higher

T. This relative shift of the maximum contribution of the spins up and down generates a double-peak structure in the in-field $D^{\mathrm{th}}(T)$ [170], as depicted in Figure 4.7 **(b)**.

Although the theoretical calculations for ideally pure integrable systems with a vanishing $[\hat{\mathcal{H}}, \hat{j}_{\mathrm{th}}]$ commutator suggests a non-dissipative transport via the *intrinsic* spin-spin processes, external perturbations such as imperfections, couplings to other transport channels, phonons specifically, or additional interactions through residual 3-D inter-chain couplings, peculiarly in the Q-1-D spin systems, can ruin the integrability of the system, see, e.g. [155, 168, 171]. In the sense of the formula, the δ peak broadens into a Lorentzian with a width inversely proportional to the finite *external* lifetime of the eigenstates of the spin system τ, and κ reduces accordingly, the value of which depends on the type and strength of the perturbation [142]. For weak coupling, the experimentally accessible quantity κ holds [171]

$$\kappa(T) = D^{\mathrm{th}}(T)\tau. \tag{4.44}$$

Comparisons between the estimated *external* mean-free path as $\lambda = \tau v$ and l_{mag} have been made for some low-D spin systems. In the case of the spin chains, the kinetic Relation 4.31 and Relation 4.42 of $D^{\mathrm{th}}(T)$ yield the same result at low T, as used in, e.g., [126, 128, 130, 142]. $CaCu_2O_3$, as an instance, shows the constant value $\lambda = l_{\mathrm{mag}} \approx 22 \pm 5\,\text{Å} \approx 5$ - 6 l.c. (l.c. for lattice constant) at the T range of 100 - 300 K [126]. In the case of the spin ladder $Ca_9La_5Cu_{12}O_{41}$, however, $\lambda(100\,\text{K}) \approx 176\,\text{Å} \approx 45$ l.c. turned out to be substantially smaller than $l_{\mathrm{mag}}(100\,\text{K}) \approx 3000\,\text{Å} \approx 770$ l.c. found using the phenomenological formulas [134, 169]. That is explained by considering a dissipative transport (non-integrable model) for the $S = 1/2$ two-leg spin ladders, similar to frustrated chains or dimerised chains [153].

To sum up, transport in the gap-less $S = 1/2$ chains is ballistic and limited by external perturbations. Conversely, the systems with a spin gap like $S = 1/2$ even-leg ladders are governed by intrinsic diffusion [142]. In the end, l_{mag} was never found larger than a few $1000\,\text{Å}$, that is, $\ll \sim 1\,\text{mm}$, well below the typical dimension of the measured samples. $\lambda(T \to 0)$ plateaus off invariably at very-low T since the impurity scattering is expected to get relevant [169].

4.6 Summary

The basic concepts of heat transport were reviewed. The Callaway model represents a full description of phonon-phonon processes. However, the Debye approximation typically models experimental data well due to appreciable impurity concentrations. The harmonic approximation predicts $\kappa_{\mathrm{ph}} \propto T^3$, at least up to where the Umklapp processes get important.

In spin systems, magnetic excitations, just as every (quasi-) particle with a specific heat and a non-vanishing group velocity, can carry heat. Thermal conductance in 1-D $S = 1/2$ Heisenberg AFM spin chains is an important example that was predicted to be dissipation-less, i.e., having no thermal resistance, by virtue of the conservation of the energy current operator. However, in real crystals, the thermal conduction is affected by non-phonon-phonon scattering processes and remains finite. The spinon energy current is limited by the scattering, mainly with defects and phonons.

5 Instrumentation: Experimental setups for thermal conductivity

5.1 Introduction

This chapter provides a general description of thermal conductivity (κ) measuring methods, the specifics of my experimental setups, measuring procedures, and computational methods. First, I explain the basics of the thermal conductivity measurements, the sample orienting method and the preparation process. Then, the measurement system for high temperature (T), the PPMS, is introduced, followed by the sample holders, the measurement procedure and the data analysis. Afterwards, I describe the thermal-transport measuring setup in the dilution fridge and the utilised sample holder. Thermometry, measuring and calibration procedures, including data analysis, are also presented in detail.

5.2 Measurement principle

Figure 5.1 schematically depicts a four-point thermal conductivity experiment. The sample is coupled at one end to a thermal bath, playing the role of the cold reservoir, the so-called *Cold Finger* (CF). Probing κ as a transport property requires a T gradient. To induce the gradient in T, a *gradient* heater is attached at the other end of the sample. If the sample is not coupled to the thermal bath, applying a finite heat pulse increases T overall to T_0 with a uniform T profile of $T(\boldsymbol{r}) = T_0$ in equilibrium. Heating continuously would hence infinitely increase the sample T. In a thermal-conductivity-measuring

Figure 5.1: Scheme of a thermal transport experiment. The sample is connected at the two ends to a cold bath and a heater producing a linear T profile in equilibrium.

setup where the sample is coupled to the bath, introducing the heat will result in a heat current flowing through the specimen. As mentioned in Chapter 4, thermal conductivity indicates the capability of a compound to conduct heat. In an extended bar-shaped sample, κ can be calculated by measuring T at two points located at a distance of l apart along the specimen, labelled as T_C (for the colder T) and T_H (for the hotter T), referring to the points close to the CF and the heater, respectively, as illustrated in Figure 5.1. In terms of the formula, the thermal conductivity κ is defined as the heat-current density $\boldsymbol{j}_Q$ (rate of heat flow $\dot{Q}$ per unit area A_s, with A_s as the sample cross-section area) per resulting T gradient $dT/l = (T_H - T_C)/l$,

$$\kappa = \frac{\dot{Q}}{A_s} \cdot \frac{l}{dT}. \tag{5.1}$$

In the ideal case without heat leak, the heat introduced by the gradient heater per unit time P_{Heater} flows entirely through the sample, i.e., $\dot{Q} = P_{\text{Heater}}$.

(a)

(b)


Figure 5.2: YbAlO$_3$ crystal and the magnetisation results confirming the orientations after the cut. **(a)** Photography of the uncut YbAlO$_3$ sample studied in this work. **(b)** $M(B)$ at 2 K along the three determined directions of $\tilde{a}$, $\tilde{b}$, and $\tilde{c}$ normal to three faces of the sample YbAlO$_3$#b. The tilde indicates the expected principal directions of the sample according to the Laue X-ray diffraction. Further discussion is provided in the main text.

5.3 Orienting the YbAlO$_3$ samples

The YbAlO$_3$ crystal used in the present work was handed to me over kindly by *Stanislav E. Nikitin* and *Manuel Brando* and is the same crystal used for the magnetisation, specific heat and neutron scattering measurements in [59, 71, 74, 79]. It stemmed originally from a high-quality single crystal of YbAlO$_3$ grown by the Czochralski technique [58, 172] and was kindly provided by *Leonid Vasylechko* from the *Lviv Polytechnic National University*. A photo of the crystal before cutting is shown in Figure 5.2 **(a)**. I did sufficient times of Laue X-ray diffraction[1] to determine the crystal orientation essentially precisely before cutting the bulk. Next, I cut the bulk sample into two bar (cuboid) shapes with a wire-saw machine, labelled YbAlO$_3$#c and YbAlO$_3$#b, prepared to be measured along the c and b directions, respectively. Given the close a and b lattice constants, I measured magnetisation (M) to validate the orientation of the prepared samples. Figure 5.2 **(b)** shows the magnetisation of sample YbAlO$_3$#b along the three directions of $\tilde{a}$, $\tilde{b}$, and $\tilde{c}$ versus field (B) up to 5 T at 2 K. $\tilde{a}$, $\tilde{b}$, and $\tilde{c}$ tags correspond to the directions determined as a, b, and c crystallographic axis via the Laue X-ray diffraction, respectively. Though not needed once working with the ratios, M values are converted to μ_B/Yb unit to make the graphs comparable with the other works, e.g., [59]. The values of $M(B = 5\,\text{T})$ along these principal directions of the sample with a mass of 4.70 mg are computed to be $M_{\tilde{a}} = 2.995 \pm 0.001\mu_B$/Yb, $M_{\tilde{b}} = 1.238 \pm 0.001\mu_B$/Yb, and $M_{\tilde{c}} = 0.0759 \pm 0.0010\mu_B$/Yb. Accordingly, the angles between the magnetic moments of the Yb^{3+} ions and the $\tilde{a}$ ($\measuredangle\tilde{a}$) and $\tilde{c}$ ($\measuredangle\tilde{c}$) directions can be calculated.

$$\measuredangle\tilde{a} \simeq 22.50° \pm 0.1° \qquad \text{and} \qquad \measuredangle\tilde{c} \simeq 88.66° \pm 0.1°. \tag{5.2}$$

That corresponds to a misalignment of the sample of $\sim$1° with the reported value $\varphi = 23.5°$ [59, 71, 74, 79]. Considering the possible misalignment sources, e.g., that the specimen was aligned and fixed only visually on the quartz holder of the vibrating sample magnetometer

---

[1]ARL EQUINOX LAUE X-Ray Diffractometer, Thermo Scientific™

(VSM), it is concluded that the sample is appreciably well-oriented. Lastly, the Yb^{3+} single-ion anisotropy along the two $\tilde{a}$ and $\tilde{c}$ directions may be investigated as well.

$$\angle(\tilde{a}-\tilde{c}) = \text{arctanh}\left(\frac{M_{\tilde{a}}}{M_{\tilde{c}}}\right) = \frac{2.995\ \mu_B/\text{Yb}}{0.0759\ \mu_B/\text{Yb}} \simeq 88.55° \pm 0.1° \tag{5.3}$$

proves that the Yb^{3+} ions can be well described by *Ising* moments. Henceforth, I assume that $\tilde{a} \parallel a$ and $\tilde{c} \parallel c$. These results also exclude presence of a large twin.

5.4 Sample preparation & cold-finger contact

In a thermal-transport measurement, sample preparation typically involves orienting the crystal, cutting (and/or polishing) the sample, mounting the sample on the CF, and making contact with T_C & T_H thermometers, plus a gradient heater.

In the case of $YAlO_3$, oriented crystals were bought[2] and cut into long, thin samples with a wire-saw machine. The $YbAlO_3$ samples were initially oriented by Laue diffraction and then cut into bar (cuboid) shapes. Table 6.1 and Table 6.3 summarise the dimensions of the prepared samples. I recall that the magnetisation measurements confirm the cut $YbAlO_3$ samples being correctly oriented with a deviation of $\sim 1°$, as discussed in Section 5.3.

I continue this section with adhesives used to prepare the sample contacts and install the thermometers and heater if needed. To excel in thermal coupling to the specimen at each of the four measuring points (in conjunction with Figure 5.1), I gold evaporated four pads on the sample in the next step. Lastly, I explain my techniques for contacting the CF contact.

Adhesives: Two adhesives were mainly utilised: (i) An air-dry silver composition[3] was used as glue for the electrical contacts. That is a solvent[4]-based adhesive containing small silver particles. Low electrical and thermal resistance down to very low T make it favourable for the electrical and thermal contacts. More information can be found in [173]. Moreover, one can use it for preparing the bath contact. The silver glue can easily be solved by acetone and, less well, by ethanol and can be removed with few effort residue-free. The easiest way to apply the silver glue on the sample is to use a very fine paintbrush. In this research, the self-made brushes were build by attaching an eyelash or 30-µm fine copper wires to the tip of individual toothpicks. (ii) *Ge varnish*[5] is a solvent-based, electrically insulating varnish. It is ideal for attaching the electrical components, such as the thermometers or the heater, to the measuring setup, where a high thermal coupling in the absence of any electrical contact is needed. It is solvable by acetone and ethanol and can be removed residue-free.

Sputtering of Au micro contacts: Since a successful thermal-conductivity measurement outcome depends on the ability to make good thermal contacts, gold micro-contacts were sputtered[6] onto the sample if mentioned. The process of gold micro-contact deposition is shown in Figure 5.3 schematically. As shown in Figure 5.3 **(a)**, I masked each sample by *Kapton* tape initially so that the two contact points of the cold reservoir and gradient heater locate at the two very ends and the two contacts for cold and hot thermometers are as-much-as-possible apart while neither touches the other. Before starting any deposition

---

[2]from CRYSTAL GmbH, Berlin

[3]DuPont 4929N

[4]DuPont 4987

[5]VGE 7031, CMR-Direct Company

[6]Axxis™, Kurt J. Lesker Company

(a) Step 1: Masking with *Kapton* tape

(b) Step 2: Argon-ion etching

(c) Step 3: Ti deposition (10 nm)

Substrate
Kapton-tape mask
Ti
Au

**(d)** Step 4: Au deposition (150 nm)

(e) Step 5: Lift-off
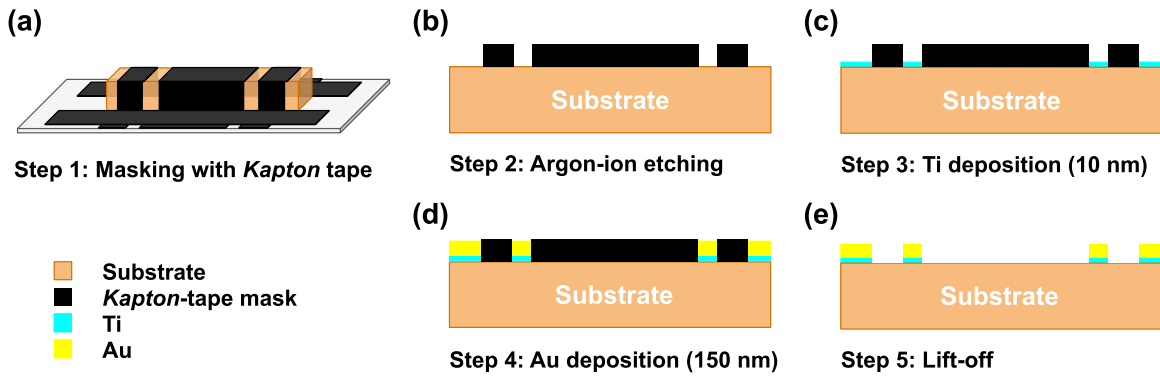
Figure 5.3: Schematic process of gold micro-contacts deposition. This type of contacts ensures the stability and thermal coupling of the contacts to the sample. **(a)** The initial step consists of masking the cuboid sample carefully with *Kapton* tape leaving the contact areas free. **(b)**-**(e)** Long cross section of the specimen under deposition. **(b)** The surface of the substrate is cleaned with an argon-ion beam. **(c)** 10 nm of titanium is deposited, over which **(d)** 150 nm of gold is sputtered. **(e)** In the last step, the taped mask is removed.

(a) Silver lid — Gold-plated copper bars

(b) Indium wrapping
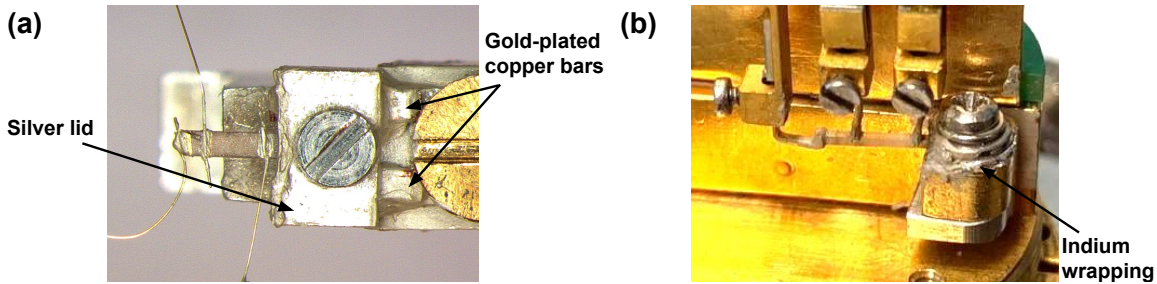
Figure 5.4: Cold-finger contacts. The sample is preferred to be mechanically clamped at the CF to maximise the thermal contact to the cold reservoir. **(a)** YbAlO$_3$ sample mounted under the silver lid of the *M* piece. Two gold-plated copper bars where fixed under the lid to ensure its stability. The remaining open area was filled by silver paste. **(b)** YAlO$_3$ sample on the normal TTO puck. CF end of the sample was wrapped with indium wire initially so by tightening the clamp the CF contacting point gets well surrounded by the indium.

process, I used argon-ion-beam etching for *in-situ* surface cleaning of the specimen (Figure 5.3 **(b)**). During this dry etching, the ions are accelerated and directed towards the surface of the substrate, transferring their energy to escape upon arrival to the surface atoms. Ion-beam milling is effective in removing contamination layers, remains from sample cutting or native oxides, and preparing the diffusion binding surface. It can considerably improve adhesion if used before thin-film deposition [174].

Then, 10 nm of titanium was sputtered on the Ar-ion-beam etched surface, as indicated in Figure 5.3 **(c)**. Titanium as a non-magnetic element is used as a glue-like layer to stick the later deposited-Au layer better. As illustrated in Figure 5.3 **(d)**, in the next level, 150 nm of gold was sputtered over the Ti layer. The gold-evaporated micro contacts help to avoid detachment of the silver-paste contacts from the shiny single-crystal surfaces as well. After Au metallisation, the process was completed by careful lift-off of the *Kapton* tape mask so as not to damage or scratch the gold-plated pads (Figure 5.3 **(e)**).

Cold-finger contact: The CF contact is vitally important in κ measurements. If coupling between the CF and the sample is poor, most of the T gradient will build up between the sample and the bath rather than along the sample (see Section 5.2). Therefore, the CF contact should be prepared carefully. Good thermal contact can be achieved mechanically by clamping the sample, electrically by using a conductive glue between the specimen and the bath, or by a combination of both methods. In this study, I connected the gold-plated specimens mechanically using the mentioned clamping methods: (i) As shown in Figure 5.4, a self-designed silver piece, called *M piece* in this text, was used for the samples investigated from sub-Kelvin to room-temperature range (the name is influenced by the piece shape). Details of the design are provided in Appendix Section D.1. Using the M piece has several advantages: Firstly, the M piece and the holding lid are prepared from silver possessing a high κ, and thus facilitating a good thermal link between the sample and the bath. In addition, the M piece is compatible with both sample holders of the high- and low-T measurements. This allows for using the same CF (including thermometers and heater) contacts and geometry spanning from the lowest to the highest measuring T range. Moreover, the particular symmetry of the design makes it possible to measure the once-mounted sample along two perpendicular directions with respect to B, depending on the chosen piece-to-holder mounting hole, without changing the contacts on the sample. (ii) If the sample is not mounted on a silver M piece but conventionally in the *mini-TTO* setup, I fixed it by a stainless-steel washer to the sample holder body, pressed between gold-plated copper bars for high-T measurements. (iii) Indium wrapping is another method I invented to improve the CF contact in case a silver piece can not be utilised. In this technique, I wrapped the CF end with indium wire initially. By tightening the clamping screw, indium as a soft metal will be crushed and fill all the free area under the clamp (see Figure 5.4 **(b)**). A difference between this method and painting silver paste around the sample is the favourable mechanical pressure from all directions. Therefore, this technique can strongly improve the sample CF interface to the cold reservoir for the samples mounted via a stainless steel washer compared to a silver lid. I compared this technique experimentally to the conventional clamping method without indium, and the result is presented in Appendix C.

5.5 Measurements in the high-temperature region: Physical property measurement system

Thermal-transport measurements in the T range of 2 - 300 K presented in this study have been performed in a commercially available Quantum Design (QD) Physical Property Measurement System (PPMS). This device has already been in use for several years, and detailed descriptions of the capabilities and the methods can be found at *Quantum Design* [176–178]. The available T range spans normally from 2 K up to room temperature (RT) with the possibility to extend it down to 0.4 K by using the so-called *³He option*; however, this option is not available for all techniques, including thermal transport. A high-vacuum option providing $\sim 10^{-4}$ mbar is available as well, which is needed for thermal transport measurements.

The thermal transport option (TTO) offers thermal conductivity and thermoelectricity measurements down to 2 K; however, the latter is useless for electrically insulating samples, including the compounds under study in this thesis. Figure 5.5 shows the two pucks I used for the high-T thermal-conductivity measurements in this research, and the red rectangle highlights the specimen. The standard commercially-available TTO puck is shown in Figure 5.5 **(a)** with an exemplary sample installed. The samples on the standard TTO puck
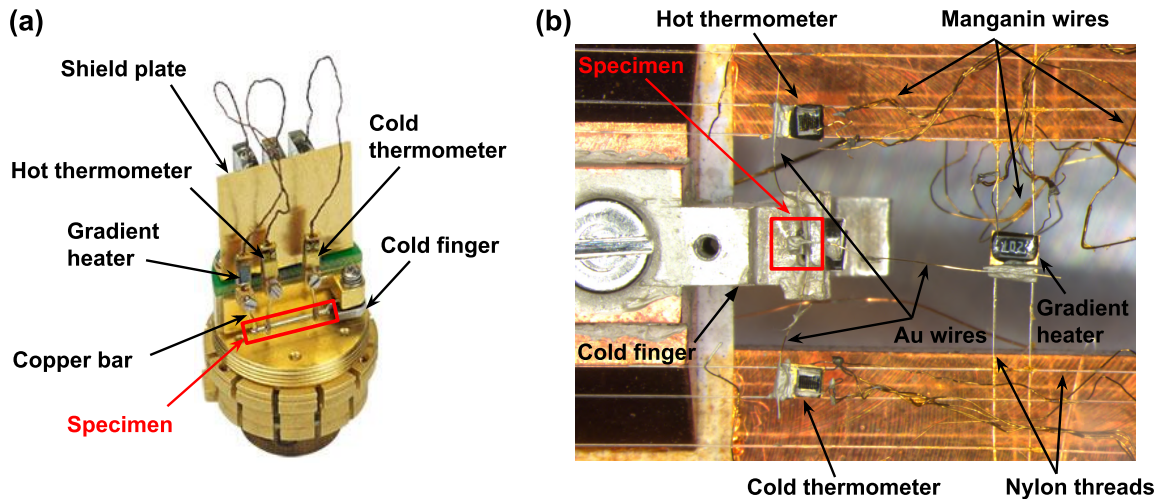
Figure 5.5: Sample holders used for the high-T measurements in PPMS. For visual help, a red rectangular is drawn around the specimen in each case. **(a)** Standard TTO puck. The right, middle and left shoe assemblies are cold and hot probes followed by the gradient heater, respectively, connected via the Au-plated copper bars to the exemplary sample. In addition to the copper iso-thermal radiation shield covering the whole setup, a shield plate is placed between the sample stage and the sockets to minimise radiation effects (Figure reproduced from [175]). **(b)** In-house-developed *mini-TTO*. Two Cernox thermometer sensors and a gradient heater are mounted on the gold islands, lying over the nylon threads to reduce the thermal coupling between the components and the puck body. Like the standard TTO puck, manganin wires are used for the electrical wiring. The gold wires from the sample are extended with same-diameter gold wires to the gold islands. Using the *mini-TTO*, the same geometry and contacts could be used for the dil fridge and PPMS devices.

were mounted to the bath using the indium wrapping technique explained in Section 5.4 paragraph § **Cold-finger contact**, named method (iii), via a screw and a stainless steel washer (see Figure 5.4 **(b)**). Modularised *shoe* assemblies, including two thermometer shoes and one heater shoe, are connected to sockets on the TTO puck. Each gold-plated copper shoe has a hole in which gold-plated copper bars are inserted and held in the shoe by a small stainless steel screw with one end. Small amounts of Apiezon-H Grease can improve the thermal coupling at the contacts between the bars and the shoes as well. The other end of the copper bar is connected with silver paint to the gold-plated micro contacts on the sample (also visible in Figure 5.4 **(b)**). The thermometer- and heater-shoe assemblies contain *capsuled* Cernox temperature sensors[7], and a 1-kΩ resistive heater chip, respectively (as well as a voltage lead on each thermometer shoe and an electrical current source lead ($I+$) on the heater shoe assembly for parallel resistivity measurement). In order to minimise heat loss via the wires of the thermometers and heater, 75-µm-diameter wires made of manganin alloy are used (except for the current ($I+$) lead, which is connected to the shoe but not used in the main project of this research) [176]. A copper iso-thermal shield plate is also placed between the sample and the sockets to reduce radiation effects (see Figure 5.5 **(a)**). Once the sample is successfully mounted, a copper shield is screwed into the base of the puck to minimise radiation loss from the sample to the environment.

---

[7]CX-1050 Cernox, Lake Shore Cryotronics, Inc.

In some cases, the high-T measurements were performed utilising an in-house-developed puck[8], labelled in this text as *mini-TTO*. The main privilege of this home-made puck is the possibility to install directly the M piece used in the low-T setup without unmounting the sample. Thus, the same contact geometry can be used in different devices, i.e., from sub-Kelvin to room-temperature measurements. That facilitates for comparability of the data. In this case, I prepared the sample CF contact on the silver M piece using method (i) mentioned in Section 5.4 paragraph § **Cold-finger contact**. Figure 5.5 **(b)** shows the *mini-TTO* holder. Similar to the standard TTO puck, two Cernox temperature sensors and a 1-kΩ gradient heater are used. Instead of the capsuled Cernox sensors, *bare* chips, being much smaller in size, are used. These electrical components are mounted on gold islands lying on nylon threads (similar to the design of the *Franz* sample holder, introduced in Section 5.6 paragraph § **Sample holder**).
The sample mounted on the M piece (design details accessible in Appendix Section D.1) is attached to the *mini-TTO* holder mediated by an *M-piece-mini-TTO* adaptor made of copper. The details on the adaptor design can be found in Appendix Section D.2.

κ is measured by applying heat from the gradient heater and generating a user-specified T gradient between T_H contacting point and the CF. MultiVu software was used to interface the high-T measuring system PPMS. The TTO models dynamically the thermal response of the sample to the low-frequency square-wave heat pulse, thus expediting data acquisition. The TTO also corrects for any heat losses that occur. Ultimately, the software calculates κ directly from the applied heater power, resultant time-dependent T difference $\Delta T(t)$ and given sample geometry. More information can be found elsewhere, e.g, [176, 179].

5.6 Measurements in the milli-Kelvin temperature range: ^{3}He-^{4}He dilution fridge

All the sub-Kelvin measurements were carried out in a commercially available ^{3}He-^{4}He dilution refrigerator[9] (dil fridge for short[10]), with a promised cooling power of 400 µW at 100 mK and a base T of 7 mK [180]. Since 1951 when London suggested the basic idea [181], it took more than ten years till London, Clarke, and Mendoza published a detailed concept for realising such a cooling system in 1962 [182]. The operation of the dil fridge relies on the ^{3}He-concentration dependency of the enthalpy as mixing the two quantum liquids, Helium-3 and Helium-4. The different zero-point motions of the two helium isotopes and the lower entropy of ^{3}He atoms in a ^{3}He-rich (concentrated) phase compared to a ^{3}He-poor (dilute) one results in a higher specific heat of the ^{3}He atom in the dilute phase than the concentrated one. Finally, cooling occurs as the ^{3}He atoms absorb heat from the environment once migrating from the concentrated phase to the dilute one.

In practice, a dilution refrigerator comprises two main containers, the so-called *mixing chamber* (MC) and the *still*. When cooling below ∼0.87 K, the ^{3}He-^{4}He mixture in the MC undergoes a separation into the dilute and concentrated phases. The still is connected to the lower dilute phase of the MC, and the osmotic pressure difference enforces the ^{3}He atoms to flow from the concentrated to the dilute phase, specifically from the MC to the still, thereby absorbing heat. The still operates like a distillation chamber where almost

---

[8]by Dr Ulrike Stockert
[9]Kelvinox MX 400, Oxford Instruments
[10]Not dill fridge for dill pickles prepared in a fridge

pure ^{3}He is evaporated so that the dilute phase has a liquid ^{3}He concentration of $<1\,\%$. By pumping on the still, almost pure ^{3}He is evaporated inside the still due to the much higher partial pressure compared to the ^{4}He. The pumped gas is reinjected into the condenser line. This gas is liquefied at the so-called *1K pot* and further pre-cooled through the capillary input line of the MC, the so-called *condensation line*. Eventually, it is refed to the MC, thus closing the cycle for continuous cooling operation. More details are available in specialised low-T physics books [97, 98].

The dilution fridge dewar has been placed on an electrically grounded stage. Mechanical damping of the pumps and environment vibrations is essential to restrict the noise and the heat input into the system. Therefore, I isolated all tubes electrically and mechanically before operating the measurements using typical wrapping air-bubble and cushioning-foam sheets as insulating-damping sheets, and fixing bands. Appropriate electrical shielding and uniform grounding was ensured as well, e.g., the lowest T measured at the CF was reduced from $23\,\mathrm{mK}$ to $12\,\mathrm{mK}$ by cancelling grounding loops. Although the feasible T range spans from $\sim 12\,\mathrm{mK}$ to $4\,\mathrm{K}$, stability at very low and very high T is difficult to be reached due to the environmental heating and the fridge cooling power, respectively.

An encapsulated resistive RuO_2[11] sensor is directly anchored at the MC within the so-called *compensated zone* where B is below $5\,\mathrm{mT}$, and the magnetoresistive effects are negligible. The compensated-zone thermometer had been calibrated by S. Hartmann as mentioned in [183] in the whole accessible T range, i.e., down to $\sim 9\,\mathrm{mK}$, according to Oxford Instruments standards. This thermometer is measured by the gas handling system of the dil fridge.

A built-in 1-axis superconducting magnet system[12] generates B up to $8\,\mathrm{T}$. The magnetic field was applied in both steady-state and field-sweep modes.

Sample holder: The used sample holder for the sub-Kelvin T range measurements in the dilution fridge was originally developed by S. Hartmann to verify the so-called *Wiedemann-Franz law* and study the thermal conductivity and/or thermopower at very-low T, and named *Franz* sample holder in this text. A detailed explanation on the *Franz* sample holder design, components and electrical connections can be found in [183]. Here, I summarise the most crucial features of the holder. Figure 5.6 **(a)** displays a photography of the *Franz* sample holder while connected to the dilution fridge (on the top) with firmly-tightened screws. The sample holder has a Vespel frame screwed to a copper body covered by a layer of deposited gold. Nylon threads are used to provide a net to hold the thermometers and gradient-heater gold islands, which will be discussed in detail below. Vespel and nylon are both known for low thermal conductance and reduce the possible heat leaking from the sample and/or the electrical components to the copper body of the holder coupled thermally to the fridge MC and the sample CF contact (check Figure 5.1, where $T_{\mathrm{CF}} < T_{\mathrm{C}} < T_{\mathrm{H}} < T_{\mathrm{contact\ to\ heater}}$ in equilibrium).

A bare RuO_2[13] thermometer is anchored at the CF. Additionally, a 70-μm Manganin wire looped around a post located at the compensated zone at the MC acts as a *setup heater* ($R \simeq 1\,\mathrm{k\Omega}$). T_{CF} was read and controlled with an AC resistance bridge[14], which offers advantages such as different resistance ranges and excitation levels for reading the thermometer resistances, Proportionality-Integral-Derivative (PID) control and low-noise measurements.

The M piece carrying the sample mounted is installed on the CF tip, as explained in

---

[11]Model RO 600, Scientific Instruments

[12]NbTi/Cu. American Magnet, Inc.

[13]RX-102A-CD, Lake Shore Rox™. Lake Shore Cryotronics, Inc.

[14]Model 370 AC Resistance Bridge. Lake Shore Cryotronics, Inc.
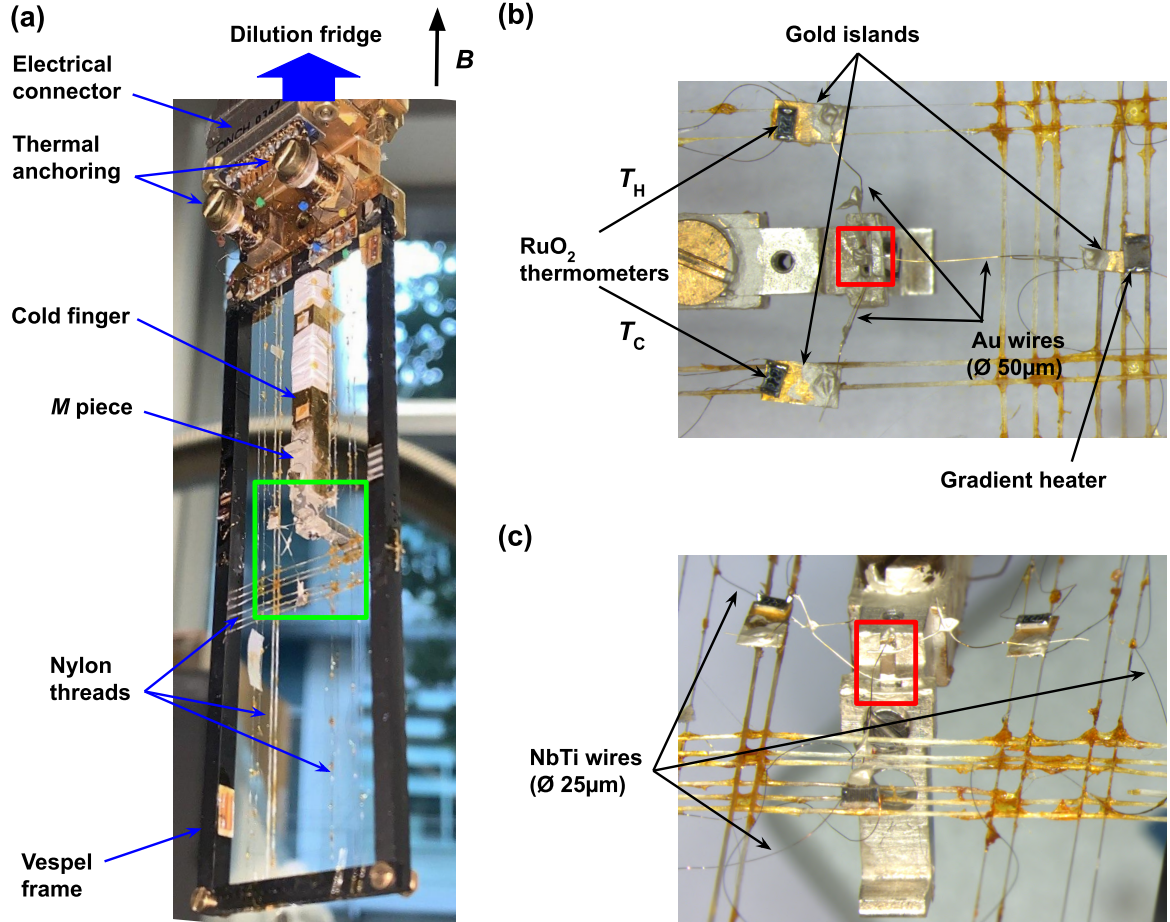
Figure 5.6: *Franz* sample holder used for the measurements in the dilution refrigerator. **(a)** The sample holder comprises a gold-plated copper body and a Vespel frame on which nylon threads form a net. The Vespel frame and the nylon threads are used both to minimise the thermal contact between the electrical components, i.e., thermometers and heater, and the sample holder copper body. A 25-pin D-sub connector, two thermal anchoring cylinders and the CF are the main components on the gold-plated copper body. The sample mounted on the *M* piece is installed on the CF tip, as highlighted by a green box. The sample is placed within the centre of the field. The sample holder is tightly screwed to the dilution fridge, as indicated. This setup will experience an in-plane *B* parallel to the CF, as indicated by the black arrow. **(b)**-**(c)** Magnification of the region marked in **(a)** by a green box. In each sub-figure, the sample is marked by a red box. **(b)** Top view. Two RuO_2 thermometers and a gradient heater are fixed on gold plates via GE varnish. The thermal connections between the sample contacts and the corresponding islands are made with 50-µm Au wires. Each gold island is fixed on the nylon net by GE varnish. **(c)** Isometric view. Superconducting NbTi ($T_c \simeq 9.7\,\mathrm{K}$) wires are used for electrical connection of the components to prevent thermovoltage and thermal-leak effects. More details are provided in the text.

Section 5.4 (method (i)). The sample is sitting in the centre of the applied field, and B is oriented along the CF (Figure 5.6 **(a)**). In this case, I applied a thick layer of silver glue directly on the interfaces of the M piece and the CF tip initially and clamped the M piece tightly with a screw so that the silver paste penetrates in all possibly-existing cavities and the connection between the two pieces is metallic everywhere resulting in a maximised thermal coupling. The green box comprising the sample connected to the thermometers and the gradient heater components, is magnified in the top and isometric views in Figure 5.6 **(b)** and **(c)**, respectively. A thin film resistor as heater and two RuO_2-chip[15] thermometers are utilised to perform one-heater-two-thermometer κ measurements. More information on the components is in § **Gradient heater** and § **RuO$_2$ thermometers**.

The heater and thermometers are fixed on Au-islands using GE varnish to produce a thermally conducting and electrically insulating connection to the sample holder body. The gold islands lie on Nylon threads to stay isolated and have minimal thermal contact with the sample holder body. However, this way of mounting makes the thermometers ultra-sensitive to mechanical vibrations. The lower the temperature, the more susceptible the thermometers. This is one of the reasons which make thermal conductivity one of the most delicate measurements in experimental solid-state physics compared to the other typical measurements, e.g., resistivity, specific heat, magnetisation, etc. The electrical connections of the thermometers and the gradient heater to the sample holder are by NbTi wires which are superconducting below $T_c(\text{NbTi}) \simeq 9.7\,\text{K}$ to prevent heat flow from the thermometers to the bath and thermovoltage effects in between. The islands are connected via $50\,\mu\text{m}$ gold wires by silver paste to the corresponding Au micro-contacts on the sample highlighted by a red box in Figure 5.6 **(b)**-**(c)**. The shown sample installation entails in $\boldsymbol{B} \perp \boldsymbol{j}_Q$ in the presence of an external magnetic field. Alternatively, it is possible to turn the M piece such that $\boldsymbol{B} \parallel \boldsymbol{j}_Q$ (see Appendix Section D.1 Figure D.2).

Due to the frangibility of the Vespel frame and the ageing of the *Franz* holder, regular repair is needed. Thus, a new sample holder is proposed in Appendix Section D.3.

RuO$_2$ thermometers: The ruthenium oxide chips used as T sensors are thick-film resistors employed for a long time in cryogenic thermometry, especially in applications involving low T and high B, and much literature on their behaviour and T sensitivity is available, e.g., [184–190]. Such types of composite sensors consist of bismuth ruthenate, ruthenium oxides, binders, and other compounds that allow them to obtain the necessary T and resistance R characteristics. The main advantage is that R increases dramatically as T decreases down to milli-Kelvin temperatures, and each RuO_2 chip adheres to a single resistance-versus-temperature curve. Initial disparities in the resistance values reduce after about the first 60 thermal cycles, and the $R(T)$ curves stabilise afterwards [97, 98, 184–189].

These resistive thermometers have a nominal R of 1 - $2\,\text{k}\Omega$ at RT which increases exponentially per cooling. The resistance of each sensor was measured by a convenient four-point technique using low-T Lake Shore (LS) 370 AC resistance bridges similar to the CF sensor. Figure 5.7 **(a)** illustrates the R behaviour of the two RuO_2 thermometers utilised to measure the T gradient of the specimen in the dil fridge named $RuO_2\#1$ and $RuO_2\#2$. $6.32\,\text{k}\Omega$ and $20\,\text{k}\Omega$, as the relevant resistance ranges of the LSs, are shown as dashed lines and the threshold resistance of the LS $6.32\,\text{k}\Omega$ range $R \sim 7.8\,\text{k}\Omega$ as a solid cyan line. The range below $\sim 7.8\,\text{k}\Omega$ measurable with both LS resistance ranges of $6.32\,\text{k}\Omega$ and $20\,\text{k}\Omega$ with high accuracy is highlighted by a grey box. To prevent the effects of auto-range tuning of the LS devices, I ran all the measurements using fixed ranges with the T limits of the runs chosen

---

[15]RX-202A-CD, Lake Shore Rox™. Lake Shore Cryotronics, Inc.
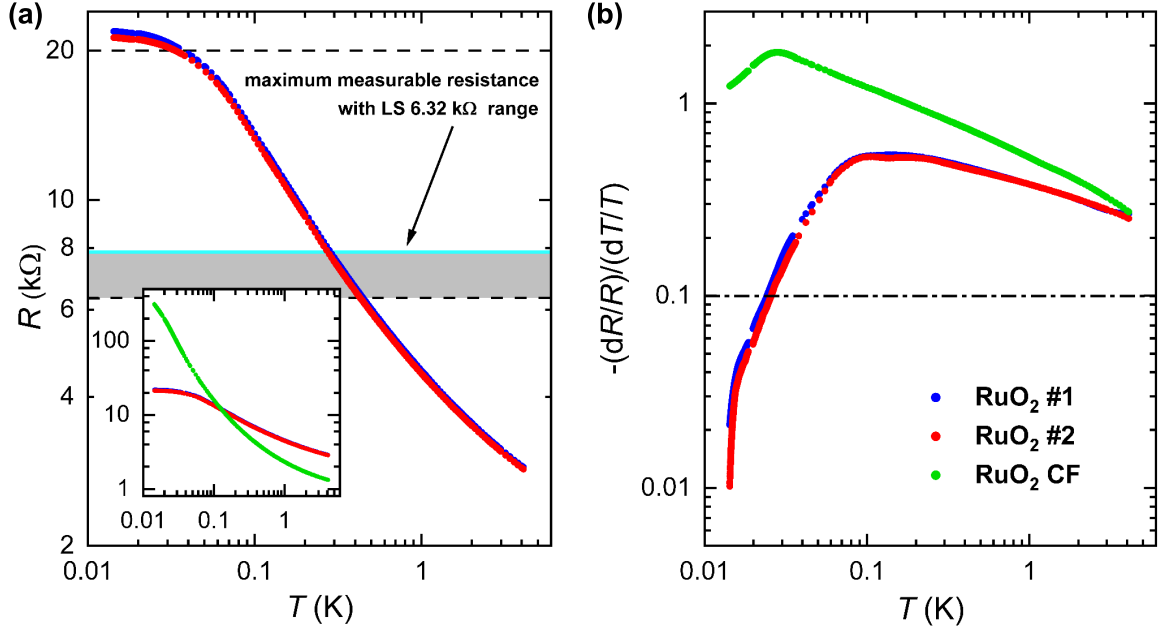
Figure 5.7: Resistance and sensitivity of the utilised RuO$_2$ chips against T_{CF} in the range of about 0.01 - 4 K. **(a)** Typical $R(T)$ behaviour of the two thermometers used to measure the T gradient of the sample, labelled RuO$_2$#1 and RuO$_2$#2. The dashed lines indicate the LSs' resistance ranges and the cyan line shows the maximum measurable resistance with a 6.32 kΩ range. The range below $\sim$7.8 kΩ, highlighted by a grey box, can be measured with both LS resistance ranges of 6.32 kΩ and 20 kΩ with high accuracy. The inset includes the CF RuO$_2$ (the green curve) as well. **(b)** Dimensionless sensitivity $-(\mathrm{d}R/R)/(\mathrm{d}T/T)$ curves of the three used thermometers. At $\sim$25 mK, the sensitivity curves of RuO$_2$#1 & RuO$_2$#2 sensors go below 0.1 (the dash-dot line), which reveals their inapplicability below 30 mK.

such that the measured curves overlap within this grey box. R of RuO$_2$#1 and RuO$_2$#2 chips span from $\sim$2 kΩ at RT to $\sim$2.8 kΩ at 4 K, and climb up to $\sim$20 kΩ at 40 mK. In the CF sensor, R increases much stronger, changes from $\sim$1 kΩ at RT to $\sim$1.3 kΩ at 4 K, $\sim$58 kΩ at 40 mK, and more than $\sim$390 kΩ at the dil fridge base T of 11 mK. The inset of Figure 5.7 **(a)** compares the typical $R(T)$ curves of the three thermometers. The difference in the $R(T)$ curves of CF, RuO$_2$#1 and RuO$_2$#2 thermometers, has two main reasons: (i) Different batches and dimensions of the RuO$_2$ thick-film resistors, observable as the difference in the R values at RT. (ii) Different coupling levels between the sensors and the bath owning to the mounting method, responsible for the huge difference at low T as well. As explained earlier in paragraph § **Sample holder**, the thermometers used to measure T_C and T_H, i.e., RuO$_2$#1 & #2, are sitting on the gold islands connected via gold wires to the sample providing less thermal anchoring than in case of the CF RuO$_2$ fixed directly on the sample holder. Assuming the coupling between the thermometers and the sample remaining unchanged during the measurements, the resistance of each thermometer sensor is a measure for the sample T at the connecting point. Even though, the sensor itself is not necessarily at the same T with the sample since it is not perfectly coupled, e.g., mechanically clamped. This effect highlights at lower T by leading to a saturation of $R(T)$ curves. I emphasise that the saturation of $R(T \rightarrow 0)$ is expected for all the RuO$_2$ sensors through
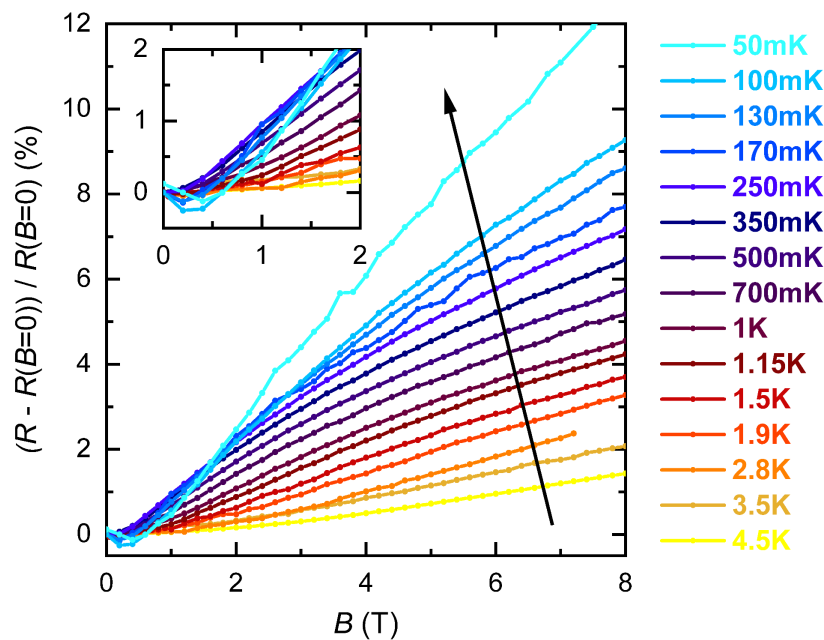
Figure 5.8: Magnetoresistance of the CF RuO_2 sensor at different T of the thermometer at the MC playing the role of the zero-B reference. The inset magnifies the graph below $2\,T$. Note the local minima in B below $\sim0.5\,T$ on the curves with $T < 350\,mK$.

impurities in the resistive-layer composite, the self-heating during the measurements, and thermalisation issues by thermal boundary resistances due to mismatch of atomic vibrating modes and disruption in phonon transfer across the interface (*Kapitza* resistance) plus the finite thickness of the chip; so, it occurs at different T depending on the sensor itself.

A proper tool to examine the applicability of a thermometer in a desired T range is to check the so-called *dimensionless sensitivity* $-(dR/R)/(dT/T)$ of the sensor, which corresponds to the absolute value of the derivative of the curve $\log R$ versus $\log T$. Dimensionless sensitivity curves against T_{CF} of the three used RuO_2 thermometers are shown in Figure 5.7 **(b)**. The dimensionless sensitivities of all three sensors are ~0.25 at $4\,K$. Once reducing T, the sensitivity curve of the CF RuO_2 continuously increases up to ~1.9 at around $28\,mK$ and turns downward to reach ~1.2 by cooling further down to $14\,mK$. In principle, the turn corresponds to an inflexion point in $\log R$ versus $\log T$, where this curve changes concavity toward saturation (as-expected in every chip) and loses serviceability. In $RuO_2\#1$ and $RuO_2\#2$ sensors, cooling raises their sensitivity to the highest points of ~0.53 within the 210 - $75\,mK$ range and lowers them below this T. Dimensionless sensitivities larger than about 0.1 are sufficient for high-resolution measurements [191]. This value is indicated with a dash-dot line in Figure 5.7 **(b)**. Unlike the CF RuO_2, the sensitivity curves of $RuO_2\#1$ & $RuO_2\#2$ sensors cross the dash-dot line at $\sim25\,mK$ revealing these two sensors are practically unreliable and unsuitable below $30\,mK$. This was predictable already from the flattening of the $R(T)$ curves at low enough T in Figure 5.7 **(a)**. Besides the usable range, the sensitivity curve provides information about possible problems with the calibration of a given measuring run appearing as, e.g., kinks or jumps, but usually not perceptible directly in the calibration curves. Such jumps correspond to tiny kinks or offsets in the calibration curves and may give rise to large but fake anomalies in the calculated κ.

Another remarkable issue is the reproducibility of the chip resistance upon thermal cycling. There is evidenced for relative shifts between the measured and nominal resistances $\Delta R = R_{\mathrm{meas}} - R_0$, as small as $\Delta R/R \leq 10^{-3}$ in subsequent measurements [190]. Such small but detectable changes were observed in this work, most probably triggered by mechanical stress at the contacts or vibrations. To minimise this source of error, I performed *in-situ calibrations* for each run of the measurements, i.e., RuO$_2$#1 & RuO$_2$#2 thermometers were carefully calibrated against the reference at the CF. More details are in Section 5.6.1.

Effects of the LS current excitation are another key factor. Self-heating due to large excitation currents can lead to inaccurate R measurements of the components; essentially, the high resistance of the chips is disadvantageous. Therefore, the input currents must be carefully selected to obtain reliable results.

In this research, I ran measurements in B as well. Figure 5.8 shows the magnetoresistance $(R - R(B=0))/R(B=0)$ of the CF RuO$_2$ thermometer in B up to 8 T at different T. For these measurements, the thermometer at the MC placed within the compensated zone with $B \leq 5\,\mathrm{mT}$ was employed as the calibration reference. Even though no simple behaviour can be identified, some important features can be observed. In principle, the lower T, the larger the influence of B. At $T > 350\,\mathrm{mK}$, the relative shift of R monotonically increases by increasing B and decreases in T. Meanwhile, for $T < 350\,\mathrm{mK}$ curves, a local minimum in the region below $\sim$0.5 T is observed (see the inset magnifying the graph below 2 T). It is noteworthy that the magnetoresistance effects on such thick-film chips had been widely studied previously, e.g., [186, 188–190, 192]. Although the results do not agree in detail and seem to depend somewhat on the batch, the magnetoresistance is negative for B up to about 1 T, then goes through a broad minimum, and is positive at higher B in agreement with the behaviour of the used thermometers. Moreover, it was reported that decreasing T causes the magnetoresistance and the minimum to enlarge and get more pronounced, which agrees with the observed behaviour depicted in Figure 5.8. In the end, the corrections for the B calibrations were considered during the data analysis process (Section 5.6.2.).

Gradient heater: A chip resistor[16] with a nominal resistance of $R_{\mathrm{Heater}} \simeq 11\,\mathrm{k\Omega}$ was connected to a high-precision ($\pm 1\,\mathrm{nA}$ or better) current source[17] to provide the required heat excitation for a desired T gradient on the sample. The resultant voltage at the gradient heater, ΔU, was measured in a two-point mode via a nanovoltmeter[18] with a resolution of $0.1\,\%$ of output, providing accurate ultra-low voltage measurements. The introduced heating power can be determined as

$$P_{\mathrm{Heater}} = \Delta U \cdot I. \tag{5.4}$$

In this work, the current was adjusted between $\sim$0.025 - 270 μA corresponding to a heating power range of $\sim$7 pW to 0.8 mW. Accuracy of calculations supposing the so-called *Joule's heating law* with $P_{\mathrm{Heater}} = R_{\mathrm{Heater}} \cdot I^2$ is diminished due to the T dependence of the resistance though small in practice. Therefore, a separate voltage measurement is needed.

In κ measurements, the heater power must be generated by a direct current (DC). Alternating currents (AC) may induce noise in the thermometer lines and thus give rise to self-heating of the thermometers and additional noise of the T measurement. That is, therefore, important to eliminate non-zero frequency contributions from the gradient heater's current source. Besides to the current supply, a thick metallic crane standing by the cryostat acted as an antenna, which can introduce unwanted signals to the experimental setup.

---

[16]Model 0302 thin film on Si resistor. State of the art, Inc.

[17]Model 263, Keithly Instruments, Inc.

[18]Model 2182/E, Keithley Instruments, Inc.

To overcome this issue, I investigated the input current of the gradient heater via an oscilloscope and recorded the major peaks of the fast Fourier transform (FFT) of the detected signal to be approximately 19 kHz, 5 kHz, and 20 Hz. Accordingly, I prepared a passive *low-pass* filter composed of resistors and capacitors (RC) to pass the desired frequencies, i.e., well below 20 Hz and close to 0 Hz, forward to other stages while attenuating higher frequencies. A first-order RC low-pass filter circuit consists of a resistor in series and a capacitor in parallel with the load. Figure 5.9 illustrates the plan of the prepared filter box circuit, which consists of
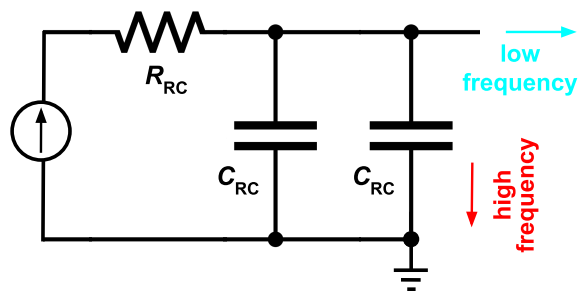

Figure 5.9: Plan of the prepared RC low-pass filter box composed of a resistor with $R_{RC} = 10 \text{k}\Omega$, and two parallel capacitors with a capacitance of $C_{RC} = 1.5 \, \mu\text{F}$ shunting $f > f_c \sim 5.3 \text{Hz}$ to the earth.

a resistor with $R_{RC} = 10 \text{k}\Omega$ and two parallel capacitors with $C_{RC} = 1.5 \, \mu\text{F}$ resulting in a cut-off frequency of $f_c = 1/(2\pi R_{RC} \cdot 2C_{RC}) \simeq 5.3 \text{Hz}$. When the power supply delivers the current to the circuit, a decoupling capacitor will create a low-impedance path functioning as a short for the high-frequency signals to get shunted. That allows the high frequencies to ground and the lower frequencies to pass into the following stage resulting in a clean DC signal. Note that higher orders of the filter help to reduce the transition bandwidth though the oscilloscope showed barely peaks using the first order. Lastly, I ensured the full gain of the signal for the full range of current values used during the experiments.

5.6.1 Measuring Procedure

After a successful sample installation, insert of the setup into the dilution fridge and cool down, an in-house-developed program in LabVIEW[19] was employed to control the system and run the measurements. The CF temperature was continuously monitored and controlled by the CF RuO_2 and the setup heater at the MC via the PID settings, as earlier mentioned. Steady-state routines were performed in all the measurements. In what follows, I will describe the measurement routines. *OFF* and *ON* labels are defined according to the status of the gradient heater, i.e., zero and non-zero current values, respectively.

Temperature-sweep routine: Figures 5.10 **(a)**-**(d)** exemplify time evolution of different properties in a typical *T*-sweep routine. During a steady-state measurement, *T* is changed in steps rather than a continuous manner (Figure 5.10 **(a)**). These steps are depicted by grey dashed lines. During any *T* sweep, the applied *B* was kept fixed (Figure 5.10 **(b)**). As it is observable in Figure 5.10 **(c)**, two different sub-set-points were aimed for a single T_{CF} set-point: (i) An OFF mode providing the data for the *in-situ* calibration, followed by (ii) an ON mode of the target *T* gradient. At each given T_{CF}, introducing heat by turning the gradient heater ON rises *T* at different points of the sample. This is observable as a resistance drop of the cold and hot RuO_2 thermometers, R_C and R_H, in Figure 5.10 **(d)**.

The selection of the *T*-gradient value induced by the current of the gradient heater is another vital aspect. The gradient should be high enough so the accuracy in measuring ΔT, and consequently, κ is not too low. The higher the *T* gradient, the lower the relative error in measuring thermal conductivity $\delta\kappa/\kappa$ (see Relation 5.1). Assuming fixed precision

---

[19]by Dr Thomas Lühmann
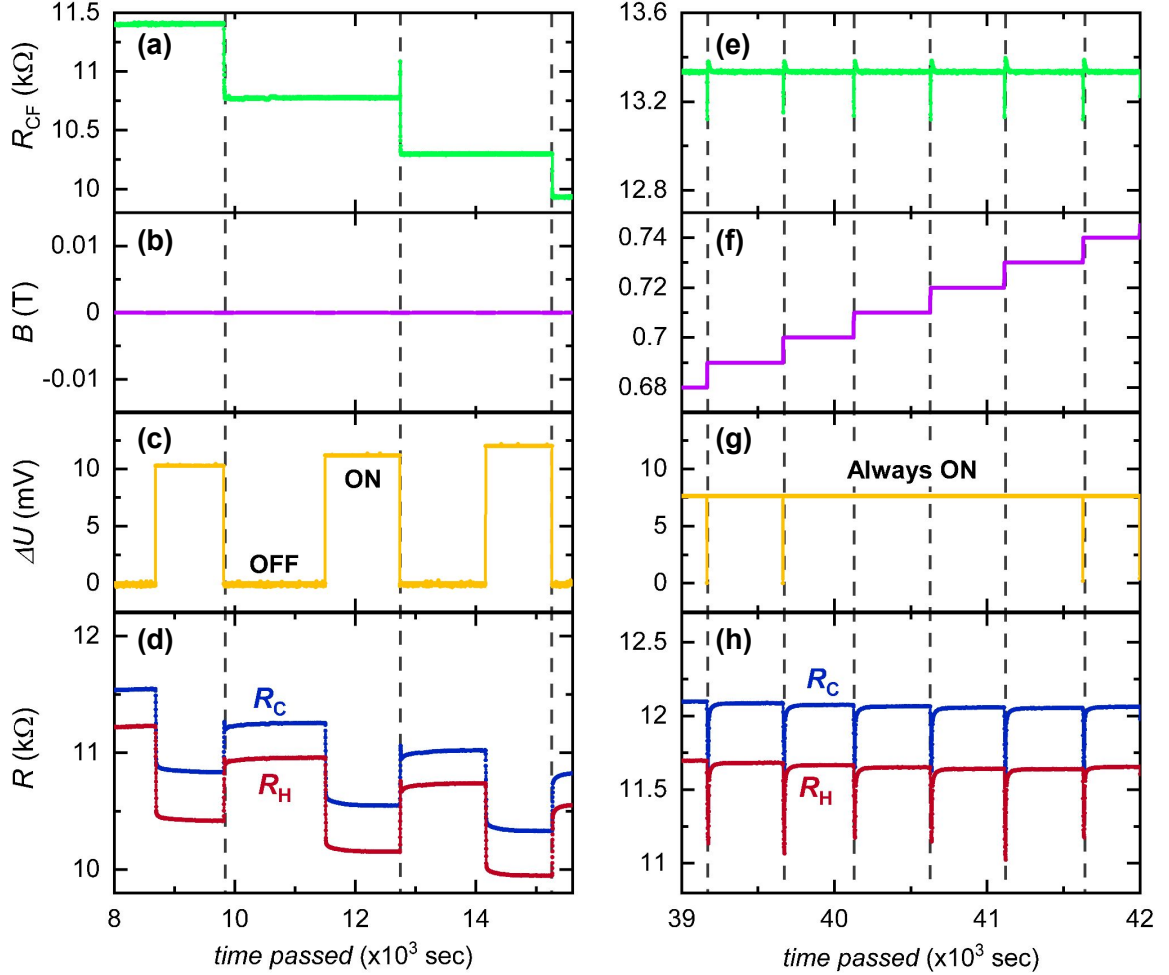
Figure 5.10: Time evolution of steady-state measuring routines. **(a)-(d)** A typical temperature sweep. **(a)** T was sampled in steps instead of a continuous change, and **(b)** B was fixed during the whole sweep (here, $B = 0$). **(c)** For a single set-point T_{CF} (the region between the grey dashed lines), the gradient heater was switched OFF and ON, providing the data for the *in-situ* calibration and the T gradient, respectively. **(d)** R_{C} and R_{H} being the resistances of the cold and hot RuO$_2$ thermometers, show a drop at switching the heater ON. **(e)-(h)** A typical field sweep. **(e)** T_{CF} was set fixed during the whole routine. **(f)** B was scanned by small steps in persistent mode. Sweeping B induces excessive heat and noise, which is perceptible on the other electrical components (follow the dashed lines). **(g)** The heater was kept ON at a fixed current, suiting the full B range. **(h)** Introducing a constant heat current through the specimen with B-dependent κ produces different T gradients in B. Once B is altered, R_{C} and R_{H} stabilise to their new values. More detail is in the text.

of measuring devices,

$$\frac{\delta\kappa}{\kappa} \propto \frac{\delta\Delta T}{\Delta T} = \frac{\delta T_{\mathrm{H}} + \delta T_{\mathrm{C}}}{T_{\mathrm{H}} - T_{\mathrm{C}}} \propto \frac{1}{T_{\mathrm{H}} - T_{\mathrm{C}}}. \tag{5.5}$$

While a large T gradient improves the precision of the measurement, too high current values are not favourable: We record an average κ over the T range between T_{H} and T_{C}, corresponding to the average T between the two pads. The higher the T gradient, the higher the difference between T_{H} and T_{C}. In a linear T-dependent κ, the average κ over any T range equals the real $\kappa(T_{\mathrm{avg}})$. However, this is not always the case. Increasing the T range along the sample elevates not only the error bar of the measured κ but also the risk of smearing the anomalies or features due to averaging over an extended T range. In this study, I aimed for a typical T gradient of $\sim 3\%$. However, I repeated several random runs with different currents to reproduce the same κ and ascertain a decent resolution.

I set a typical step of $4\,\mathrm{mK}$ for $T < 0.1\,\mathrm{K}$, $5\,\mathrm{mK}$ for 0.1 - $0.2\,\mathrm{K}$, $10\,\mathrm{mK}$ for 0.2 - $0.3\,\mathrm{K}$, $15\,\mathrm{mK}$ for 0.3 - $0.5\,\mathrm{K}$, $20\,\mathrm{mK}$ for 0.5 - $1\,\mathrm{K}$, $50\,\mathrm{mK}$ for 1 - $2\,\mathrm{K}$, $100\,\mathrm{mK}$ for 2 - $2.5\,\mathrm{K}$, $150\,\mathrm{mK}$ for 2.5 - $3\,\mathrm{K}$, and $200\,\mathrm{mK}$ for 3 - $4.2\,\mathrm{K}$. Lastly, barriers like LS's resistance ranges prevent running a full T scan between the lowest and highest possible T. Hence, several T scans were done for each B at very low (below $0.15\,\mathrm{K}$), low (below $0.4\,\mathrm{K}$), middle (0.28 - $1.2\,\mathrm{K}$), high (0.8 - $2\,\mathrm{K}$), or very high (1.8 - $4.2\,\mathrm{K}$) T. I incorporated a considerable overlap for neighbouring T ranges to obtain smooth κ curves and confirm the reproducibility of the data.

Field-sweep routine: Figures 5.10 **(e)**-**(h)** show a typical B-sweep routine. The base temperature T_{CF} was kept fixed, as shown in Figure 5.10 **(e)**. Special care has to be taken when measuring in B; the aimed range was scanned by small steps of $0.01\,\mathrm{T}$ or $0.02\,\mathrm{T}$, as depicted in Figure 5.10 **(f)**. Sweeping B discretely helps to prevent introducing an excessive heating continuously. In addition, κ measurements were taken always in persistent mode to avoid extra noise. The gradient heater was kept always ON (Figure 5.10 **(g)**) with a fixed current equal to the average current needed for a 3% T gradient over the spanned B. Introducing a fixed heat current flowing through the sample will provide different T gradients if κ changes in B. In addition, it was also ensured that the minimum gradient is not below $\sim 1\%$. Changing B heats the electrical components up, which is observable in Figure 5.10 **(h)** as drastic reduction in the resistance of the cold and hot $\mathrm{RuO_2}$ thermometers.

Which points were recorded? Time-dependent T data for T_{CF}, T_{C} and T_{H}, including ΔU at the gradient heater, were recorded during every single run with an acquisition rate of $0.2\,\mathrm{s}$. I considered a typical delay of 6 - $10\,\mathrm{min}$ after changing the set T_{CF} and 4 - $6\,\mathrm{min}$ after switching the gradient heater ON/OFF before checking for any stabilities. Standard deviations of the measured T and voltage points, including slopes over a user-defined time interval, typically $5\,\mathrm{min}$, were continually determined. Accordingly, a parameter called *drift*, as

$$\mathrm{drift} = \left(\tanh\left(\left(\frac{\mathrm{slope}}{\mathrm{noisewidth}} \right) \times \mathrm{arctanh}\left(\mathrm{sensitivity} \right) \right) \right) \times 100\% \tag{5.6}$$

was computed constantly. The locally-defined *sensitivity* value indicates the desired drift value when the slope equals the noise level within the aimed window and was fixed at 40. The drift parameter gives a sense of the stability over the given window and was monitored during each run for the measured T_{CF}, T_{C} & T_{H}, and ΔU to impose stability criteria. I recorded a data point only and only if the drift of all four specified quantities had remained for $30\,\mathrm{s}$ below their threshold values. The threshold values were set typically below 10% for all the thermometers, and below 20% for the ΔU of the gradient heater.

The recorded data points are averaged over the last 5 min of the time window as highlighted via black points in Figure 5.11. For some arbitrary runs of the measurements, I set OFF-ON-OFF three-step set-points to check the reproducibility of calibration data, namely the OFF-mode data points. An instance is shown in Figure 5.11. Two light-grey dashed lines are drawn for visual help to compare the first and second OFF sub-set-points of the cold and hot sensors. Once the drifts are adjusted properly and thermometers are well stabilised with a large enough waiting time, both the first and second OFF modes stabilise to the same value. Thus, the shorter two-step OFF-ON routine was preferred.
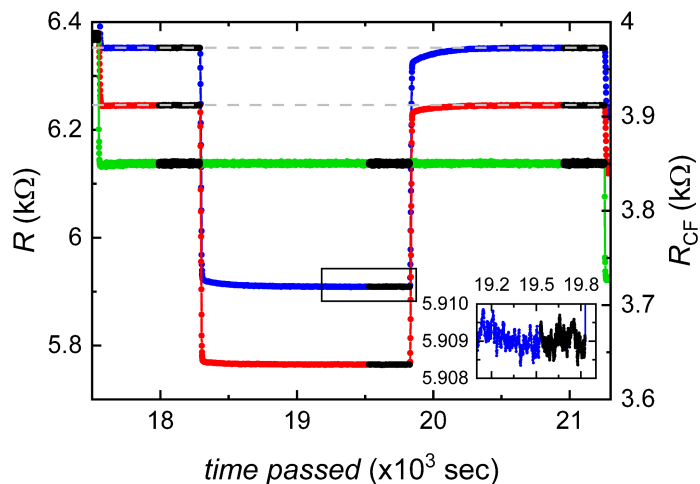

Figure 5.11: Example of a data point measured by the OFF-ON-OFF routine. Black points indicate the range used for averaging once all thermometers are stable. The inset zooms one of the curves in as an instance, so the fluctuations of the curve are visible. The grey lines show that the sample returns to the initial OFF state after heating.

5.6.2 Data Analysis

I coded my numerical calculations of calibrations and κ computation scripts in Python. My first step in processing the obtained data was calculating the correct temperatures, T_H and T_C. Therefore, I digress to describe the calibration procedure of the cold and hot RuO_2 thermometers before moving to the κ computation.

For non-zero B measurements, I eliminated the effects of the magnetoresistance on the determined T at the CF. To this end, CF RuO_2 was initially calibrated against the thermometer at the MC that serves as the zero-B reference (Figure 5.8). Once T_CF is calibrated and reliable, calibration process on $RuO_2\#1$ and $RuO_2\#2$ thermometers can be performed.

Calibration procedure: As explained earlier, I opted for the *in-situ* calibrations to get exact values for T_C and T_H. This implies that the OFF data points of the cold and hot thermometers of the same run were used as the source to read the ON data points. Making a good calibration requires a good fitting and a fair knowledge of the calibration curve behaviour. The *R-T* relation of the thick-film chip resistors based on RuO_2 fits the empirical equation of $\ln(R) = \sum_{n=0}^{2} A_n (\ln T)^n$ well [189]. The expression $R = R_0 \exp(T/T_0)^{-\alpha}$ is also reported to fit the data well in a limited T range with α, R_0 and T_0 depending on composition and the T range [184, 187, 189, 190, 193, 194]. Hence, I performed a *linear log-log interpolation* of

$$\log T_\mathrm{int} \;=\; \mathrm{interpolation}(\log R,\ \log T,\ \log R_\mathrm{int}), \tag{5.7}$$

with $\log R$ and $\log R_\mathrm{int}$ as the independent and dependent variables recorded during the OFF and ON mode, respectively. In case the calibration has some irregularity or kinks, the effects will remain just for T within the nearest neighbourhood of the kink. A smooth behaviour of both R_C and R_H versus T_CF curves was ensured for every single run. Moreover, I checked

Property	length	I	ΔV	T_{CF}	R
Measuring resolution	$10^{-6}\,\mathrm{m}$	$10^{-9}\,\mathrm{A}$	$10^{-9}\,\mathrm{V}$	$10^{-6}\,\mathrm{K}$	$10^{-6}\,\Omega$

Table 5.1: Resolution of measuring systems used for different properties.

for anomalies in $dR = R_{\mathrm{H}} - R_{\mathrm{C}}$ versus T_{CF} since we are interested in the T gradient of the specimen. This curve may magnify an anomaly which is not visible in the individual $R(T)$ curves. I considered the κ calculation of a single point valid only if all these three curves behaved smoothly, and I omitted any individual data point without reliable T_{C} and T_{H} interpolations. For sufficiently dense data points, this interpolation is accurate enough. Furthermore, I always cut off the ON sub-points close to the upper boundary of the T-sweep scans requiring an extrapolation, i.e., $R < R_{\mathrm{min}}^{\mathrm{OFF}}$.

Using a *Chebyshev fitting* of $T(R)$ on a log-log scale is also convenient. In this case, a fit of nth-order Chebyshev-polynomial functions is used. For $x \in [-1, +1]$, the nth Chebyshev polynomial is defined by the formula $T_{\mathrm{n}}(x) = \cos(\mathrm{n} \cdot \arccos(x))$. In fact, the Chebyshev-polynomial basis often provides a better representation for the polynomials than a power-series basis. In oxide-compound thermometry, the Chebyshev fitting should result in higher errors compared to the linear interpolation of $\log T$ versus $\log R$, which is not proper for the thermal transport where $\Delta T \ll T$. I tried the Chebyshev-polynomial fitting for arbitrary runs and found the linear log-log interpolation superior: Firstly, the best order for fitting remains always a question. A low polynomial order n will produce a line passing between the calibration-source points with high residual values; yet, one can reduce the residual values close to zero if accepting the induced up and downs of a high-order polynomial. Second, the Chebyshev polynomials leave artificial sinus-type wiggles on the two ends of the fitting. Third, if the calibration has some irregularities, they will affect the whole T range.

κ calculation & error estimation: I deduced the thermal conductivity κ by Relation 5.1 for each step using the input power from Relation 5.4 and the geometrical factor $g = l/A_{\mathrm{s}}$. The standard deviation of the signals revealed measuring errors of less than $1\,\%$ owing to the highly-precise measurements. The finite width of the contacts and the inability to determine the effective distance between the T_{C} and T_{H} pads (l_{eff}) affect the accuracy of the calculated κ as systematic errors. In this research, I considered the average distance between the T_{C} and T_{H} pads l_{av} for the calculations (see Table 6.1 and Table 6.3 for the numerical value of each sample). Accordingly, it is possible that the calculated results of one sample need to be multiplied by a fixed factor. This factor ranges in $1 \pm \delta l / l_{\mathrm{av}}$ with the average width of the contacts $\delta l \simeq 0.2\,\mathrm{mm}$ in this work. Note that for a fixed T_{CF}, the cold and hot thermometers record an increase in T for each step. Thus, I consider a mean temperature of $T_{\mathrm{mid}} = (T_{\mathrm{C}} + T_{\mathrm{H}})/2$ rather than T_{CF} defining the sample T. I have omitted the calculated data with the gradients out of the 1 - 3.5 % range. If many points were cut-off, I repeated the measurement with recalculated current values that would produce a T gradient of 3 %.

Considerations on field sweeps: B sweeps were performed mainly to detect phase transitions and anomalies in κ. Since *in-situ* calibration in not possible in a B-sweep routine, one may employ a T-sweep calibration data file. Figures 5.12 compares the results of $\kappa(B)$ using two different zero-B calibration data sets labelled *Cal. I* and *Cal. II*. As is evident, the calculated value of κ depends on the employed calibration data points. Two leading problems in such circumstance are: (i) choice of calibration files and (ii) that B varies during the sweep. Foremost, although the choice of the calibration has significant influence
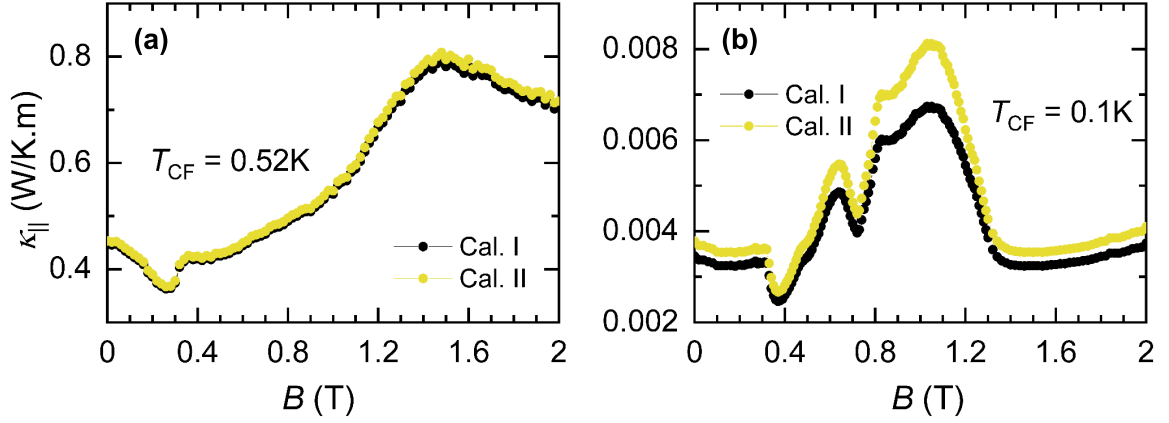
Figure 5.12: Effects of exemplary calibration data sets on calculated values of κ in B sweeps.

on the absolute calculated value of κ, the overall trend and features appearing in the curves are similar. As mentioned, the B sweeps are aimed for studying anomalies and features of $\kappa(B)$ curves thanks to the higher density of data points while absolute values of κ can be determined from T sweeps. Secondly, concerning the use of a zero-B calibration data set also in B, one may note that: (i) The B dependence of the calibration is expected to be smooth. (ii) Deviations from the real value of κ stay below 3% for $B < 2\,T$ (see Figure 5.8 for the magnetoresistance of the CF RuO$_2$ at different T). Hence, ignoring this B dependence and using a zero-B calibration can neither produce nor extinct anomalies in $\kappa(B)$.

To have a reliable value of κ from the B sweeps, a correction of the calculated $\kappa(B)$ is required. Figure 5.13 exemplifies correction procedures of B-sweep curves with $\kappa_\parallel(B)$ at $T_{CF} = 0.52\,K$ calibrated with a zero-field T-sweep calibration file. An index of $\parallel$ is used to indicate the direction of the heat current along the spin chains. Figure 5.13 **(a)** displays the T_{mid} behaviour of the sample in B. The above-mentioned T_{CF} with fixed electrical current of the heater provided an average T_{mid} of $612\,mK \pm 1\%$, indicated by a dashed line. Figure 5.13 **(b)** depicts the $\kappa_\parallel(T)$ curves within the aimed T range. Initially, a smooth behaviour of every single $\kappa(T)$ curve was checked; in case of any small wiggles, the $\kappa(T)$ curve was ignored in next steps. The value of $\kappa_\parallel$ at $T_{avg} = 612\,mK$ (dashed line) is read for different B from the $\kappa_\parallel(T)$ curves. The interpolation of $\kappa_\parallel(T)$ for the given T_{avg} are shown in Figure 5.13 **(c)** by cyan circles. The dark red curve is $\kappa_\parallel(B)$ carrying *uncorrected* κ absolute values. I mapped the uncorrected curve using a linear interpolation of the distance to the cyan points, which are actually the reference points. That renders the empty circles indicating *corrected* $\kappa_\parallel(B)$ at the given average T. The interpolated points from the T sweeps are combined to the corrected B-sweep curves for the final curves. The same correction procedure was performed for every B sweep. The initial and corrected $\kappa(B)$ curves for heat current along and perpendicular to the spin chains, i.e., $\kappa_\parallel(B)$ and $\kappa_\perp(B)$, are illustrated in Chapter 6, Figure 6.19 and Figure 6.20, respectively. Note, $T_{mid}(B)$ has a non-trivial relation to $\kappa(B)$. The difference between the initial and corrected curves varies by calibration files, but has also a $\kappa(B)$ functionality; the higher κ, the greater the deviation.

Although the overall behaviour of the initial and corrected curves are similar, some features can get more pronounced after correction compared to the directly measured initial curves (see Figure 5.13 **(c)** around 1.2 - 1.6 T). For this reason, it is preferred to use the original initial curves once investigating the anomalies. From the other side, the κ absolute
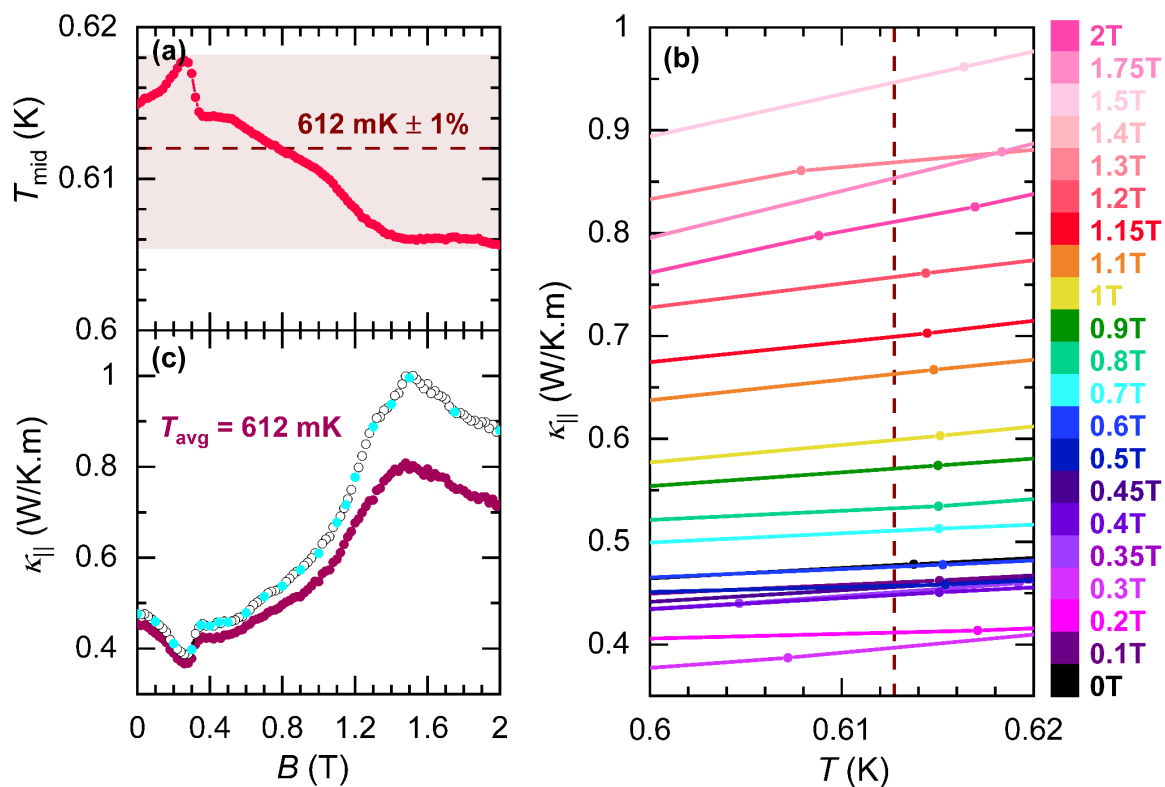
Figure 5.13: An example of the correction procedures of the B-sweep curves. **(a)** T_{mid} versus B deviates less than $\pm 1\%$ around the average value indicated by a dashed line. **(b)** $\kappa_{\parallel}(T_{av} = 612\,mK)$ for different B is read from the T sweeps. **(c)** Measured and corrected $\kappa_{\parallel}(B)$ curves. The dark red circles are obtained from a B-sweep run calibrated with calibration data points of a zero-B T sweep. The cyan circles are interpolated from the $\kappa_{\parallel}(T)$ curves. The empty circles indicate corrected $\kappa_{\parallel}(B)$ of given average T. More explanation is in the text.

value before and after the correction can differ significantly, in some cases by more than 200 %. Thus, it is crucial to correct the curve in studying the absolute value of $\kappa(B)$.

5.7   Summary

Thermal conductivity measurements, particularly in the milli-Kelvin T range, are among the most challenging experiments in solid-state physics due to the high delicacy of the preparation and measuring techniques. In this research, I measured κ using a conventional two-thermometer-one-heater technique from RT down to 30 mK. The investigated single crystals were precisely oriented and cut to samples with an adequate aspect ratio. Great care was bestowed on contact preparation: I deposited gold micro contacts directly on the samples to ensure good thermal coupling to the thermometers and the bath. Before running measurements, noise suppression of the setup was improved. Special attention was also paid to thermal stability and the calibrations of the thermometers, especially in dilution fridge measurements: I carried out *in-situ* calibrations during each T sweep to reduce uncertainties of the T gradient measurement. In the case of B-sweep measurements, a sophisticated data analysis and correction procedure ensures the reliability of the presented data.

6 Thermal conductivity of the quasi-one-dimensional quantum magnet YbAlO₃

6.1 Introduction

In this chapter, I will present the results of milli-Kelvin and high-temperature (T) thermal conductivity (κ) measurements with heat current along the spin chains ($\boldsymbol{j}_Q \parallel c$) and perpendicularly ($\boldsymbol{j}_Q \parallel b$) that I did on the quasi-one-dimensional (Q-1-D) quantum magnet YbAlO₃ (see Chapter 3 for an extended description of the compound YbAlO₃). Figure 6.1 depicts schematically the directions of the spin chains in YbAlO₃, $\boldsymbol{j}_Q$ and magnetic field (B) during the measurements. $\kappa_\parallel$ and $\kappa_\perp$ (κ_c and κ_b) denote κ along and perpendicular to the spin chains at low T. The field B is applied along the a-axis.

Figure 6.1: Thermal transport is studied along and perpendicular to the spin chains, i.e., $\boldsymbol{j}_Q \parallel c$ and $\parallel b$, respectively. $B \parallel a$ for all the in-field measurements. Figure reproduced from [74].

I start the chapter with a motivation to study heat transport in such compounds. Next, I show the κ results for the non-magnetic reference material YAlO₃ along the same axes, c and b, as studied in the main target compound YbAlO₃ at high T, including fits to the Callaway model. The rest of the chapter is dedicated to the results of YbAlO₃ presented in two parts: (i) measurements in the fully-polarised (FP) state and zero B to understand the phononic thermal conductivity (κ_{ph}) and (ii) B-dependent κ data with discussion of the magnetic heat conductivity (κ_{mag}).

The main findings are the following. A huge enhancement of κ in the mid-B regime is observed in both T and B sweeps, likely due to an extra magnetic contribution. At the known phase transitions, anomalies are visible in $\kappa(T)$ and $\kappa(B)$. New features in $\kappa(B)$ with no comparable counterparts in the up-to-date magnetisation (M) or specific heat (C) data suggest the existence of another transition in the mid-B regime. Lastly, the phase diagram is established using the thermal conductivity results, confirming a good agreement between transport and thermodynamic probes and a new transition inside the incommensurate (IC) anti-ferromagnetic (AFM) phase.

6.2 Motivation

Orthorhombic perovskite materials, with the general chemical formula of $Re^{3+}M^{3+}O_3{}^{2-}$, Re being a trivalent rare-earth (RE) ion, are in a focus of attention in modern solid state physics and materials science as they exhibit interesting magnetic [74, 195–197], multiferroic [198] and optical [199] effects. Among these compounds, YbAlO₃ is an interesting case due

Sample	Compound	$l_a \times l_b \times l_c$ (mm³)	$\boldsymbol{j}_\mathrm{Q}$ direction	l_av (mm)
YAlO₃#b	YAlO₃	$0.5 \times 5 \times 0.5$	b	2.7
YAlO₃#c	YAlO₃	$0.5 \times 0.5 \times 5$	c	2.7

Table 6.1: Dimensions and contact geometries of the measured YAlO₃ samples. l_a, l_b and l_c are the sample lengths along the a-, b- and c-axis, respectively. l_av is the average distance between the T_C and T_H pads.

to the fascinating properties arising at low T. Magnetic properties and anti-ferromagnetic (AFM) ordering of this electrically-insulating compound were investigated in 1970-80s [75, 76], and the optical properties were studied in 2010-11 [172, 200]. Despite our long-term familiarity with this material, it was discovered only in 2019 that YbAlO₃ shows a Q-1-D behaviour at low T, well described by spin-1/2 Heisenberg chains and Tomonaga-Luttinger liquid (TLL) physics in a large T-B regime. Below $1\,\mathrm{K}$, Ising anisotropic inter-chain coupling becomes relevant leading to long-range AFM order at $0.88\,\mathrm{K}$. Besides, a rich phase diagram is observed in field. This compound is predicted to host various types of magnetic heat carriers, e.g., spinons, gapped magnons, and psinons [59, 66, 71, 74, 79, 201].

Thermal transport provides important information about the mobility and the elastic and inelastic scattering of excitations in solids. Thermal conductivity and inelastic neutron scattering (INS) are two probes for studying delocalised magnetic carriers [202]. The initial objective of this work was to study the behaviour of magnetic excitations as heat carriers within the different phases in particular spinons in the TLL state. In a recent publication, neutron scattering measurements suggest multiple fermion scattering in the IC-AFM region, providing (i) a small gap in the spin excitation spectrum and (ii) a new channel of scattering [79]. Thermal conductivity is an appropriate tool to explore such a mechanism. However, during the work, more interesting features popped up. The thermal conductivity data showed several unexpected new features, which widened the research focus of this work, especially to new anomalies appearing within the IC-AFM state (see Section 6.7).

6.3 Heat transport in the non-magnetic reference material YAlO₃

The high-T κ of YAlO₃ (or YALO for short), the non-magnetic iso-structural sister compound of YbAlO₃, was measured from room temperature (RT) down to $2\,\mathrm{K}$ in a PPMS device as described in Chapter 5 Section 5.5. Dimensions of the samples can be found in Table 6.1. The κ results for $\boldsymbol{j}_\mathrm{Q} \parallel c$ (κ_c) and $\boldsymbol{j}_\mathrm{Q} \parallel b$ (κ_b) analogous to the directions studied in YbAlO₃ as a function of T are plotted in Figure 6.2 **(a)-(b)** marked in blue and black. The crossed diamonds represent the results from the work of Aggarwal *et al.* [88]. Note that the orientation convention in [88] is different from this work. Though T dependencies are very similar to the results of this work, the absolute values of κ are up to $20\,\%$ different, and in particular, $\kappa_c > \kappa_b$ in our case but $\kappa_c < \kappa_b$ in the work of Aggarwal. These deviations may have various origins, such as differences in sample quality, uncertainties in determining contact geometry and general measurement uncertainties. Concerning the last point, the κ data by Aggarwal were obtained from diffusivity and specific heat measurements, both having an accuracy of $\pm 7\,\%$ [88]. On the other hand, contact widths and geometry of small samples easily lessen
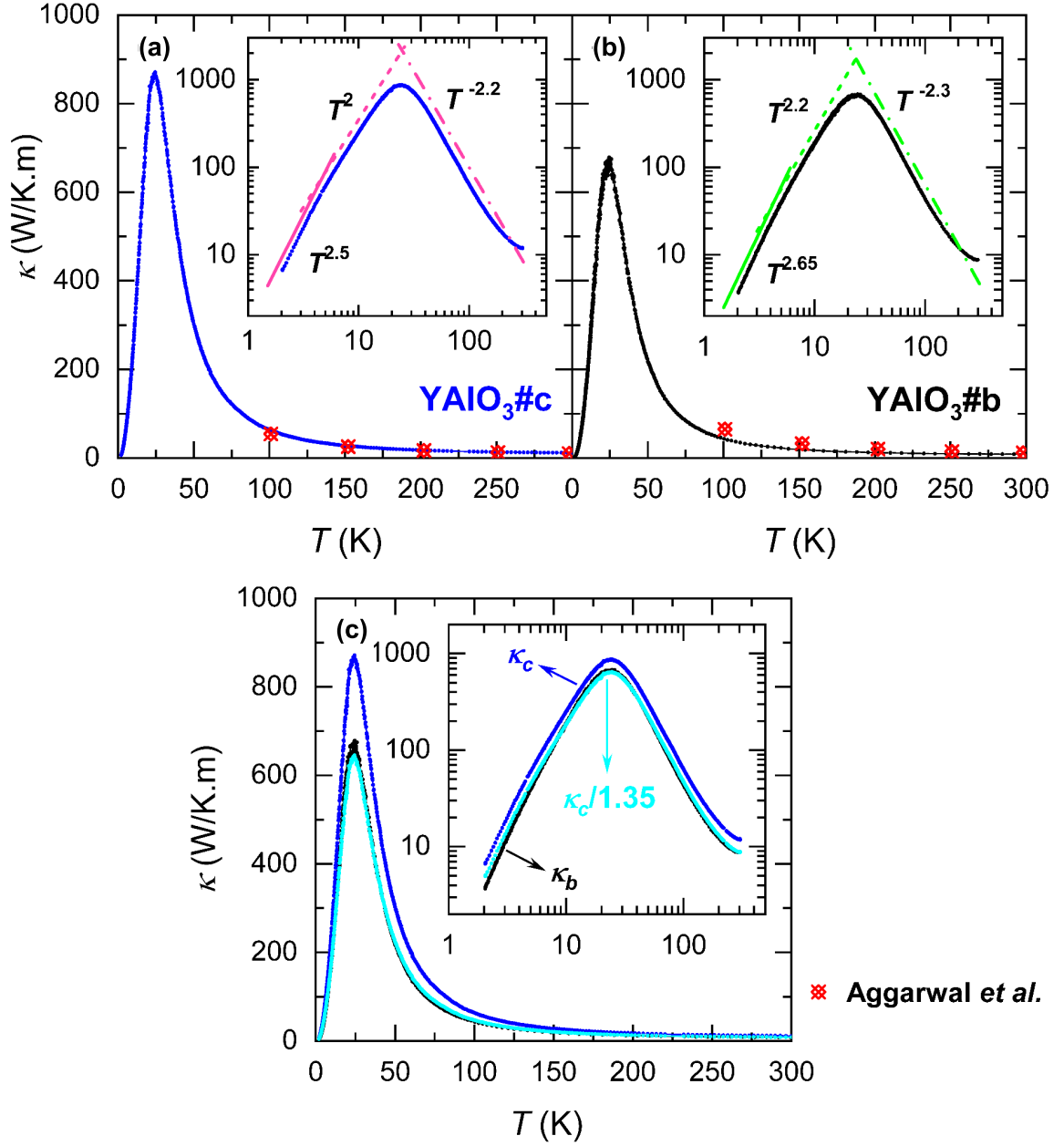
Figure 6.2: Thermal conductivity versus temperature down to 2 K of YAlO₃. κ along **(a)** the *c*-axis (κ_c) and **(b)** the *b*-axis (κ_b) is shown in blue and black, respectively. Literature data from Aggarwal *et al.* [88] are added for comparison (crossed diamonds). The insets demonstrate the same data on a log-log scale with the dominant power laws in different T ranges. **(c)** κ_b and κ_c are illustrated on the same graph, along with the $\kappa_c/1.35$ curve in cyan. The inset shows the results on a log-log scale. κ_c can be scaled to κ_b curve for $T > 10$ K. Clear deviations are observed below 5 K.

the accuracy of the absolute κ values by $\delta l/l_{av} \simeq 0.2/2.7$, namely $\sim 8\%$ (see § κ **calculation & error estimation** in Chapter 5). In combination with the relevance of sample purity for transport measurements, these effects may account for the observed deviations in $\kappa(T)$. The insets of Figures 6.2 **(a)**-**(b)** demonstrate the data on a log-log scale, and the straight lines approximate dominant power laws in different T ranges. κ along both directions shows a peak at around 20 K. This type of T dependence is typical for clean, non-metallic single crystals. At low T, thermal transport is limited by boundaries and defects. The maximum arises due to the onset of the Umklapp (U) scattering of the phonons with large momentum. κ_c can be approximately scaled to κ_b by a factor of $1/1.35$. Figure 6.2 **(c)** illustrates the κ_c (blue) and κ_b (black) curves on the same graph. The cyan curve shows κ_c over 1.35, which seems to sit on the κ_b curve acceptably above 10 K (see the inset of Figure 6.2 **(c)**). For $T < 10$ K, however, deviations are observed as better seen on the logarithmic scale.

κ_c/κ_b is the anisotropy of κ, computed as a function of T and illustrated in Figure 6.3. The anisotropy varies within $\pm 10\%$ around the RT value of 1.35 above 5 K. As mentioned above, this is opposite to the anisotropy found by Aggarwal *et al.* of 0.82 ± 0.04. The ratio increases at lower T to about 1.8 at 2 K. Absolute values of κ and consequently κ_c/κ_b have some uncertainties due to the aforementioned limited accuracy of the contact-geometry determination. That may explain part of the measured anisotropy in κ, although not the T dependence. Above 5 K, one possible scenario to explain the observed transport anisotropy of $1.35 \pm 10\%$ is a direction-dependence of the sound velo-


Figure 6.3: κ_c/κ_b of YAlO₃ versus T ranging 2 - 300 K. A light yellow box is used to indicated the $\pm 10\%$ deviation around the initial value. This value is violated strongly particularly below 5 K.

city. Assuming an isotropic mean-free path (λ) in a simple model, the anisotropy of thermal conductivity would be $\kappa_c/\kappa_b = (c_v|\boldsymbol{v}_c|\lambda)/(c_v|\boldsymbol{v}_b|\lambda) = \overline{v}_c/\overline{v}_b$ (Relation 4.6). Notwithstanding that in the literature, Zhan *et al.* found the mean sound velocity of $5.29\,\mathrm{km\,s^{-1}}$ by a method of averaging on the longitudinal and shear velocities of poly-crystalline ceramics of YAlO₃ (see Table 3.1) [90], there is no report on the direction-dependent velocities of the sound in a single crystal of this compound, yet. Here, I use the stress tensor for an orthorhombic crystal structure to compute the sound velocity along different principal axes from the calculated elastic constants of YAlO₃ from *ab* initio method available in [90]. For each crystallographic direction of ijk (e.g. i-axis), one may define one longitudinal velocity v_l ($v_{l,i}$) and two transverse velocities of v_{t1} and v_{t2} ($v_{i,j}$ and $v_{i,k}$). Once the longitudinal and transverse velocities are calculated, the direction-dependent mean sound velocities can be found via $v^{-3} = (v_l^{-3} + v_{t1}^{-3} + v_{t2}^{-3})/3$. We have

$$\hat{v} = \begin{pmatrix} v_{l,x} & v_{x,y} & v_{x,z} \\ v_{y,x} & v_{l,y} & v_{y,z} \\ v_{z,x} & v_{z,y} & v_{l,z} \end{pmatrix} = \frac{1}{\sqrt{\rho}} \begin{pmatrix} \sqrt{c_{11}} & \sqrt{c_{66}} & \sqrt{c_{55}} \\ \sqrt{c_{66}} & \sqrt{c_{22}} & \sqrt{c_{44}} \\ \sqrt{c_{55}} & \sqrt{c_{44}} & \sqrt{c_{33}} \end{pmatrix}, \tag{6.1}$$

where ρ is the density, c_{11}, c_{22}, and c_{33} represent stiffness against uni-axial strains, and c_{44},

YAlO$_3$ sample	$N_{\max}$ (normal) (K^{-4})	A (point defects) (10^{-45} s^3)	D (dislocations) (10^{-6})	C (resonance) (10^{36} s^{-3})	ω_0 (10^{13} s^{-1})	B (Umklapp) (10^{-20} s/K^2)	b
#b	$\sim 10^{39}$	2.2 ± 0.1	5.1 ± 0.1	0.9 ± 0.1	6.0 ± 0.1	2.8 ± 0.1	8.4 ± 0.1
#c	$\sim 10^{38}$	≤ 1.5	≤ 0.2	6.0 ± 0.2	5.50 ± 0.05	1.8 ± 0.1	8.6 ± 0.1

Table 6.2: Best parameters found to model the T dependence of κ_{ph} in YAlO$_3$ samples with Relation 6.3. An example of resultant fitting curves for each of the measured thermal conductivity data is shown in Figure 6.4. More details can be found in the text.

c_{55}, and c_{66} correspond to shear deformations (see, e.g., [92] or [203][1]). Calculated numerical values are obtained from [90]: The elastic constants given in GPa are $c_{11} = 367$, $c_{22} = 396$, $c_{33} = 310$, $c_{44} = 110$, $c_{55} = 174$, $c_{66} = 152$, and density equals $\rho = 5.35\,\mathrm{g\,cm^{-3}}$. That gives

$$\hat{v} = \frac{10^2}{\sqrt{\rho}} \begin{pmatrix} 6.06 & 3.90 & 4.17 \\ 3.90 & 6.29 & 3.32 \\ 4.17 & 3.32 & 5.57 \end{pmatrix} = \begin{pmatrix} 8.28 & 5.33 & 5.70 \\ 5.33 & 8.60 & 4.53 \\ 5.70 & 4.53 & 7.61 \end{pmatrix}, \tag{6.2}$$

in km s^{-1}. Thus, $\overline{v}_a = 6.02$, $\overline{v}_b = 5.41$, and $\overline{v}_c = 5.46$ in km s^{-1}. First, the net $\overline{v}$ in YAlO$_3$, according to this calculation, equals $5.63\,\mathrm{km\,s^{-1}}$, $\sim 6\,\%$ different from the previously calculated report of $5.29\,\mathrm{km\,s^{-1}}$ by Zhan *et al.* [90]. $6\,\%$ shows a good agreement, taking possible approximations in first-principle calculations of the computed stress tensor into account.

Secondly, the computed direction-dependent mean sound velocities reveal a higher value along the a-axis compared to the other two. $\overline{v}_b \approx \overline{v}_c$ yields that the mean velocity of sound behaves almost isotropic between the b- and c-axis. In this circumstance, the ratio of the mean sound velocities $\overline{v}_c/\overline{v}_b = 1.01$ does not explain the observed transport anisotropy κ_c/κ_b in neither this work nor that of Aggarwal *et al.* [88]. Furthermore, adjusting the assumption of an isotropic mean-free path to an isotropic scattering rate (τ^{-1}) gives $\kappa_c/\kappa_b = (c_v v_c^2 \tau)/(c_v v_b^2 \tau) = (\overline{v}_c/\overline{v}_b)^2 = 1.02$, which still does not bring any improvement in predicting the observed behaviour of the transport anisotropy. Most likely, the applied simplifications of reducing the full phonon dispersion relation to three sound velocities and relating the thermal conductivity directly to them are too strong to analyse the transport properties.

The situation worsens at T below $5\,\mathrm{K}$, and the transport anisotropy considerably enlarges. Though the surfaces of the samples in this work were rough and not aimed to be polished, a possibility could be a surface-quality effect, e.g., see [97]. Specular phonon reflection can increase the effective λ in a well-polished specimen if boundary scattering is dominant at low T, surpassing that of a rough surface. Another possibility is an intrinsic change in the bulk scattering mechanisms. Since the YAlO$_3$ samples were from two purchased oriented bulks of crystal, different defect concentrations may exist. That is negligible at high T where scattering is mainly due to the U processes but can set the rule at low enough T, providing a possible scenario to explain the increasing anisotropy of κ at low T at any rate.

[1]The orientation convention in [203] is different from this work.
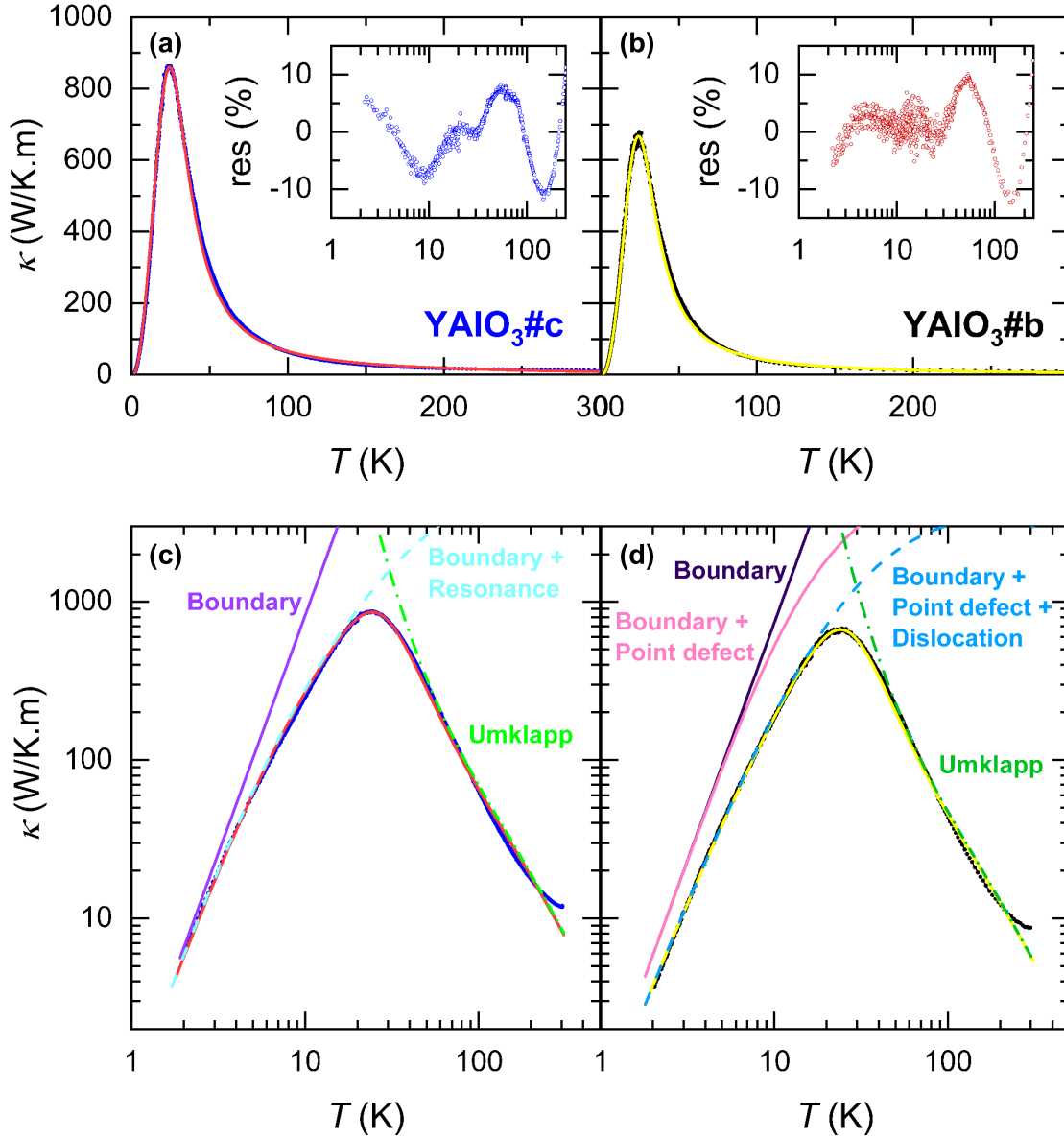
Figure 6.4: Modelling of thermal conductivity data of $YAlO_3$ in temperature. The red and yellow lines represent the calculated κ_{ph} for **(a)** $YAlO_3$#c with the parameters of $N = 1 \cdot 10^{36}\,\mathrm{K}^{-4}$, $A = 0.1 \cdot 10^{-45}\,\mathrm{s}^3$, $D = 0.2 \cdot 10^{-6}$, $C = 6.2 \cdot 10^{36}\,\mathrm{s}^{-3}$, $\omega_0 = 5.55 \cdot 10^{13}\,\mathrm{s}^{-1}$, $B = 1.9 \cdot 10^{-20}\,\mathrm{s/K}^2$, and $b = 8.7$, and for **(b)** $YAlO_3$#b with $N = 5 \cdot 10^{37}\,\mathrm{K}^{-4}$, $A = 2.3 \cdot 10^{-45}\,\mathrm{s}^3$, $D = 5 \cdot 10^{-6}$, $C = 0.8 \cdot 10^{36}\,\mathrm{s}^{-3}$, $\omega_0 = 6 \cdot 10^{13}\,\mathrm{s}^{-1}$, $B = 2.8 \cdot 10^{-20}\,\mathrm{s/K}^2$, $b = 8.4$. The insets show the residual values of the fits defined as res. $(\%) = [(\kappa_{\mathrm{meas.}} - \kappa_{\mathrm{fit}})/\kappa_{\mathrm{meas.}}] \times 100$. **(c)**-**(d)** The effects of the different scattering mechanisms used in the calculations of the model separately. More descriptions can be found in the text.

As the next step, the experimental data of $\kappa_b(T)$ and $\kappa_c(T)$ at all temperatures were fitted to the formula given by the Callaway model of thermal conductivity as described in Relation 4.18 and Relation 4.19. The average sound velocity of $\overline{v} = 5.29\,\mathrm{km\,s^{-1}}$ and Debye temperature of $\Theta_\mathrm{D} = 760\,\mathrm{K}$ were used (see Table 3.1). The phonon relaxation rates of the normal (N) and resistive processes were approximated respectively by $\tau_N^{-1}(\omega,T) = N\omega T^4$ and

$$\tau_q^{-1}(\omega,T) = \frac{\overline{v}}{l_\mathrm{C}} + A\omega^4 + D\omega + C\frac{\omega^2}{(\omega^2 - \omega_0^2)^2} + B\omega^2 T^2 \exp\left(-\frac{\Theta_\mathrm{D}}{bT}\right). \tag{6.3}$$

The terms in Relation 6.3 correspond to the phonon scattering at the sample boundaries, at the point defects, at dislocations, via nonmagnetic phonon-resonance scattering and due to phonon-phonon U-scattering processes, respectively. l_C describing the boundary scattering is the geometric mean of the dimensions of the sample cross-section. N, A, D, C, ω_0, B, and b are free parameters of the model. The best fitting parameters are presented in Table 6.2. Note that the parameters strongly correlate, and a slight change of one can alter the proper value of the others largely. An example of the fitting to the κ_c curve is plotted in Figure 6.4 **(a)**. The solid line represents the calculated κ_ph with the parameters of $N = 1\cdot10^{36}\,\mathrm{K^{-4}}$, $A = 0.1\cdot10^{-45}\,\mathrm{s^3}$, $D = 0.2\cdot10^{-6}$, $C = 6.2\cdot10^{36}\,\mathrm{s^{-3}}$, $\omega_0 = 5.55\cdot10^{13}\,\mathrm{s^{-1}}$, $B = 1.9\cdot10^{-20}\,\mathrm{s/K^2}$, and $b = 8.7$. The inset shows the residual value of the fit defined as res. $(\%) = [(\kappa_\mathrm{meas.} - \kappa_\mathrm{fit})/\kappa_\mathrm{meas.}] \times 100$. Following panel **(a)**, Figure 6.4 **(b)** illustrates the calculated κ_ph for κ_b with the parameters of $N = 5\cdot10^{37}\,\mathrm{K^{-4}}$, $A = 2.3\cdot10^{-45}\,\mathrm{s^3}$, $D = 5\cdot10^{-6}$, $C = 0.8\cdot10^{36}\,\mathrm{s^{-3}}$, $\omega_0 = 6\cdot10^{13}\,\mathrm{s^{-1}}$, $B = 2.8\cdot10^{-20}\,\mathrm{s/K^2}$, and $b = 8.4$. Concerning the residual values, both modelled curves fit better than 95 % in most of the T ranges and ~90 % at least. The main deviations are at very high and very low T. Given the simplicity of the model and the possible existence of other scattering processes, the overall agreement between fit and data is very well. The difference at high T may be, at least to some extent, explained by radiation losses from the heater and the sample to the environment. These are known to give rise to a systematic error with cubic-T dependence [106]. Although the PPMS measurement routine automatically corrects this effect, the adjustment is probably imperfect. To avoid this effect, one may use, e.g., the *laser-flash diffusivity* method described in [204].

Figures 6.4 **(c)**-**(d)** show the effects of the scattering processes used in the calculations separately. Starting from very low T, point defects appear to be more relevant in YAlO₃#b. This might be caused by a differing impurity concentration in the samples, for instance if the samples stem from different bulks. In addition, the scattering at dislocations is more or less negligible for YAlO₃#c. The dislocations act like a new effective boundary inside the sample and push κ to lower values than expected originally at low T, which is best seen in Figure 6.3 **(d)**. The phonon-resonance scattering, on the other hand, is more effective along the c-axis. This disparity of the coefficients is crucial to reproduce the different curvature of κ_c and κ_b curves observed below the phononic peak. Eventually, the contribution of the U-scattering processes to thermal resistive processes at higher T prevails dominant compared to the one of the boundaries, defects and resonance.

6.4 In pursuit of phononic thermal transport in YbAlO₃: high temperatures

To study the heat transport of the lattice of YbAlO₃, one may look at T regions well above the energy scale of magnetic interactions at fully polarised or ordered states close to 0 K.

Sample label	Compound	$l_a \times l_b \times l_c$ (mm³)	j_Q direction	l_{av} (mm)
YbAlO₃#b	YbAlO₃	$0.45 \times 2 \times 0.45$	b	1.2
YbAlO₃#c	YbAlO₃	$0.5 \times 0.5 \times 1.95$	c	1.15

Table 6.3: Dimensions and contact geometries of the measured YbAlO₃ samples. l_a, l_b, l_c are the sample lengths along the a-, b- and c-axis, respectively; l_{av} is the average length of the distance between the T_C and T_H pads.
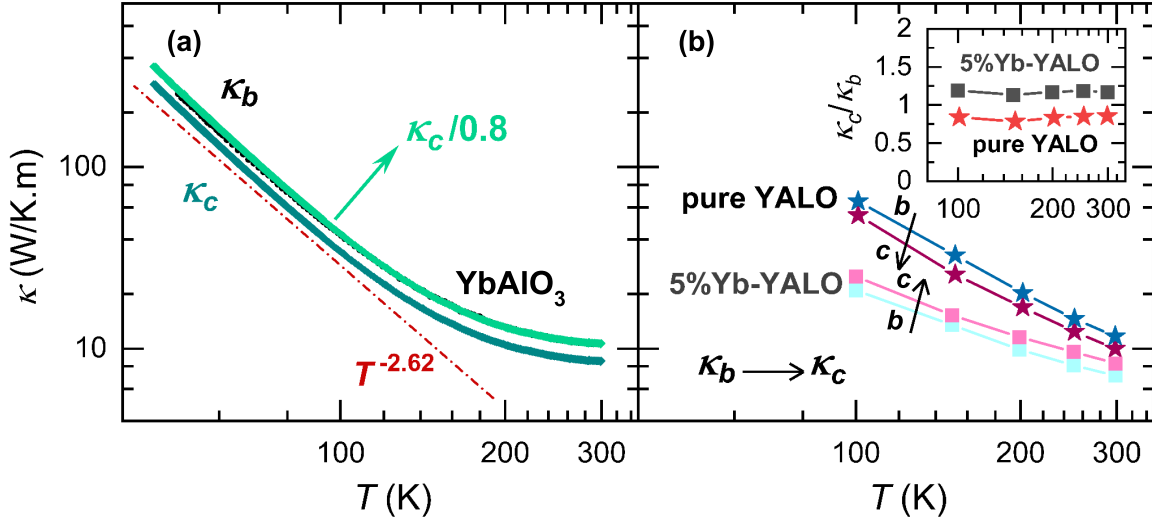

Figure 6.5: Zero-field κ of YbAlO₃ at the T range well above the magnetic-interaction energy scale. **(a)** Thermal conductivity of YbAlO₃ between 50 - 300 K measured along the b- and c-axis is depicted in black and dark teal, respectively. κ_c can be scaled to κ_b by a factor of 1/0.8. The red dotted-dashed line shows the power law between 50 - 100 K. **(b)** The report of Aggarwal *et al.* [88] on κ of pure YALO and 5 %-Yb-doped YALO (5 %Yb-YALO) is plotted with stars and squares, respectively. The inset presents the transport anisotropy (κ_c/κ_b) of the main graph, following the same marker code. More details are in the text.

The results of the low-T measurements are provided and discussed in Section 6.5. The high-T κ along the c- and b-axes (κ_c and κ_b) were measured in the PPMS T range. Whereas PPMS devices provide a base T of ~2 K, the data at $T < 50$ K are disregarded here. The enormous thermal conductance required way higher heating power than what the measuring set-up was designed for. On the one hand, a very high heating power was required to reach the desired T gradient of 1 - 3 %, particularly around the phononic peak. That broke the thermal decoupling of the gradient heater from the thermometers and involved unwanted heating of the sensors via, e.g., radiation or heat conducted along the fixing threads. Using lower heating powers, conversely, to avoid extensive heating of the environment provided infinitesimal T gradients, i.e., below 0.1 %, resulting in too large error bars below 50 K. Due to these limitations, no reliable data were obtained below ~50 K in the PPMS T range.

As explained in Chapter 5, § κ **calculation & error estimation**, the calculated κ contains an uncertainly of a factor between 0.83 - 1.17 ($1 \pm \delta l/l_{av} \simeq 1 \pm 0.2/1.2$), by the contact finite widths and geometry of the small samples. That may lower the accuracy by up to 16 %.

Figure 6.5 **(a)** shows zero-field κ_c and κ_b versus T from RT down to ~50 K on a log-log

scale. The plot also depicts κ_c over 0.8, matching the κ_b curve within a precision of $\pm 5\%$. Accordingly, the transport anisotropy of YbAlO₃, $\kappa_c/\kappa_b = 0.8$, is different from the reference material YAlO₃, where $\kappa_c/\kappa_b = 1.35$. Note, these values are obtained assuming the effective length l_{eff} between the hot and cold probes approximately equals l_{av}, i.e., the distance between the midpoints of the corresponding contacts. Considering the discussed effects of the geometrical factor on the accuracy of the measured κ, in particular 8% in YAlO₃ and 16% in YbAlO₃, $\kappa_c/\kappa_b \simeq 1.13$ in an unexpected condition that κ_b and κ_c in YbAlO₃ get the longest and shortest l_{eff}, and $\kappa_c/\kappa_b \simeq 1.16$ in YAlO₃ in a vice versa condition (l_{eff} in κ_b and κ_c adopt the closest and furthest points of the contacts). If this is the case, $\kappa_c/\kappa_b \sim 1.1$ in both compounds. The red dotted-dashed line shows the observed power law between 50 - 100 K. For the reference material, a weaker decrease of κ as warming up is observed close to RT, here above ~ 100 K (Section 6.3). Figure 6.5 **(b)** demonstrates the effects of Yb-doping of YAlO₃ on the lattice-transport anisotropy. The report of Aggarwal *et al.* [88] on κ of pure YAlO₃ and 5%-Yb-doped YAlO₃ (5%Yb-YALO) is plotted with stars and squares, respectively. The data reveal the effect of the Yb substitution with switching the order of κ values along the *b*- and *c*-axis at constant T. The inset presents $\kappa_c/\kappa_b = 0.85 - 0.92$ for pure YAlO₃ and 1.33 - 1.35 upon doping with 5% Yb. Accordingly, substituting Y ions with Yb influences κ even in the first few percentages: The lattice-transport anisotropy increases by about 62.5% upon doping YAlO₃ with only 5% Yb. Even considering the accuracy of $\pm 7\%$ of the Aggarwal *et al.* measurements, the observed transport anisotropy is not comparable to the measured values in this work, where YAlO₃ carries higher κ_c/κ_b values than pure YbAlO₃ (or 100% Yb-doped in other words).

Similar to YAlO₃, I compute the direction-dependent sound velocities for the three principal crystallographic axes. Xiang *et al.* [89] calculated the stress tensor of YbAlO₃, of which I take the numerical values of the elastic constants of $c_{11} = 352$, $c_{22} = 265$, $c_{33} = 330$, $c_{44} = 141$, $c_{55} = 122$, $c_{66} = 84$ in GPa, and the density of $\rho = 8.14\,\text{g cm}^{-3}$. That gives

$$\hat{v} = \begin{pmatrix} 6.58 & 3.21 & 3.87 \\ 3.21 & 5.71 & 4.16 \\ 3.87 & 4.16 & 6.37 \end{pmatrix}, \tag{6.4}$$

in km s^{-1}. Thus, $\overline{v}_a = 3.89$, $\overline{v}_b = 3.93$, $\overline{v}_c = 4.41$, and the overall mean sound velocity $\overline{v} = 4.08$, all in km s^{-1}. First, the calculated $\overline{v}$ has only a 4% deviation from the previous report of $3.91\,\text{km s}^{-1}$ calculated via the longitudinal and shear velocities [90], which proves a good agreement. Unpublished ultra-sound measurements by Galeski *et al.* for propagation along the *c*-axis revealed the transverse and longitudinal velocities $v_{c,a} = 3.7$, $v_{c,b} = 4.4$, $v_{l,c} = 5.6$ [205], and thus $\overline{v}_c = 4.32$, all in km s^{-1}. That proves $v_{a,c} < v_{b,c} < v_{l,c}$ in consonance with the given calculations with a 4 - 12% deviation in the absolute values. Also, $\overline{v}_c$ from the ultra-sound measurements by Galeski *et al.* agrees with the calculated value above within 2%. Second, the sound velocity along the *c*-axis is the highest, with $\overline{v}_c/\overline{v}_b = 1.12$. That predicts the transport anisotropy κ_c/κ_b for isotropic mean-free path and scattering rate, respectively, to be $(\overline{v}_c/\overline{v}_b) = 1.12$ and $(\overline{v}_c/\overline{v}_b)^2 = 1.26$. In this case, the isotropic scattering-rate assumption seems to agree better with the observed transport anisotropy. A more detailed discussion on the T-dependency of κ_c/κ_b is performed in Section 6.6.

Figure 6.6 **(a)** plots the measured κ of YbAlO₃ with the reference compound YAlO₃ from RT down to 50 K. κ along both directions starts at about $\sim 8 - 10\,\text{W K}^{-1}\text{m}^{-1}$ at RT and climbs to about $250 - 300\,\text{W K}^{-1}\text{m}^{-1}$ upon cooling down to 50 K. Investigating the absolute values of κ, YAlO₃ (black curve) shows almost identical κ values as YbAlO₃ (green curve)
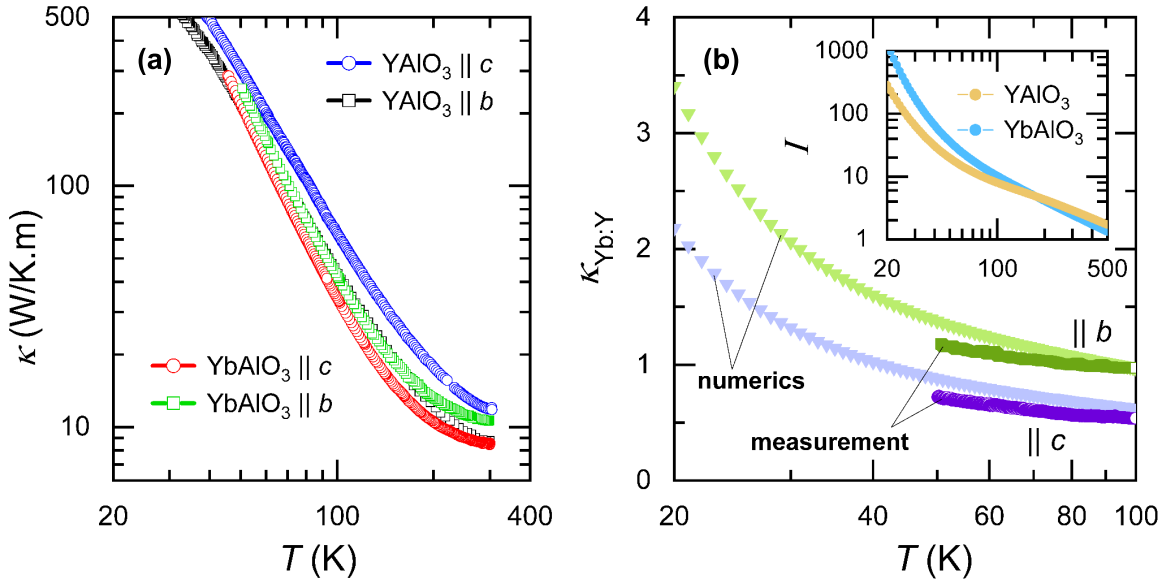
Figure 6.6: Modelling the relative behaviour of κ for YAlO$_3$ and YbAlO$_3$ materials at high T. **(a)** Thermal conductivity of YbAlO$_3$ in comparison with the reference compound YAlO$_3$ from RT down to 50 K. The squares represent the data along the b-axis and the circles along the c-axis. **(b)** $\kappa_{\text{Yb:Y}}$ obtained from the measurement compared with the numerical simulation using the Debye assumption for κ_{ph} and Slack *et al.* [206] model for U-scattering processes relaxation time are shown in violet and green, respectively, for κ along the b- and c-axis. Inset: Numerically-calculated $I\,(T, \Theta_{\text{D}})$ for YAlO$_3$ (ochre marker) and YbAlO$_3$ (blue marker) with $\Theta_{\text{D}} = 760\,\text{K}$ and $538\,\text{K}$, respectively. More discussion can be found in the text.

along the b-axis. Bear in mind that the mean atomic mass $(\overline{M})$ of YbAlO$_3$ is ∼50 % higher than the iso-structural system YAlO$_3$ (Table 3.1). Hence, higher thermal conduction for YbAlO$_3$ is expected at high T based on the mean atomic masses. This relation entirely violates along the c-axis where κ_c of YbAlO$_3$ is well below the one of YAlO$_3$. In fact, κ depends not only on $\overline{M}$ but also on other factors, e.g., Θ_{D}, Grüneisen parameter (Γ), elastic constants, purity, etc. For instance, a difference in Γ of two systems reveals distinct anharmonic content in the phononic branches. In such a case, an interplay between the harmonic and anharmonic properties gives rise to unexpected behaviour of κ_{ph} with respect to $\overline{M}$, making the analysis of harmonic properties, e.g., group velocity and scattering phase, insufficient to predict κ trends [207]. Consequently, proper numerical anticipation of the relative behaviour of $\kappa(T)$ involves careful consideration of the effective factors.

To evaluate the influence of the differing Γ on κ in a simple model, I use the Debye expression for phononic thermal conductivity described in Relation 4.17. Assuming that the only significant scattering in the investigated T range is the U-processes, one finds

$$
\kappa_{\text{Yb:Y}}(T) = \left[\frac{1}{\overline{v}} \int_0^{\Theta_{\text{D}}/T} \mathrm{d}x \; \frac{e^x x^4}{(e^x - 1)^2} \cdot \tau_U \right]_{Yb:Y} = \left[\frac{1}{\overline{v}} \int_0^{\Theta_{\text{D}}/T} \mathrm{d}x \; \frac{e^x x^4}{(e^x - 1)^2} \cdot \frac{e^{\frac{\Theta_{\text{D}}}{bT}}}{Bx^2} \right]_{Yb:Y}
$$

$$
= \left[\frac{e^{\frac{\Theta_{\text{D}}}{bT}}}{B\overline{v}} \int_0^{\Theta_{\text{D}}/T} \mathrm{d}x \; \frac{e^x x^2}{(e^x - 1)^2} \right]_{Yb:Y}, \tag{6.5}
$$

where the index *Yb:Y* indicates the ratio between the values for YbAlO$_3$ and the ones for YAlO$_3$. Slack *et al.* [206] proposed a functionality of Γ, $\overline{M}$, $\overline{v}$, and Θ_D for the B coefficient of the U-processes scattering rate, following the form of

$$B \propto \frac{\Gamma^2}{\overline{v}^2 \overline{M} \Theta_D}. \tag{6.6}$$

I define $I(T, \Theta_D)$ as

$$I(T, \Theta_D) = \exp\left(\frac{\Theta_D}{bT}\right) \int_0^{\Theta_D/T} \mathrm{d}x \, \frac{e^x x^2}{(e^x - 1)^2}. \tag{6.7}$$

Inserting Relation 6.6 and Relation 6.7 into Relation 6.5, we reach

$$\kappa_{\mathrm{Yb:Y}}(T) = \left[\frac{\overline{v} \overline{M} \Theta_D}{\Gamma^2} I(T, \Theta_D)\right]_{Yb:Y}. \tag{6.8}$$

$\overline{v}_{\mathrm{Yb:Y}} = 0.808$ ($\parallel b$) and 0.726 ($\parallel c$) referring to the calculated sound velocities for each crystallographic direction, and $\overline{M}_{\mathrm{Yb:Y}} = 1.512$, $\Theta_{\mathrm{D, Yb:Y}} = 0.708$, and $\Gamma_{\mathrm{Yb:Y}} = 1.119$ with the values in Table 3.1. The inset of Figure 6.6 **(b)** shows the T dependence of I between 20 - 500 K, calculated for YAlO$_3$ and YbAlO$_3$ with $\Theta_D = 760$ K and 538 K, respectively. $I_{\mathrm{Yb:Y}}$ starts below 1 at 500 K and increases by decreasing T, passing 1 at ~ 175 K. Note that the significant T dependence of $I_{\mathrm{Yb:Y}}$ is due to the difference in Θ_D of YAlO$_3$ and YbAlO$_3$.

Figure 6.6 **(b)** compares the numerical calculations of Relation 6.8 with the experimental $\kappa_{\mathrm{Yb:Y}}$ for $T \leq 100$ K. Data at $T \geq 100$ K were neglected since they are likely influenced by radiation losses. Green and violet curves represent the results for κ along the *b*- and *c*-axis. Starting at 100 K, the model predicts $\kappa_{\mathrm{Yb:Y}}(\parallel b) = 0.97 (\simeq 1)$; that already is in line with the identical κ observed along the *b*-axis of both compounds with an accuracy better than 1 %. In addition, $\kappa_{\mathrm{Yb:Y}}(\parallel c) = 0.62$, being well below 1, is calculated, which deviates from the measured value by around 15 %. By decreasing T, both curves show an upward trend. At 51 K, the model predicts $\kappa_{\mathrm{Yb:Y}}(\parallel b) = 1.36$ and $\kappa_{\mathrm{Yb:Y}}(\parallel c) = 0.87$. These values match the measured ones with an accuracy of ~ 20 % and 16.5 %. According to Figure 6.6 **(a)**, in both directions, a strong increase of κ for decreasing T is observable, and the curves for YbAlO$_3$ seem to surpass the YAlO$_3$ one at lower T. Although a limited T range of data is available from the measurements, the calculations reproduce the general trend of $\kappa_{\mathrm{Yb:Y}}$. Notably, simplifications were applied in this simulation, e.g., the N-processes of scattering at high T or the T dependence of Γ were ignored. One must note that even if the data below 50 K were not ignored, the provided numerical calculation above is based on the assumption that the U-processes of scattering are dominating. Hence, this is valid for the high-T region mostly above the phononic peak, which appears in the non-metallic compounds within the intermediate-T range. The difference in the κ behaviour in YAlO$_3$ and YbAlO$_3$ reveals, though YAlO$_3$, being the non-magnetic sister compound of YbAlO$_3$, is sometimes used as the reference sample [74, 89], it is not a proper choice for thermal-transport properties.

In conclusion, (i) the numerical calculation of κ_{ph} using the Debye model and the U-processes scattering rate proposed by Slack *et al.* [206] reproduced the measured values between 50 - 100 K with error bars up to 20 % and a similar T dependence. (ii) The difference in Θ_D and Γ and their T dependence lead to a significantly different T dependence of κ_{ph} in both compounds. Hence, YAlO$_3$ cannot be used to determine κ_{ph} of YbAlO$_3$. Due to the limited data range for YbAlO$_3$, no extrapolation to low T as estimation of κ_{ph} is possible.
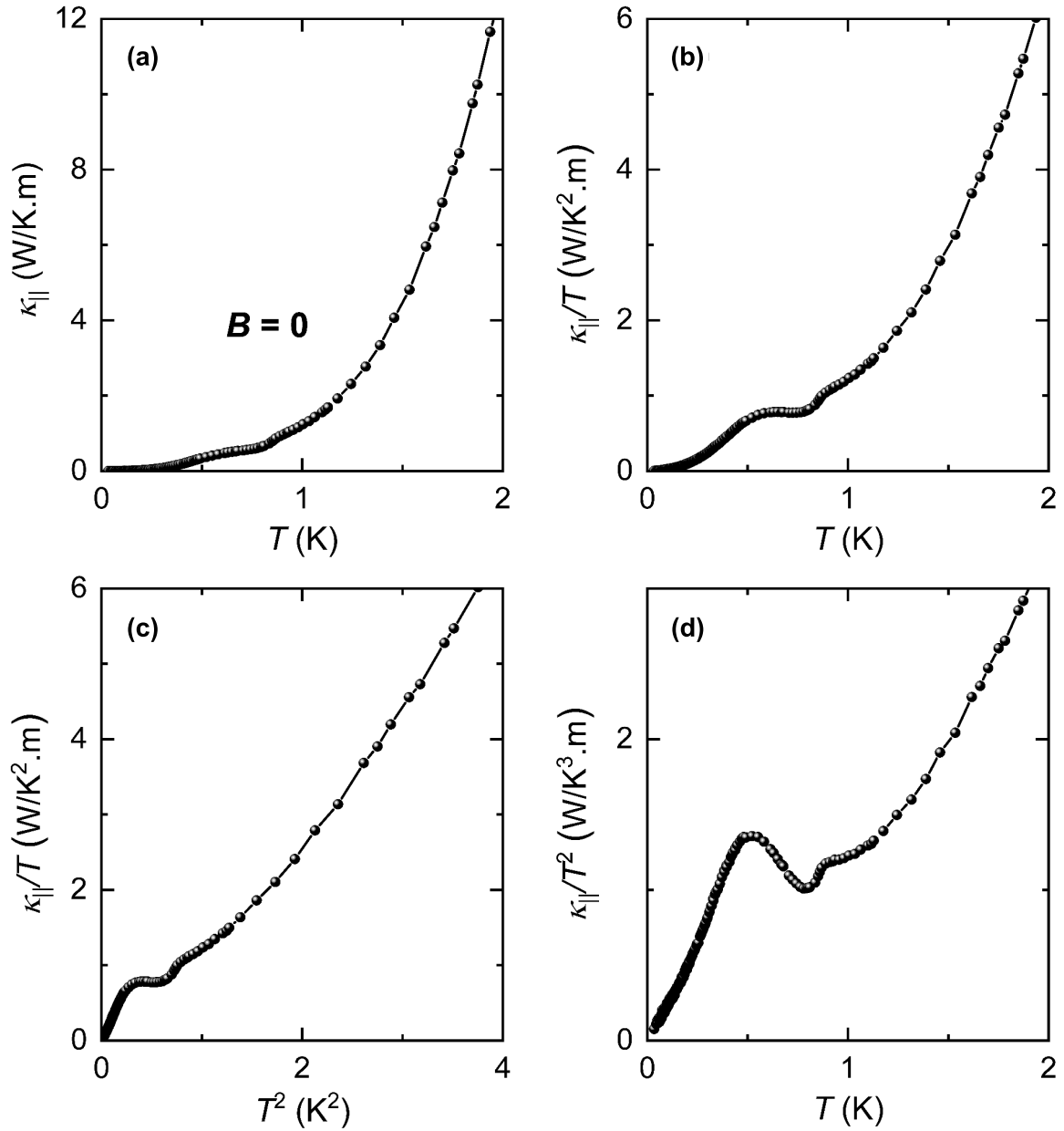
Figure 6.7: Zero-field thermal conductivity along the spin chains ($\boldsymbol{j}_Q \parallel c$) below 2 K as **(a)** κ and **(b)** κ/T vs. T, **(c)** κ/T vs. T^2, and **(d)** κ/T^2 vs. T. Features are well visible in the last presentation. In this graph, the positive slope and intercept of a linear behaviour correspond to cubic and square contributions, being the typical behaviours expected for phonons and 3-D FM magnons at low T, respectively. More details are given in the text.

6.5 In pursuit of phononic thermal transport in YbAlO₃: close to zero temperatures

To determine the heat transport and understand its origin, I studied the high-T κ in the non-magnetic YAlO$_3$ (Section 6.3) and the magnetic YbAlO$_3$ (Section 6.4) compounds. I pursue inquiring about the phononic thermal conductivity in YbAlO$_3$ in the low-T range in a ^{3}He-^{4}He dilution refrigerator down to $30\,$mK for both longitudinal and transverse heat currents to the spin chains, i.e., $\boldsymbol{j}_{\mathrm{Q}} \parallel c$- and b-axis, respectively (see Figure 6.1). In all the measurements in the magnetic field, $B \parallel a$. See Chapter 5 Section 5.6 for experimental techniques. From now on, I call κ_c and κ_b, respectively $\kappa_{\parallel}$ and $\kappa_{\perp}$, as we are at the T scale of the magnetic coupling. In a simple picture, magnetic excitations from the spin chains are supposed to contribute to the thermal transport only along the chains $\kappa_{\parallel}$, while heat transport perpendicular to the spin chains $\kappa_{\perp}$ is expected to be purely due to phonons.

I start this section by describing the presenting style of the low-T results. In pursuit of the phononic thermal transport in YbAlO$_3$, I investigate the $\kappa(T)$ curves in the fully polarised states, $B \geq 2\,$T. In the next step, I look at the $\kappa(T)$ curves in zero B and $0.2\,$T as the ordered state, close to the zero T where the excitations are frozen out. The in-field results are presented in detail in Section 6.7. I recall that Table 6.3 gives the dimensions of the measured samples.

Presentation style: Figure 6.7 **(a)** illustrates $\kappa_{\parallel}$ versus T. The curve appears almost smooth except for a tiny drop at around $0.9\,$K per cooling, presumably the Néel ordering as expected from the previous works (see Chapter 3). A plot of κ versus T, however, is not always the best choice for an analysis of thermal conductivity data. Depending on the system and the relevant conduction mechanisms, other presentations, such as κ/T versus T or κ/T versus T^2, may be more suitable. The latter type is often used for metals at low T, with phonons and electrons as heat carriers. The corresponding contributions to κ behave typically cubic and linear in T, respectively, as explained in Chapter 4 or [91, 92, 100–104]. Accordingly, in a non-magnetic metal, low-T κ behaves conventionally as

$$\kappa = a \cdot T^3 + b \cdot T. \tag{6.9}$$

In such a case, a presentation of $\dfrac{\kappa}{T}$ versus T^2 yields a linear behaviour with slope a and intercept b. In the case of YbAlO$_3$, the system is electrically insulating, meaning that the lattice and the magnetic excitations are the candidates to take part in the thermal transport. The magnetic excitations, however, are reported to exhibit different T dependencies depending on the type of the excitations, e.g., $\propto T^2$ for 3-D FM magnons, $\propto T$ for spinons in 1-D spin chains, $\propto T^3$ for 3-D AFM magnons, $\propto \exp(-\Delta/k_{\mathrm{B}}T)$ for the thermal excitation of magnetic heat carriers via a spin gap, and so on (see Section 4.5 for instance). I remind the reader that YbAlO$_3$ has a complex B-T phase diagram below $1\,$K, consisting of TLL, three-dimensional (3-D) AFM, IC-AFM with spin-density wave (SDW) & transverse AFM (TAF), and FP phases, i.e., no unique T dependency is expected. Therefore, it is not simple to choose the best presentation of $\kappa(T)$. Figure 6.7 compares different types of plots for zero-field thermal conductivity results along the spin chains of YbAlO$_3$: **(a)** $\kappa_{\parallel}$ and **(b)** $\kappa_{\parallel}/T$ vs. T, **(c)** $\kappa_{\parallel}/T$ vs. T^2, and **(d)** $\kappa_{\parallel}/T^2$ vs. T. Although the same features are observable in all the graphs, they are best visualised for κ/T^2 versus T. Moreover, a straight line with positive slope and intercept represents cubic and square contributions in this type of plot as typically expected for phonons or 3-D AFM magnons and 3-D ferromagnetic (FM)
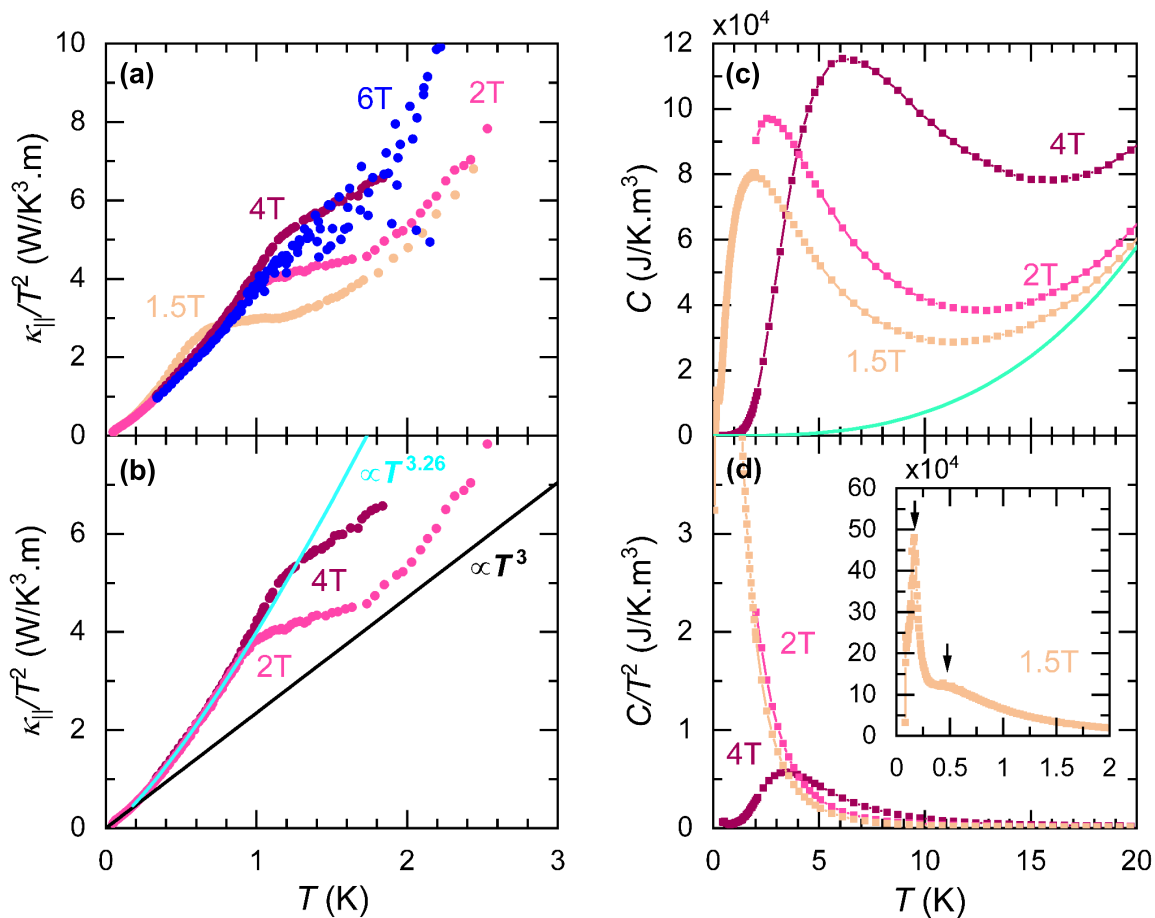
Figure 6.8: $\kappa_\parallel(T)$ and $C(T)$ of YbAlO$_3$ in the FP state. **(a)** $\kappa_\parallel/T^2$ versus T in $B \geq 1.5\,$T. **(b)** A cubic-T dependency is observed in $\kappa_\parallel(T)$ in $2\,$T below $160\,$mK. $\kappa \propto T^3$ is changed to $\propto T^{3.26}$ up to some T above $160\,$mK. **(c)** C versus T in the FP state from [74]. The green line approximates the cubic phononic contribution. **(d)** C/T^2 versus T in the FP state. The inset focuses on the $1.5\,$T curve below $2\,$K. Further discussion is given in the text.

magnons, respectively. Hence, I opt for this type of plot in the remainder of this work, otherwise mentioned. The zero-B curve is described more in subsection 6.5.2.

6.5.1 Fully-polarised state

I start the low T results with the FP state. In such a circumstance, a pure phononic thermal transport is expected for T corresponding to energies well below the Zeeman energy in B, i.e., in a T range where thermal excitations of higher magnetic states giving rise to the so-called *Schottky* anomaly in specific heat are negligible. $\kappa_\parallel(T)$ and $\kappa_\perp(T)$ were measured in B up to $6\,$T and $2\,$T, respectively. Note that the formation of the FP state is continuous, and thus, no rigid line is expected to define the state boundary. Therefore, the $1.5\,$T curve is included in the FP curves in the subsequent paragraphs to help follow the trend from lower B. I start first with the thermal conductivity results along the spin chains in the FP state. Then, I move on to the perpendicular direction, $\kappa_\perp(T)$, and compare it to $\kappa_\parallel(T)$.

Heat transport along the spin chains: Figure 6.8 shows the $\kappa_\parallel(T)$ results of this work in $B \geq 1.5\,\mathrm{T}$, along with the $C(T)$ results of Wu *et al.* [74]. $\kappa_\parallel/T^2$ versus T in $B = 1.5\,\mathrm{T}$, $2\,\mathrm{T}$, $4\,\mathrm{T}$, and $6\,\mathrm{T}$ are presented in Figure 6.8 **(a)**. At $T < 0.2\,\mathrm{K}$, all the curves lie on each other, which agrees with the polarisation of the spins in this T range. By increasing T, however, the $1.5\,\mathrm{T}$ curve does not follow the curves perfectly: Compared to the higher B, for instance, $2\,\mathrm{T}$, the $1.5\,\mathrm{T}$ curve shows first a bit of increase (around 0.4 - 0.7 K) and goes below the $2\,\mathrm{T}$ curve by increasing T further. Similar behaviour is observable between each curve and the higher B, but the separation moves to higher T in higher B, cf. $4\,\mathrm{T}$ and $6\,\mathrm{T}$. Notably, the $2\,\mathrm{T}$ curve does not show a clear hump compared to the $4\,\mathrm{T}$ with the available data. Two significant points in these T and B range are notable: (i) Collecting these data points required many times repeating the measurements due to the instability of the mixing chamber, which is the best obvious in the $6\,\mathrm{T}$ data points where the data resolution decreases drastically per increasing T. (ii) Possible vibrations of the electrical components mounted on the gold islands of the probe induce eddy currents to the measuring set-up. Such heating reduces the precision of the measurement. Considering these points and the stability issues during the high B measurements, i.e., above $2\,\mathrm{T}$ and $1\,\mathrm{K}$, these data are worth repeating.

Figure 6.8 **(b)** focuses on the T dependence of the $2\,\mathrm{T}$ curve. The $4\,\mathrm{T}$ curve is also included for comparison purposes given later. At the lowest T, no magnetic excitations are expected, and thus, a cubic-T dependence of the thermal conduction via the lattice is observed. By increasing T, the phononic contribution of $\kappa_\parallel \propto T^3$ changes to $\propto T^{3.26}$ above $\sim 160\,\mathrm{mK}$. The source of the observed deviation from the T^3 behaviour above $\sim 160\,\mathrm{mK}$ is still not fully clarified. Two main scenarios exist: (i) hydrodynamic flow of phonons along the c-axis (the spin chains in zero B), and (ii) thermally-excited magnetic carriers contributing to the heat transport in the FP state. I explain these two possibilities in what follows.

- **Hydrodynamic flow of phonons:** Figure 6.8 **(c)** shows $C(T)$ in $B = 1.5\,\mathrm{T}$, $2\,\mathrm{T}$ and $4\,\mathrm{T}$ in T up to $20\,\mathrm{K}$. The Schottky peak sits on top of the green line as an approximation of the cubic phononic contribution. Using the approximated phononic background (green line) and the $\kappa_\parallel(T)$ results below $160\,\mathrm{mK}$, I calculate the mean free path (λ) of the phonons in this T range from Relation 4.6.

$$\lambda = d \cdot \left(\frac{\kappa(T)}{C(T)} \right) \cdot \left(\frac{1}{v} \right) = 3 \cdot \left(\frac{2.35\ T^3\ [\mathrm{W\,K^{-1}\,m^{-1}}]}{7.22\ T^3\ [\mathrm{J\,K^{-1}\,m^{-3}}]} \right) \cdot \left(\frac{1}{4.34 \cdot 10^3\ [\mathrm{m/sec}]} \right)$$

$$\Rightarrow \lambda \simeq 2.25 \cdot 10^{-4}\,\mathrm{m} \sim 200\,\mathrm{\mu m}, \tag{6.10}$$

  for a three-dimensional phononic heat transport and the mean sound velocity calculated in Section 6.4. Therefore, $\lambda \sim 200\,\mathrm{\mu m}$ and thus of the same order as the sample width being $\sim 500\,\mathrm{\mu m}$ (see Table 6.3). In such a circumstance, transport is mainly limited by the sample boundaries, and thus, the so-called ballistic transport is expected. If the electrically-insulating sample contains very few impurities, the N-processes of phonons can dominate the diffusive ones, and hydrodynamic flow of phonons with $\kappa \propto T^n$ and $n > 3$ can take place [208]. Two main phonon hydrodynamic phenomena are (i) the so-called *second sound*, in which scattering by boundaries is negligible, and (ii) *Poiseuille flow*, in which λ is comparable to the sample width though the scattering rate of the N-processes is above the scattering rate of the boundaries. Hence, the Poiseulle flow can occur in YbAlO₃, where λ is of the order of the sample width, while the second sound flow is irrelevant. In such a boundary-limited regime, T above which thermal conductivity shows a faster than T-cubic behaviour is interpreted as the onset

of the Poiseuille flow. Experimentally, this is observed in rare compounds, specifically ^{4}He [209], ^{3}He [210], Bi [211] and the 2-D compound black phosphorus [212].

The change of $\kappa_\parallel(T)$ from T^3 to higher than T cube, namely $T^{3.26}$, in the 2 T curve is in line with the hydrodynamic flow of phonons with the onset T of the Poiseuille flow at ∼160 mK. To prove this scenario, one must measure other samples in the FP state with various smaller cross-sections. If the hydrodynamic flow is responsible for the above-cube behaviour of $\kappa_\parallel(T)$, this type of behaviour will still be present, though the prefactor of the T^3 close to zero T governed by the sample width will lessen. In addition, a pure phononic heat transport with negligible magnetic contribution is imperative to support this idea. In other words, a B-independent behaviour of the $\kappa_\parallel(T)$ curves is expected, c.f. Figure 6.8 **(b)**.

Figures 6.8 **(a)**-**(b)** show a reduction of $\kappa_\parallel(T)$ around $T > 1$ K from the above-cube behaviour of the lower T, which I call a flattening of the $\kappa(T)/T^2$ curve. This flattening may be related to the scattering effects of the thermal excitations, which pronounce by increasing T and approaching the Schottky peak in the specific heat.

- **Additional contribution to phonons:** Figure 6.8 **(d)** displays $C(T)/T^2$ comparable to the $\kappa_\parallel(T)/T^2$ curves of panels **(a)**-**(b)**. Unfortunately, very low T measurements in $B = 2$ T are unavailable; however, the overall behaviours are distinct in the two curves of 1.5 T and 4 T. Starting from zero and increasing T, the 4 T curve is almost zero at $T < 1$ K. By increasing T, C/T^2 reaches around 3 K a maximum and lowers back to slightly above zero. The inset of Figure 6.8 **(d)** zooms the 1.5 T curve below 2 K. Note that the height and position of the peaks in terms of $C(T)/T^2$ differ from the case of $C(T)$. In particular, the features at lower T get more pronounced. In addition to the Schottky peak around 0.4 K, a second peak appears at lower $T < 200$ mK (indicated by the arrows). The peak below 200 mK also appears in other B, the source of which is not yet understood and thus not published in [74].

  In the scenario of an additional contribution to the phononic heat transport, thermally-excited magnetic carriers around the Schottky peak in the FP state take part in the heat transport and give rise to the increase of $\kappa(T)$ stronger than T^3. In this case, an extra contribution is anticipated, and the corresponding peak should move to higher T once increasing B, similar to the 1.5 T and 4 T curves in Figure 6.8 **(a)**.

Heat transport perpendicular to the spin chains: $\kappa_\perp$, being κ along a perpendicular direction to the spin chains, is widely used to determine the phononic background of low-D spin systems, as mentioned in Chapter 4 Section 4.5, see, e.g., [126, 129, 134, 136]. That is because $\kappa_\perp(T)$ is expected to include only the phononic contribution, so $\kappa_\perp = \kappa_{\mathrm{ph},\perp}$. But scattering can influence the behaviour perpendicular to the spin chains as well. Figure 6.9 shows the T dependency of $\kappa_\perp(T)$ in $B = 2$ T of the FP state. Figure 6.9 **(a)** plots $\kappa_\perp(T)/T^2$ up to 5 K in 2 T. I must note that the 1.5 T curve of $\kappa_\perp(T)$ is available up to around 1 K. Moreover, the 1.5 T curve behaves similarly to the 2 T curve within the available T range and is thus not included in Figure 6.9 **(a)**. $\kappa_\perp(T)$ in 1.5 T is shown later in Figure 6.17. Starting from zero and increasing T, $\kappa_\perp$ behaves as T^3 initially (black line). By increasing T above about 150 mK, the exponent lowers approximately to $\propto T^{2.56}$, shown by a blue line. The reason for this huge suppression of $\kappa_\perp(T)$ compared to the low T behaviour is not yet well understood, though a couple of possibilities and similar reports are remarkable:

(i) As mentioned in Chapter 4 Section 4.5, an immense suppression of $\kappa_\perp(T)$ was observed along two perpendicular directions of the 1-D spin chain CaCu$_2$O$_3$ [126] (see also Figure 4.5). Hess *et al.* associate this observation with the disorder and/or contribution of optical
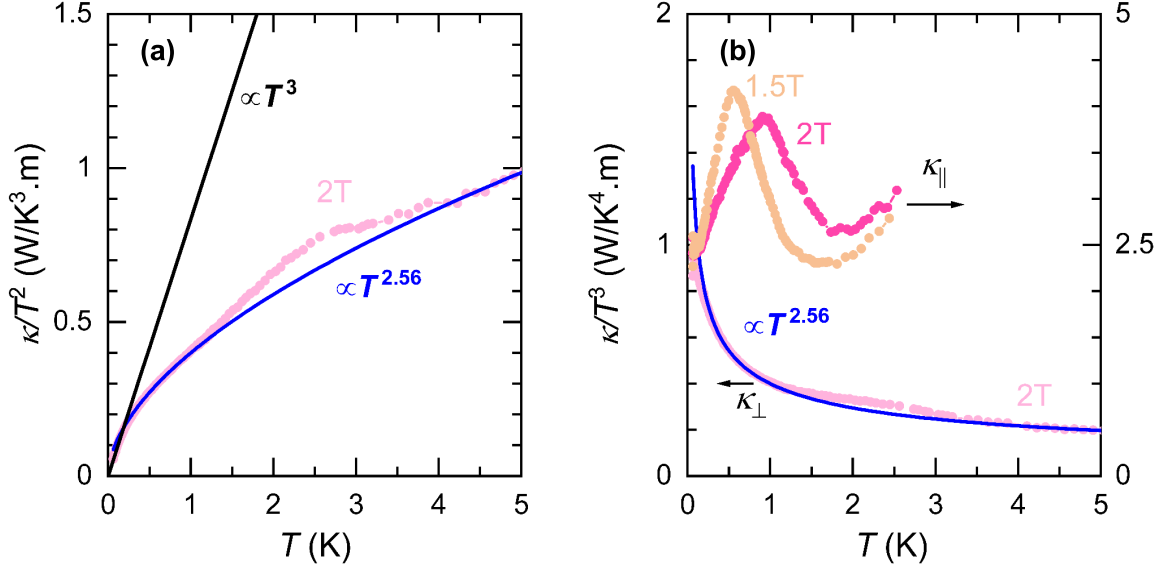
Figure 6.9: $\kappa_\perp(T)$ of YbAlO$_3$ in the FP state. **(a)** A cubic-T dependency is observed in $\kappa_\perp(T)$ for $B = 2\,\text{T}$ below 160 mK. $\kappa \propto T^3$ is decreased to $\propto T^{2.56}$ up to some T above 160 mK. **(b)** κ/T^3 versus T for $\kappa_\perp$ (left axis) and $\kappa_\parallel$ (right axis) in the FP state. Note a scale of 1:2.5 between the left and right axes. More explanation is provided in the text.

phononic branches [126]. The optical branches of phonons have a lower group velocity than the acoustic ones (see Figure 4.1), so a significant reduction in the propagating phonons occurs. In another work, Hess *et al.* studied acoustic and optical phononic thermal conductivity on the 2-D lattice La$_2$CuO$_4$ and suggested dispersive optical phonons along with the magnetic heat transport responsible for the unusual T-dependency of the low-D spin system [213]. For CaCu$_2$O$_3$, the change of T dependency of the $\kappa_\perp$ curves occurs around 20 K (1.7 meV). In the case of YbAlO$_3$ of this research, however, the change of the T^3 behaviour to $T^{2.56}$ is observed below 200 mK (0.017 meV). Numerical calculation of the phononic structure by *Maxim Pavlovskii* from the *Kirensky Institute of Physics* revealed the lowest optical branch around 100 cm^{-1} ($\sim$10 meV or 140 K). Therefore, the scenario, including heat transport by the dispersive optical branches below 200 mK, is invalid.

(ii) Wybourne *et al.* reported a change of $\kappa(T)$ from $\propto T^3$ close to zero T to T^n with $n < 3$ above 1 K in polydiacetylene [214, 215]. Wybourne *et al.* showed that this suppression could be modelled by the Callaway relation only if optical-acoustic phonon scattering is included in the sample boundaries, point defects, and dislocations [214]. In such a circumstance, however, the optical modes are associated with side-group motions of the monomers. In the case of YbAlO$_3$, the huge suppression above $\sim$160 mK may be interpreted by low-energy modes associated with the motion of the side groups of the spin chains with strong magnetoelastic coupling to the lattice. In addition, that may explain the unknown peak appearing in the $C(T)$ curves below 200 mK as thermal excitation of the side-group optical modes. In such a case, a side group adds to the lattice vibrations of the ions due to the dynamics and relative motion of the spin chains. Therefore, the acoustic phonons may sense extra scattering in the perpendicular directions via the side-group motion of the spin chains. It is noteworthy that the suppression of the $\kappa_\perp$ curves appear at $T/k_\text{B} \sim 0.2 J_\perp$ (0.16 K/0.8 K = 0.2) in YbAlO$_3$ and $T/k_\text{B} \sim 0.1 J_\perp$ (20 K/200 K = 0.1) in the case of CaCu$_2$O$_3$, which means the suppression

is observed around $T/J_\perp \sim 0.2$. If this scenario is the case in these spin chains, the suppression must disappear as we go well above the intra-chain coupling $J_\parallel$ in T, particularly well above $3\,K$ and $2000\,K$ in YbAlO$_3$ and CaCu$_2$O$_3$, respectively. Unfortunately, data points in these T ranges are not available. Lastly, as plotted in [214], the optical-acoustic phonon scattering mechanism combined with stacking-fault scattering can reproduce both types of change of slopes observed in the $\kappa_\perp(T)$ curves of CaCu$_2$O$_3$ shown in Figure 4.5 **(a)**.

(iii) Another scenario is the existence of thermally-induced magnetic excitations in the FP state with the dominant contribution to κ along the spin chains but suppression of κ in the perpendicular direction. Even though, the tiny hump in the $\kappa_\perp(T)$ curve above the $T^{2.56}$ line around 1.5 - 4 K would not be explained by this scenario. Note that the thermal excitations exist from the lowest T and increase rather exponentially but continuously and well-behaved in T. Therefore, these excitations are not associated with the unknown peak in the $C(T)$ curves below 200 mK. Finally, I must note the observed suppression of $\kappa(T)$ from the T^3 behaviour above $\sim$150 mK is not in line with the scenario of the hydrodynamic flow of phonons mentioned to explain the $\kappa_\parallel(T)$ behaviour in the FP state.

Figure 6.9 **(b)** depicts $\kappa_\perp/T^3$ versus T in $B = 2\,T$. The 1.5 T and 2 T curves of $\kappa_\parallel(T)$ are also plotted on the right axis of Figure 6.9. Note a scale of 1:2.5 between the left and right axes. The lower limits of all the curves tend to a constant number since $\kappa(T) \propto T^3$ as T tends to zero. At $T > 160\,mK$, however, $\kappa_\perp$ ($\kappa_\parallel$) shows a slower (faster) than cubic T dependency. The $\kappa_\perp(T)/T^3$ may tend to a constant number around $0.2\,W\,K^{-4}\,m^{-1}$ at $T > 5\,K$, which means $\kappa_\perp(T)$ may tend to a T-cube functionality. The $\kappa_\parallel(T)$ curves of 1.5 T and 2 T shown in Figure 6.9 **(b)** get close to a T^3 behaviour around 1 - 2 K, though they do not settle to a cubic-T dependency up to the available $T\sim$2.5 K.

6.5.2 Ordered state at low field

The magnetic excitations within the ordered states may influence the thermal transport in two ways: (i) Contribute as an additional channel in conducting heat and enhance the thermal conductivity hence, and/or (ii) act as scattering centres to reduce κ. In the Q-1-D spin system YbAlO$_3$, a 3-D AFM GS in $B < 0.35\,T$ with a phase transition from the 3-D AFM to the TLL below 1 K was identified via specific heat, magnetisation and neutron scattering measurements [59, 72, 74]. In this research, I measured $\kappa(T)$ in zero B and 0.2 T down to $T < 100\,mK$.

Figure 6.10 displays the $\kappa(T)$ curves in $B = 0$ and 0.2 T close to absolute zero, where the magnetic excitations are frozen out and negligible. The graph is limited up to 1.2 K to focus on the very-low T and features around the AFM ordering transition. The arrows indicate T_N from the specific heat results in [74]. Starting from zero T, the


Figure 6.10: $\kappa_\parallel/T^2$ versus T in $B = 0$ and 0.2 T with 3-D AFM GS below 1.2 K.

$\kappa_\parallel(T)$ curves behave $\propto T^3$ up to $\sim$160 mK. By increasing T further, $\kappa_\parallel(T)$ grows faster

Field	α (W m^{-4}K^{-1})	β (W m^{-1}K^{-1})	Δ (K)	2Δ (meV)	Δ_{INS} (meV)
0 T	2.35	2.2	1.62	0.279	0.31 ± 0.03 meV
0.2 T	2.31	4.5	1.54	0.265	

Table 6.4: Fitting parameters of the spin gaps to $\kappa_\parallel(T)$ in the 3D AFM state plotted in Figure 6.11, with a cubic phononic background. Δ_{INS} is from [74].
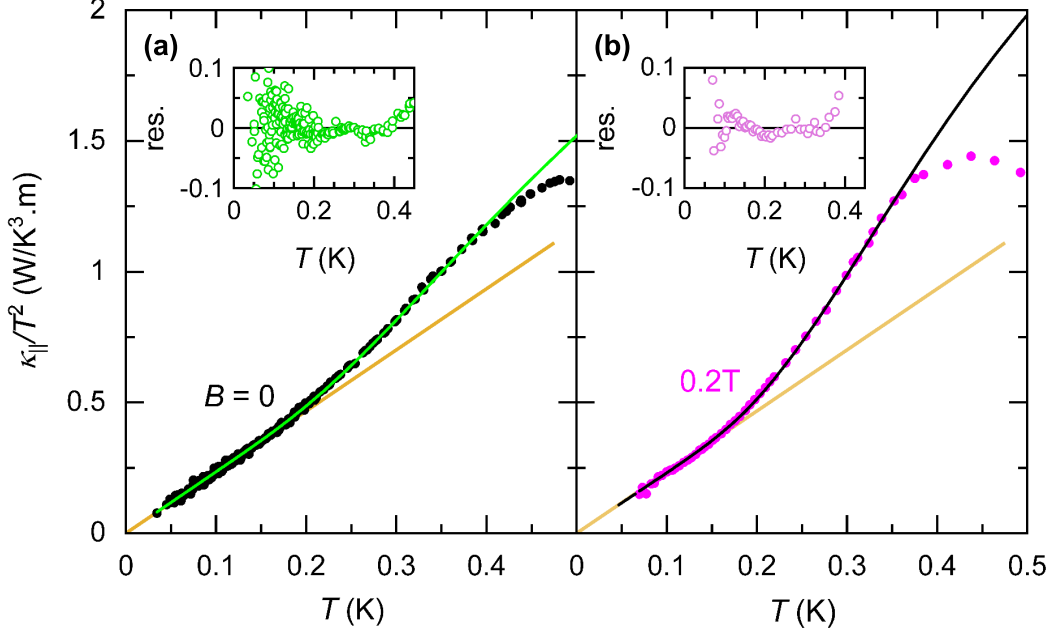

Figure 6.11: Spin-gap fittings to the thermal conductivity measured in **(a)** 0 T and **(b)** 0.2 T with the best fitting parameters as noted in Table 6.4. Residual values of each fit, defined as res. $= (\kappa_{\mathrm{meas.}} - \kappa_{\mathrm{fit}})/\kappa_{\mathrm{meas.}}$, are plotted in the insets.

than the extrapolation of the T-cube behaviour at the lowest T (yellow line). At least two scenarios conceivably explain the enhancement above the T^3 at $T > {\sim}160$ mK: $\kappa_\parallel(T)$ may be due to (i) dominant phononic contribution of $\propto T^n$ with $n > 3$ as described in the case of FP state, or (ii) summation of a cubic contribution of the phonons and a non-negligible transport of heat via the magnetic carriers within the 3-D AFM phase, namely gapped magnons by confinement of spinons (Chapter 3 Section 3.3), which are thermally-excited. The enhancement from the cubic behaviour in 0.2 T starts at a similar T range but goes higher in values than in the case of zero B. That is a strong hint for magnetic heat transport within the 3D-AFM phase; however, it is unclear whether κ_{mag} contributes considerably in $\kappa_\parallel(T)$ in zero B to grow faster than T^3. Notably, the special magnetic structure of the Yb^{3+} ions in the ordered state generates a local molecular staggered field of $B_{\mathrm{st}} \sim 0.3$ T, and the magnetic moments sense a non-zero net B even in zero external B. Details on the magnetic structure of YbAlO₃ are available in Chapter 3 Section 3.3 and Appendix B.

Assuming a cubic-T lattice contribution and spin-gapped excitations, one can fit the enhancement compared to the T^3 behaviour dominating at the lowest T with

$$\kappa = \kappa_{\mathrm{ph}} + \kappa_{\mathrm{mag}} = \alpha T^3 + \beta \exp(-\Delta/k_{\mathrm{B}}T), \tag{6.11}$$
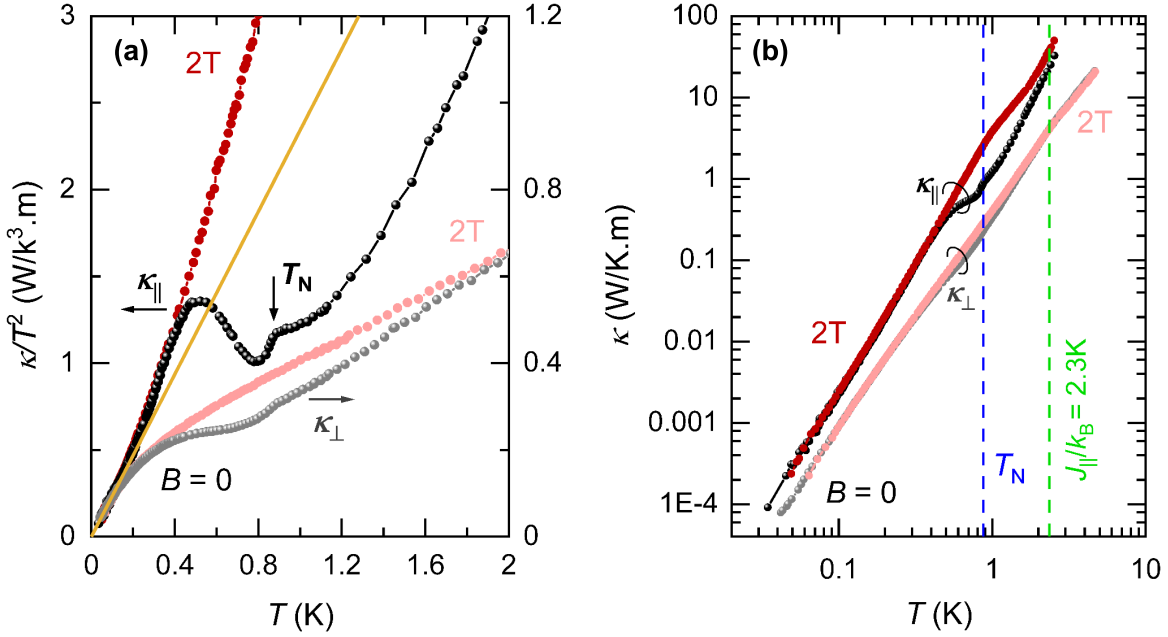
Figure 6.12: Thermal transport of YbAlO$_3$ in zero B compared to 2 T in the FP state. **(a)** $\kappa(T)/T^2$ along and perpendicular to the the spin chains in zero B and 2 T below 2 K. Note a scale of 2.5:1 between the left and right axes. The yellow line is extrapolation of the T^3 behaviour at $T \to 0$. **(b)** $\kappa(T)$ results within the dil-fridge T range on a log-log scale.

e.g., see [216]. In Relation 6.11, α and β are free parameters, Δ is the energy gap, and k_B is the Boltzmann constant. Figure 6.11 shows the 0 T and 0.2 T curves below 0.5 K, including the fitting curves according to Relation 6.11 with the parameters noted in Table 6.4. The insets plot the residual values of the fits defined as res. $= (\kappa_{\mathrm{meas.}} - \kappa_{\mathrm{fit}})/\kappa_{\mathrm{meas.}}$.

Concerning the best-fitting parameters and curves, (i) Relation 6.11 is valid as long as the phononic contribution is well-described by a cubic behaviour and the scattering of phonons by the magnetic excitations is not so strong. (ii) The best fit for the 0 T data gives β and α values such that κ_{ph} is about $0.87\kappa_{\|}$ at 0.3 K. With a slight change of α and thus κ_{ph}, the κ_{ph} value decreases to $0.7\kappa_{\|}$ at the same T in 0.2 T, suggesting a doubling of the magnetic contribution responsible for the increase in $\kappa_{\|}(T)$ in 0.2 T compared to 0 T. (iii) The energy gaps are about half that measured via neutron scattering in [74] and shown in Figure 3.3. That implies the measured spin gap in the thermal transport is half of the two confined spinons measured in INS, in line with the statement that thermodynamics carries the information of a single spinon, while spectroscopy is associated with spinon pairs [217].

By increasing T further, an abrupt suppression of κ/T^2 is observed around $T > 0.4$ K below T_N in the 3-D AFM state. The suppression of κ at the magnetic phase boundaries can be explained by intense scattering of phonons by critical spin fluctuations near a magnetic transition and magnon-phonon interactions, e.g., [218–220]. By increasing T further, an upward turn appears up to ~0.88 K. One may note that this upward turn per rising T can be called a *drop* once entering the 3-D AFM phase from the TLL state.

Figure 6.12 **(a)** displays the T dependency of $\kappa_{\|}$ (left axis) and $\kappa_{\perp}$ (right axis) in zero B in terms of κ/T^2, respectively, in black and grey markers. Note a scale of 2.5:1 between the left and right axes. The results for $B = 2$ T in the FP state are over-plotted for comparison

purposes. At the lowest T, the zero-B curves lie on the corresponding FP curves. In case the $\kappa_\parallel(T)$ curve in the FP state with $B = 2\,$T is the correct description of $\kappa_{\mathrm{ph}}(T)$, the coincidence of the $\kappa_\parallel(T)$ curves of $0\,$T and $2\,$T up to $\sim 0.4\,$K indicates a dominant phononic contribution and freeze-out of magnetic excitations. Then, by increasing T around $0.4\,$K, the $0\,$T curve departs from the $2\,$T one by virtue of strong scattering and spin-phonon coupling.

The overall behaviour of $\kappa_\perp(T)$ in zero B is similar to the FP state: A T-cube behaviour appears below $200\,$mK, followed by an enormous suppression to lower than $\propto T^{2.6}$ at higher T. Moreover, magnetic scattering of phonons is observable between 0.3 and $2\,$K in zero B. Both departure from the $2\,$T curve and the upward turn around the Néel ordering T are more pronounced for the heat current along the chains, meaning the direction with stronger exchange interaction. Figure 6.12 **(b)** illustrates the $\kappa_\parallel(T)$ and $\kappa_\perp(T)$ curves of $0\,$T with the 3-D AFM GS and $2\,$T in the FP state up to the highest measured T. The blue and green dashed lines indicate $T_{\mathrm{N}} = 0.88\,$K and $J_\parallel = 2.3\mathrm{K}k_{\mathrm{B}}$. The $\kappa_\perp(T)$ curves begin to gather by increasing $T > T_{\mathrm{N}}$ and meet around $2\,$K by getting close to the intra-chain coupling. Though the $\kappa_\parallel(T)$ curve in zero B is still below the $2\,$T curve up to the measured $T\sim 3\,$K, the difference between the curves diminishes per increasing T in line to reach each other.

To sum up this section, three possible methods to determine $\kappa_{\mathrm{ph}}(T)$ are via (i) $\kappa_\perp(T)$, (ii) extrapolation of the T^3 as $T \to 0$, and (iii) $\kappa_\parallel(T)$ in $2\,$T in the FP state. Note that the $2\,$T curve is above the other possible phononic backgrounds in items (i) and (ii). Therefore, if $\kappa(T)$ in B below the FP state appears above the $2\,$T $\kappa_\parallel(T)$ curve, magnetic heat transport is present indeed. $\kappa_{\mathrm{mag}}(T)$, assuming each of these three phononic backgrounds, is studied in Chapter 7 Section 7.2.

6.6 Lattice transport anisotropy of YbAlO₃

Figure 6.13 shows $\kappa(T)$ results studied in Section 6.4 and Section 6.5 in zero B at low and high T on the same graph. I recall that κ could not be measured reliably in the PPMS device at $T < 50\,$K, as explained in Section 6.4. Dashed lines in Figure 6.13 connect the low- and high-T results with a typical behaviour of a non-metal as rough estimates of the purely phononic κ for T ranging between 3 - 50 K. Panel **(a)** depicts the measured κ data versus T from $30\,$mK up to the RT on a log-log scale. Despite the loss of resolution between 3 - 50 K, it is still clear that the two curves intersect and cross each other in this T range since κ at T below and above this intermediate T limit is larger along the c- and b-axis, respectively.

Figure 6.13 **(b)** plots $\kappa_\parallel/\kappa_\perp(T)$ for zero B (black) and $2\,$T (red) from $\sim 30\,$mK up to the RT. Starting from the lowest T, where the magnetic excitations in both cases of the FP and ordered states are frozen out, $\kappa_\parallel/\kappa_\perp(T \to 0) = 2.5$, yielding a higher lattice thermal transport along the spin chains, namely the c-axis. The thermal transport anisotropy remains almost 2.5 from the lowest T up to around $160\,$mK. By increasing T, however, the FP and ordered states appear differently: In the case of the $2\,$T curve in the FP state, deviation from the constant thermal transport anisotropy of the lowest T is expected to appear in forms of $\kappa_\parallel/\kappa_\perp(T) \propto T^{3.26}/T^{2.56} \propto T^{0.7}$ up to around $1\,$K as discussed in Section 6.5. $\kappa_\parallel/\kappa_\perp \simeq 2.5$ at $T < 160\,$mK increases and shows a maximum of about 10 at $\sim 1\,$K, similar to the hump that appeared in $\kappa_\parallel(T)$ close to the Schottky anomaly. I remind the reader that it is still unclear whether this observation in $\kappa_\parallel(T)$ is due to hydrodynamic phenomena and Poiseulle flow of the phonons or the additional contribution of the thermally excited magnons.

In the $0\,$T curve, increasing T above $160\,$mK results in two consecutive local maxima, as the one related to the Néel ordering transition is considerably smaller than the one appearing at
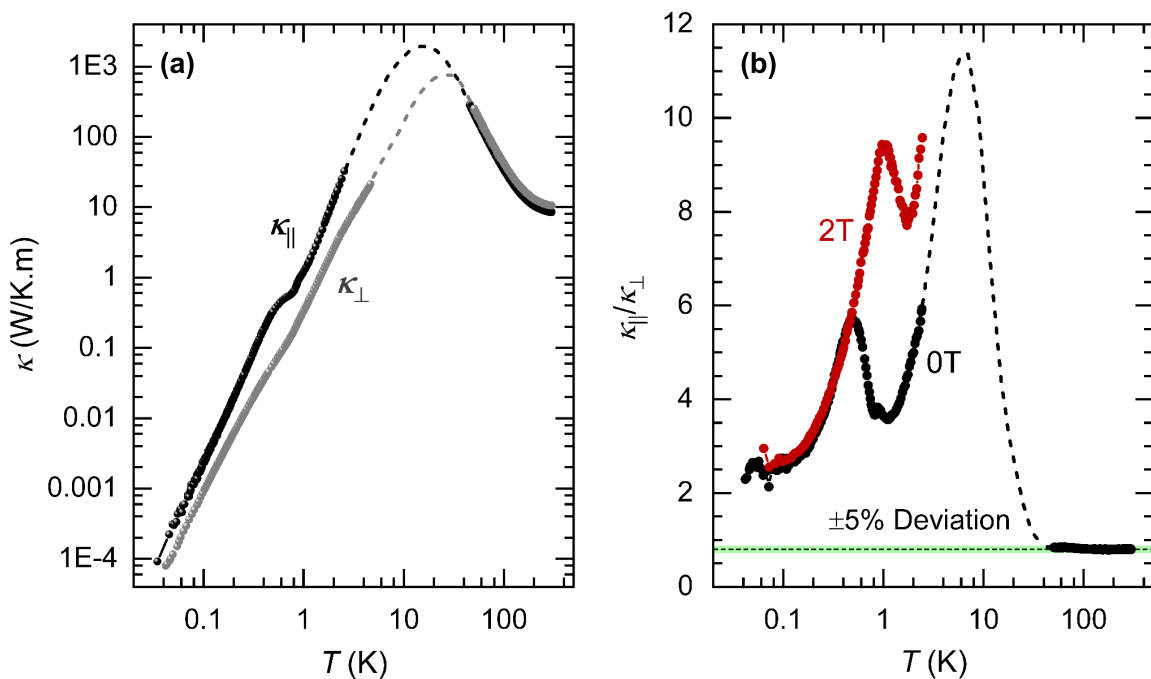
Figure 6.13: *T* dependence of the lattice transport aniosotropy in YbAlO$_3$. **(a)** κ versus T of the low-T results along with the high-T one. Note the logarithmic scaling for clarity of data in all orders of magnitude of both κ and T. Dashed lines are plotted to give a rough estimate of κ in the T range between $\sim$3 - 50 K where the measured data are excluded due to a low resolution. **(b)** $\kappa_\parallel/\kappa_\perp$ versus T, from RT down to $\sim$30 mK. A light green box indicates the $\pm$5 % deviation around 0.8. More discussion in given in the text.

lower T. If one considers the local maximum at lower T in zero B due to the extra magnetic contribution within the 3-D AFM phase and not the Poiseulle flow only along the spin chains, this observation is in line with the fact that the magnetic contributions add to the phononic channel only along the chains but take part in the scattering processes generating thermal resistivity in the perpendicular direction. Warming above T_N results in continuous growth of $\kappa_\parallel/\kappa_\perp$ up to the highest measured T. The dashed line is the ratio of the black and grey imaginary lines of panel **(a)**, representing the corresponding transport anisotropy. By increasing T above 50 K, the thermal conduction anisotropy of YbAlO$_3$ reaches an almost constant value of 0.8 up to RT. The light green box indicates a $\pm$5 % deviation around the RT value of 0.8, within which the points are located. Although the dashed line is calculated for the exemplary lines in panel **(a)**, a maximum for the thermal transport anisotropy curve $\kappa_\parallel/\kappa_\perp(T)$ is expected between 3 - 50 K owing to (i) the increasing trend of the curve at the discontinuity point due to lack of data points at around 3 K, plus (ii) $\kappa_\parallel/\kappa_\perp(T = 3\,\mathrm{K}) \sim 6$ and thus higher than that of the RT being 0.8.

The phononic transport anisotropy of 2.5 and 0.8 at low and high enough T reveal an increase of 212.5 % per cooling from the RT to zero T, and thus, a large T-dependent lattice transport anisotropy. According to Relation 4.6, the lattice transport anisotropy can be written as

$$\kappa_\parallel/\kappa_\perp(T) = \kappa_c/\kappa_b(T) = \lambda_c/\lambda_b(T) \cdot \bar{v}_b/\bar{v}_c(T). \tag{6.12}$$

Notably, the T dependency of the anisotropy is seldom reported, e.g., for thin films in [221],

which is irrelevant to the case of the bulk compound YbAlO$_3$ in this study. Though the strong T dependence of the phononic transport anisotropy observed in YbAlO$_3$ is not well understood, possible scenarios are noteworthy:

- **T dependency of direction-dependent velocities:** According to Relation 6.12, a T dependency of $\overline{v}_b/\overline{v}_c$ can generate a T-dependent $\kappa_\parallel/\kappa_\perp(T)$. Nevertheless, more than 200% change of $\overline{v}_b/\overline{v}_c$ is required to explain the observed lattice transport anisotropy. In other words, instead of a rather synchronised change of the direction-dependent velocities, $\overline{v}_b$ has to increase way faster than $\overline{v}_c$, which is typically unexpected. In the case of magnetic materials, the range of the relative changes of the sound velocity and sound attenuation, a measure of energy loss of a travelling wave, is not more than one order of magnitude typically expected, e.g., see the review article [222]. Still, ultrasound measurements will be performed in collaboration with *Stanislaw Galeski* from the *Physikalisches Institut* of the *University of Bonn* to have a more accurate idea of the changes and effects of T on the direction-dependent ultrasonic properties.

  One may consider dominant ballistic transport close to zero T. In this case, the mean free path is determined by the sample geometry at the lowest T, and thus $\lambda_c/\lambda_b \sim 1$, thanks to the similar geometries of the samples (see Table 6.3). $\overline{v}_b/\overline{v}_c \sim 2.5$, hence in the zero T limit. $\overline{v}_b/\overline{v}_c = 1.12$, on the other hand, in the RT limit as calculated in Section 6.4. Thus, 100% growth of $\overline{v}_b/\overline{v}_c$ by decreasing T from the RT to zero is still required if the T dependency of $\overline{v}_b$ and $\overline{v}_c$, plus the boundary-limited/ballistic transport, are the only phenomena leading to the change of $\kappa_c/\kappa_b = 0.8$ to 2.5.

- **Change of the transport dimensionality:** According to Relation 4.6, thermal conductivity is divided by the transport dimension d. The lattice transport anisotropy at the lowest T equals $2.5/0.8 \simeq 3$ times the RT value, which may be described by a change of the transport dimensionality of the phonons from 3 at the RT to 1 along the spin chains at the lowest T.

- **Acoustic and optical phonons:** Such an incident may occur due to sensible changes in the acoustic and optical phononic contributions with T, which affect the interplay between the harmonic and anharmonic phonon properties, see Chapter 4 Section 4.3 or, e.g., [207]. That being the case, the T-dependency of the anisotropy commits a non-cubic behaviour of the phonons even at low T till it settles down. This circumstance can induce a change in the ratio $\overline{v}_b/\overline{v}_c$ at $T \to 0$ compared to the RT one.

To sum up, the observation of a strong T dependency of the phononic transport anisotropy between zero T and the RT highlights the importance of a comprehensive understanding of the transport and/or interplay between the harmonic and anharmonic phonon properties to get insights into the phonon thermal transport in YbAlO$_3$.

6.7 Thermal conductivity of YbAlO$_3$ in field

I continue investigating the low-T thermal conductivity of YbAlO$_3$ along and perpendicular to the spin chains, $\kappa_\parallel$ and $\kappa_\perp$, in magnetic fields between 0 - 2 T. The results are for T- and B-sweep measurements with the magnetic field applied along the a-axis.

6.7.1 Temperature sweeps

Figure 6.14 presents an overview of the in-B thermal conductivity along the spin chains in $\kappa_\parallel/T^2$ versus T. The curves are classified according to the applied B into three panels,
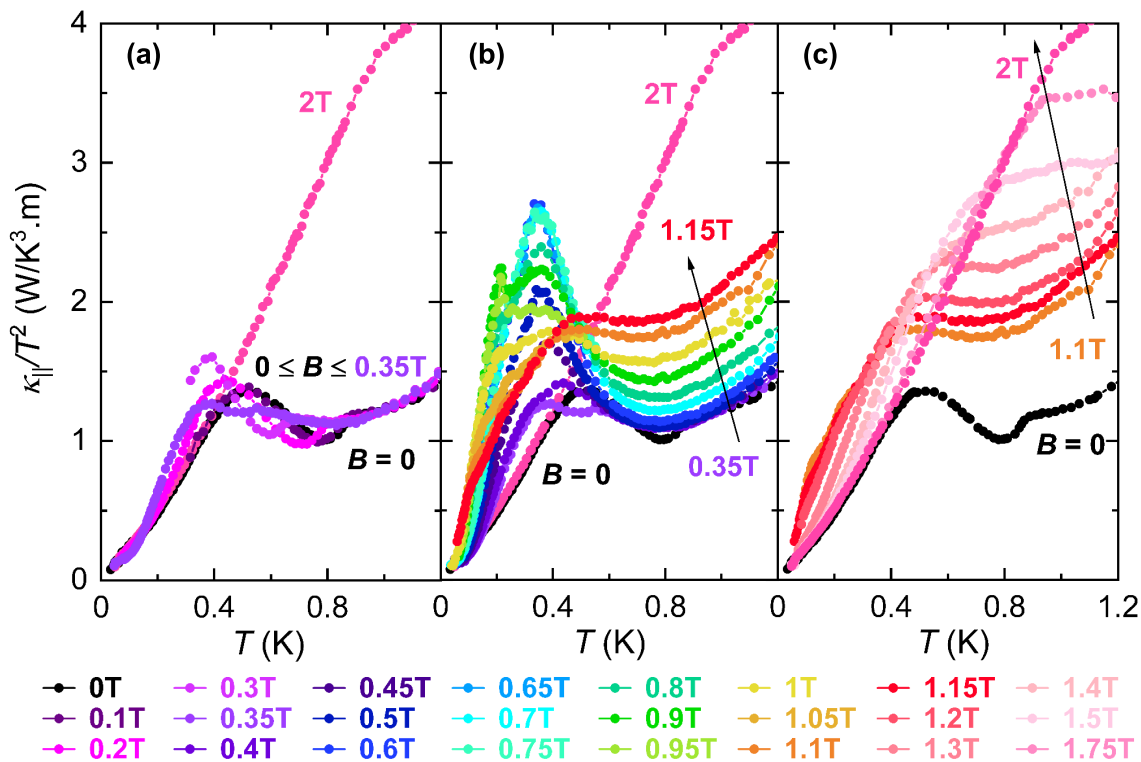
Figure 6.14: $\kappa_{\parallel}/T^2$ versus T for **(a)** regime 1, **(b)** regime 2, and **(c)** regime 3. The same y-axis scaling is used in all plots, and some curves are shown repeatedly to simplify comparison. The colour code is included at the bottom.

each with the zero-B and 2 T curves for comparison purposes. Figures 6.15 **(a)**-**(c)** display selected curves between 0 - 0.4 T, 0.7 - 1 T and 1 - 1.3 T, respectively, shifted subsequently per increasing B for each panel to improve the visual clarity of every single one. The Néel temperatures determined from specific heat in [66, 74, 79] are marked by arrows. The $B = 1$ T curve is included in Figures 6.15 **(b)**-**(c)** to help the reader follow the sequence and trend between the panels. Aiming for improved visual clarity and better identification of the emerging features around the transition, I study Figure 6.14 in parallel with Figure 6.15 in the following. The phase transitions are discussed further in Section 6.8.

   Figure 6.14 **(a)** shows the results for B ranging from 0 to 0.35 T corresponding to regime 1 of the phase diagram. The general behaviour of $\kappa_{\parallel}(T)$ in B up to 0.35 T is similar to zero B. The 3-D AFM ordering T, however, is gradually suppressed with increasing B in this region. That is reflected in the thermal conductivity curves as well: The anomaly at T_N shifts to lower T with increasing B as expected from the lowering of T_N. This trend of the transition feature is better visualised in Figure 6.15 **(a)**. The absolute values of $\kappa_{\parallel}$ above T_N are almost B-independent in this regime. Below T_N, $\kappa_{\parallel}(T)/T^2$ is enhanced with increasing B as the maximum observed in this T region shifts to lower T. At the lowest investigated T, $\kappa_{\parallel}(T)$ curves for $B < 0.3$ T fall again on top of each other. Figure 6.14 **(b)** demonstrates the results for $0.35 \leq B \leq 1.2$ T as the full B range of regime 2 of the phase diagram. Within regime 2 with an IC GS, a huge enhancement of $\kappa_{\parallel}$ is observed both above and below ordering T compared to the zero-B and 2 T data. Figure 6.14 **(b)** for regime 2 is expanded in Figure 6.16 and described carefully in the next paragraphs. Figure 6.14
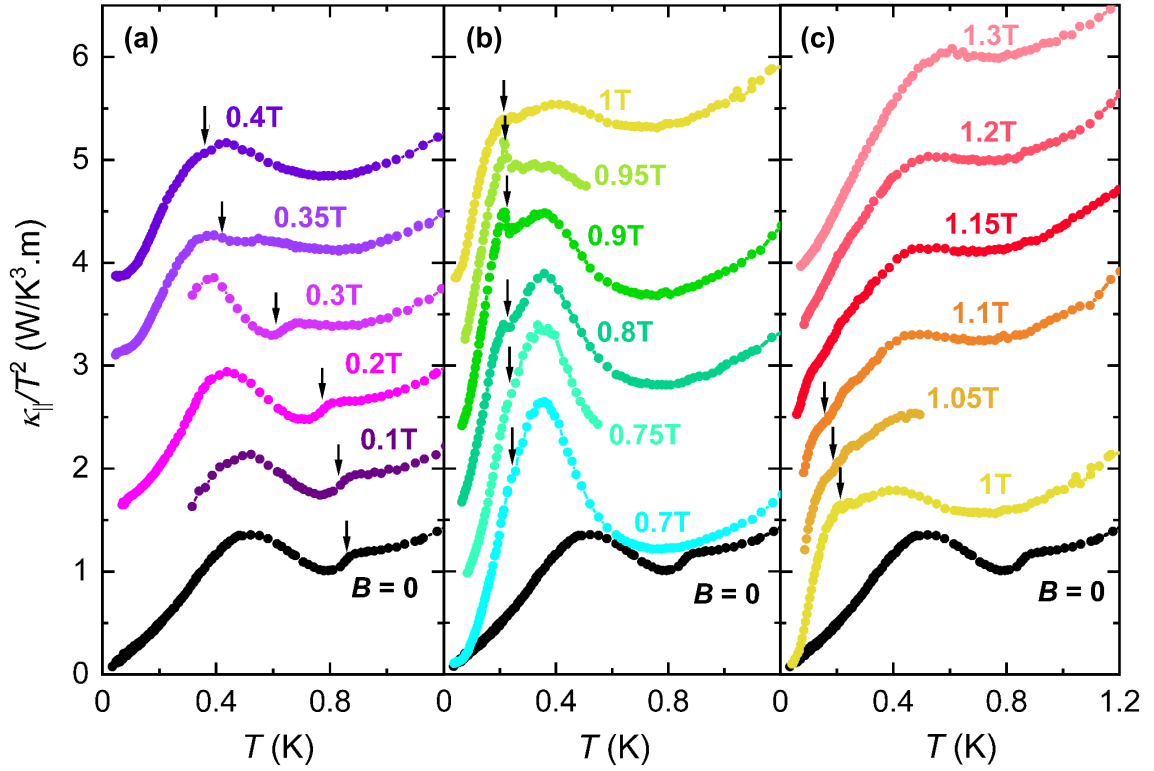
Figure 6.15: $\kappa_\parallel/T^2$ versus T for selected B in **(a)** regime 1, **(b)** regime 2-II, and **(c)** regime 2-III. To better identify the emerging features, the curves are subsequently shifted by $0.5\,\mathrm{W\,K^{-3}\,m^{-1}}$. The arrows denote T_N extracted from the specific heat results [66, 74, 79]. The $B = 1\,\mathrm{T}$ curve is added to regime 2-III as well to help the reader follow the sequence and trend between the panels. More discussion in the main text.

(c) presents the third regime, above $1.2\,\mathrm{T}$, where the FP state is expected. As can be seen, the higher B, the closer $\kappa_\parallel(T)$ to the $0\,\mathrm{T}$ curve at low T. As discussed in Section 6.5, pure phononic behaviour of κ is expected in the FP state. However, due to the Zeeman effect, the thermal population of excited magnetic states may influence heat transport. That appears as the flattening of the $\kappa_\parallel(T)/T^2$ curve at high T, similar to $2\,\mathrm{T}$ or $4\,\mathrm{T}$ shown in Figure 6.8.

Figure 6.16 shows the curves of Figure 6.14 **(b)** split into three regimes of 2-I (0.35 - $0.6\,\mathrm{T}$), 2-II (0.6 - $0.8\,\mathrm{T}$), and 2-III (0.8 - $1.2\,\mathrm{T}$), as defined in Section 3.5. Note the same y-axis scaling in all the plots. Besides, the curves measured at $B = 0$, $0.6\,\mathrm{T}$, $0.8\,\mathrm{T}$ and $2\,\mathrm{T}$ are included in different panels, facilitating comparison and following the trends between them. As observable in Figure 6.16 **(a)**, within the region predicted to exhibit a spin-density wave (SDW) GS at low T, increasing B brings about a significant increase above and below T_N, being largest at around 0.6 - $0.75\,\mathrm{T}$. Despite the huge increase at low T, a B-independent behaviour at higher T above $0.5\,\mathrm{K}$ is present, similar to regime 1 in Figure 6.14 **(a)** and the $0\,\mathrm{T}$ curve with dominating magnetoelastic scattering effects. That means $\kappa_\parallel(T)$ behaviour within the TLL phase below $\sim 0.6\,\mathrm{T}$ is almost B-independent. Figure 6.16 **(b)** shows the curves with theoretically-expected transverse AFM (TAF) GS in which the $\kappa_\parallel$ values decrease slightly compared to the largest values reached around 0.6 - $0.75\,\mathrm{T}$; nevertheless, it stays well above the $0\,\mathrm{T}$ and $2\,\mathrm{T}$ curves below $0.5\,\mathrm{K}$. Above the transition T, the thermal conduction starts to increase in contrast to the observed B-independent manner
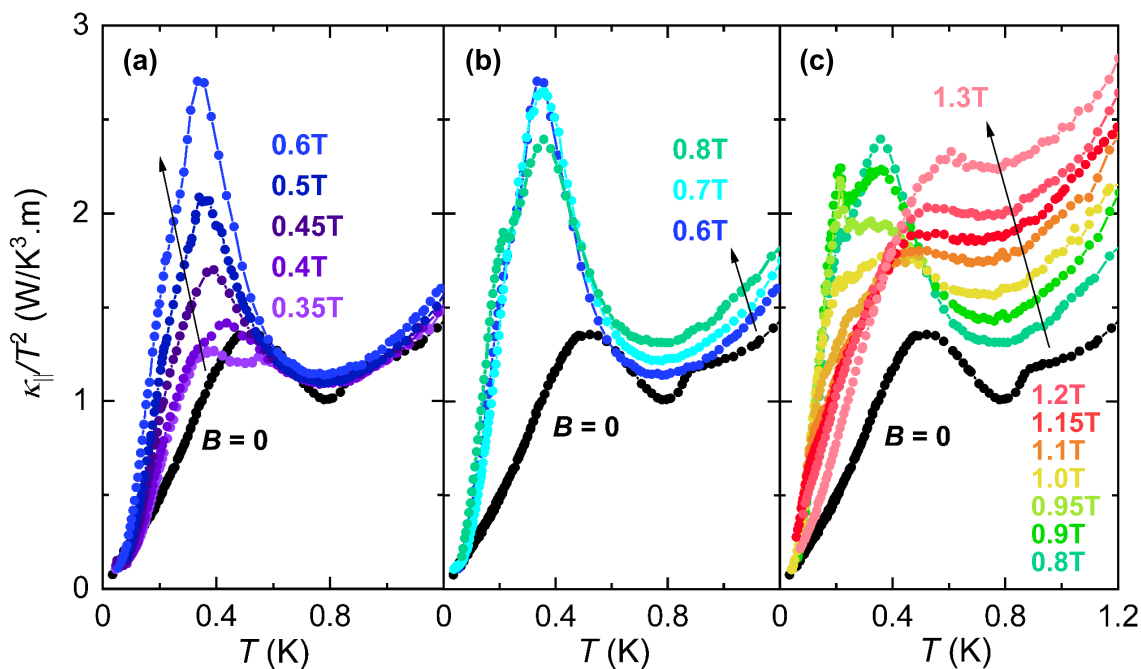
Figure 6.16: $\kappa_\parallel/T^2$ versus T for B within regime 2, separated in **(a)** 0.35 - 0.6 T (regime 2-I), **(b)** 0.6 - 0.8 T (regime 2-II), and **(c)** 0.8 - 1.2 T (regime 2-III). For comparison, curves measured at $B = 0$ and 1.3 T are added, and the same y-axis scaling is used in all the plots.

in the TLL phase in the same T range but lower B. That is close to the expected quantum critical (QC) region (see Chapter 3). The last panel, Figure 6.16 **(c)**, shows regime 2-III covering the QC region around 1.15 T. Though $\kappa_\parallel(T)$ keeps growing by increasing B at high T, it reduces at lowest T such that for $B > 1.3$ T reproduces the 0 T curve at very-low T.

To get information about the relevance of magnetic scattering, $\kappa_\perp(T)$ was studied in different magnetic fields as well. $\kappa_\perp$ is expected to contain no magnetic contribution from the spin chains but may be influenced by magnon-phonon scattering. Figure 6.17 **(a)** shows $\kappa_\perp(T)$ results in different B. All the curves are below or on top of the 2 T curve; thus, one may assume $\kappa_{\mathrm{ph}} = \kappa(2\,\mathrm{T})$, i.e., no extra contribution along the spin chains is visible or might only be hidden by scattering. That is discussed in detail in Chapter 7 Section 7.2. Figure 6.17 **(b)** offsets the curves at different B are offset by $+0.025\,\mathrm{W\,K^{-3}\,m^{-1}}$ relatively for visual help. Evidently, the drop close to the 3-D AFM Néel ordering is detectable and lasts by increasing B up to 0.4 T; however, the B dependence in the $\kappa_\perp(T)$ curves is much weaker than in the $\kappa_\parallel(T)$. Once increasing B further to the transitions of the TLL to the IC-AFM phase, no anomalies are visible anymore. All the curves show a downturn below 0.4 K and gather at T below $\sim$0.15 K. The inset of Figure 6.17 **(a)** focuses on T between 0.1 - 0.2 K. The 0.9 T and 1.1 T curves show reduced κ values due to additional scattering compared to the other B, which is also observed in the B sweeps, as discussed in the following subsection.

Following the lattice transport anisotropy discussed in Section 6.6, I close this subsection by exploring $\kappa_\parallel/\kappa_\perp(T)$ behaviour in B. These observations are anticipated: (i) similar behaviour to zero B for curves with 3-D AFM GS and to the 2 T curve in the FP state with the hump around the Schottky anomaly moving to higher T once increasing B. $\kappa_\parallel/\kappa_\perp(T)$ in $B = 0$ and 2 T was widely discussed in Section 6.6.
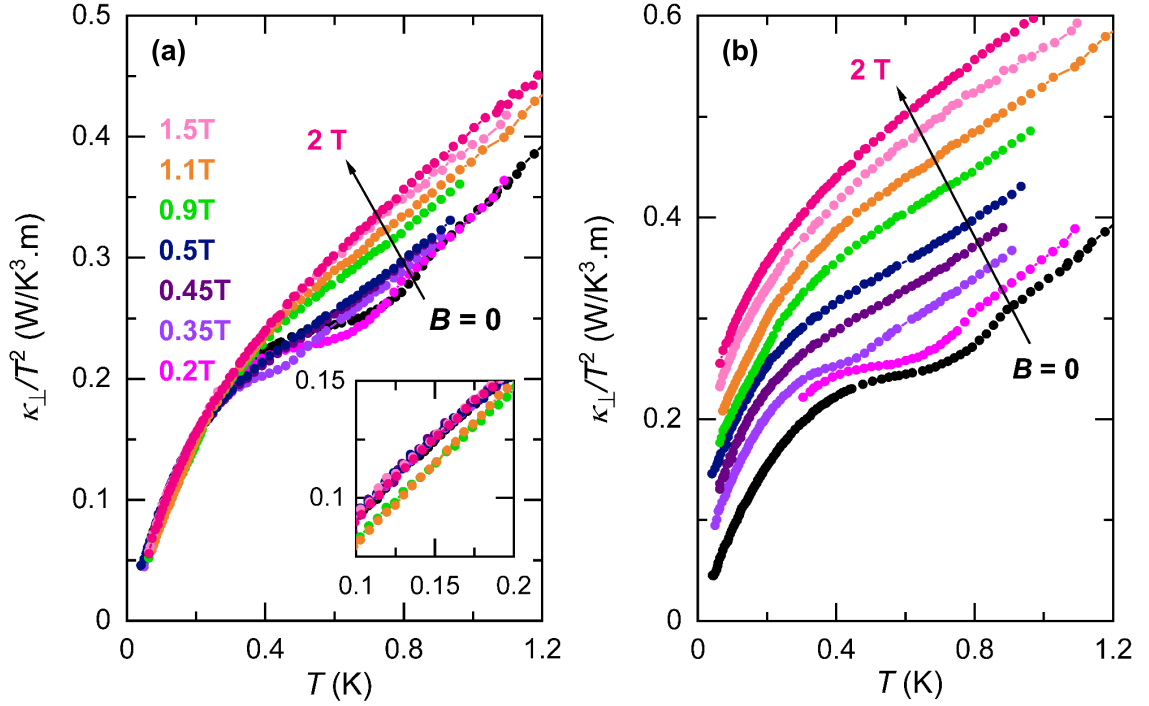
Figure 6.17: $\kappa_\perp/T^2$ versus T, **(a)** absolute values and **(b)** curves shifted subsequently by 0.025 W K^{-3} m^{-1} with increasing B. The inset focuses on T between 0.1 - 0.2 K, where the 0.9 T and 1.1 T curves show extra scattering compared to the others.

(ii) Weak B dependency of $\kappa(T > 0.5\,\mathrm{K})$ in $B < 0.6\,\mathrm{T}$ with 3-D AFM and SDW GS should also be detectable in $\kappa_\parallel/\kappa_\perp(T)$. Moreover, a considerable increase of the transport anisotropy within regime 2 with the IC GS, particularly below 0.5 K, is anticipated from the substantial growth of $\kappa_\parallel(T)$ (see Figure 6.16). $\kappa(T > 0.5\,\mathrm{K})$ begin rising in $B > 0.6\,\mathrm{T}$.

(iii) Extra scattering of $\kappa_\perp(T)$ observed in 0.9 T and 1.1 T curves compared to zero B below $\sim 200\,\mathrm{mK}$ should bring about an auxiliary rise in the transport anisotropy in this T range.

(iv) $\kappa_\parallel/\kappa_\perp(T)$ approach to 2.5 at zero limits of T.

Figure 6.18 displays $\kappa_\parallel/\kappa_\perp$ versus T in different B. In the available $B \leq 0.5\,\mathrm{T}$ curves (see Figure 6.18 **(a)**-**(b)**), namely states with 3D-AFM and SDW GS, $\kappa_\parallel/\kappa_\perp(T)$ lies almost on the zero-B curve between 0.5 - 1 K as expected in item (ii) above. $\kappa_\parallel/\kappa_\perp$ increases per decreasing T due to the extra magnetic heat transport along the spin chains. The additional magnetic contribution to the phononic one is predictable to vanish at low enough T that only the pure lattice conductivity survives, recovering an anisotropy of $\kappa_\parallel/\kappa_\perp = 2.5$ at low T. For the curves between 0.35 - 0.5 T, $\kappa_\parallel/\kappa_\perp(T)$ goes below the zero-T limit of 2.5 within a T range below 0.15 K. This effect was detectable before in the T-sweep data, e.g., in Figure 6.14, the 0.35 T curve goes lower than the zero-B one below 200 mK and sits on the zero-B curve only at the lowest T. Besides the T sweeps, that is also seen in the B sweeps in the shape of a drop once increasing B at the phase transition from the 3-D AFM state to the IC AFM one. The B-sweep results are provided later in this section. The decrease reflects additional scattering and/or a reduction of the magnetic excitations, affecting κ along the spin chains more than the perpendicular one. Recovery to the ordered state of the zero-B curve is expected at low T and already observable in the 0.35 T and 0.45 T curves measured down to around 50 mK.
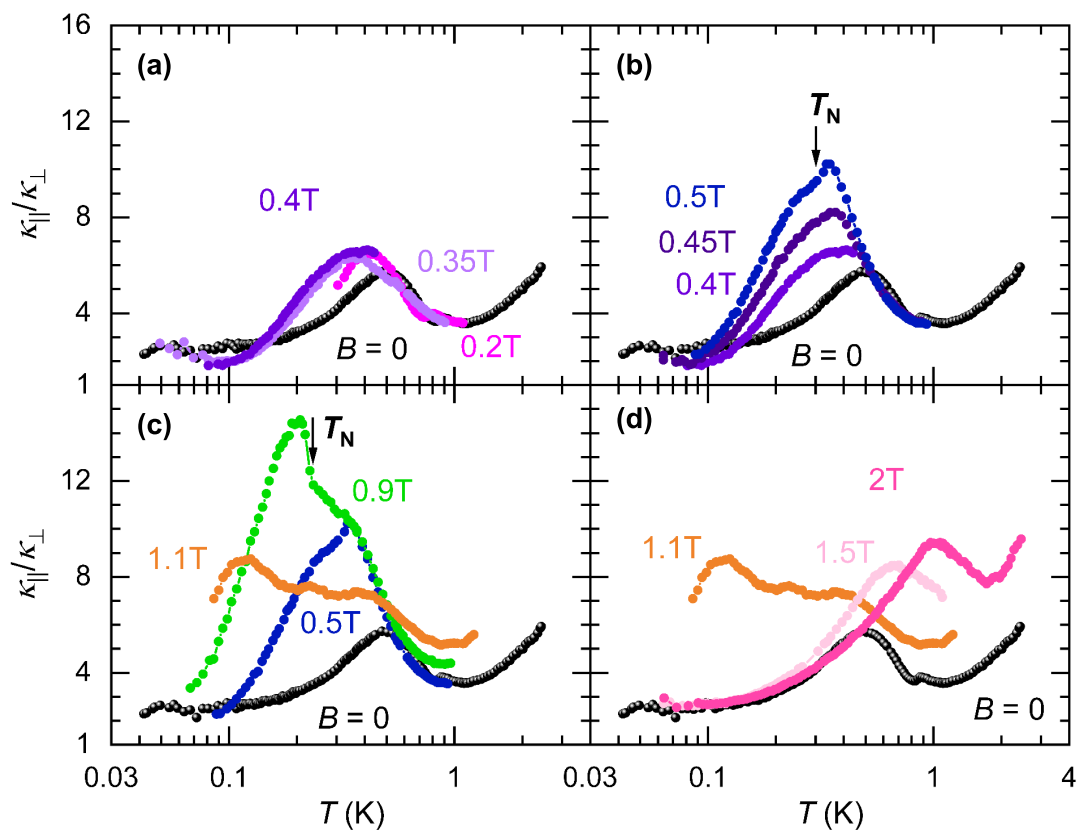
Figure 6.18: Thermal transport anisotropy $\kappa_\parallel/\kappa_\perp$ versus T in different B. The anomalies at the phase transitions (arrows labelled with T_N) are more pronounced in $\kappa_\parallel/\kappa_\perp(T)$ than in $\kappa_\parallel(T)/T^2$ plotted in Figure 6.15.

Figure 6.18 **(c)** displays the T dependency of the thermal-transport anisotropy in 0.9 T and 1.1 T with the theoretically expected TAF GS. The 0 T and 0.5 T curves are included for comparison purposes. From the highest measured $T{\sim}1$ K, $\kappa_\parallel/\kappa_\perp(T)$ curve in 0.9 T and 1.1 T sit above the zero-B, in line with the behaviour observed before that $\kappa_\parallel(T)$ in $B > 0.6$ T starts rising above 0.5 K (item (ii) explained above). The highest thermal transport anisotropy of $\kappa_\parallel/\kappa_\perp{\sim}15$ is measured in $B = 0.9$ T around 0.1 - 0.2 K below the transition T from the TLL phase to the IC AFM state. That is a result of a huge extra contribution along the spin chains plus the accompanying extra scattering perpendicularly. In the 0.5 T and 0.9 T curves in Figure 6.18 **(b)-(c)**, arrows labelled with T_N point to the phase transition T from the specific heat results in [74]. The anomaly at the phase transition of the 0.5 T curve is more pronounced in the transport anisotropy than in $\kappa_\parallel(T)/T^2$, in which the phase transition appeared as a tiny shoulder (cf. Figure 6.16 **(a)**). The 1.1 T curve shows $\kappa_\parallel/\kappa_\perp \simeq 7$ with a weak T dependency down to ${\sim}0.1$ K, below which the curve shows a downturn. Though $\kappa_\parallel/\kappa_\perp(T)$ in 1.1 T is available only down to ${\sim}80$ mK, the drop in the $\kappa_\parallel/\kappa_\perp$ value is believed to appear to approach the phononic transport anisotropy of 2.5 close to zero T.

In the last panel, Figure 6.18 **(d)**, the 1.5 T and 2 T curves in the FP GS lie on the zero-B curve at the lowest T. The curves separate from the zero-B curve by increasing T and reach a local maximum of ${\sim}10$. The higher B, the higher T at which deviations from the zero-B curve and the local maximum appear, as in item (iii) above.

6.7.2 Field sweeps

Seeking for the emerging anomalies and features, B-sweep measurements were performed at various T between 0.1 - 0.65 K. κ in B at higher T are interpolated from the T sweeps.

Correction of absolute values: Figure 6.19 and Figure 6.20 show an overview of the $\kappa(B)$ results. Full symbols are the initial data points ($\kappa^{\mathrm{i}}(B)$) obtained using a B-independent calibration curve. The average T_{mid} of each $\kappa^{\mathrm{i}}(B)$ curve is noted in the same colour in each panel. $\kappa(T = T_{\mathrm{avg}})$ determined from T sweeps at constant B are shown in cyan or purple full circles. General behaviours of the $\kappa^{\mathrm{i}}(B)$ curves are in agreement with $\kappa(T)$; however, the absolute values of $\kappa^{\mathrm{i}}(B)$ are different due to systematic errors from using the zero-B calibrations. Hence, a correction procedure based on the $\kappa(T)$ curves was applied to each of the $\kappa^{\mathrm{i}}(B)$ curves (see Chapter 5 Section 5.6.2). The empty circles are the corrected kappa (κ^{c}) values, assuming a fixed T of the sample equal to the average T_{mid} over the B sweep.

Starting from the data along the spin chains, the $\kappa_{\parallel}(B)$ curves have essentially similar behaviour as the cyan circles, $\kappa^{\mathrm{c}}(B)$, being the interpolation of the in-B $\kappa_{\parallel}(T)$ results at the corresponding T_{avg}. Though the step-like feature below 0.26 K at $\sim$0.32 T is not reproduced by interpolating the $\kappa_{\parallel}(T)$ curves, it is believed to be resolvable by reducing the B steps between the T sweeps. In addition to pronouncing the features, correcting the directly measured $\kappa_{\parallel}^{\mathrm{i}}(B)$ curves has added a kink at 0.75 T, e.g., at 518 mK, not visible in the initial curves. Since the $\kappa_{\parallel}(T)$ curve at 0.75 T behaved smoothly, that is not ignored in correction. $\kappa_{\perp}(B)$ is illustrated in Figure 6.20 for various T. The overall behaviour and the features in the B sweeps shown in Figures 6.20 **(a)-(b)** are reproduced by the interpolation of $\kappa(T)$ curves at given T (purple points). As it is observable in Figures 6.20 **(c)-(e)**, two features emerge in $\kappa^{\mathrm{i}}(B)$ below 225 mK: (i) A relatively shallow well around 0.7 - 1.2 T, and (ii) a drop around 0.45 T, which gets increasingly sharper and deeper per cooling, e.g., a drop of $\sim$40 % in the 124 mK curve. While the former was already visible in $\kappa_{\perp}(T)$ curves (see the inset of Figure 6.17 **(a)**), the latter was never reproduced via spanning T at fixed B. Furthermore, hysteresis effects can be ruled out since setting B either via a sweep-up or -down made no anomaly or drop in $\kappa_{\perp}(T)$ curves around 0.45 - 0.5 T. Accordingly, this drop is crossed in Figure 6.20 **(c)-(e)** and ignored in the $\kappa_{\perp}^{\mathrm{c}}(B)$ curves.

Hereafter, I study the anomalies from the initial $\kappa^{\mathrm{i}}(B)$ curves and the absolute values from $\kappa^{\mathrm{c}}(B)$. That means additional features due to the interpolation procedure are ignored.

V-shaped anomaly and flatlands: Starting from the lowest T, Figure 6.21 **(a)** plots relative changes in thermal conductivity in B compared to the zero-B value, $\Delta\kappa_{\parallel}/\kappa_0$, defined as

$$\Delta\kappa_{\parallel(\perp)}/\kappa_0 = \frac{\kappa_{\parallel(\perp)}(B) - \kappa_{\parallel(\perp)}(B=0)}{\kappa_{\parallel(\perp)}(B=0)}, \tag{6.13}$$

and calculated from the corrected κ^{c} values at 127 mK as a representative. My goal here is to compare the B evaluation of thermal conductivity and magnetisation at the lowest T, which shows a great correlation between $\Delta\kappa_{\parallel}/\kappa_0$ and the magnetic susceptibility, indicating that the anomalous $\kappa_{\parallel}(B)$ is of magnetic origin. The absolute changes in the $\kappa^{\mathrm{c}}(B)$ values are described later in paragraph § **Relative changes** along with the curves at other T. Figure 6.21 **(b)** shows the normalised magnetisation M/M_{s} measured at 95 mK by Wu *et al.* [74] on the same x-axis scale as panel **(a)**. M_{s} is the saturation moment for B along the a-axis. The red curve plots the corresponding magnetic susceptibility $\mathrm{d}M/\mathrm{d}B$. The vertical dashed line at the lowest B is the characteristic field $B_{\mathrm{c}} = 0.35$ T, around which a phase transition from 3D-AFM to SDW occurs. The horizontal dashed lines indicate the
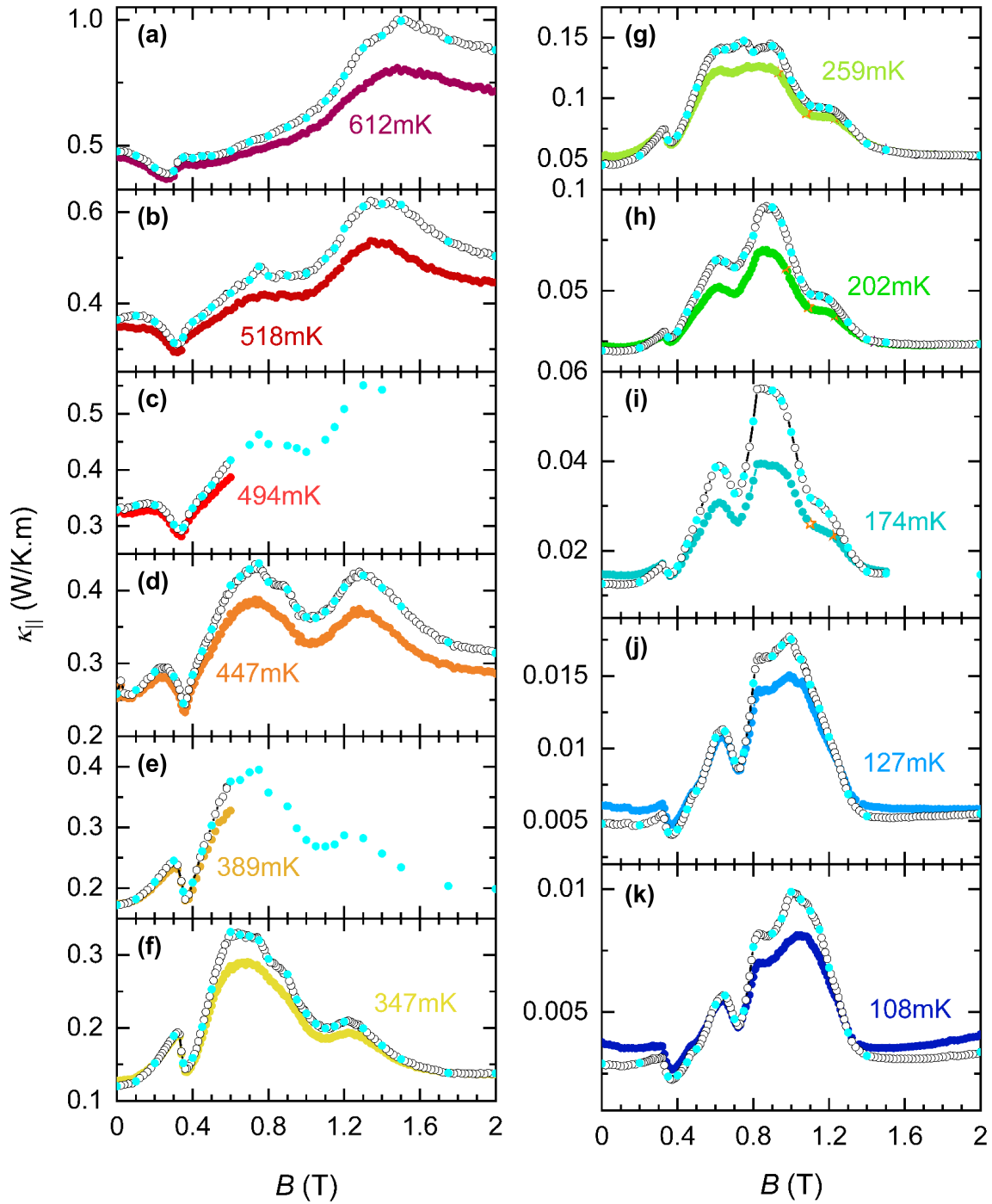
Figure 6.19: Initial and corrected $\kappa_\parallel(B)$ curves. The colourful curves are obtained from direct measuring of $\kappa_\parallel(B)$, labelled as $\kappa_\parallel^i(B)$ in this text. The cyan circles are read from the $\kappa_\parallel(T)$ curves. The empty circles indicate corrected $\kappa_\parallel(B)$ of given average T, thus named $\kappa_\parallel^c(B)$.
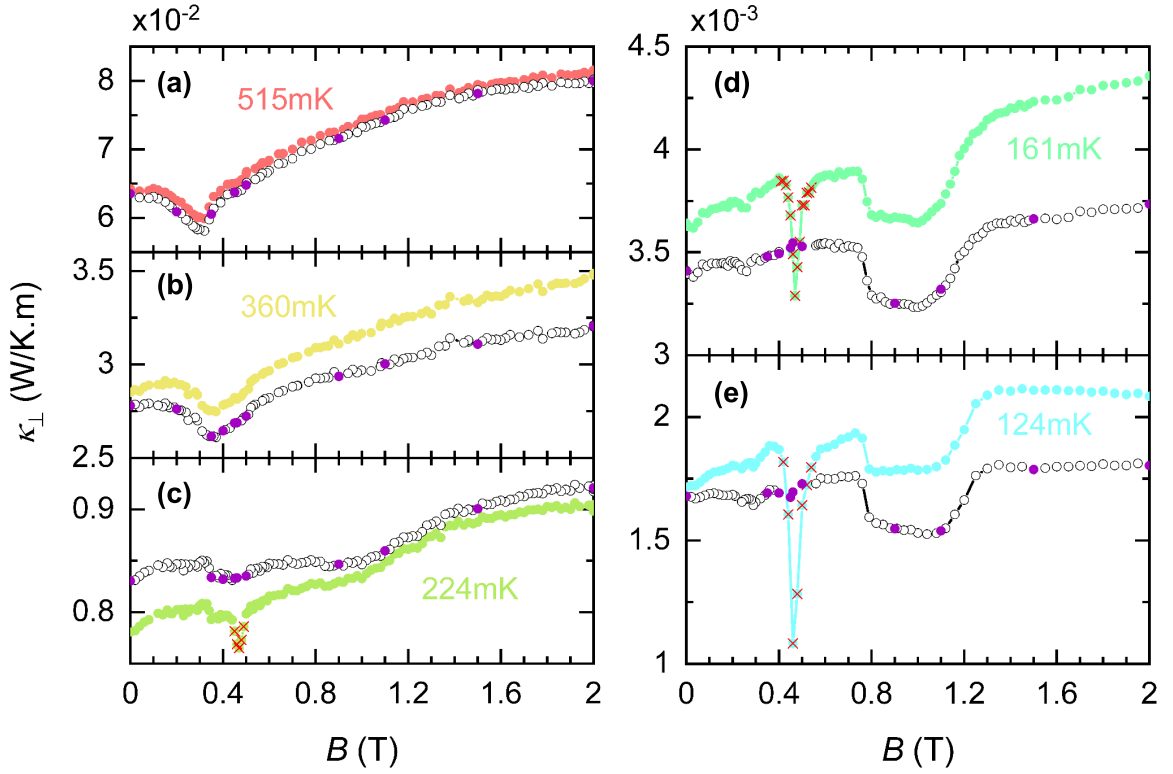
Figure 6.20: Initial and corrected $\kappa_\perp(T)$ curves. The purple circles are interpolated from the $\kappa_\perp(T)$ curves. The curves with colourful and empty circles display respectively initially and corrected $\kappa_\perp(B)$ at given T, namely $\kappa_\perp^i(B)$ and $\kappa_\perp^c(B)$. The deep drop emerging at ~ 0.45 T was not reproducible in T sweeps thus ignored completely.

positions of $M = M_s/3$ and $M_s/5$, around which two new features emerge in $\kappa_\parallel(B)$ (panel **(a)**): (i) a *V-shaped* feature around ~ 0.6 - 0.8 T. The only available experimental feature in this region was a tiny plateau in $M(B)$, around $M_s/3$. The two vertical dashed lines extended between panels **(a)** and **(b)** at mid-B depict the width of this plateau in $M(B)$. Therefore, the pronounced V-shaped feature is the first firm experimental consolidation of the magnetisation plateau at $M_s/3$ and a clear confirmation that the plateau in $M(B)$ is an intrinsic feature. The drop observed in the V-shaped anomaly in $\kappa_\parallel(B)$ is a result of a spin gap of ~ 120 mK (0.01 meV) opening, which is too small to be determined from the INS measurements but is detectable in thermal transport. Considering this V-shaped anomaly observed in thermal conductivity, one should double-check the B evaluation of the energy-dependent INS spectrum in Figure 3.3 **(d)**, where a regime with high intensity below 0.2 meV around 0.75 T was present, though never discussed in the previous works.

The next astonishing result of this work is (ii) the new feature observed as a plateau in $\kappa_\parallel(B)$ at ~ 0.5 T. Taking the positive slope of $\kappa_\parallel(B)$ on which the anomaly sits into account, this plateau around ~ 0.5 T can also be a V-shaped feature similar to the one around 0.7 T. This anomaly appears at the field where $M = M_s/5$ and no previous reports on this compound had revealed any feature. However, a more careful look at dM/dB shows a tiny dip in the same B, corresponding to a local change of slope in $M(B)$ around 0.5 T and a rudimentary plateau in $M(B)$. Consequently, two magnetisation plateaus at $M = M_s/3$ and $M_s/5$ are detected in the $S = 1/2$ Heisenberg spin chain material YbAlO$_3$ via the thermal-conductivity
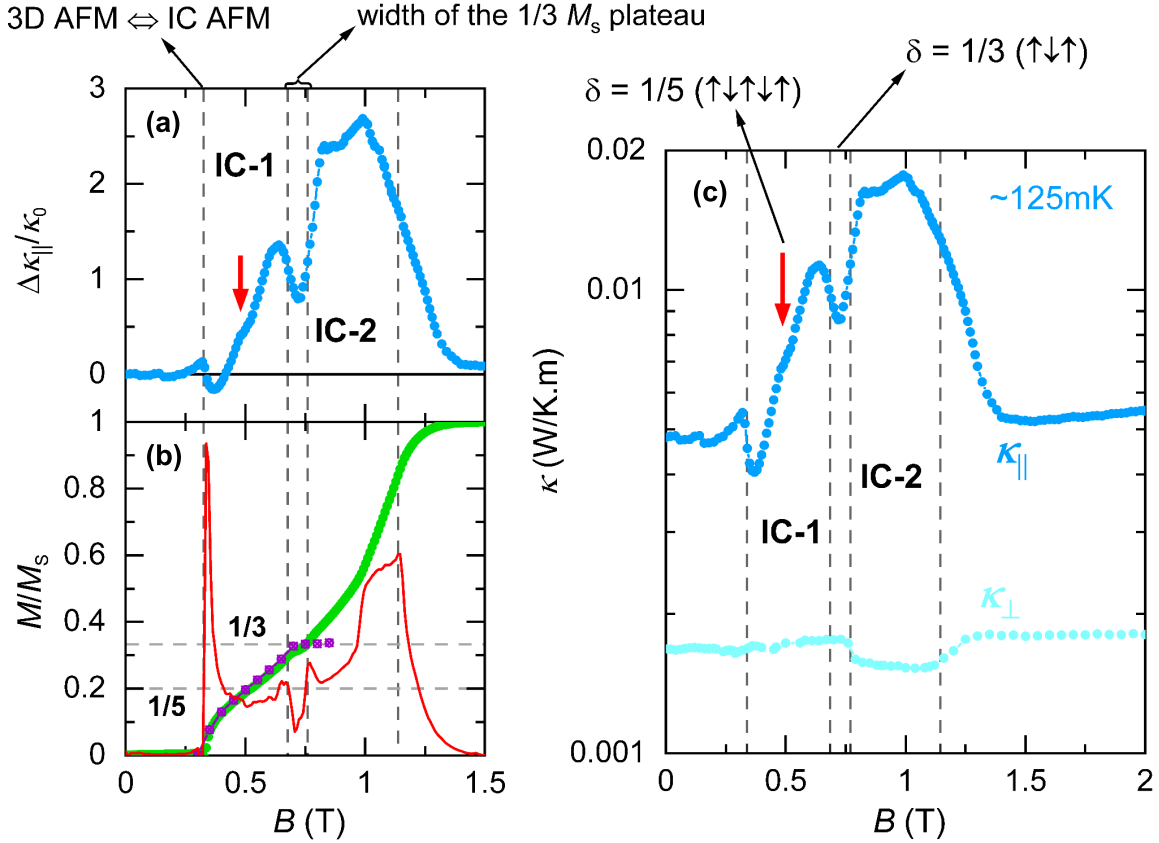
Figure 6.21: New features in B sweeps below $0.2\,$K. **(a)** $\Delta\kappa_\parallel/\kappa_0$ at $127\,$mK between 0 - $1.5\,$T. A plateau (pointed with a red arrow) arises in $\kappa_\parallel$ at $\sim 0.5\,$T. By increasing B, a *V-shaped* anomaly is observed starting at $\sim 0.64\,$T and ending at $\sim 0.82\,$T, which reaches a local minimum at $0.72\,$T. **(b)** $M(B)$ reveals two plateaus at the same B as the as-describes features. The ordering wave vectors $\boldsymbol{q} = (001\pm\delta)$ have $\delta = 1/5$ and $1/3$, respectively. The red line and purple markers indicate $\mathrm{d}M/\mathrm{d}B$ and $\delta(B)$, respectively. **(c)** An excessive scattering in observed in $\kappa_\perp$ within IC-2.

measurements at very-low T in this work. The article including theoretical modelling of these anomalies is in preparation [3] in collaboration with *Oleg Starykh* from the *University of Utah*. It is noteworthy that the experimental observation of these features was later confirmed by magnetostriction measurements [223].

Figure 6.21 **(c)** illustrates the $\kappa_\parallel^c(B)$ and $\kappa_\perp^c(B)$ curves at $127\,$mK and $124\,$mK, thus $\sim 125\,$mK. In comparison, κ along the spin chains is distinctly higher than for the perpendicular direction. Note that the y-axis is on a logarithmic scale. The plateau anomaly in $\kappa_\parallel(B)$ at $\sim 0.5\,$T is marked with a red arrow. Considering the ordering wave vector $\boldsymbol{q} = (001\pm\delta)$, the shift of the IC wave vector is directly proportional to the B-induced magnetisation, i.e., $\delta \sim 2\pi M/M_\mathrm{s}$ [74], see also panel **(b)**. Thus, the V-shaped feature around 0.6 - $0.8\,$T and the plateau anomaly in $\kappa_\parallel(B)$ at $0.5\,$T occur at $\delta = 1/3(\uparrow\downarrow\uparrow)$ and $1/5(\uparrow\downarrow\uparrow\downarrow\uparrow)$, respectively, as presented in Figure 6.21 **(c)**. Note, no parallel feature emerge in the corrected $\kappa_\perp^i(B)$ curve at $\sim 0.5\,$T. However, an abrupt decrease of $\kappa_\perp(B)$ around this B range was observed in the measured initial curve before correction $\kappa_\parallel^i(B)$ (see Figure 6.20 **(e)**). Since the abrupt decrease was not reproduced via the T sweeps, it was cut during the correction procedure
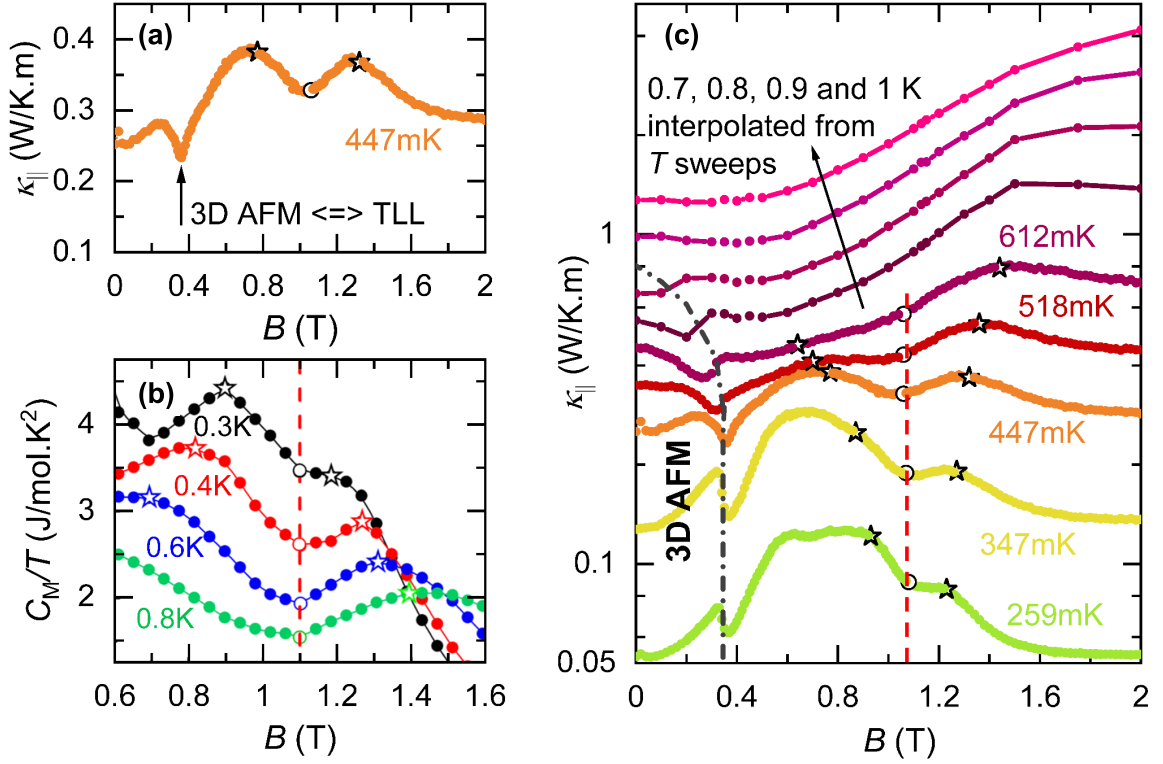
Figure 6.22: $\kappa_{\parallel}(B)$ at $T \geq 0.25\,\mathrm{K}$. **(a)** Exemplary curve of $\kappa_{\parallel}^{i}(B)$ at 447 mK. As discussed in the text, two consequent huge humps are observed, and indicated by empty starts here. An empty circle is used to point the crossover between the two humps. **(b)** Similar behaviour of the *double humps* is reported in the specific heat of YbAlO₃ [74]. **(c)** More $\kappa_{\parallel}^{i}(B)$ curves with $T \geq 0.25\,\mathrm{K}$ including as-explained features in panel **(a)**. The double humps are not visible for curves with $T \geq 0.7\,\mathrm{K}$.

of the $\kappa_{\perp}(B)$ curves. It may not be excluded that the appearance of the sharp drop in $\kappa_{\perp}(B)$ is induced by the anomaly at 0.5 T, e.g., via a change in the thermal coupling of the thermometers. Such an effect would not be visible in $\kappa(T)$ thanks to the *in-situ* calibration.

Regarding the anomaly at ∼0.7 T: A phase transition from SDW as *IC-1* to TAF phase as *IC-2* is predicted theoretically within the IC AFM state [77, 78] described in Section 3.5. Even though $\kappa_{\perp}$ behaves practically B independently below ∼0.75 T, an auxiliary scattering is observed in the IC-2 phase, which is a sign that the scattering mechanisms in the IC-1 and IC-2 states are not identical. Notably, the plateau regions appear within the SDW phase [224], and the TAF state is considered to start at B above the plateau region around 0.7 T.

As the last point, the vertical dashed line at the highest B is the saturation field $B_{\mathrm{s}} = 1.13\,\mathrm{T}$, defined by Wu *et al.* from the peak position of $\mathrm{d}M/\mathrm{d}B$ [74]. $\kappa_{\parallel}(B)$ at the as-defined B_{s} is around 3 times larger than the zero B and still enhanced till 1.3 T, above which the curve settles back to $\kappa_{\parallel}(B=0) = \kappa_{\parallel}(2\,\mathrm{T})$ and is supposed to be purely phononic in this T range. B_{s} in $\kappa_{\perp}(B)$ corresponds to the field where the curve turns toward the zero-B values. The saturation of $\kappa(B)$ ascribed to polarisation is discussed in Chapter 7 Section 7.3.

Double-hump anomaly: Figure 6.22 shows $\kappa_{\parallel}^{i}(B)$ above 0.25 K. Figure 6.22 **(a)** shows the $\kappa_{\parallel}^{i}(B)$ curve at 447 mK as an example. Starting from zero and increasing B, an anomaly

corresponding to the 3-D AFM to TLL phase transition is observed below 0.4 T. At higher B, a giant enhancement of $\kappa_\parallel(B)$ is observable in agreement with what is observed in $\kappa_\parallel(T)$, suggesting a huge contribution of magnetic excitations in heat transport. By increasing B further, $\kappa_\parallel(B)$ decreases with a local minimum around the saturation B followed by a second hump. This behaviour is akin to the reported behaviour in magnetic specific heat $C_M(B)$ [74], around the same T and B range: Figure 6.22 **(b)** zooms in C_M/T curves above Néel ordering B. The empty stars and empty circles correspond to the positions of the peaks and the local minima in $C_M(B)$, respectively. The first enhancement at lower B can be the result of the creation of the magnetic excitations and a growth in the density of the carriers, thus observable in both the specific heat (panel **(b)**) and thermal conductivity (panel **(a)**). The latter peak at higher $B > B_s$ was associated with the thermal excitation of the polarised states, namely the *Schottky* anomaly [74]. As it turns out by comparison to panel **(a)**, the hump around the Schottky anomaly (higher B) is detectable in both the specific heat and heat transport. This observation is contrary to the typical expectation that the excitations around the Schottky point are not mobile and thus do not contribute to the thermal transport. Ultimately, the empty circles showing the position of the local minima in $C_M(B)$ appear in the dM/dB curve as maxima before saturation (shown previously in Figure 6.21 **(b)**) and can be treated as a characteristic of the saturation field B_s. The as-described two consequential humps may be called a *double-hump* feature.

Figure 6.22 **(c)** shows the $\kappa_\parallel^i(B)$ curves above 0.25 K. Starting from zero and increasing B, anomalies below 0.4 T match phase transitions from the 3-D AFM phase (separated via a dashed line to low T and low B) to the TLL or IC-AFM phase depending on T: As is evident, the step of the 612 mK curve transforms to a drop for increasing B. This transformation of the transition type by changing T is focused more in Section 6.8. For $B > 0.4$ T, the peaks and bellies of the two-hump features are indicated as the breaking points (sudden change of the slope) of the curves and marked with the stars and balls similarly to the C_M curves in panel **(b)**; However, the form of the double-hump feature appearing in the other curves is not necessarily identical but rather comparable to the one presented in panel **(a)**. As an instance, an upward trend of $\kappa_\parallel(B)$ by increasing B is observed at higher T thanks to eliminating thermal fluctuations of the spins and the corresponding scatterings through B-induced spin polarisation. In this case, the two subsequent humps sit on an increasing background of $\kappa_\parallel(B)$. As the last point, a linear change in the position of the humps in B-T is expected for isolated spin chains [225]. This trend is discussed in detail as an argument for the dimensionality near the quantum critical point in Chapter 7 Section 7.3. By increasing T further, the humps are hardly resolvable in curves interpolated for $T \geq 0.7$ K.

Relative changes: Here, I look at the relative changes of κ^c in B at the transitions and features observed in different T. Figure 6.23 plots the normalised changes of $\kappa(B)$ as defined in Relation 6.13. Arrows follow the order of the curves per increasing T. Figure 6.23 **(a)** shows $\Delta\kappa_\parallel/\kappa_0$ curves for $T < 0.25$ K. At 108 mK, increasing B up to around 0.32 T does not affect κ till the 3-D-to-IC AFM transition, where $\kappa_\parallel$ drops suddenly by about 30 %. $\kappa_\parallel^c(B)$ grows by ∼200 % by increasing B and passing the V-shaped anomaly. This trend is followed by another ∼50 % increase, though moderate, between 0.8 - 1 T. From another perspective, one may characterise the initial increase below 0.32 T as the beginning of the huge hump with a maximum in 1 T, thus as an increasing background with a drop-like feature due to the transition sitting on top and another one around 0.7 T. Increasing B beyond ∼1 T leads to a continuous lowering of $\kappa_\parallel^c(B)$ till it reaches similar values as of $B = 0$ at 1.3 T.

The general behaviour of the curves in panel **(a)** is similar; however, four main differences
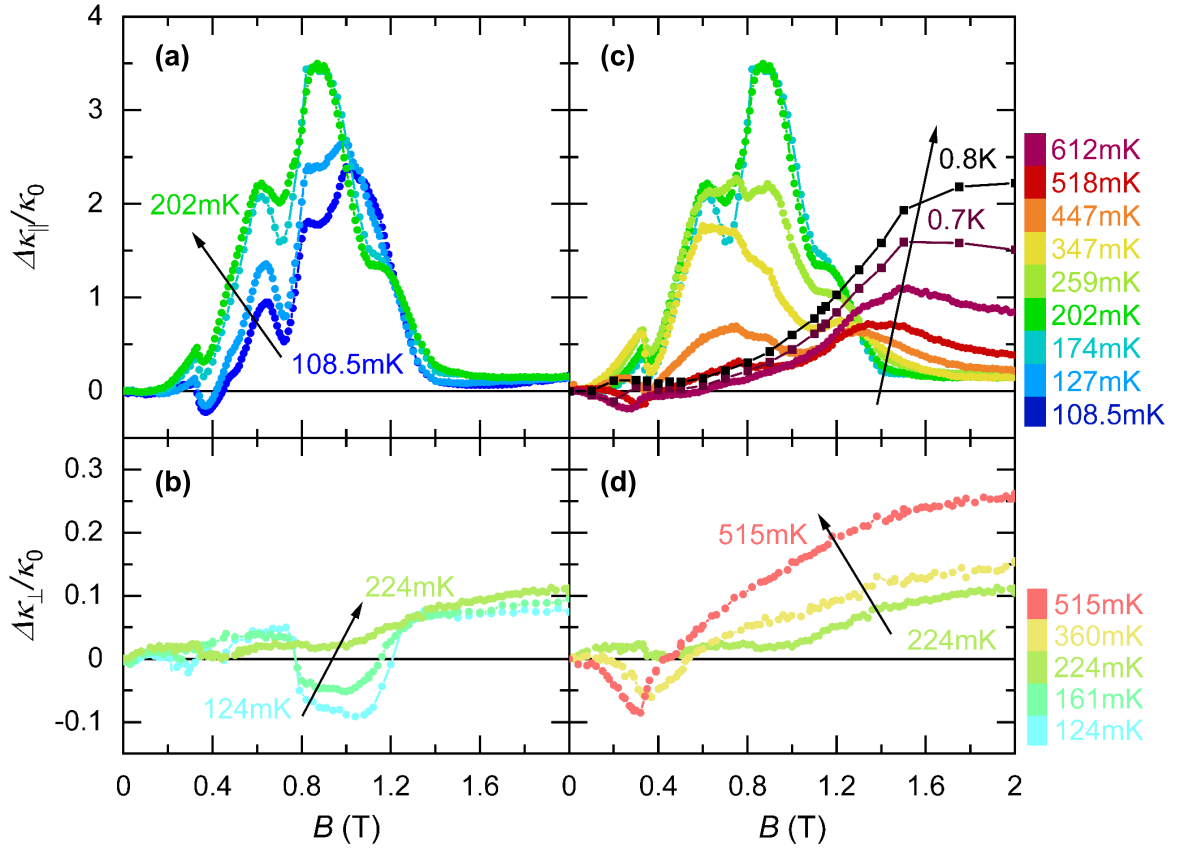
Figure 6.23: Normalised changes of κ in B. **(a)-(b)** $\Delta\kappa/\kappa_0$ curves for T_{av} below 0.25 K **(a)** along and **(b)** perpendicular to the spin chains. One curve is shown in both sub-figures for comparison. **(c)-(d)** $\Delta\kappa_{\parallel(\perp)}/\kappa_0$ curves are shown similar to panels **(a)-(b)** above 0.25 K. The 0.7 K and 0.8 K curves are interpolated from the T sweeps. The arrows indicate the order of the curves per cooling. More arguments is in the text.

exist between the 108 mK and the higher T curves: (i) The gentle behaviour of the $\kappa_{\parallel}^{\text{c}}(B)$ curves before the 3-D to IC-AFM phase transition turns to a great increase reaching up to around 50 % of its initial value in the 174 mK and 202 mK curves. (ii) The plateau in $\kappa_{\parallel}(B)$ around 0.5 T is barely visible above 200 mK, and (iii) the giant growth of $\kappa_{\parallel}$ in the mid-B region, i.e., 0.8 - 1 T, exceeds up to 350 % of its zero-B value. (iv) A new hump appears at 1.2 T in the 174 mK and 202 mK curves, which was not visible at lower T.

Panel **(b)** illustrates $\Delta\kappa_{\perp}/\kappa_0$ for $T < 0.25$ K. By increasing B, $\kappa_{\perp}^{\text{c}}(B)$ drops at $\sim$0.7 T (e.g., $\sim$10 % at 124 mK) to stay almost stable up to 1.1 T within the theoretically predicted TAF state. A further increase in B causes $\kappa_{\perp}^{\text{c}}(B)$ initially to increase step-wise to reach $\sim$20 % above the zero-B value and then can be considered practically independent of B. That is the general behaviour at $T < 0.2$ K; the depth of the drop around 0.7 - 1.1 T, however, decreases per increasing T. This feature fades more or less at 224 mK.

Panel **(c)** plots $\Delta\kappa_{\parallel}/\kappa_0$ curves for $T > 0.25$ K. Starting from zero and increasing B, the curves around 0.2 - 0.35 K with a growth of $\sim$75 % before the 3-D to IC-AFM phase transition show the largest among the measured curves in this region. Furthermore, the yellow curve at 347 mK has the deepest drop before the transition, going almost back to its zero-B value. By increasing T, the feature of the transition from the 3-D AFM to TLL

states appears more gently with a deviation from the zero-B value of the utmost of $25\,\%$. For B above the intermediate fields (0.4 - 1 T), the V-shaped feature exists clearly below $0.25\,\mathrm{K}$ and converts to a single hump at higher T (the $202\,\mathrm{mK}$ curve was described in panel **(a)**): In the case of the $259\,\mathrm{mK}$ curve, $\kappa_\parallel^\mathrm{c}(B)$ has an improvement up to around $225\,\%$ at $0.6\,\mathrm{T}$, similar to the $202\,\mathrm{mK}$ curve. The strong enhancement of $\kappa_\parallel^\mathrm{c}$ of the $202\,\mathrm{mK}$ curve between 0.6 - 0.9 T is suppressed in the $259\,\mathrm{mK}$ curve. That indicates that the V-shaped feature at $0.7\,\mathrm{T}$ is related to the IC AFM state, not the TLL phase. The main feature in the $\kappa_\parallel(B)$ curves for $T \geq 0.25\,\mathrm{K}$ is the double-hump anomaly investigated in paragraph § **Double-hump anomaly**. The low-B hump of the double-hump feature is responsible for the giant increase of $\kappa_\parallel^\mathrm{c}$ around $0.4\,\mathrm{T} < B < 1\,\mathrm{T}$, and the hump at $\sim\!1.2\,\mathrm{T}$ in the $174\,\mathrm{mK}$ and $202\,\mathrm{mK}$ curves, which was not visible at lower T, is a continuation of the higher-B hump (see also Figure 6.22). $\Delta\kappa_\parallel/\kappa_0(B)$ at the maximum of the lower hump lowers drastically per increasing T such that it looks almost flattened around $0.61\,\mathrm{K}$. The max of $\Delta\kappa_\parallel/\kappa_0(B)$ at higher B, however, shows initially a slight reduction per increasing T and then increases. Furthermore, an overall enhancement of $\Delta\kappa_\parallel/\kappa_0$ is observed at higher B, such that, e.g., $\kappa_\parallel^\mathrm{c}(B = 2\,\mathrm{T})$ for the $612\,\mathrm{mK}$ curve stays about $100\,\%$ above its zero-B value. Above $0.7\,\mathrm{K}$, the double-hump feature is not resolvable. $\Delta\kappa_\parallel/\kappa_0$ at higher T is shown later in Figure 6.24.

$\Delta\kappa_\perp/\kappa_0$ for $T > 0.25\,\mathrm{K}$ is shown in Figure 6.23 **(d)**, including the $224\,\mathrm{mK}$ curve in common with panel **(b)**. The 3-D-AFM-to-TLL phase transition is observed as a dip in $\kappa_\perp^\mathrm{c}(B)$, followed by a steady increase in the TLL phase at higher B, e.g., at least by $15\,\%$ at $2\,\mathrm{T}$. $\kappa_\perp(B)$ increases uniformly in the perpendicular direction instead of the double humps: The hump observed for $\Delta\kappa_\parallel/\kappa_0$ at lower B is absent in $\Delta\kappa_\perp/\kappa_0$, in line with the assumption that it is due to an extra spinon contribution in $\kappa_\parallel$ which is absent in $\kappa_\perp$. By contrast, the hump in $\Delta\kappa_\perp/\kappa_0$ at higher B, which is presumably due to excitations Zeeman-split levels, is also visible in $\Delta\kappa_\perp/\kappa_0$, although with a much lower magnitude.

Normalised changes of $\kappa_\parallel(B)$ from $0.8\,\mathrm{K}$ up to $1.5\,\mathrm{K}$ (in steps of $0.1\,\mathrm{K}$) are calculated as defined in Relation 6.13 based on the values interpolated from $\kappa_\parallel(T)$. Figure 6.24 illustrates the resultant curves. The arrow follows the order of the curves per increasing T. Starting from the $0.8\,\mathrm{K}$ curve, $\kappa_\parallel(B)$ is almost constant for 0 - 0.1 T. A slight increase and decrease is detectable per increasing B between 0.2 - 0.4 T, corresponding to the 3-D AFM to TLL phase transition. $\Delta\kappa_\parallel/\kappa_0$ grows only above by $\sim\!50\,\%$ around 1 T and reaches up to $225\,\%$ at $B = 2\,\mathrm{T}$. Although $\Delta\kappa_\parallel/\kappa_0$ increases up to $0.8\,\mathrm{K}$ (Figure 6.23), it decreases at higher T. That reveals a local maximum in the $\Delta\kappa_\parallel/\kappa_0$ values around the 0.7 - 0.9 K T range.

Figure 6.24: $\Delta\kappa_\parallel/\kappa_0$ in B for T between 0.8 - 1.5 K. The points are interpolated from the T sweeps.

For $T > 1\,\mathrm{K}$, a continuous increase of $\Delta\kappa_\parallel/\kappa_0$ in B is observed. Per increasing T, the relative changes of $\kappa_\parallel(B)$ increase slightly below around 1 T and decrease within 1 - 2 T. Note, at

T above the exchange interaction energy that is $T > J_\perp/k_B$, the thermal fluctuations ruin magnetic correlations arising from the interactions.

It must be noted that although Nikitin *et al.* suggested presence of Umklapp scattering between the left- and right-moving spin excitations within the SDW state [79], no distinct signature of extra suppression of the multiple fermion scattering was observed. This can be due to weak effects of the suggested scattering compared to the other scattering processes.

6.8 Phase diagram from thermal transport

I close this chapter by rebuilding the phase diagram of $YbAlO_3$ based on the phase transitions in $\kappa_\parallel(T)$ and $\kappa_\parallel(B)$. To plot the phase diagram, the transitions determined from the T and B sweeps are analysed more deeply here. Different methods to define a transition are accepted in the literature depending on the type of anomaly, e.g., a crossing of two tangent lines before and after the transition, *or* the point where the measured value drops to 20% of its normal value, *or* the point at which the curve has the highest slope corresponding to an extremum in the derivative, etc. In this text, the already-existing phase diagram from magnetisation and specific heat was considered in opting for transition features and defining transition points. The starting and ending points of the observed features are labelled as T^{ON} and T^{OFF} (B^{ON} and B^{OFF}), limiting the region of the transition. T^{ON}- T^{OFF} (B^{ON}-B^{OFF}) gives the width, and the average of the onset and offset is taken as the transition temperature T_N (the characteristic field B_c).

Temperature sweeps: The transitions from the TLL to 3-D and IC AFM phases show different features upon cooling. The overall behaviour is as follows: (i) Similar to the case of $B = 0$, the TLL to 3-D AFM phase transition in regime 1 takes the shape of a drop per decreasing T, as observable in Figure 6.15 **(a)**. The transition feature between TLL to IC AFM phase in regime 2 is not only less pronounced than in the first regime with TLL to 3-D AFM phase transition but also the shape of the transition anomaly differs depending on B. (ii) The transition from TLL to IC AFM in regime 2-I (0.7 and 0.75 T curves, for instance) appears as a gentle shoulder. (iii) In contrast to regime 2-I, clear kinks appear at the AFM transitions between 0.8 - 0.95 T (see Figure 6.15 **(b)** for cases (ii) and (iii)). (iv) The transition gets weaker with a further increase of B and disappears totally above $\sim$1.1 T, as depicted in Figure 6.15 **(c)**. That yields that no clear feature is detectable in regime 2-III. Figure 6.25 shows examples of the features at T_N in the $\kappa_\parallel(T)/T^2$ curves in different B, on top of which the transition widths with the onset and offset T are marked by pink boxes and arrows. Panel **(a)** shows one representative curve of each ordering regime: (i) $B = 0$ for TLL to 3-D AFM, (ii) $B = 0.6$ T for TLL to first IC-AFM (i.e., SDW) and (iii) $B = 0.9$ T for TLL to second IC-AFM (i.e., TAF) phases. The transitions' characteristic points T^{ON} and T^{OFF} of $B = 0$ (panel **(b)**), 0.6 T (panel **(c)**), and 0.9 T (panel **(d)**) are taken as the onset and offset of the drop (i.e., for TLL to 3-D AFM), the sides of the shoulder (i.e., for TLL to SDW), and the start and the summit of the peak (i.e., for TLL to TAF), respectively.

Field sweeps: Based on the T range of the B sweeps, different numbers and types of transitions occur. Above 0.9 K, no transition is found. The 3-D AFM to TLL transition is observed below 0.35 T down to around 0.5 K. By cooling further, in addition to the 3-D-to-IC AFM transition at $\sim$0.32 T, the extra transition between the SDW and TAF sub-phases arises, as described in Section 6.7. Figure 6.26 depicts exemplary transitions in the B sweeps below 0.35 T. Figure 6.26 **(a)** exemplifies the *high-T type* transition feature by the curve measured at 612 mK. That is a transition from the 3-D AFM to the TLL state. As can be
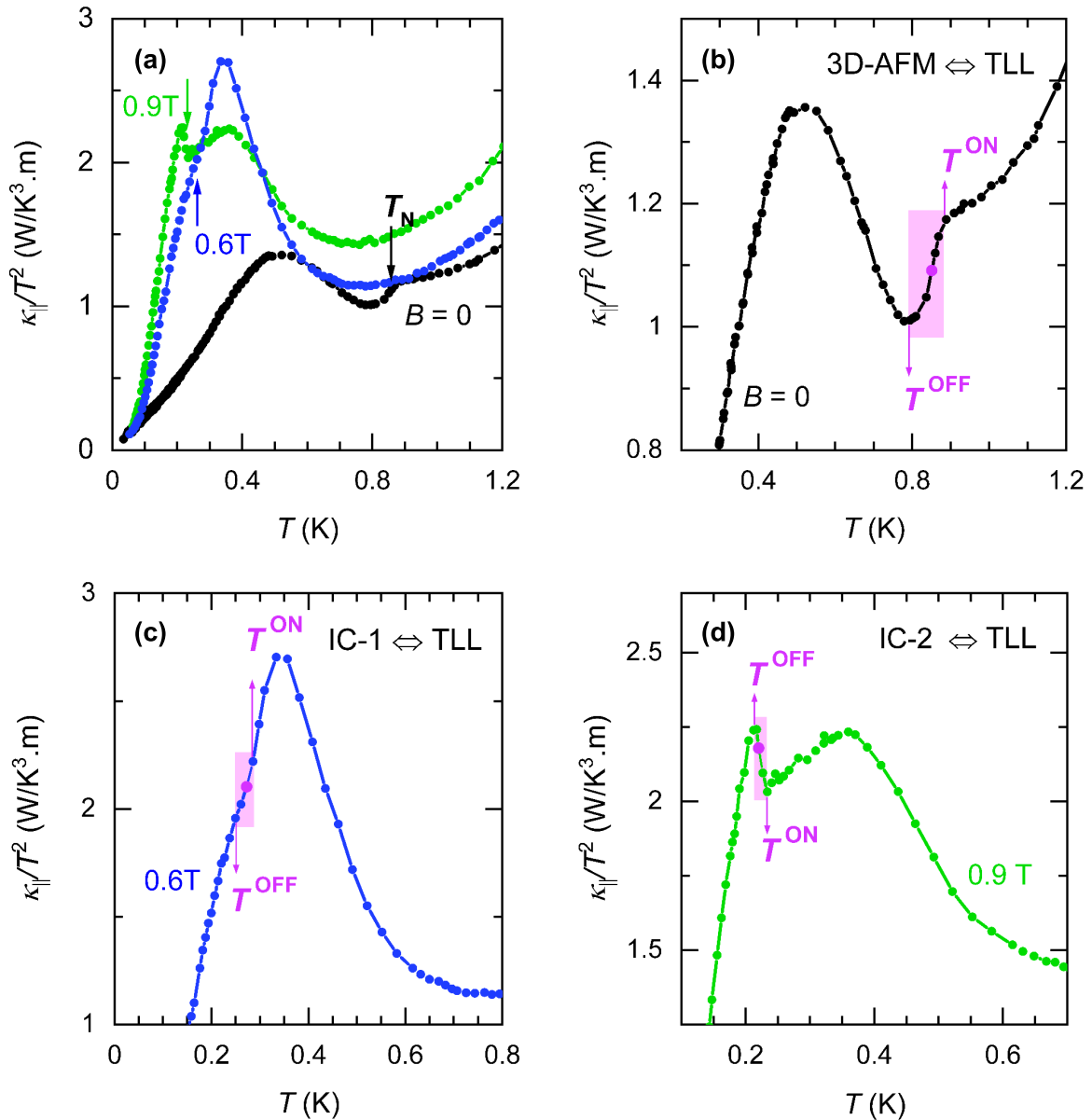
Figure 6.25: The features of the Néel ordering phase transitions at T_N in $\kappa_\parallel(T)$ curves in different fields. **(a)** Selected fields of $B = 0$, 0.6 and 0.9 T, as representatives of regime 1, 2-I and 2-II, respectively. No clear feature was observed in regime 2-III. Upon cooling the transition from the TLL to the AFM ordered phase appears differently, depending on the type of AFM. T_N shows up as **(b)** a clear drop for 3-D AFM, **(c)** like a slight shoulder for IC-1 AFM, and **(d)** as a jump for IC-2 AFM. The transition widths with onset and offset T are marked by pink boxes and arrows.
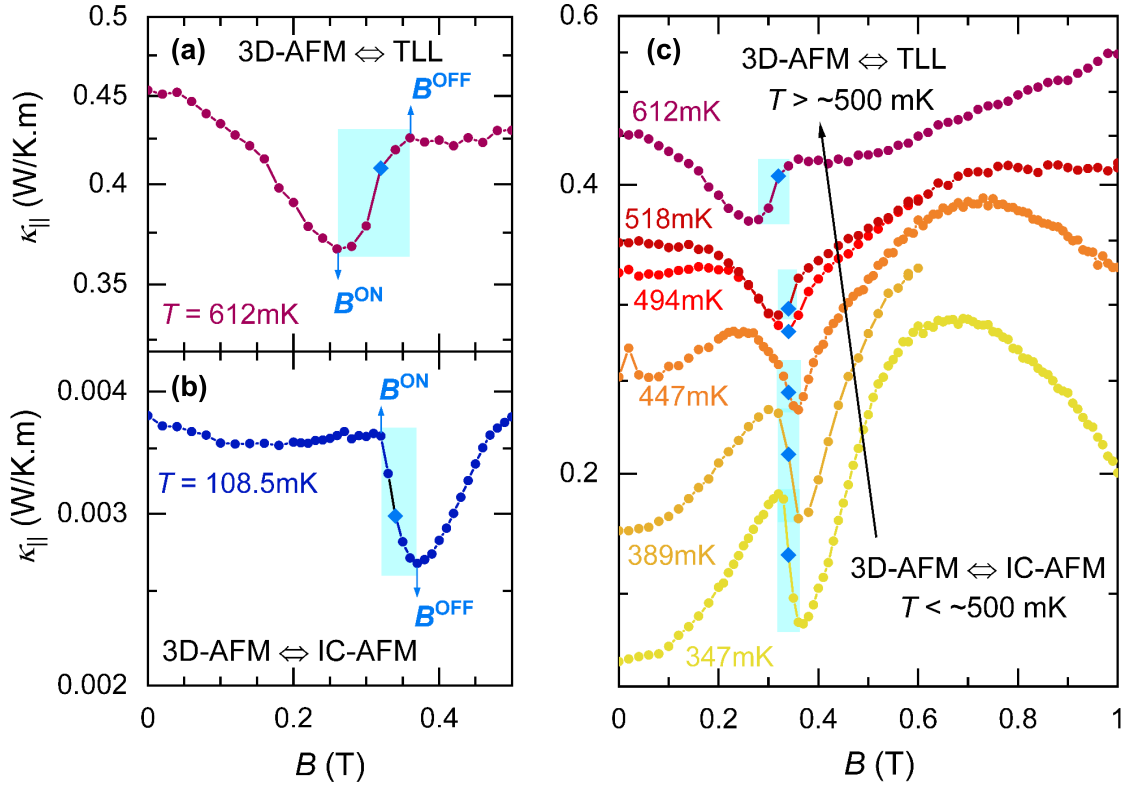
Figure 6.26: Phase transitions below $0.35\,\mathrm{T}$ in $\kappa_\parallel(B)$. **(a)-(b)** B sweeps below $0.5\,\mathrm{T}$ for two selected curves of $612\,\mathrm{mK}$ and $108\,\mathrm{mK}$, as representatives of high and low T regions experiencing 3-D AFM to TLL and IC AFM phase transitions, respectively, by increasing the magnetic field. As B increases, the phase transitions appear as **(a)** a jump, and **(b)** a drop, as indicated by light blue boxes. The width is defined from the transition onset to the offset. **(c)** The phase transition feature changes from one to the other type, by changing T.

seen, the transition generates a step, so the onset has a lower κ compared to the offset. On the other hand, the 3-D-to-IC AFM transition poses a drop in the same B range but at lower T. That can be found in the exemplary curve of $108\,\mathrm{mK}$ in Figure 6.26 **(b)** (*low-T type*). The onset and offset of these transitions are defined as denoted. Figure 6.26 **(c)** shows the *transformation of the high-T-type to the low-T-type transition*. Around $0.5\,\mathrm{K}$, the phase transition appears as a sharp-cornered anomaly with similar arms (see $T = 494\,\mathrm{mK}$ curve). By increasing (decreasing) T, the slope on the right (left) arm gets steeper, reforming to a jump (drop) feature for increasing B. At around $(B,T) = (0.32\,\mathrm{T}, 0.5\,\mathrm{K})$, there is a so-called *triple point* in the phase diagram. The curve at $494\,\mathrm{mK}$ apparently shows no predilection for either a jump or a drop. This curve is almost going through the triple point, which might be the reason for the distinct form of the transition.

The next feature is the plateau regions arising within the SDW state. The foremost appears around 0.6 - $0.8\,\mathrm{T}$ as an immense V-shaped valley in $\kappa_\parallel$ versus B, though as a diminutive plateau in the magnetisation at $M(B) \sim M_\mathrm{s}/3$. The second one is the new plateau-type anomaly in $\kappa_\parallel(B)$ at low enough T around $0.5\,\mathrm{T}$ with a tiny dip around $M(B) \sim M_\mathrm{s}/5$ in $\mathrm{d}M/\mathrm{d}B$. Figure 6.27 demonstrates these two plateau regions in the $\kappa_\parallel(B)$ curves. The inset zooms in $\kappa_\parallel$ versus B at $108\,\mathrm{mK}$ between 0.5 - $1\,\mathrm{T}$. The *V-shaped* anomaly comes
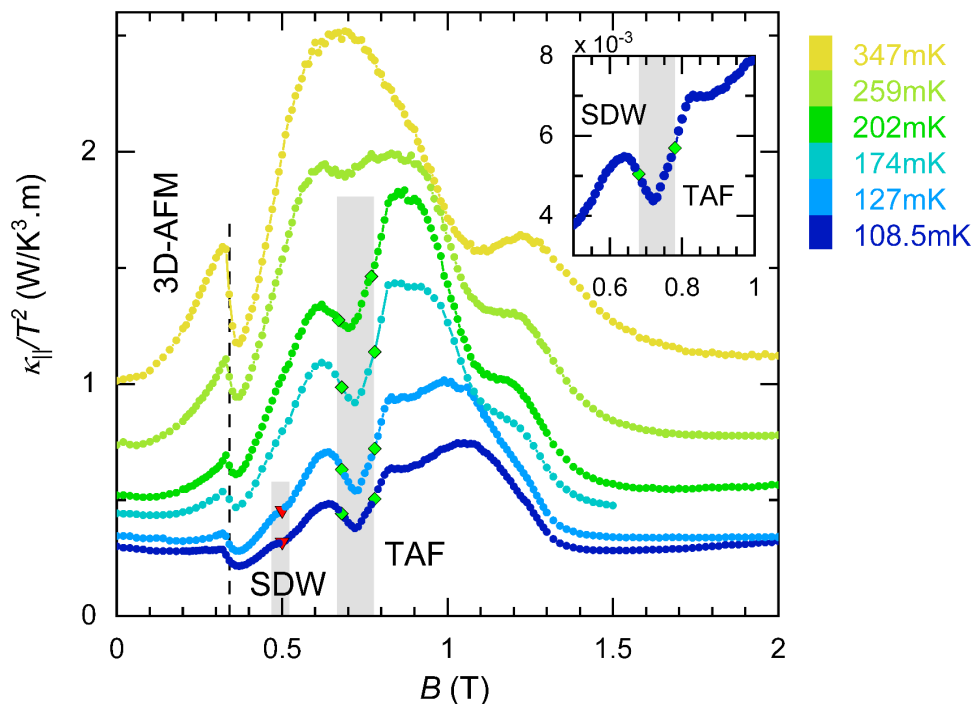
Figure 6.27: IC-1 to IC-2 phase transitions appearing below $0.35\,\mathrm{K}$ in $\kappa_\parallel(B)$. The inset zooms in the curve at $108\,\mathrm{mK}$ between 0.5 - 1 T. By increasing the magnetic field, a *V-shaped* anomaly is observed starting at $\sim 0.64\,\mathrm{T}$ and ending at $\sim 0.82\,\mathrm{T}$, which reaches a local minimum at $0.72\,\mathrm{T}$. A tiny plateau had been observed before in magnetisation in the same B region limited by the green diamonds, which correspond to the mid points of $0.68\,\mathrm{T}$ and $0.78\,\mathrm{T}$ on the left and right wings in $\kappa_\parallel(B)$, respectively. The V-shaped anomaly is well observable below $\sim 0.26\,\mathrm{K}$ within the identical B span detected for the $T = 108\,\mathrm{mK}$ curve.

forth between ~ 0.64 - $0.82\,\mathrm{T}$, with a local minimum at $0.72\,\mathrm{T}$. With an eye on magnetisation (see, e.g., [79]), the plateau borders at $M(B) \sim M_\mathrm{s}/3$ are at $0.68\,\mathrm{T}$ and $0.78\,\mathrm{T}$, as marked by green diamonds on the curve. It needs to be noted that the taken points are tighter than the V-shaped anomaly itself. The green diamonds correspond to the mid-points of the left and right wings of the V-shaped anomaly in $\kappa_\parallel(B)$; nevertheless, the whole anomaly is believed to expose one feature. The main panel of Figure 6.27 shows the trend of the same transition at higher T. In respect of the T-independent width of the plateau in $M \sim M_\mathrm{s}/3$ down to $50\,\mathrm{mK}$, a grey box is over-plotted to extend an identical B span from the $108\,\mathrm{mK}$ curve to higher T. As noted before, this transition shows up to $\sim 0.25\,\mathrm{K}$, above which the sharp-cornered valley transmutes to a hump. Due to the narrowness of the plateau region around $0.5\,\mathrm{T}$, only the mid B is marked by red triangles.

Diagram of phase transitions: In Section 6.7, the phase transitions and the new features emerging in the thermal transport of YbAlO₃ were discussed in detail. Here, the phase diagram, including all transitions and features observed in the thermal conductivity along the spin chains, is plotted in Figure 6.28. In this figure, the phase transitions detected in $\kappa_\parallel(T)$, along with the widths of the transitions, are displayed in pink circles and shades. The phase transitions revealed in $\kappa_\parallel(B)$ are denoted via blue diamonds, illustrating the 3-D to IC AFM transitions. The V-shaped and plateau-type anomalies in $\kappa_\parallel(B)$ corresponding
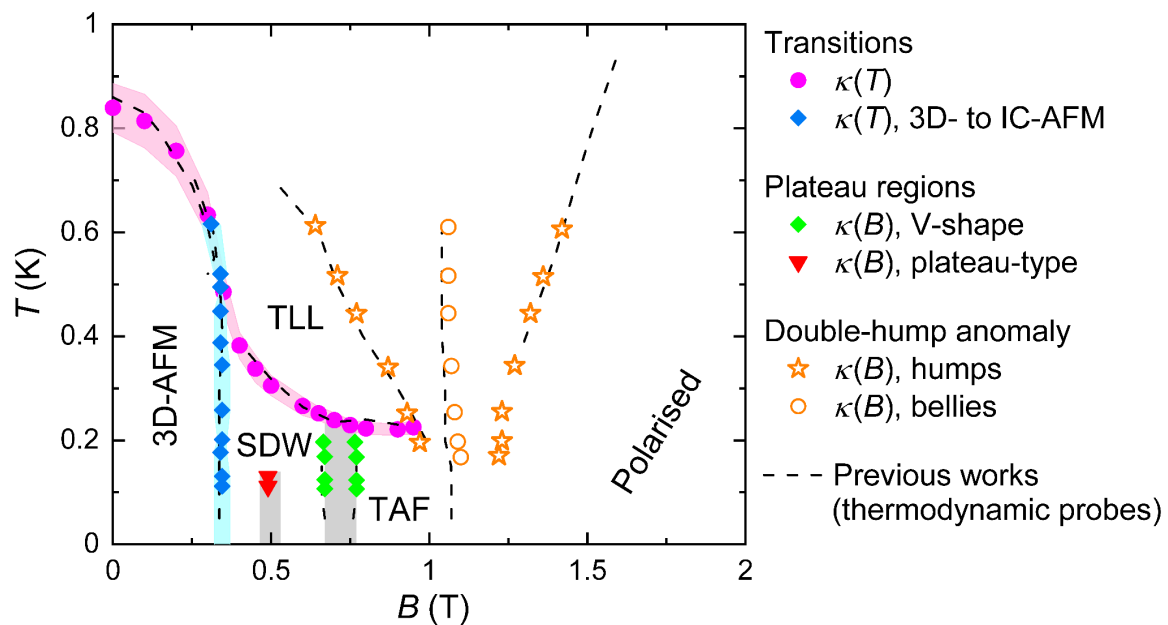
Figure 6.28: Field-temperature phase diagram of YbAlO$_3$ for $T \leq 1\,\mathrm{K}$ and $B \leq 2\,\mathrm{T}$ along the a-axis via thermal conductivity measurements along the spin chains. Ball, diamond and triangle markers indicate the anomalies observed in this study in $\kappa_\parallel(T)$ and $\kappa_\parallel(B)$, some known as phase transitions from the previous works. Dashed lines show the previous specific heat and magnetisation results from [59, 71, 74, 79].

to the plateau regions in $M(B)$ around $M \sim M_\mathrm{s}/3$ and $M_\mathrm{s}/5$ are shown in green diamonds and red triangles, respectively. The areas corresponding to the plateau regions in $M(B)$ are shaded in grey. I recall that the plateau regions belong to the SDW state [224]. The theoretically predicted TAF phase is thus considered to start at the upper B limit of the plateau region around $M \sim M_\mathrm{s}/3$. The position of the maxima and minima in the double-hump anomaly are included in the phase diagram of Figure 6.28 as well. The old data from the previous studies found via specific heat and magnetisation measurements in [59, 71, 74, 79] are plotted as dashed lines. All the features observed in thermodynamics probes are detected here by thermal transport. The agreement of the points is remarkable, which also demonstrates the high quality of the thermal coupling to my sample down to the lowest T at the prepared microcontacts.

To sum up, the phase diagram of YbAlO$_3$ is reproduced successfully via thermal transport. By adding new features resolved in the transport data, a completed version of the phase diagram is established.

6.9 Summary

Thermal transport as a sensitive probe of scattering and magnetic contribution was utilised. YAlO$_3$ was opted for as the non-magnetic iso-structural reference compound to YbAlO$_3$. The high-T thermal conductance of YAlO$_3$ and YbAlO$_3$ was measured along the b- and c-axis. The difference in Θ_D, Γ and the T dependence disables YAlO$_3$ to be used to determine κ_ph of YbAlO$_3$.

At low T, a cubic T dependency of $\kappa_\parallel$ was observed close to zero T, which changed to

$\kappa_{\parallel}(T) \propto T^n$ with $n > 3$ for $0.16\,\mathrm{K} < T < 1\,\mathrm{K}$. Moreover, the mean free path was found to be $\lambda \sim 200\,\mu\mathrm{m}$. YbAlO₃ is hence found to be a candidate for showing hydrodynamic transport and Poiseuille flow of phonons.

A pure phononic contribution is observed in YbAlO₃ at the lowest T. A huge enhancement of $\kappa_{\parallel}$ with B was observed in the mid-field region due to a large magnetic contribution. In addition, V-shaped anomalies and the new plateau-type features are observed in $\kappa_{\parallel}(B)$ within the SDW phase, corresponding to plateau regions in $M(B)$ around $M \sim M_{\mathrm{s}}/3$ and $M \sim M_{\mathrm{s}}/5$. Two humps were observed in $\kappa_{\parallel}(T)$ below $0.7\,\mathrm{K}$, in accordance with expected c_v of isolated chains. The phase diagram was reproduced successfully by the thermal transport probe. The new features, e.g., the clear V-shaped anomaly and the plateau observed around $0.5\,\mathrm{T}$ in $\kappa_{\parallel}(B)$, are included in the phase diagram, providing a complemented version compared to the phase diagram from thermodynamic probes.

Discussion and conclusion

7.1 Introduction

Following descriptions of phononic thermal conductivity (κ_{ph}) of YbAlO$_3$ pursued from room temperature (T) down to about 30 mK and the thermal conductivity (κ) results in field (B) at milli-Kelvin T ranges given in Chapter 6, in this chapter, I continue with a more detailed discussion of the thermal conductivity of magnetic excitations (κ_{mag}). I will compare the experimental thermal conductivity results assuming different possible κ_{ph} backgrounds (BG) with calculated thermal Drude weight (D^{th}). I note that the discussions here are for electrically insulating low-dimensional spin systems. Then, I add some remarks on (i) quantum criticality near the quantum critical point (QCP) and (ii) the influence of spin polarisation on B dependency of κ in YbAlO$_3$. I close the chapter with the main conclusions of this research, plus suggestions for further work and measurements on YbAlO$_3$.

7.2 Thermal transport via the magnetic excitations

To study the thermal conductivity of the magnetic excitations, I consider two approaches: (i) Taking the total measured thermal conductivity along the spin chains ($\kappa_{\parallel}$) and subtracting κ_{ph}, and (ii) calculating the thermal Drude weight of the magnetic channel. Although an exact description of the phononic contribution in thermal transport in YbAlO$_3$ in the full T range and B is unknown yet, possible $\kappa_{\mathrm{ph}}(T)$, particularly within the dilution fridge T range, was discussed widely in Chapter 6 Section 6.5. Finally, I compare the two methods in the discussion.

Subtraction of the phononic thermal conductivity: Determination of the phononic contribution in YbAlO$_3$ is complicated and vital at the same time, owing to its huge contribution. Here, I look at the main possible descriptions of the lattice thermal conductivity for $\kappa_{\parallel}(T) = \kappa_{\mathrm{ph}}(T) + \kappa_{\mathrm{mag}}(T)$, where κ_{ph} is a short form of $\kappa_{\mathrm{ph},\parallel}$, otherwise mentioned.

- **Perpendicular direction:** κ along a perpendicular direction to the spin chains ($\kappa_{\perp}$) is expected to include only the phononic contribution, namely $\kappa_{\perp} = \kappa_{\mathrm{ph},\perp}$. In this case, a B dependency of κ_{ph}, i.e., different scattering of the phonons by magnetic excitations in different B, is detectable. Taking $\kappa_{\perp}(T)$ times an anisotropy factor as $\kappa_{\mathrm{ph}}(T)$ is widely used in low-D spin systems, e.g., [126, 129, 134, 136], as reviewed in Section 4.5. I label this BG here $\kappa_{\mathrm{ph, perp}}$. In the case of YbAlO$_3$, one can assume $\kappa_{\mathrm{ph},\parallel} = 2.5 \times \kappa_{\perp}$, where the factor 2.5 is $[\kappa_{\parallel}/\kappa_{\perp}]_{T \to 0}$ described in Relation 4.27. In the $\kappa_{\mathrm{ph, perp}}$ BG, we assume that the anisotropy of the magnetic scattering of the phonons and the phononic transport are similar.

- **Cubic-temperature dependency:** According to the Debye model, a T^3 behaviour is expected for the phononic specific heat and κ at the lowest T (see Relation 4.13 and Relation 4.17). Accordingly, considering a cubic-T behaviour of κ_{ph} at low T is another possibility. This BG is practical as long as the magneto-elastic contribution is weak and the mean free path λ is constant, e.g., boundaries and disorders are the limits. That is labelled $\kappa_{\mathrm{ph, cube}}$ here. Note that in the case of the Poiseuille flow of phonons, $\kappa_{\mathrm{ph, cube}}$ underestimates the phononic contribution in κ.
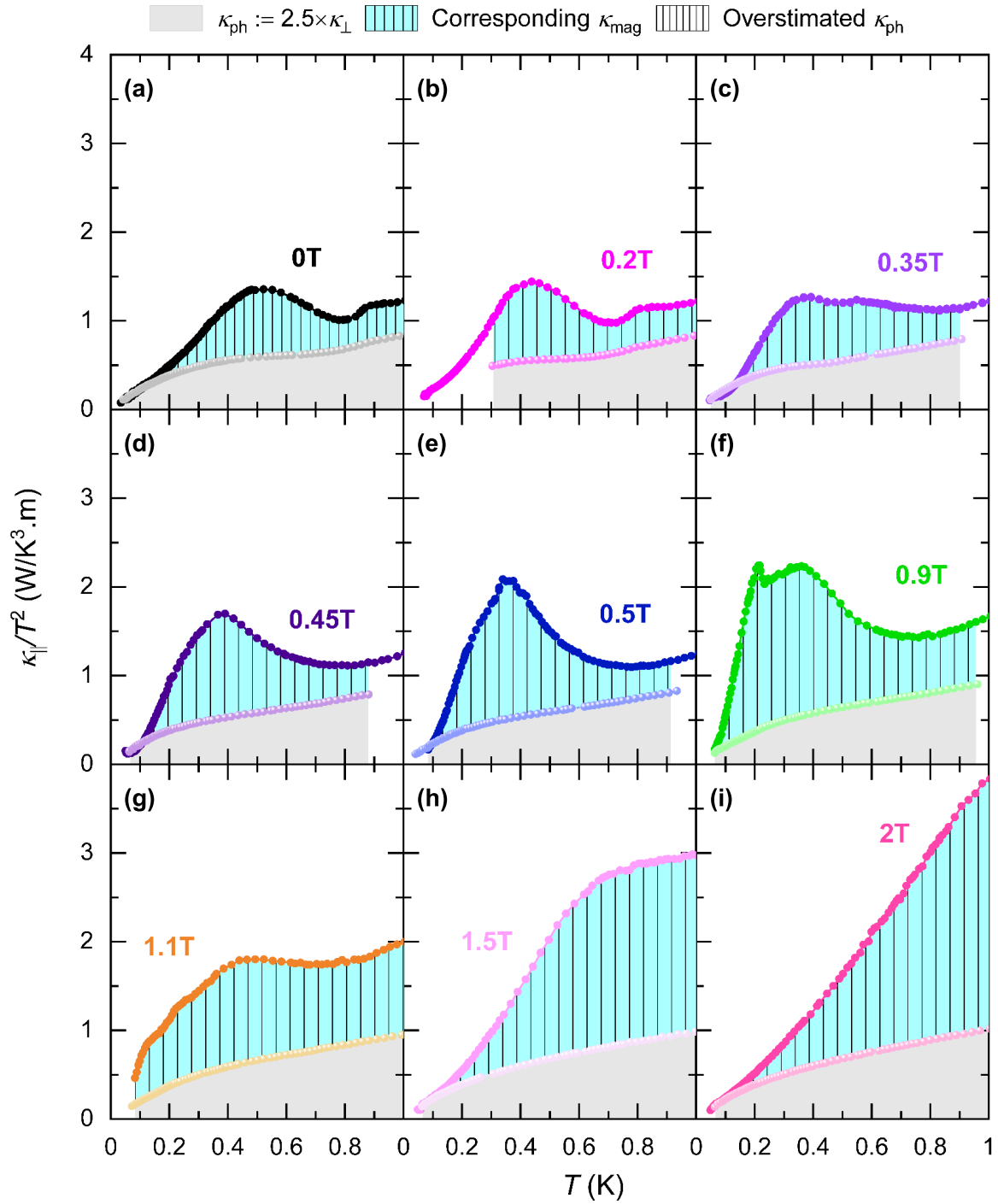
Figure 7.1: κ/T^2 as a function of T for $\kappa_\parallel$ and $\kappa_{\mathrm{ph,\ perp}}$ phononic BG obtained from $\kappa_{\mathrm{ph}} = 2.5 \times \kappa_\perp$. **(a)-(i)** $\kappa_\parallel(T)/T^2$ in different B, including the corresponding $\kappa_{\mathrm{ph,\ perp}}(T)/T^2$ are shown in bold and pale colours respectively. The area underneath the $\kappa_{\mathrm{ph,\ perp}}$ curves is shaded in grey. The corresponding $\kappa_{\mathrm{mag}}(T) = \kappa_\parallel(T) - \kappa_{\mathrm{ph,\ perp}}(T)$ is shown in blue. Overestimation of the phononic contribution, i.e., $\kappa_{\mathrm{ph,\ perp}}(T) > \kappa_\parallel(T)$, is barely visible, see panels **(c)-(e)** at the lowest T. More explanation is in the main text.
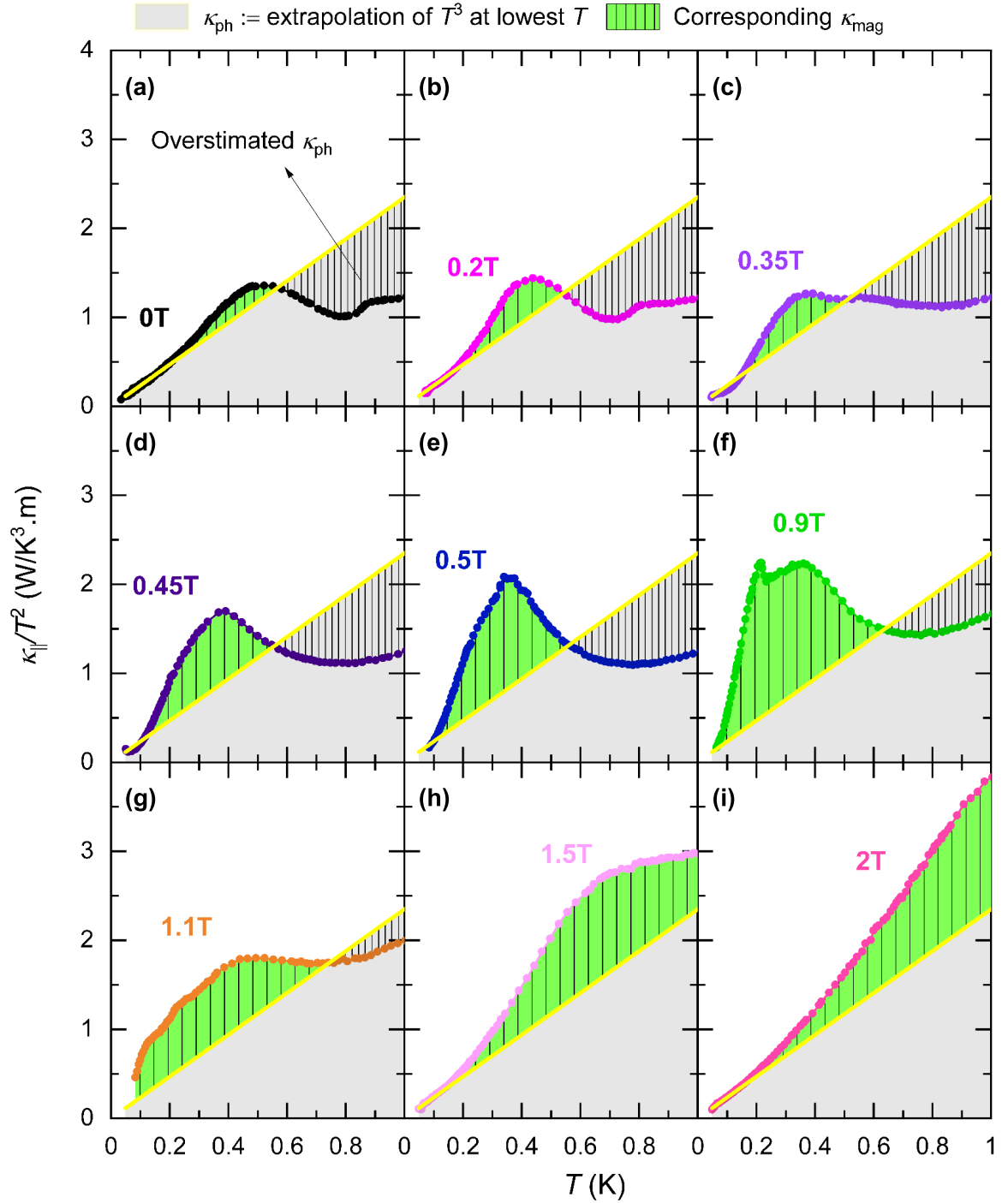
Figure 7.2: κ/T^2 as a function of T for $\kappa_\parallel$ and $\kappa_{ph,\,cube}$ phononic BG as extrapolation of the T^3 behaviour of the ordered states at the lowest T. **(a)-(i)** $\kappa_\parallel(T)/T^2$ in different B, including the corresponding $\kappa_{ph,\,cube}(T)/T^2$ are shown by yellow lines. The area underneath the $\kappa_{ph,\,cube}$ curves is shaded in grey, similar to Figure 7.1. The corresponding $\kappa_{mag}(T) = \kappa_\parallel(T) - \kappa_{ph,\,cube}$ is coloured in green. Grey areas with dense patterns of the vertical lines correspond to $\kappa_{ph}(T) > \kappa_\parallel(T)$, indicating an overestimation of the phononic BG. More explanation is in the text.
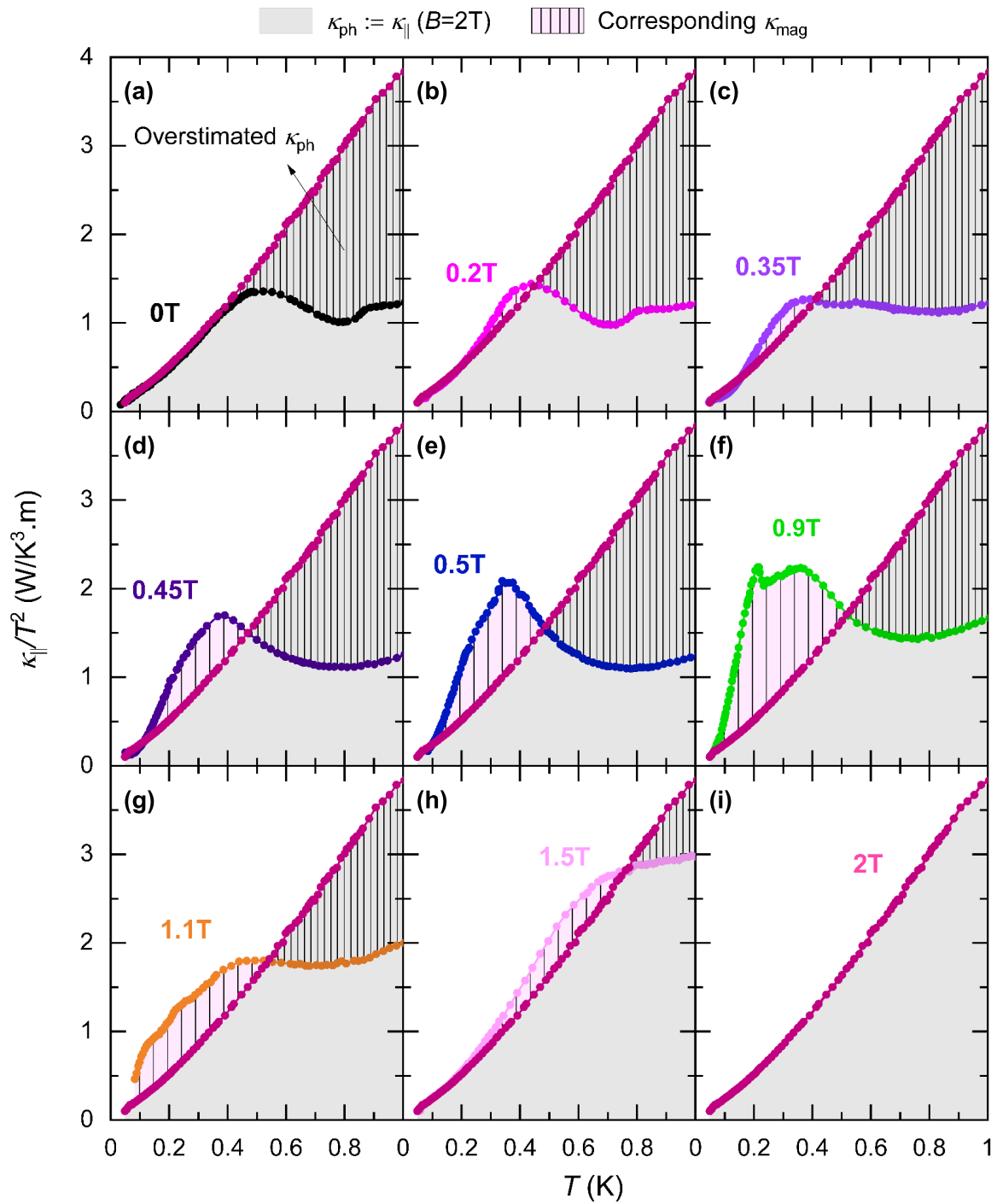
Figure 7.3: κ/T^2 as a function of T for $\kappa_\parallel$ and $\kappa_{\mathrm{ph,\ 2T}} = \kappa_\parallel(B = 2\,\mathrm{T})$ phononic BG. **(a)-(i)** $\kappa_\parallel(T)/T^2$ in different B, including $\kappa_{\mathrm{ph,\ 2T}}(T)/T^2$ (dark red curve). The area underneath the $\kappa_{\mathrm{ph,\ 2T}}$ curve is shaded in grey, similar to Figures 7.1- 7.2. The corresponding $\kappa_{\mathrm{mag}}(T) = \kappa_\parallel(T) - \kappa_{\mathrm{ph,\ 2T}}$ is coloured in pink. Overestimated phononic BG ($\kappa_{\mathrm{ph}}(T) > \kappa_\parallel(T)$) is shaded in grey with dense patterns of the vertical lines. More explanation is given in the text.

- **Fully polarised states:** Using $\kappa_\parallel(T)$ for B in a fully-polarised (FP) state at low T compared to the Zeeman splitting energy and apart from the broad maximum appearing in specific heat, the so-called *Schottky* anomaly, is another possible way of determining the pure phononic thermal transport. Assuming the contribution and/or scattering from the magnetic carriers thermally excited across the gap via the Zeeman splitting in B is negligible, the thermal transport is only via phonons. In the following, this phononic BG is labelled $\kappa_{\mathrm{ph,\,2T}}$. I remark that phonon scattering via the magnetic excitations and its B dependency are neglected in $\kappa_{\mathrm{ph,\,2T}}$, similar to $\kappa_{\mathrm{ph,\,cube}}$.

$\kappa_\parallel(T)/T^2$ for different B between 0 - 2 T, including κ_{ph}/T^2 with κ_{ph} by definition equal to $\kappa_{\mathrm{ph,\,perp}}$, $\kappa_{\mathrm{ph,\,cube}}$, and $\kappa_{\mathrm{ph,\,2T}}$, are plotted in Figures 7.1- 7.3, respectively. In each panel, the grey area is below the assumed $\kappa_{\mathrm{ph}}(T)$, the grey pattern marks the region where κ_{ph} is definitely overestimated, and the coloured shade is the lower bound of the estimate of κ_{mag}.

Panels **(a)-(b)** of Figures 7.1- 7.3 plot the results in $B = 0$ and $0.2\,\mathrm{T}$ with three-dimensional (3-D) antiferromagnetic (AFM) ground state (GS). Starting from the lowest T, all curves have a T^3 dependency, and neither extra magnetic contribution nor phononic overestimation is expected. By increasing T above $\sim160\,\mathrm{mK}$, the T dependency of $\kappa_{\mathrm{ph,\,perp}}$ (Figures 7.1 **(a)-(b)**) decreases from $\propto T^3$ to $\propto T^{2.56}$. Thus, $\kappa_{\mathrm{ph,\,perp}}(T)$ separates from the $\kappa_\parallel(T)$ curves, resulting in a non-zero magnetic contribution along the spin chains. In the case of $\kappa_{\mathrm{ph,\,cube}}$ (Figures 7.2 **(a)-(b)**), additional thermal conductivity is also observed by dint of the faster-than-cubic growth of the $\kappa_\parallel(T)$ curves. This extra contribution was modelled in Chapter 6 Section 6.5 by $\kappa_{\mathrm{mag}} \propto \exp(-\Delta/k_{\mathrm{B}}T)$, where Δ and k_{B} are the energy gap and the Boltzmann constant since inelastic neutron scattering (INS) measurements had revealed a gapped state in this T and B range. $\kappa_{\mathrm{ph,\,perp}}$ goes above the $\kappa_\parallel$ curves for $T > 0.5\,\mathrm{K}$ and thus never overestimates the phononic BG for this T range.

$\kappa_{\mathrm{ph,\,2T}}$, however, grows as $\propto T^{3.26}$ faster than the T cube (Figures 7.3 **(a)-(b)**). $\kappa_\parallel \simeq \kappa_{\mathrm{ph,\,2T}}$ below $\sim160\,\mathrm{mK}$. For $0.16 < T < 0.4\,\mathrm{K}$, $\kappa_\parallel$ sits almost on (slightly below) the $\kappa_{\mathrm{ph,\,2T}}$ curve in zero B and shows extra contribution from the magnetic excitations in $0.2\,\mathrm{T}$ (red shade in Figure 7.3 **(b)**). For $T > 0.4\,\mathrm{K}$, $\kappa_{\mathrm{ph,\,2T}}$ increases beyond the zero B and $0.2\,\mathrm{T}$ curves.

Panels **(c)-(g)** of Figures 7.1- 7.3 plot the results with incommensurate (IC) AFM GS. Panels **(c)-(e)** are for $B = 0.35\,\mathrm{T}$, $0.45\,\mathrm{T}$ and $0.5\,\mathrm{T}$ with spin-density wave (SDW) GS. Starting from the lowest T, the curves show excessive scattering for a B range above the phase transition from the 3D AFM phase to the IC AFM state, as detected both in T sweeps and in B sweeps as a drop after the phase transition (see Chapter 6 Section 6.7) but affecting more the transport along the spin chains rather than the perpendicular one. That is, however, expected to turn back to the cubic behaviour at lower T similar to all the three suggested κ_{ph}. Panels **(f)-(g)** depict the curves with transverse AFM (TAF) GS, namely $0.9\,\mathrm{T}$ and $1.1\,\mathrm{T}$. In the TAF GS, extra scattering was observed both in the T and B sweeps of $\kappa_\perp$, which affects $\kappa_{\mathrm{ph,\,perp}}$ but is disregarded in both the $\kappa_{\mathrm{ph,\,cube}}$ and $\kappa_{\mathrm{ph,\,2T}}$ backgrounds. Nevertheless, this excessive scattering in $\kappa_\perp$, and hence $\kappa_{\mathrm{ph,\,perp}}$, appears tiny and barely visible in these plots. At higher T around 0.2 - 0.5 K, a thermal conductivity larger than the phononic BG is observed in the B range with IC GS regardless of the chosen κ_{ph}. In other words, even for the largest considered phononic BG, namely $\kappa_{\mathrm{ph,\,2T}}$, $\kappa_\parallel(T) > \kappa_{\mathrm{ph}}(T)$, which strongly hints to the presence of magnetic heat transport. By increasing B within the IC phase, the magnetic thermal conductivity rises initially, with an anticipated maximum around 0.6 - 0.8 T as observed in $\kappa_\parallel(T)$ in Chapter 6 Section 6.7 (e.g., see Figure 6.16), and decreases then by getting closer to the FP state. By increasing T above 0.6 K, the $\kappa_{\mathrm{ph,\,cube}}$ and $\kappa_{\mathrm{ph,\,2T}}$ backgrounds overestimate the phononic thermal conductivity.

Finally, panels **(h)**-**(i)** of Figures 7.1- 7.3 plot the results in $B = 1.5\,\text{T}$ and $2\,\text{T}$ with FP GS. In these cases, $\kappa_{\text{ph, perp}}$ and $\kappa_{\text{ph, cube}}$ predict additional thermal transport to the phononic one; however, the $1.5\,\text{T}$ curve shows some further contribution compared to the $\kappa_{\text{ph, 2T}}$ phononic BG only between 0.2 - 0.7 K and overestimation of κ_{ph} above. For the $2\,\text{T}$ curve, $\kappa_{\text{ph, 2T}}$ predicts pure phononic heat transport.

As a final point, I recall that a correct BG cannot be larger than an intrinsically non-negative signal, here the magnetic thermal conductivity. This necessary but not sufficient condition is satisfied only by the perpendicular BG since $\kappa_{\text{ph, perp}}(T) \leq \kappa_\parallel(T)$ in the whole T range.

Figure 7.4 compares the subtraction of the three possible phononic contributions displayed in Figures 7.1- 7.3 in terms of $(\kappa_\parallel - \kappa_{\text{ph}})/\kappa_\parallel = \kappa_{\text{mag}}/\kappa_\parallel$ versus T. $\kappa_{\text{mag}}/\kappa_\parallel$ magnifies the κ_{mag} behaviour of small $\kappa_\parallel$ down to the lowest T. If the lattice thermal conductivity is correctly determined and subtracted from the net κ, the remaining thermal transport is $\kappa_{\text{mag}} \geq 0$, and thus $0 \leq \kappa_{\text{mag}}/\kappa_\parallel \leq 1$, in particular, above zero and below the dashed lines in Figure 7.4. $\kappa_{\text{mag}}/\kappa_\parallel = 1$ would indicate a pure magnetic heat transport, though not realised since $\kappa_{\text{ph}} \neq 0$. In Figure 7.4, negative values of $\kappa - \kappa_{\text{ph}}$, highlighted by grey colour, demonstrate excessive scattering of phonons by the magnetic excitations not considered in the chosen phononic BG. Note, considering too low values of $\kappa_{\text{ph}}(T)$ gives unreal extra conductivity in the magnetic thermal transport on the other hand. From Figure 7.4, it is pretty manifest that in the whole T and B range, $\kappa_{\text{mag}}/\kappa_\parallel$ is the largest for BG determination from $\kappa_\perp$ and least for the $2\,\text{T}$ BG, with the results for the cubic BG in between. That is simply since $\kappa_{\text{ph, 2T}} > \kappa_{\text{ph, cube}} > \kappa_{\text{ph, perp}}$ for all B. See Chapter 6 Section 6.4 for further discussion.

Independent of the chosen BG, $(\kappa_\parallel - \kappa_{\text{ph}})/\kappa_\parallel$ approaches zero in the curves with 3-D AFM order and FP GS at the zero T limit, in line with the absence of magnetic excitations. That is trivial for some cases, e.g., for the $2\,\text{T}$ curve calculated with the $2\,\text{T}$ BG, but more complex for a short B range within the IC AFM GS: Close to the transition from the 3-D AFM to the IC AFM state, e.g., for 0.35 T and 0.45 T, $(\kappa_\parallel - \kappa_{\text{ph}})/\kappa_\parallel$ is going through a minimum with negative values at low $T < 0.2\,\text{K}$. That is attributed to excessive magneto-elastic scattering close to the transition. The magneto-elastic scattering close to the transition is reputed to be anisotropic since analogous excessive scattering was not detected in $\kappa_\perp$, neither in the T sweeps nor B sweeps. The anisotropy of the scattering close to the transition might explain why $\kappa_{\text{ph, perp}}$ does not work as BG in this T range below 0.2 K in some B extensions above the 3-D to IC AFM phase transition. At even lower T, $(\kappa_\parallel - \kappa_{\text{ph}})/\kappa_\parallel$ turns upward to approach zero, as already observable in the 0.35 T and 0.45 T curves in Figures 7.4 **(c)**-**(d)**.

While $(\kappa_\parallel - \kappa_{\text{ph}})/\kappa_\parallel$ at the lowest $T < 0.2\,\text{T}$ is rather independent of the choice of BG, large differences are observed at higher T. With the largest possible phononic contribution, namely $\kappa_{\text{ph, 2T}}$, in all B except zero and $2\,\text{T}$, an extra magnetic contribution corresponding to $\kappa_{\text{mag}} = \kappa - \kappa_{\text{ph, 2T}} > 0$ is present (marked by the red shades in Figure 7.3). For the T range of 0.2 - 0.5 K, all the curves show magnetic heat transport reaching up to about $\kappa_{\text{mag}} \sim 0.8\kappa_\parallel$ specifically in B within the IC AFM state. For the T range that the three backgrounds give similar values of κ_{mag}, the magnetic mean-free path (λ_{mag}) can be calculated. The group velocity of the magnetic carriers is estimated from the dispersion relation via the INS measurements as $v = 2\pi \times 20\,\text{m/sec}$, also [83]. Taking the cubic BG, e.g. in 0.5 T at 0.4 K,

$$\lambda_{\text{mag}} = \left(\frac{\kappa_{\text{mag}}}{C_{\text{mag}} \cdot v} \right) = \left(\frac{1.6 \cdot 10^{-1}\,[\text{W K}^{-1}\,\text{m}^{-1}]}{4.3 \cdot 10^4\,[\text{J K}^{-1}\,\text{m}^{-3}] \cdot 40\pi\,[\text{m/sec}]} \right) \simeq 29.1 \cdot 10^{-9}\,\text{m} \sim 30\,\text{nm}, \quad (7.1)$$

and in 0.6 T at 0.36 K $\lambda_{\text{mag}} = 45\,\text{nm}$, which are large since the purity of the rare-earth (RE)
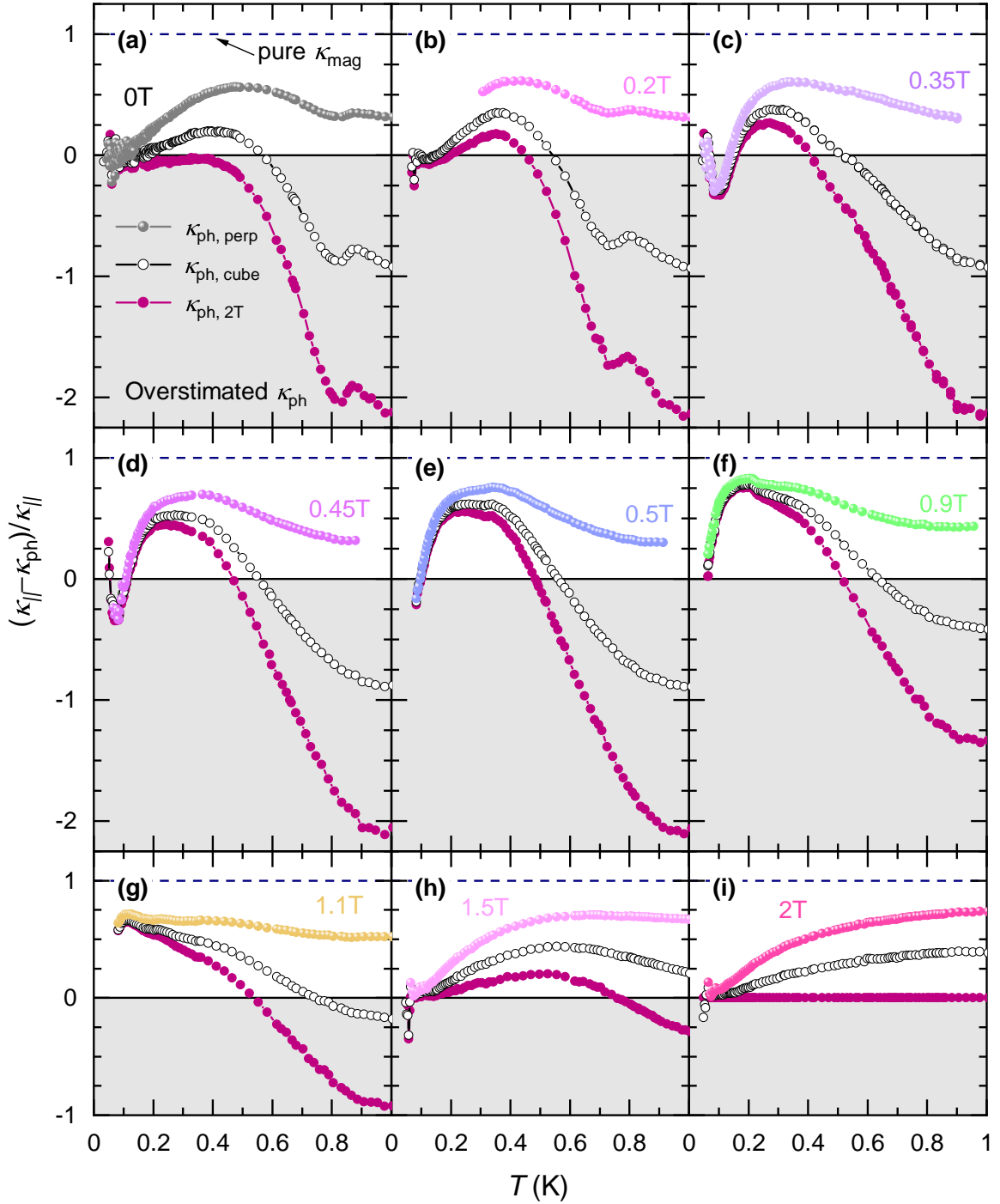
Figure 7.4: Influence of the choice of phononic BG on $\kappa_{\mathrm{mag}}/\kappa_{\parallel} = (\kappa_{\parallel} - \kappa_{\mathrm{ph}})/\kappa_{\parallel}$. **(a)-(i)** $(\kappa_{\parallel} - \kappa_{\mathrm{ph}})/\kappa_{\parallel}$ versus T in different B. In each panel, the negative values indicate an overestimation of κ_{ph} coloured in grey, following Figures 7.1- 7.3. $(\kappa_{\parallel} - \kappa_{\mathrm{ph}})/\kappa_{\parallel} = 1$ corresponds to pure magnetic thermal transport and is shown by dashed lines. Note that the pure magnetic heat transport, i.e., $\kappa_{\mathrm{mag}}/\kappa_{\parallel} = 1$, is not attainable since κ_{ph} never approaches zero. Full balls, empty circles and red markers are results for $\kappa_{\mathrm{ph, perp}}$, $\kappa_{\mathrm{ph, 2T}}$ and $\kappa_{\mathrm{ph, cube}}$, respectively.

materials is typically lowered by the presence of the other RE elements. These λ_{mag} values are calculated above the transition T, and the dimension $d = 1$. Closer to the transition, λ_{mag} is affected by the immense quantum fluctuations, and below that, the specific heat data of Nikitin *et al.* are too noisy. Though the three backgrounds have some deviations in the mentioned T, the order of magnitudes is valid.

Modelling magnetic thermal conductivity within the SDW state is in progress in theoretical collaboration with *Oleg Starykh* from the *University of Utah*. The obtained $\kappa_{\mathrm{mag}}(T)$ is later compared to the primary numerical calculations of the thermal Drude weight.

At $T > 0.5\,\mathrm{K}$, κ_{mag} shows a downturn due to the Umklapp scattering of the spinons. Non-negative values of κ_{mag} are only achievable with the $\kappa_{\mathrm{ph,\ perp}}$ BG, and use of $\kappa_{\mathrm{ph,\ 2T}}$ and $\kappa_{\mathrm{ph,\ cube}}$ at this T range leads to negative $(\kappa_{\parallel} - \kappa_{\mathrm{ph}})/\kappa_{\parallel}$ in almost the full B range. That means κ_{ph} is significantly overestimated by these backgrounds in the corresponding regime. This effect is absent in the $\kappa_{\mathrm{ph,\ perp}}$ BG, as it takes the decrease from $\propto T^3$ to $\propto T^{2.56}$ into account as well. If this overall suppression in $\kappa_{\perp}(T)$ is an intrinsic feature of the lattice and affects both directions, subtracting the $\kappa_{\mathrm{ph,cube}}$ and $\kappa_{\mathrm{ph,\ 2T}}$ backgrounds simply ignores it and removes part of the magnetic thermal transport together with the BG.

At last, I would focus on the phase transition feature at the Tomonaga-Luttinger liquid (TLL) to 3-D AFM phase transition in Figures 7.4 **(a)-(b)**, which is less pronounced in the $\kappa_{\mathrm{ph,\ perp}}$ BG-subtracted curves than the other two. That is attributed to excessive magneto-elastic scattering close to the transition. $\kappa_{\mathrm{ph}}(T) := \kappa_{\mathrm{ph,\ perp}}(T)$ is determined for the same state and scattering situation as $\kappa_{\parallel}(T)$ and thus should be a more reliable BG than $\kappa_{\mathrm{ph,\ cube}}$ and $\kappa_{\mathrm{ph,\ 2T}}$ missing the B independence of magnetic scattering.

Thermal Drude weight calculations: *Rong Yu* and his student *Guijing Duan* from the *Renmin University of China* computed $D^{\mathrm{th}}(T)$ for YbAlO$_3$ with a macroscopic perspective of the system. In the model, Yu *et al.* considered only spin current density with no magneto-elastic effects. They adopted an exact diagonalisation [226] to calculate D^{th} in the Ising AFM and TAF phases and Heisenberg chains without inter-chain coupling in the TLL phase. In the SDW state, Yu *et al.* studied the properties by adding an incommensurate field described in Relation 7.2. Yu *et al.* emphasise that their numerical result is best understood at the qualitative level and suits for studying the overall behaviour, not the absolute values. Particularly, the total partition function Z is an unknown factor in the case of the SDW [227]. Yu *et al.* adopted a matrix product state (MPS) calculation based on the finite time-evolving block decimation (TEBD) algorithm [228, 229] to obtain the GS dynamical spectrum of the spin model defined as [79]

$$\hat{\mathcal{H}} = \sum_i J \hat{\boldsymbol{S}}_i \cdot \hat{\boldsymbol{S}}_{i+1} - \hat{S}_i^z (h_z + h_{ic} \cos(k r_i)). \tag{7.2}$$

h_z refers to the applied longitudinal external magnetic field. The term including h_{ic} appears as a mean-field approximation of the inter-chain incommensurate molecular field produced by the neighbouring chains, and k is determined for each h_z as $2k = \pi(1 - 2m)$ with $m(h_z)$ as the magnetisation normalised by its saturation value, $M(h_z)/M_{\mathrm{s}}$. Considering a chain of L sites with d-dimensional local state spaces of $\{\sigma_i\}$ on sites $i = 1, \ldots, L$, the Hilbert space has a dimension of d^L with $d - 2$ equal to the local state space of a spin-1/2. In the TEBD algorithm, any state $|\psi\rangle$ is represented by an MPS as

$$|\psi\rangle = \sum_{\sigma} c_{\sigma_1, \sigma_2, \sigma_3, \ldots, \sigma_L} |\sigma_1 \sigma_2 \sigma_3 \ldots \sigma_L\rangle, \tag{7.3}$$
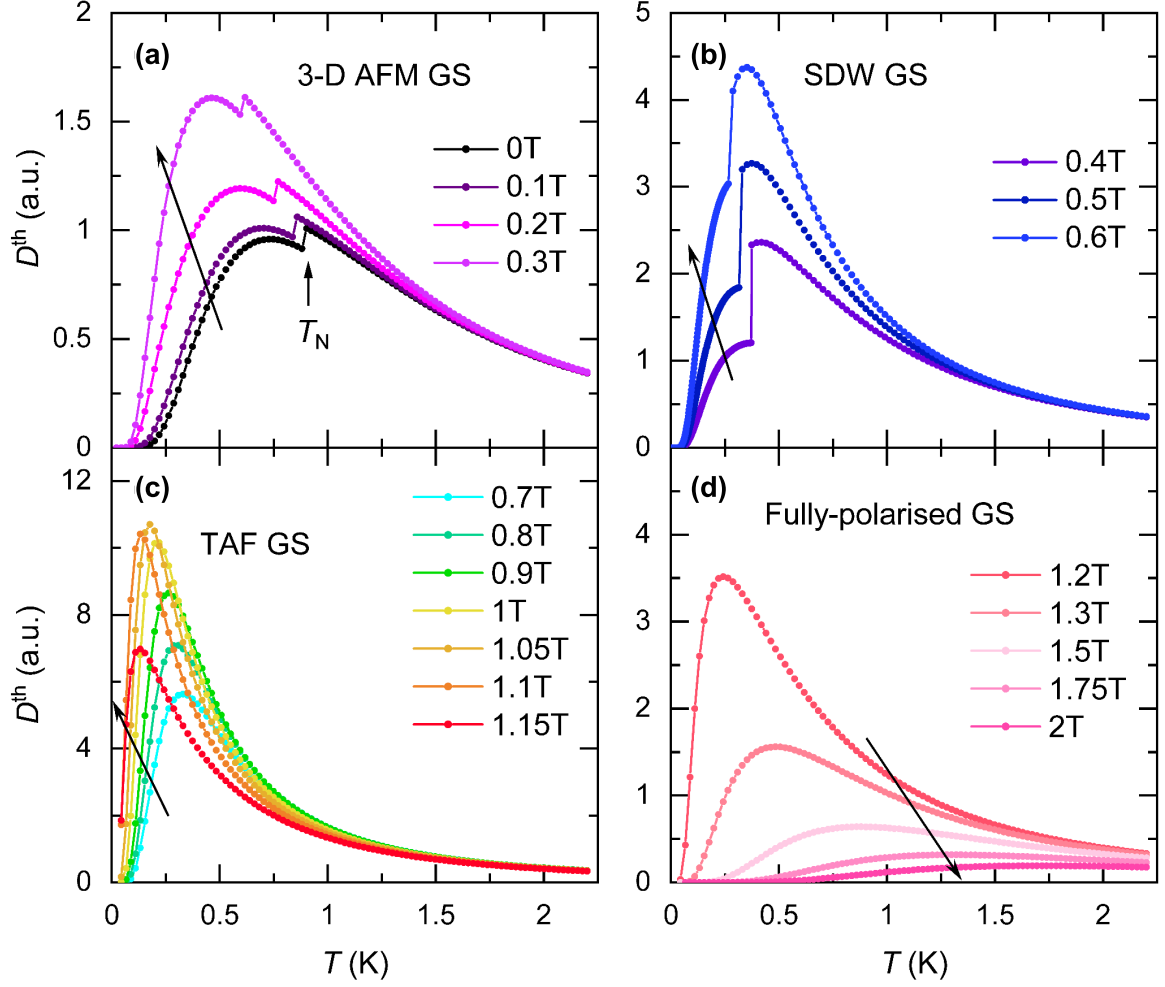
Figure 7.5: Overview of the calculated thermal Drude weight in terms of Dth versus T with **(a)** 3D-AFM, **(b)** SDW, **(c)** TAF, and **(d)** FP ground states. Note different scales of the y-axis in different panels. The arrows indicate the order of the curves per increasing B.

where $c_{\sigma_1, \sigma_2, \sigma_3, \ldots, \sigma_L}$ is to normalise the wavevector. The GS can be obtained by TEBD from an arbitrary initial state

$$|\Psi_t\rangle = \frac{\exp\left(-\hat{\mathcal{H}}t\right)|\psi\rangle}{\left\|\exp\left(-\hat{\mathcal{H}}t\right)|\psi\rangle\right\|}, \tag{7.4}$$

and $\|\|$ is to get the norm of a wave vector. Once the imaginary time evolution of the state is converged to the GS, one can calculate the current-current correlation function from real time evolution

$$J^{\text{th,th}}(\omega) = \int \mathrm{d}t e^{i\omega t} < \hat{j}_{\text{th}}(t)\hat{j}_{\text{th}}(0) >, \tag{7.5}$$

and the energy-current operator

$$\hat{j}_{\text{th}} = J^2 \sum_l \hat{\boldsymbol{S}}_l \cdot (\hat{\boldsymbol{S}}_{l+1} \times \hat{\boldsymbol{S}}_{l+2}), \tag{7.6}$$

sums over all the sites of the chain [161]. Finally, the thermal Drude weight is

$$D^{\mathrm{th}}(T) = \lim_{E_n = E_{n'}} \frac{\pi\beta^2}{N} \sum_{n,n'} \frac{e^{-\beta E_n}}{Z} \frac{\langle n|\hat{j}_{\mathrm{th}}|n'\rangle \langle n'|\hat{j}_{\mathrm{th}}|n\rangle}{\omega + E_n - E_{n'} + i\nu}$$

$$\approx \frac{\pi\beta^2}{N} \sum_{\substack{n,n' \\ E_n = E_{n'}}} \frac{e^{-\beta E_{n'}}}{Z} \left| \langle n|\hat{j}_{\mathrm{th}}|n'\rangle \right|^2, \tag{7.7}$$

with $\beta = 1/k_{\mathrm{B}}T$, N is the number of the lattice sites, Z being the partition function, $|n\rangle$ ($|n'\rangle$) refers to the eigenstate of the Hamiltonian $\hat{\mathcal{H}}$ with the eigenenergy of E_n ($E_{n'}$) as described in Relation 4.37 in Chapter 4.

This numerical work, including different magnetic phases, requires a longer time. In what follows, I present the primary results of the calculated thermal Drude Weight by the theoretical colleagues, *Rong Yu* and *Guijing Duan*. The results are given in arbitrary units because Yu *et al.* considered a single chain with no finite cross-section, not a 3-D sample. Therefore, they leave the units in calculation arbitrary to emphasise that the results are only to make a qualitative comparison between experiments and theory. Since these results are irrelevant for the quantitative comparisons or any further calculations of the transport properties, I will also discuss the overall trends and/or features in the following.

Starting with T evolution, Figure 7.5 illustrates the calculated $D^{\mathrm{th}}(T)$ curves with different GS. In any phase, Yu *et al.* found a single peak, the position of which changes slightly with increasing B. Within the 3-D AFM phase in panel **(a)**, the Dth increases per increasing B and the peak position shifts to lower T smoothly. The same behaviour of Dth is observed within the SDW phase shown in panel **(b)**, which appears to have a faster rise of Dth but a slower shift of the peak position to lower T. Within the TAF phase (panel **(c)**), however, the peak height grows much faster to reach its maximum around 1.1 T, and the position of the peak moves to lower T by increasing B, similar to the lower B within the 3-D and IC phases in panels **(a)**-**(b)**. Aside from the overall growth of the peak height in the TAF state, $D^{\mathrm{th}}(T)$ increases drastically at T below the peaks and lowers above. No transition is added to the curves with the TAF GS since the calculations of Yu *et al.* are not for the QC region [227]. Inside the FP state (panel **(d)**), the evolution changes in the other direction; the spectral weight decreases in B, and the peak position shifts to higher T.

Figure 7.6 **(a)** depicts $D^{\mathrm{th}}(B)$ at $T = 0.1$ K and 0.25 K. The points are interpolated from the $D^{\mathrm{th}}(T)$ curves plotted in Figure 7.5. D^{th} within the 3-D AFM region increases gradually per increasing B and then undergoes a first-order transition (according to the calculations in [77]), where the GS changes to the SDW phase. D^{th} grows stronger in the 3-D AFM phase than within the SDW state. It is noteworthy that in these calculations, Yu *et al.* considered the TAF GS starting above 0.6 T; however, as discussed in Chapter 6 Section 6.7, the V-shaped anomaly found in this work and the corresponding plateau region around $M(B) \sim M_{\mathrm{s}}/3$ belong to the SDW state. Therefore, recalculation of Dth in B up to 0.8 T with the SDW GS is required. The next first-order transition emerges from the SDW to the TAF phase, as theoretically predicted in [77]. A giant growth is observed by increasing B further to 1 T in the TAF phase. This growth and strong B dependence are attributed mainly to the increase in density of states and density of magnetic heat carriers with B [227]. Next, the system becomes fully polarised at about 1.1 T, where the Drude weight reaches a peak value. Comparing the curves at 0.1 K and 0.25 K, the overall behaviour is very similar; nevertheless, the detected giant growth appears mostly between 0.8 - 1.1 T at 0.1 K but from the lowest B at 0.25 K.
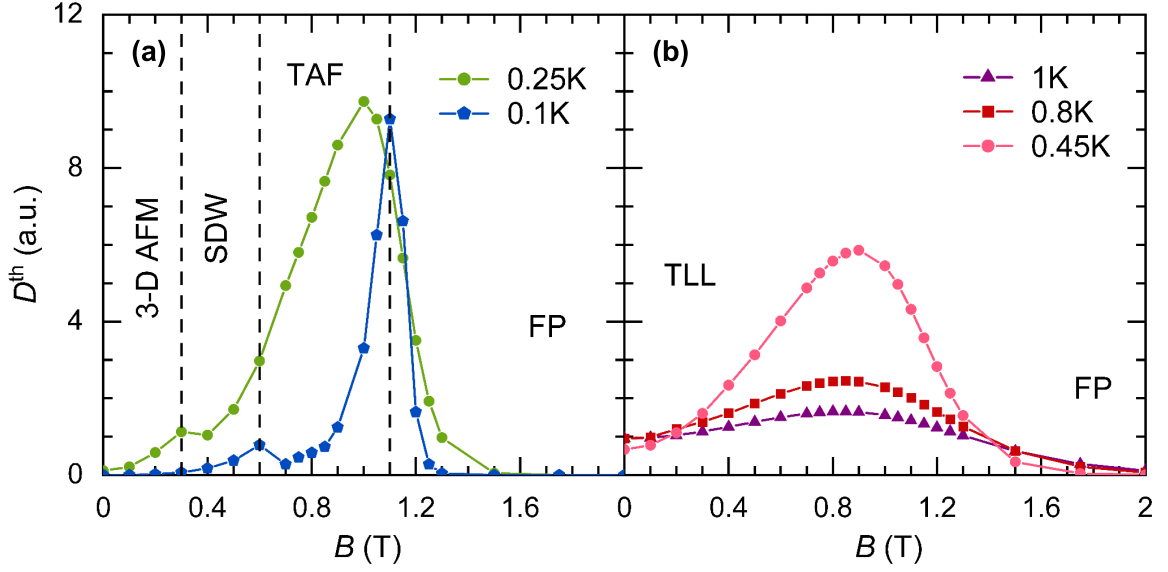
Figure 7.6: Overview of the calculated thermal Drude weight in terms of Dth versus B at T **(a)** below $0.3\,\text{K}$, and **(b)** above. More discussion is provided in the text.

Before moving on to panel **(b)**, one point is remarkable: By sweeping B around the first-order transitions, a jump/drop is expected [227]. In Figure 7.6 **(a)**, nevertheless, $D^{\text{th}}(B)$ appears more or less smooth at the first-order transitions. That is because the results at the phase boundary are inaccurate, e.g., do not consider the fluctuations. In addition, Yu *et al.* expect an unknown factor (< 10), which needs to be added to D^{th} in the SDW phase.

Figure 7.6 **(b)** represents D^{th} versus B at $T > 0.3\,\text{K}$. The TLL phase is expected above $0.8\,\text{K}$ at zero B and $0.3\,\text{K}$ for $B > 0.35\,\text{T}$ before spin polarisation. At $T = 0.45\,\text{K}$, D^{th} in zero B is already above zero (comparable with $D^{\text{th}}(0.35\,\text{T})$ at $0.25\,\text{K}$, for instance). $D^{\text{th}}(B)$ appears like a broad hump by increasing B with a maximum at $\sim 0.9\,\text{T}$ before going to zero around $2\,\text{T}$ within the FP region. Similar behaviour is observed for the $0.8\,\text{K}$ and $1\,\text{K}$ curves, with a decrease in the maximum height per increasing T. In fact, thermal fluctuations close to the exchange interaction energy destroy the magnetic ordering.

Finally, yet important, the peak position in $D^{\text{th}}(T)$ is around $J_{\parallel}$ in a simple model, e.g., [170]. Nevertheless, Yu *et al.* found the peak position at T much less than $J_{\parallel}$ and explained the difference as the theory provided in Section 4.5 is rather a rough estimate [227]. In the current calculation, the peak position varies with increasing B, but in a non-monotonic way.

Discussion: Here, I compare my experimental thermal conductivity of the magnetic excitations in YbAlO$_3$ with the numerical thermal Drude weight computed with the as-mentioned considerations. I recall that the calculations consider only the spin current without the effects of the phonons. Figure 7.7 compares $\kappa_{\text{mag}}(T) = \kappa_{\parallel}(T) - \kappa_{\text{ph}}(T)$ in zero B with 3-D AFM GS (panel **(a)**), $0.5\,\text{T}$ with SDW GS (panel **(b)**), $0.9\,\text{T}$ with TAF GS (panel **(c)**), and $2\,\text{T}$ with FP GS (panel **(d)**). Within the 3-D AFM state displayed in Figure 7.7 **(a)**, an exponential increase of $D^{\text{th}}(T)$ is predicted numerically owing to the spin gap, which reaches a peak around $0.4\,\text{K}$ in zero B. In this region, experimental $\kappa_{\text{mag}}(T)$ with $\kappa_{\text{ph}} = \kappa_{\text{ph, perp}}$ reveals a similar behaviour to the calculated $D^{\text{th}}(T)$, though the peak appears at about $20\,\%$ higher T at $\sim 0.5\,\text{K}$. Note that Yu *et al.* considered $J_{\parallel} = 2.2\,\text{K}$ in their calculations, which can scale the T values by $5\,\%$ by tuning the $J_{\parallel}$ value to $2.3\,\text{K}$. The Néel ordering
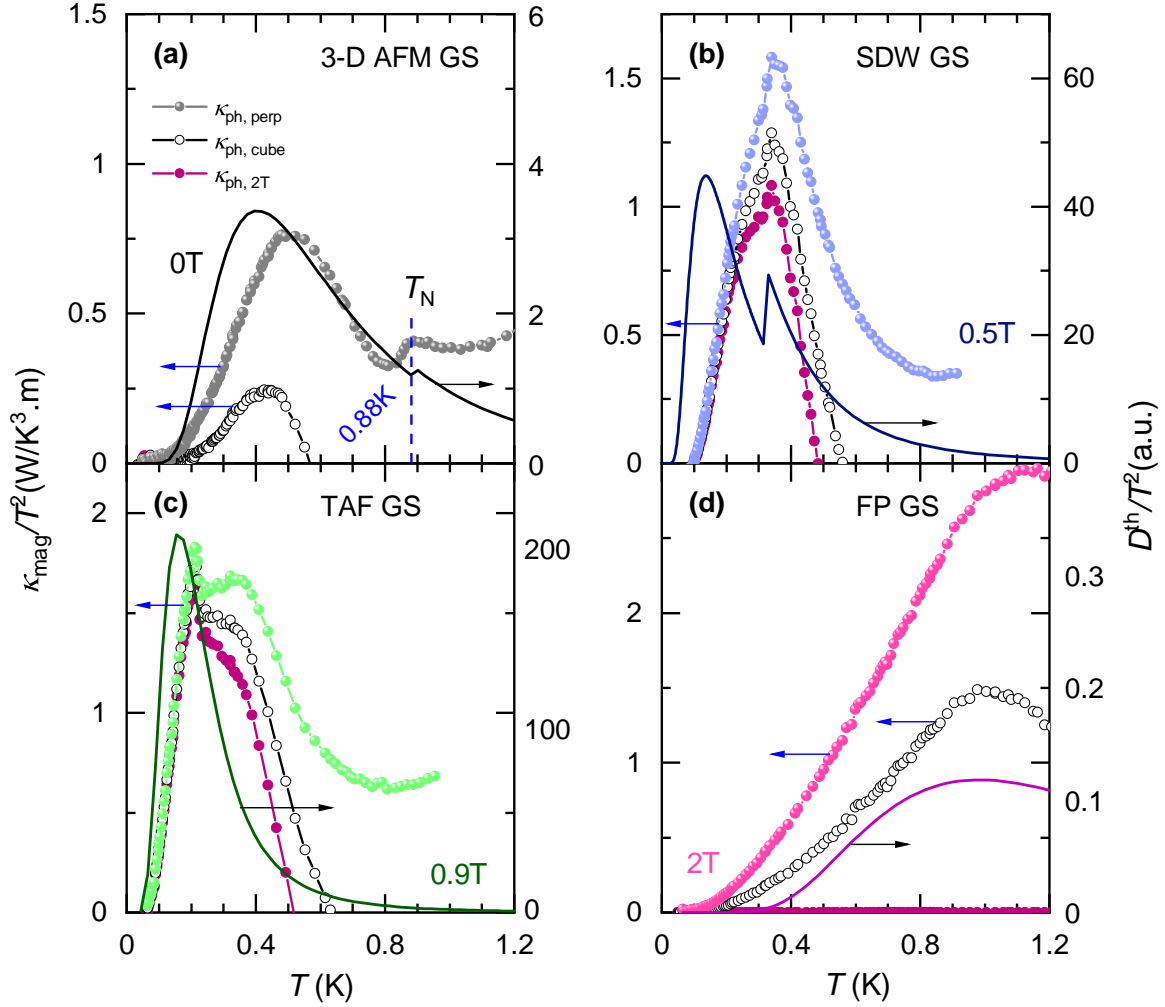
Figure 7.7: Comparison of experimental κ_{mag} with different possible phononic backgrounds (circle markers) and calculated thermal Drude weight (solid lines) of representative B with **(a)** 3-D AFM GS, **(a)** SDW GS, **(a)** TAF GS, and **(d)** FP GS. $\kappa_{ph,\ perp}$, $\kappa_{ph,\ cube}$, and $\kappa_{ph,\ 2T}$ as defined in Figure 7.1-7.4. Further discussion is provided in the text.

T in zero B is $\sim 0.88\,\mathrm{K}$. The corresponding phase transition appears as a drop in D^{th}/T^2 once lowering T, similar to $\kappa_{mag}(T)/T^2$ obtained from $\kappa_{ph} = \kappa_{ph,\ perp}$. Even though $0.88\,\mathrm{K}$ is the onset of the drop-like feature in the experiment, Yu *et al.* considered $T_N = 0.88\,\mathrm{K}$ as the drop offset at the transition and cut the curve before the transition at a slightly higher T. For $T > T_N$, Yu *et al.* considered Heisenberg chains without inter-chain couplings. The resultant $D^{th}(T)/T^2$ curve decreases per increasing T; however, $\kappa_{mag}(T)/T^2$ keeps rising in T. First, Yu *et al.* believe the numerical work and the model, especially within the TLL state, require further work. Second, the chains are isolated in the treatment of Yu *et al.* Hence, there can be an increasing trend in the theoretical curve depending sensitively on how to treat the inter-chain coupling. Another possibility is that $\kappa_{ph,\ perp}$ underestimates the phononic conductivity. In that case, κ_{ph} grows faster than $\kappa_{ph,\ perp}$ in T.

In the case of $\kappa_{ph} = \kappa_{ph,\ cube}$ shown with empty circles, the position of the peak within the 3-D AFM phase is akin to $D^{th}(T)$ around $0.4\,\mathrm{K}$. That is, while above $0.6\,\mathrm{K}$, $\kappa_{ph,\ cube}$ gives

negative values to κ_{mag}, i.e., overestimation of the phononic contribution. $\kappa_{\mathrm{ph,\,2T}}$ predicts $\kappa_{\mathrm{mag}} \leq 0$ within the full T range (see also Figure 7.4). That can be in line with the numerics if the calculated $D^{\mathrm{th}}(T)$ is too small to be probed in the laboratory in the whole T range.

In the case of the $0.5\,\mathrm{T}$ curves shown in Figure 7.7 **(b)**, $D^{\mathrm{th}}(T)/T^2$ grows faster than all the three $\kappa_{\mathrm{mag}}(T)/T^2$ curves at $T < 0.1\,\mathrm{K}$. That is followed by a maximum around $0.15\,\mathrm{K}$ and a reduction up to the transition $T \sim 0.3\,\mathrm{K}$. By increasing T, the curve shows a jump at the transition, above which the $D^{\mathrm{th}}(T)/T^2$ decreases continuously. In the experimental curves of $\kappa_{\mathrm{mag}}(T)/T^2$, a strong scattering was observed below $0.1\,\mathrm{K}$, as discussed earlier, with magneto-elastic origin ignored in the calculations. As a result, the slower rise of the $\kappa_{\mathrm{mag}}(T)/T^2$ curves is not surprising. Per increasing T up to the transition, no peak is detectable, though a slope change appears around $0.2\,\mathrm{K}$, which can correspond to a peak suppressed by the scattering effects. At the transition, the experimental curves show a sudden rise of $\kappa_{\mathrm{mag}}(T)/T^2$ similar to the calculated thermal Drude weight of $D^{\mathrm{th}}(T)/T^2$. For T above the ordering point, experimental data points show a reduction per increasing T, though slower than the calculations. A significant factor within the SDW phase is that the system orders with an incommensurate wave vector, which makes it non-trivial to find exact results with a perfectly periodic lattice with the size of the system [227]. As mentioned earlier, the data in the SDW phase require renormalisation by a factor from the partition function calculations, which is unknown but still below 10 [227].

Figure 7.7 **(c)** compares $D^{\mathrm{th}}(T)/T^2$ to $\kappa_{\mathrm{mag}}(T)/T^2$ in $B = 0.9\,\mathrm{T}$ with the TAF GS. $D^{\mathrm{th}}(T)/T^2$ shows a peak at around $0.2\,\mathrm{K}$ and continuously decreases at higher T. In the B range with the TAF GS, the transition feature is weak, given that the order parameter is transverse, while in the model, the inter-chain coupling is treated as Ising type [227]. The experimental $\kappa_{\mathrm{mag}}(T)/T^2$ curves show a huge increase by rising T within the TAF state, with a maximum at about $0.2\,\mathrm{K}$, at which a drop appears at the transition T. This giant growth is in line with the behaviour of the $D^{\mathrm{th}}(T)/T^2$ curve. By increasing T further, the experimental data points show a weak T dependency up to around $0.4\,\mathrm{K}$, above which the curves decrease strongly. In $\kappa_{\mathrm{ph}} = \kappa_{\mathrm{ph,\,perp}}$, as the only BG giving non-negative κ_{mag}, the slope tends to an increasing trend at $T > 1\,\mathrm{K}$. However, data points above this T are not available. That is quite similar to the results in the previous panels at $T > T_{\mathrm{N}}$. I recall that Yu *et al.* completely neglected the inter-chain coupling in the disordered phase, which may explain deviations in the calculations from the measurements [227].

Figure 7.7 **(d)** plots the calculated $D^{\mathrm{th}}(T)/T^2$ and the experimental $\kappa_{\mathrm{mag}}(T)/T^2$ curves in $2\,\mathrm{T}$ representative of the fully-polarised GS. By virtue of the gap state, an exponential increase of $D^{\mathrm{th}}(T)$ is observed at low T in the numerical curve. Experimentally, the $\kappa_{\mathrm{ph,\,2T}}$ curve shows absolute zero since it assumes pure phononic contribution in this B. The $\kappa_{\mathrm{ph,\,perp}}$ and $\kappa_{\mathrm{ph,cube}}$ curves, however, show humps similar to the numerical curve. Notably, similar humps were also observed in the specific heat results (Figures 6.8 **(c)**-**(d)**). The hump in specific heat was also numerically predicted using quantum Monte Carlo simulations of a chain mean-field version of a 3-D model like the Hamiltonian in Relation 7.2 [77, 78]. Therefore, similar behaviour to the specific heat results is expected even though Yu *et al.* did not use the same method for calculating the thermal transport [227].

To sum up, $D^{\mathrm{th}}(T)/T^2$ shows a peak in all the states. In the experimental $\kappa_{\mathrm{mag}}(T)/T^2$ curves, similar behaviour is observed, nevertheless, with peak positions at higher T. κ_{mag} for $\kappa_{\mathrm{ph,\,2T}}$ is zero or negative at all T in the full T range of zero B and $2\,\mathrm{T}$ dissimilar to the numerical results, which can be the case if the predicted magnetic heat transport is too small to be probed or has dominant scattering effects. Above the ordering T, numerics

expect a faster decay of the magnetic thermal transport than the experiment. The main source of deviations between the numerics and experiment can be:

(i) In all the T ranges, the phononic channel of thermal conductance and the corresponding magneto-elastic effects are entirely ignored. That can lower thermal transport by suppressing and slowing the propagating magnetic heat carriers.

(ii) In the calculation, Yu *et al.* performed a mean-field approximation to the inter-chain coupling and treated the magnetic order parameter as a mean-field (see the Hamiltonian in Relation 7.2). To get more accurate data, we need to know how the order parameter evolves with T and whether this is consistent with the experiment. That is the information we currently do not know precisely. Therefore, Yu *et al.* adopted an empirical way by assuming the order parameter does not change in the ordered phase while it drops to zero in the disordered phase. Yu *et al.* believe that to be the most influential reason why the calculated curves do not match the experimental ones below T_N [227].

(iii) As mentioned, Yu *et al.* believe the numerical work and the model require further work above T_N. Furthermore, they predict that ignoring the inter-chain coupling is a significant source of deviations above the ordering T and around the QC region [227].

(iv) The provided calculations are believed to explain qualitatively the general trend of the magnetic thermal conductivity decoupled from the lattice. In fact, Yu *et al.* calculated the thermal Drude weight which is actually the weight of thermal conductivity in the zero frequency limit, i.e., $\kappa(\omega) = D^{\text{th}}(\omega) \cdot \tau$, where $\tau = \delta\omega$ is a delta function corresponding to zero frequency (see Chapter 4 Section 4.5). However, Yu *et al.* included the effect of scattering time in some form in the formula. They worked within the linear response theory and added the perturbation slowly, corresponding to a very long relaxation time [227]. Notwithstanding, the scattering time has T and B dependencies. That is among the corrections Yu *et al.* are working on to improve the primary results shown here. This last item also explains the difference in the order of magnitude of $D^{\text{th}}(T)$ and $\kappa_{\text{mag}}(T)$.

The $D^{\text{th}}(B)$ curves at different T were described in Figure 7.6. Here, I focus more on similarities and dissimilarities between the numerical thermal Drude weight and the $\Delta\kappa(B)$ curves from the experiment. Figure 7.8 compares $D^{\text{th}}(B)$ curves (full markers) interpolated from $D^{\text{th}}(T)$ plotted in Figure 7.5 and measured $\Delta\kappa(B)$ (empty markers) defined as $\Delta\kappa(B) := \kappa(B) - \kappa(B = 0)$ in this plot, at selected T.

Panel **(a)** plots $D_{\text{th}}(B)$ and $\Delta\kappa(B)$ at $T = 108.5\,\text{mK}$. Note that the scale between the calculated thermal Drude weight and experimental thermal conductivity is $1000 : 1$; in panels **(b)**-**(d)**, the curves are zoomed in to visualise the features the best, though black full markers follow the same scale of the panel (a). In $B \leq 0.3\,\text{T}$, a gradual increase of thermal conductivity and thermal Drude weight is observed per increasing B. Around 0.3 - 0.4 T, a first-order transition between the 3-D AFM and SDW phases occurs, which emerges as a sudden drop of $\Delta\kappa(B)$ once increasing B though rather smooth in $D^{\text{th}}(B)$. As mentioned earlier, an anomaly, e.g., jump/drop, is also expected theoretically in the thermal Drude weight; however, the current calculations are not very accurate at the phase boundary. Within the SDW, both D_{th} and $\Delta\kappa$ grow in B faster than in the 3-D AFM phase. Nonetheless, the measurements show a stronger change of $\kappa(B)$. I recall that calculating the total partition function within the SDW is non-trivial, and there remains an unknown factor. Yu *et al.* contemplate a renormalisation factor (still below 10) with a weak T and B dependency applied to the calculated D^{th} curves with SDW GS. Besides the renormalisation factor in the SDW state, as mentioned, they assumed the TAF GS to begin already above 0.6 T. B, above which the TAF GS starts, was found above 0.8 T in this research since
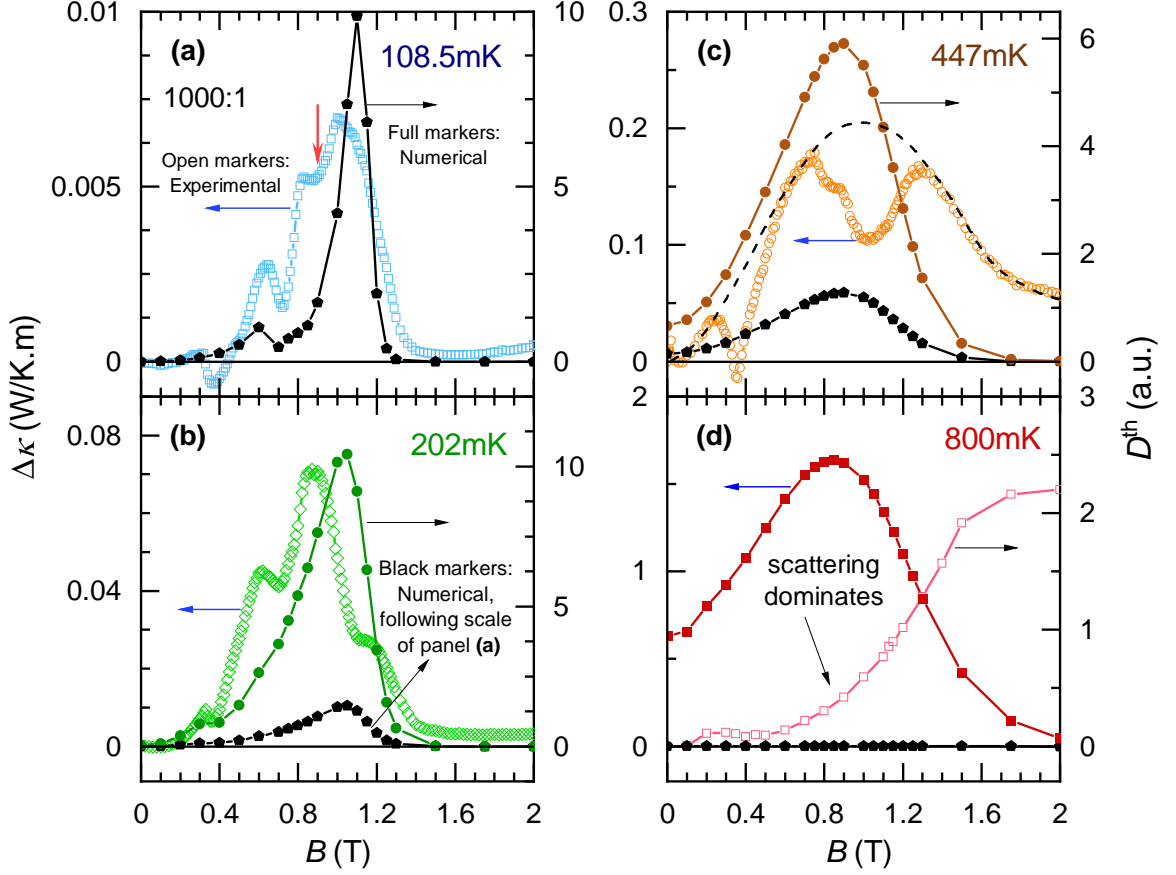
Figure 7.8: Calculated $D_{\text{th}}(B)$ and measured $\Delta\kappa(B)$ defined as $\kappa(B) - \kappa(B = 0)$ at **(a)** 108.5 mK, **(b)** 202 mK, **(c)** 407 mK, and **(a)** 800 mK. In each panel, the empty markers are experimental $\Delta\kappa$, and the full points are from the numerics. In panel **(a)**, $D^{\text{th}} : \Delta\kappa$ is $1000 : 1$. In the other panels, scales are changed to zoom the features, though the black full markers follow the same scale to panel **(a)**. More discussion is provided in the text.

the plateau region belongs to the SDW phase (see Chapter 6 Section 6.7). That means the tiny anomaly around 0.6 - 0.7 T must shift to higher $B > 0.8$ T, where the phase transition from the SDW to the TAF phase state takes place. Bear in mind that the plateau-type and V-shaped anomalies observed in $\kappa_{\parallel}(B)$ within the SDW state require more complicated calculations, including the inter-chain interactions. As mentioned earlier, investigations on the magnetisation plateaus and their effects on thermal conductivity are going on in theoretical collaboration with *Oleg Starykh* from the *University of Utah*.

Within the TAF phase, a huge B dependency and a change of slope is detectable in both D^{th} and $\Delta\kappa(B)$ (red arrow) at about 0.9 T, which reflects the rise of the density of states and the density of the magnetic quasiparticles carrying heat with B [227]. By increasing to $B \sim 1.4$ T, both curves drop almost to zero and remain B independent above as the system reaches the FP state. Panel **(b)** plots the calculated D^{th} and measured $\Delta\kappa$ versus B at 202 mK. The behaviours of both numerical and experimental curves are similar to the case of 108.5 mK described in panel **(a)**. The great increase within the mid-B region of the IC state is also observable in both D^{th} and $\Delta\kappa$ curves with a broader range. Some details in

$\kappa(B)$, such as the hump around 1.2 T, are not resolvable with the model used in the current calculations [227] (see also discussions above).

Panel **(c)** represents the Dth and $\Delta\kappa$ curves at 447 mK. At B above the Néel ordering B, two humps are observable in the specific heat, along with the thermal conductivity. However, one single hump is found numerically and does not match B of the two measured ones. That appears very different at first glance. Notwithstanding, two possibilities can simply explain the discrepancy: (i) Since the calculations do not include any magneto-elastic effects, the observed single hump of the numerics corresponds to an overall broad hump shown by a dashed line for visual help, and extra scattering effects around the phase transition between the 3-D AFM to the IC phase about 0.2 - 0.4 T and within the QC region. (ii) The observed peak in the calculations corresponds to the peak at higher B in the experiment. Whether there can be an additional low-B peak in the theoretical curve depends sensitively on how to treat the inter-chain coupling. Modifying the adopted isolated Heisenberg chains to one, including the couplings between them, may give rise to a second peak [227]. In Figure 7.7, it was already observed that the model does not describe the measured κ behaviour above the ordering T, and the given calculations cannot get the low-B peak [227]. The latter, however, is less probable since the specific heat capacity of the isolated Heisenberg chains, both theoretically and numerically, predicts the existence of the double-humps anomaly, e.g. in [77, 225]. Therefore, Yu *et al.* expect the single hump to merely appear in their primary calculations and not describe the physics of the system. Another feature is the substantial overall increase of the $\Delta\kappa(B)$ curve between zero and 2 T. I recall that in Figure 7.7, the measured κ_{mag} decayed slower than the calculated curves as well.

$D^{\text{th}}(B)$ and $\Delta\kappa(B)$ at 800 mK are shown in panel **(d)**. Substantial growth of $\Delta\kappa$ in B is seen, which is absent in the calculations similar to panel **(c)** at 447 mK. On top of the rising BG, $\Delta\kappa(B)$ is convex, while $D^{\text{th}}(B)$, carrying only the magnetic current, is concave downward. The opposite concavity can stem from the dominant scattering effects in the system. Still, as mentioned several times, in this T range, the adopted model is too simple, and it is not certain if the primarily calculated $D^{\text{th}}(T)$ is reliable, as revealed by the dissimilarities in panel **(c)** at 447 mK as well.

In conclusion, the theoretical results are consistent with the experiment qualitatively, both confirming considerable thermal conductivity via the magnetic excitations, particularly in the mid-B region with IC GS. Quantitatively, given that the experimental system is 3-D with more complicated interactions than captured by the simple 1-D model adopted numerically, the observed differences are not surprising.

7.3 Other remarks

Besides the aforementioned notes on YbAlO$_3$, two additional remarks are noteworthy here.
Quantum criticality near the QCP: Wu *et al.* reported two peaks in $C(B)$, one between the TLL and QC regions and the other before the FP state [74]. A similar feature with a two-hump structure is detected in $\kappa_{\parallel}(B)$ of the current work. The phase diagram, including the transitions and humps, is plotted in Figure 7.9. See Section 6.7 for a detailed description. As mentioned before, the position of the hump anomalies in $\kappa_{\parallel}(B)$ lies almost on top of the $C(B)$ data. Here, I investigate the behaviour of the maxima of the double-hump structure observed in $\kappa_{\parallel}(B)$. In what follows, I call the position of the maxima at lower and higher B, respectively, *left* and *right* arms of the QC fan in the phase diagram, though no rigid line is supposed to indicate the borders of the QC state. In a simple model,
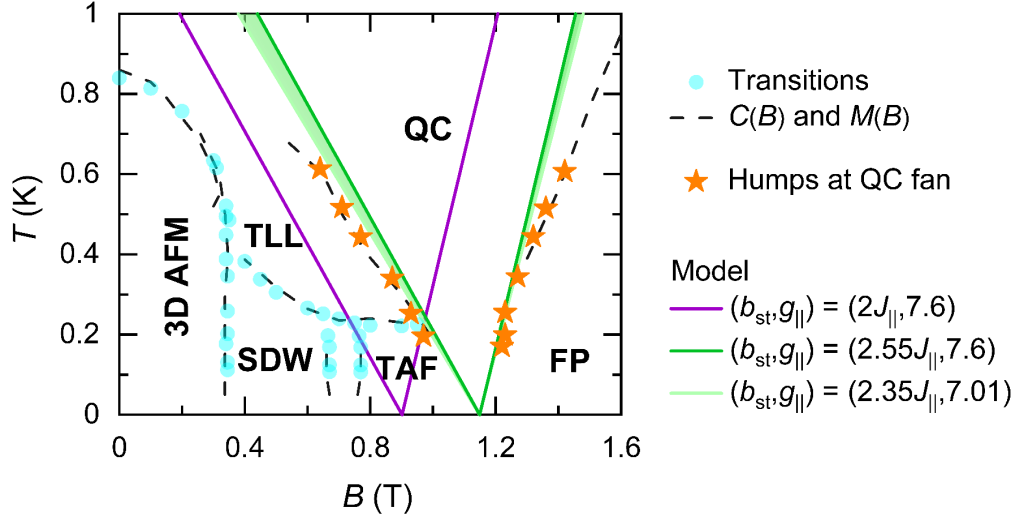
Figure 7.9: QC fan behaviour of YbAlO$_3$ as a Q-1-D spin system. The stars are from the $\kappa_\parallel(B)$ measurements of this work. The dashed lines refer to the phase diagram obtained via the specific heat and magnetisation measurements in previous studies [71, 74, 79]. The solid lines show the predictions for the QC fan of the 1-D Heisenberg chains within the TBA framework with the parameters in the legend. More explanation is in the main text.
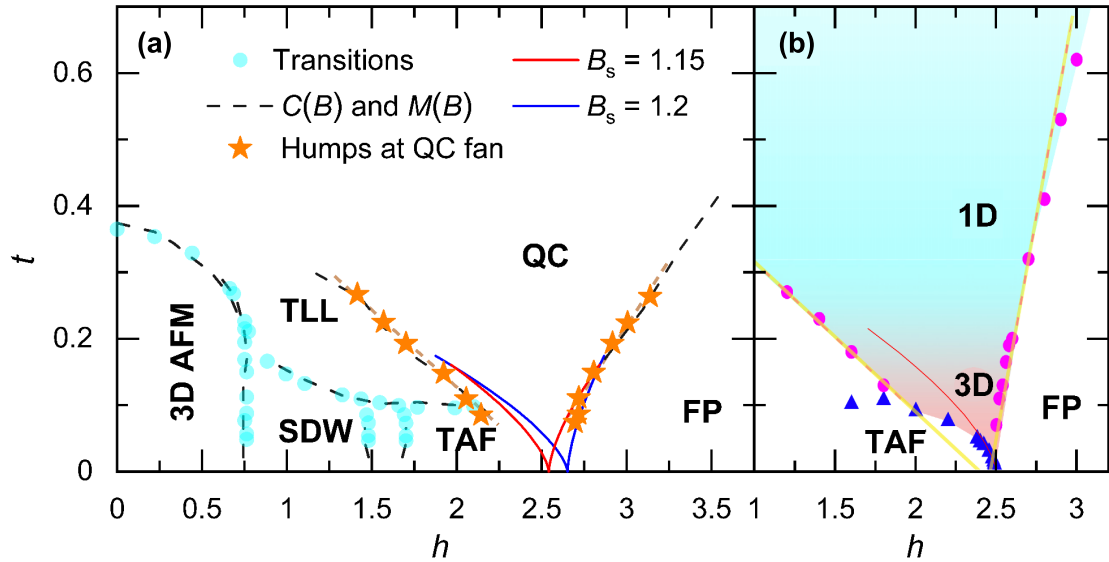

Figure 7.10: Quantum criticality and dimensionality near the QCP. **(a)** Reduced phase diagram of this work. The red and blue lines are the fit with $B_s = 1.15\,\mathrm{T}$ and $1.2\,\mathrm{T}$, respectively. **(b)** Crossover from 1-D to 3-D, reproduced from [78]. More explanation is given in the text.

I adopt the thermodynamics Bethe ansatz (TBA) describing the specific heat behaviour of isolated 1-D Heisenberg spin chains in the vicinity of the 1-D saturation QCP as [230, 231]

$$\frac{c}{T} = R\sqrt{\frac{m}{T}}F(\frac{r}{T}). \tag{7.8}$$

In this relation, the universal scaling function $F(X)$ is

$$F(X) = \frac{1}{4\sqrt{2\pi}}[-4X(XLi_{-\frac{1}{2}}(-e^{-X}) + Li_{\frac{1}{2}}(-e^{-X})) - 3Li_{\frac{3}{2}}(-e^{-X})], \tag{7.9}$$

where $Li_n(Z)$ has a polylogarithmic functionality (see Supplementary Materials of [225]). Moreover, $R = 8.314\,\mathrm{J\,mol^{-1}\,K^{-1}}$ is the gas constant, $m = 1/J_\parallel$, and r is the deviation of the field from the saturation that is $r = b - b_{\mathrm{s}}$. The saturation field b_{s} of the 1-D Heisenberg chains equals $2J_\parallel$ [225]. It must be noted that having the input of the $F(X)$ function requires X to be dimensionless, and thus, $r = b - b_{\mathrm{s}}$ in Relation 7.8 is in units of Kelvin. The conversion relation between b in Kelvin and B in Tesla can be found simply by

$$B[\mathrm{T}] = b[\mathrm{K}] \times \left(\frac{k_{\mathrm{B}}}{J_\parallel} \cdot \frac{J_\parallel}{g\mu_{\mathrm{B}}}\right) = b[\mathrm{K}] \times \left(\frac{k_{\mathrm{B}}}{g\mu_{\mathrm{B}}}\right), \tag{7.10}$$

$$\Rightarrow B[\mathrm{T}] = b[\mathrm{K}] \times \left(\frac{1}{g} \cdot \frac{8.617 \cdot 10^{-5}[\mathrm{eV\,K^{-1}}]}{5.788 \cdot 10^{-5}[\mathrm{eV\,T^{-1}}]}\right) = b[\mathrm{K}] \times \left(\frac{1.489}{g}\,[\mathrm{T\,K^{-1}}]\right). \tag{7.11}$$

To explore the behaviour of the arms of the QC fan in the system of 1-D Heisenberg spin chains, I determine the position of the peaks in the specific heat and thus request $\partial_B c = 0$. Considering $\partial_B T = 0$ as T and B are independent tunable parameters, one finds

$$\partial_B c = R\sqrt{mT}\,\partial_B F(\frac{r}{T}) = R\sqrt{mT}\,\frac{\partial_B r}{T} \cdot \partial_X F(X) = R\sqrt{\frac{m}{T}}\partial_X F(X), \tag{7.12}$$

$$\partial_B c = 0 \qquad \Rightarrow \qquad \partial_X F(X) = 0. \tag{7.13}$$

The maxima of the scaling function $F(X)$ occur at $X_1 \simeq -3.62$ and $X_2 \simeq 1.56$, corresponding to the extrema with B below and above the saturation field, respectively [225].

$$X_i = r_{\mathrm{c}}/T \qquad \Rightarrow \qquad r_{\mathrm{c}} = X_i T \qquad \Rightarrow \qquad b_{\mathrm{c}} = b_{\mathrm{s}} + X_i T \qquad i \in \{1,2\},$$

$$\Rightarrow \qquad b_{\mathrm{c}} = \begin{cases} b_{\mathrm{s}} + X_1 T = b_{\mathrm{s}} - 3.62T, \\ b_{\mathrm{s}} + X_2 T = b_{\mathrm{s}} + 1.56T. \end{cases} \tag{7.14}$$

Relation 7.14 gives equations of the left and right arm of the QC fan of the isolated chain, and the index *cr* stresses the position of the extrema. The linear behaviour of the QC fan borders is a characteristic of a 1-D world [225]. Relation 7.14, describing the expected borders of the QC fan of the isolated 1-D Heisenberg spin chains ($b_{\mathrm{s}} = 2J_\parallel$), with $g_\parallel = 7.6$ as obtained via the magnetisation experiments in [59], is plotted in Figure 7.9 in purple. I recall Relation 7.8, and thus the following Relation 7.14, carries a universal scaling due to the assumption of the ideally isolated 1-D chains. Entanglements between the spin chains in the case of YbAlO$_3$, however, can arise in non-universal terms in the relation functionality [227]. That can be relevant that the plotted lines with the assumption of isolated chains (purple lines) are offset horizontally compared to the position of the humps in the $\kappa_\parallel(B)$

data of YbAlO$_3$. A better description of the experimental data is by $b_s = 2.55 J_\parallel$. That is shown by green lines in Figure 7.9. Although the extrapolation to zero T of the corresponding fitted lines fits well to the centre of the left and right border of the QC region (stars), the slopes of the green lines are steeper in both arms. According to Relation 7.11, reducing g can help to steepen the slopes. The shaded area indicates the influence of changing $g_\parallel$ from 7.6 to 7.01, reported from the ESR measurements [73]. Lowering the g value lessens the slopes slightly; nevertheless, the solid lines do not meet the experimental points perfectly. Ultimately, I would like to emphasise that within the theories like the used TBA, the thermodynamics property, namely specific heat, is calculated. The calculated specific heat, however, is one of the components of the thermal conductivity formula (see Relation 4.6). Serious complexities arise in the modelling and computing of the scattering rates/mean-free paths. The fact that the results of the current work reveal that the linear behaviour of the 1-D QC fan is also observable in the thermal-transport measurements is fascinating.

By decreasing T, the system is expected to display a crossover from 1-D to 3-D owing to the Q-1-D structure of YbAlO$_3$. In the following, I look at the scaling behaviour of the peak positions $B_c(T)$ at lower T for a 3-D system. Fan *et al.* [78] argued that at finite-T in the vicinity of the QCP, $h_c(t)$ follows the scaling relation of $|h_s - h_c(t)| \sim t^{d/2}$, where $d = 3$ is the spatial dimension, hence

$$|h_s - h_c(t)| \sim t^{3/2}, \tag{7.15}$$

and the reduced T and B are defined as

$$t = \frac{1}{k_B J_\parallel} T, \qquad \text{and} \qquad h = \frac{g \mu_B}{J_\parallel} B. \tag{7.16}$$

Though the work of Fan *et al.* is for the thermodynamics probes, I apply the same model to the thermal conductivity data since the position of the QC fan border obtained via $\kappa_\parallel(B)$ matches the specific heat data well. Figure 7.10 **(a)** shows the reduced phase diagram. The crossover between 1-D and 3-D is modelled by Relation 7.15 using $B_s = 1.15\,\text{T}$ and $1.2\,\text{T}$ shown in a red and a blue line, respectively. Though the data points are only down to $\sim 0.2\,\text{K}$, the deviation of the right arm of the QC fan at low T is already somewhat reproduced by the blue line. Figure 7.10 **(b)** shows the calculated crossover $h_c(t)$ close to the QCP by Fan *et al.* in [78]. The red circles and the blue triangles are for the specific heat and the magnetic susceptibility. The dashed lines are linear fits. The red solid line is a power-law fit similar to Relation 7.15. The colour scheme illustrates a 1-D to 3-D crossover in the QC regime upon cooling.

Spin polarisation: At last, I would like to argue the influence of spin polarisation on the measured thermal conductivity. Note that I use the corrected $\kappa(B)$ curves to avoid the effects of non-*in-situ* calibrations in B sweeps, e.g., unreal BG of the curves increasing in B. Determining the polarisation point at B above which $\kappa^c(B)$ gets almost B independent, Figure 7.11 **(a)** displays the $\kappa_\parallel^c(B)$ results in different T including full violet stars which indicate the polarisation points. The empty stars and circles are for the double-hump anomaly described in Chapter 6 Section 6.7. An exemplary curve of $\kappa_\parallel^c(B)$ at $259\,\text{mK}$ is given in panel **(b)**, with dashed lines used to show big changes in the slopes of the curves. The empty stars and circles are for the double-hump anomaly described in Chapter 6 Section 6.7. Figure 7.11 **(c)** plots $\kappa_\parallel^c(B)$ at $127\,\text{mK}$ and $\kappa_\perp^c(B)$ at $124\,\text{mK}$, thus $T \sim 125\,\text{mK}$. The red hexagonal markers point out the boundaries of the B range with the TAF GS indicated by the excessive scattering leading to reduced $\kappa_\perp$. Through a similar treatment as in panels
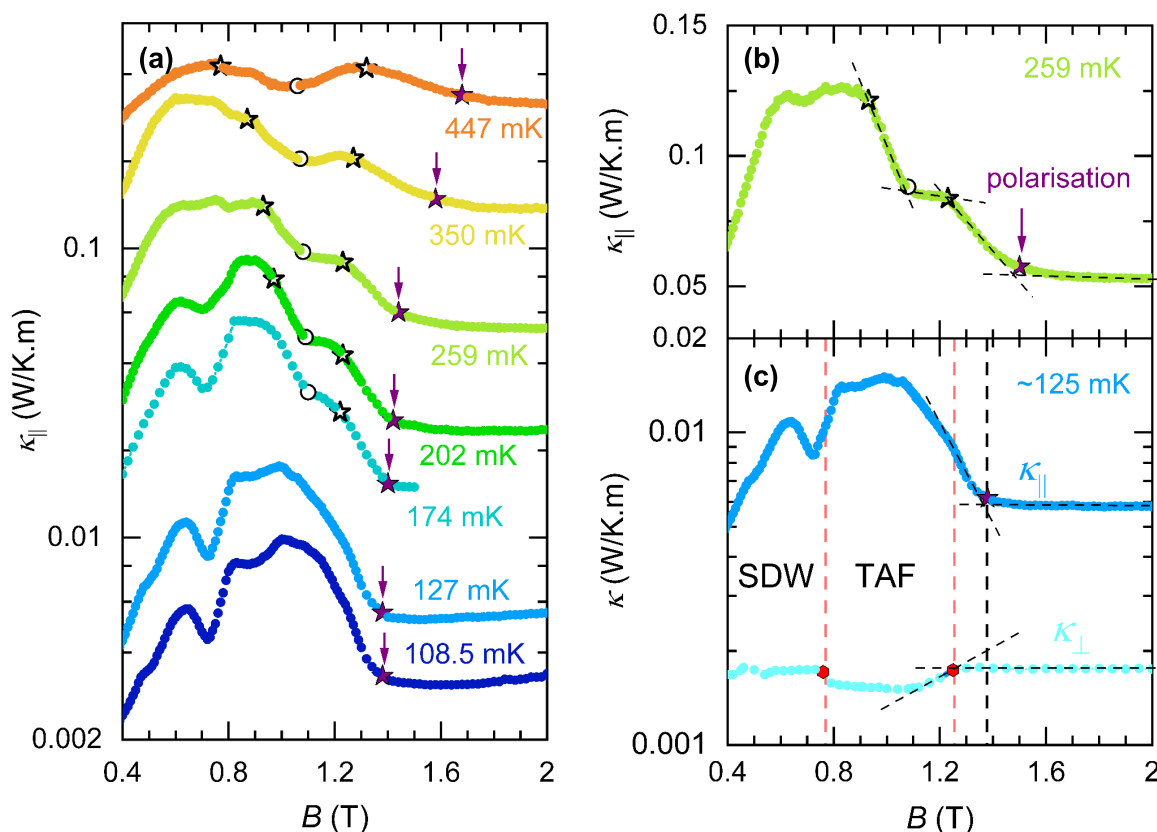
Figure 7.11: Polarisation effect on the thermal conductivity results. **(a)** $\kappa_\parallel^c(B)$ curves including the polarisation point as indicated in panel **(b)**. **(b)** Exemplary curve of $\kappa_\parallel^c(B)$ at 259 mK. **(c)** $\kappa^c(B)$ at $T \sim 125$ mK along and perpendicular to the spin chains. $\kappa_\perp(B)$ gets independent at lower B compared to the $\kappa_\parallel(B)$ curve. More discussion is given in text.

(a)-(b), here, the red marker at higher B shows B above which $\kappa_\perp^c(B)$ gets almost B independent. Therefore, $\kappa_\perp(B)$ gets independent at lower B than the $\kappa_\parallel(B)$ curve. The vertical lines are guides for the eyes between the curves. Such phenomena can be a result of differences between the spin-spin and spin-lattice relaxations, which can be characterised by probes sensitive to lattice relaxation, for instance, nuclear magnetic resonance (NMR) spectroscopy. NMR spectroscopy, as a strong proper tool to resolve the fluctuating moments, is hence suggested to be performed on YbAlO₃, in particular, close to saturation around the TAF phase, to study the decay to equilibrium of the excited moments.

Finally, Figure 7.12 shows the phase diagram from $\kappa_\parallel(T)$ and $\kappa_\parallel(B)$ measurements as discussed in Chapter 6 Section 6.8, including the points above which $\kappa_\parallel(B)$ (purple stars) and $\kappa_\perp(B)$ (red hexagonal) get almost B independent. The polarisation points for $\kappa_\parallel$ follow a fair linear behaviour in B and T, while those of $\kappa_\perp$ seem to coincide with the TAF phase boundary.
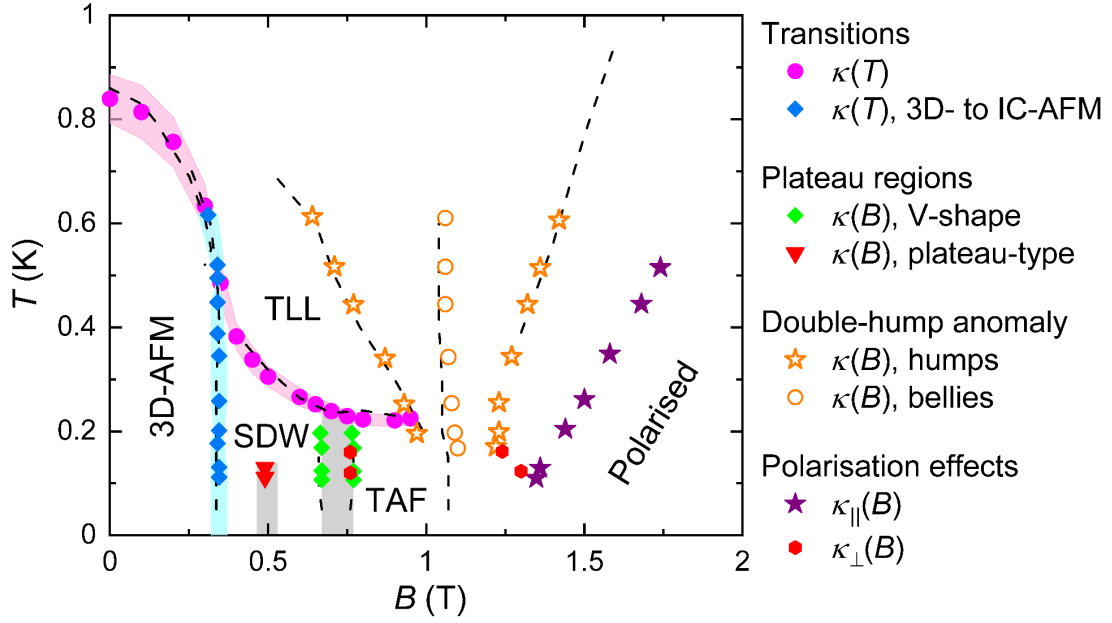
Figure 7.12: Phase diagram including the as-described polarisation points. The dashed lines are the points from the previous works with thermodynamics probes in [59, 71, 74, 79].

7.4 Conclusion and further work

Thermal conductivity κ of YAlO$_3$ from room temperature T down to 2 K was measured along the b and c crystallographic directions in order to get information on the phonon thermal transport in the iso-structural compound YbAlO$_3$. Experimentally-obtained κ along both axes was fitted numerically by the Callaway model with maximal 20 % deviations. The relative behaviour of κ of the two iso-structural sister compounds YAlO$_3$ and YbAlO$_3$ at high T was reproduced numerically and explained considering the Debye expression of phononic thermal conductivity and Umklapp phonon-phonon processes. Comparison between the high-T κ results of YAlO$_3$ to YbAlO$_3$ revealed that YAlO$_3$ is not beneficial for studying the lattice-thermal transport of YbAlO$_3$ due to the differences in the Debye temperature Θ_D, the Grüneisen parameter Γ and the T dependencies.

Thermal conductivity of YbAlO$_3$ was investigated within the dilution fridge T range, down to 30 mK. The mean free path λ of YbAlO$_3$ was found to be $\sim$200 µm, i.e., of the same order as the sample boundaries. Thermal conductivity along the spin chains $\kappa_{\parallel}$ show a cubic T dependency close to zero $T < 0.16$ K in $B = 2$ T, which changes to faster growth of $\kappa_{\parallel} \propto T^{3.26}$ up to about 1 K. That makes YbAlO$_3$ a candidate for hydrodynamic transport and Poiseuille flow of phonons. More measurements on YbAlO$_3$ are necessary to firmly prove the presence of the rarely-observed Poiseuille flow.

In the perpendicular direction, a reduction is observed in the exponent of $\kappa_{\perp} \propto T^3$ of YbAlO$_3$ to $\propto T^{2.56}$ for about $T > 0.15$ K. A significant suppression of κ perpendicular to the spin chains was reported before in one-dimensional spin systems such as CaCu$_2$O$_3$ and attributed to disorder or optical branches, which lessen the density of the propagating heat carriers. In the case of YbAlO$_3$, however, the calculations on the lattice band structure revealed the first optical branch at about 140 K, i.e., one to two orders of magnitude higher than T at which the suppression is detected. The anisotropy of the thermal transport between the two

crystallographic axes of c and b reduces about $1/3$ by increasing T from $30\,\mathrm{mK}$ to $300\,\mathrm{K}$. The reason for the strong T dependency of the lattice transport is still in question. The optical modes may play a role in abnormal thermal transport anisotropy. Further experimental investigation on the phononic branches and possible softening of the optical phonons are thus suggested via high-energy inelastic-neutron spectroscopy and Raman spectroscopy.

A pure phononic thermal conductivity with a cubic-T dependency is observed in $YbAlO_3$ at the lowest T within the ordered and fully-polarised states. The three-dimensional anti-ferromagnetic state is gapped owing to the confinement of the spinon pairs once cooling from the Tomonaga-Luttinger liquid phase below the ordering Néel T. Therefore, the additional thermal conductance to the extrapolation of T^3 at the lowest T within the three-dimensional anti-ferromagnetic ground state was modelled by an $\exp(-\Delta/k_{\mathrm{B}}T)$ term as expected for the thermal conductivity of the gapped magnons. The measured curves fitted the best with an energy gap half of the values from the neutron spectroscopy, which means that thermodynamics carries the information of a single spinon while spectroscopy is associated with spinon pairs. Three possible cases for phononic thermal transport for higher T are considerable: (i) Thermal conductivity of the perpendicular axis multiplied by the lattice-anisotropy coefficient, (ii) extrapolation of the T^3 behaviour at the lowest T, and (iii) the thermal conductivity along the spin chains in a field B which is high enough so that the spins are fully polarised. A vast enhancement of $\kappa_\parallel$ was observed in the mid-B region with an incommensurate anti-ferromagnetic ground state, which exceed the highest possible description of the phononic thermal conductivity. Thus, the enormous rise is attributed to an immense contribution of the magnetic channel to thermal transport.

$\kappa_\parallel$ showed a strong B dependency, particularly at $T < 0.5\,\mathrm{K}$. Within the spin-density wave state, two plateau regions around $M \sim M_{\mathrm{s}}/3$ and $M \sim M_{\mathrm{s}}/5$ are discovered, which appear in the $\kappa_\parallel(B)$ curves as a V-shape anomaly at $0.7\,\mathrm{T}$ and a plateau-type feature, respectively. These plateau regions in $YbAlO_3$ are under-study in collaboration with theorists.

For intermediate fields, the transverse anti-ferromagnetic ground state shows higher thermal conductance parallel to the spin chains than the spin-density wave phase. The canted transverse anti-ferromagnetic order,however, affects as a source of scattering in the perpendicular direction. A two-hump anomaly is observed in $\kappa_\parallel(B)$ below $0.7\,\mathrm{K}$, following the expected behaviour of the specific heat of the isolated chains.

The phase diagram was reproduced successfully by the thermal transport probe. All the features detected before via the specific heat and magnetisation measurements are detectable in thermal conductivity. In addition, the new features within the spin-density wave phase, namely the V-shaped anomaly and the plateau around $0.5\,\mathrm{T}$ in $\kappa_\parallel(B)$, are included in the phase diagram.

The transverse anti-ferromagnetic ground state is theoretically expected but not experimentally approved with the neutron scattering measurements due to the strong spin anisotropy of $YbAlO_3$. That makes the longitudinal excitations the main signal and the Bragg peak from the transverse anti-ferromagnetic phase with the cross-section of the transverse excitations $\propto g^2$ too weak. In this circumstance, the muon spin spectroscopy with incident beam carrying intrinsically perpendicular polarisation and moments or the polarised neutron spectroscopy is suggested. Besides, nuclear magnetic resonance spectroscopy is another proper tool to resolve the transversely excited moments via their relaxation times. For the latter, I made a successful proposal to *Stuart Brown*, University of California, Los Angeles. The milli-Kelvin NMR measurements shall start in October 2023.

Thermal Drude weight calculations approve strong magnetic heat transport specifically within the mid-B region with the incommensurate anti-ferromagnetic ground state.

To close, YbAlO$_3$ turned out as having sensitive phases to thermal transport. New existing physics, particularly within the spin-density wave incommensurate state, was discovered via thermal conductivity probe. A huge magnetic heat transport was detected. The phase diagram was reproduced including new features to what was reported via thermodynamic probes. There still exist open questions, which require further study and application of other type of measurements as proposed.

A Tomonaga-Luttinger liquid concept

As mentioned in Chapter 2, no individual excitations exist in one dimension, and the Landau description of the Fermi liquid collapses in favour of Haldane's description of the Tomonaga-Luttinger liquid (TLL). Looking for a way to describe the low-energy properties of one-dimensional (1-D) systems, in this appendix, I introduce shortly the concepts of *labelling field* and *bosonisation*, the TLL Hamiltonian and the spin-spin correlation functions, namely the most important properties of the TLL theory. For complete details on the TLL theory, the reader is referred to [7, 35, 232].

Labelling field and bosonisation: A density operator $\rho(x)$ of a 1-D system of particles is

$$\rho(x) = \sum_i \delta(x - x_i), \tag{A.1}$$

with x_i as the position operator of the i-th particle. In one dimension, the particles can be *labelled*, e.g., starting at $x = -\infty$ and processing to the right. Haldane proposed using a continuous function of labelling field $\phi_l(x)$ to write the density operator, taking the value

$$\phi_l(x_i) = 2\pi i, \tag{A.2}$$

at the position of the i-th particle [233]. Figure A.1 shows two instances of the labelling fields for particles in **(a)** equilibrium and **(b)** non-equilibrium positions. In the case of particles in an imaginary perfect equilibrium with lattice spacing d, $\phi_l^0(x) = 2\pi x/d$, where the index 0 emphasises on the equilibrium condition (Figure A.1 **(a)**). For the non-equilibrium case, it can be shown that $\phi_l(x) = 2\pi \rho_0 x - 2\phi(x)$, where ϕ is the displacement from the perfect crystalline position. That will be used later.

Substituting the labelling field and using the rules of transforming variable of the δ function, one can re-write the density operator in Relation A.1 as

$$\rho(x) = \sum_i \delta(x - x_i) = \sum_i |\nabla \phi_l(x)| \cdot \delta\left(\phi_l(x) - 2\pi i\right), \tag{A.3}$$
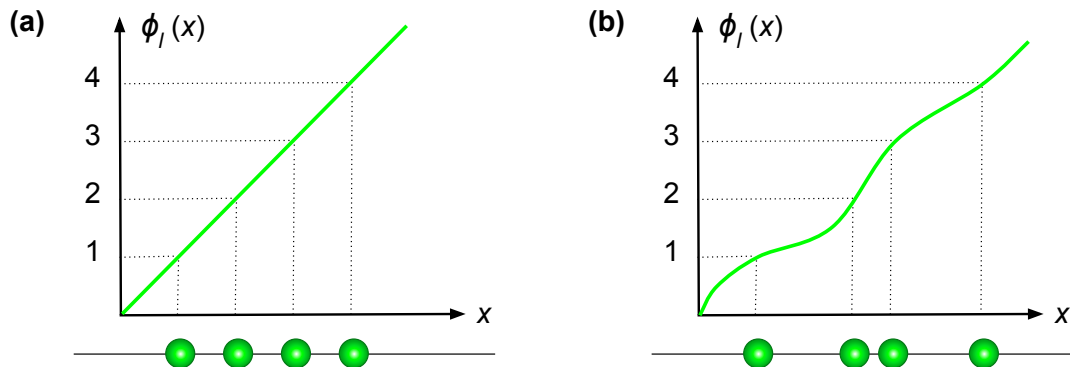
Figure A.1: Examples of the labelling field $\phi_l(x)$. **(a)** Particles forming a perfect lattice with lattice spacing d, then $\phi_l^0(x) = 2\pi x/d$ appears as a straight line. **(b)** $\phi_l(x)$ for particles out of equilibrium. Figure reproduced from [7].

though $\nabla\phi_l(x)$ is always greater than zero. Applying the Poisson summation formula, it can be shown that

$$\rho(x) = \frac{\nabla\phi_l(x)}{2\pi}\sum_p e^{ip\phi_l(x)}, \qquad \text{with} \quad p \in \mathbb{Z}. \tag{A.4}$$

The density can obviously be expressed in the same way in terms of the field $\phi(x)$

$$\rho(x) = \frac{\nabla\phi_l(x)}{2\pi}\sum_p e^{ip\phi_l(x)} = [\rho_0 - \frac{1}{\pi}\nabla\phi(x)]\sum_p e^{i2p(\pi\rho_0 x - \phi(x))}, \qquad \text{with} \quad p \in \mathbb{Z}. \tag{A.5}$$

Relation A.5 appears more complex than Relation A.1. However, the density in Relation A.1 is extremely singular as a set of delta functions at the places of the particles while in Relation A.5, everything is described in displacement off the perfect crystal. Therefore, the density is re-expressed by ϕ as a slowly-varying field changing at the scale of the lattice spacing at the inter-particle distance d via the representation of the collective variable. Thus, using the coordinate proposed by Haldane, one can apply a continuous description which is favourable in stabilising the effective low-energy theory. Note that the achieved expression is a kind of Fourier decomposition of the density. Different terms of the summation can be investigated, e.g. retaining the term $p = 0$ says that the density is the divergence of the field ϕ, but that is beyond the general description aimed here.

It is known that a single-particle creation operator $\psi^\dagger(x)$ can be described with the density operator and a second operator $\theta(x)$ giving the phase, e.g., in the case of a *bosonic* gas of particles

$$\psi_B^\dagger(x) = [\rho(x)]^{1/2}e^{-i\theta(x)}. \tag{A.6}$$

This technique of changing the variables is known as *bosonisation*, as it transforms fermionic degrees of freedom into new excitations with bosonic nature[1]. Note that the main idea is not to transmute the statistics but to find collective variables and excitations to describe the physics. Finally, the ϕ and θ phases are conjugate variables, i.e.,

$$[\frac{1}{\pi}\nabla\phi(x), \theta(x')] = -i\delta(x - x'), \tag{A.7}$$

yielding that the operators do not commute, the density is maximally disordered once the phase is ordered, and vice-versa. The density and phase do not order simultaneously and that is related to the extreme quantum fluctuations of the 1-D physics.

Hamiltonian: The Hamiltonian built of a summation of the kinetic and potential energies is

$$\hat{\mathcal{H}} = \int dx \cdot \frac{\nabla\psi^\dagger\nabla\psi}{2m} + g\int dx \cdot (\psi^\dagger(x)\psi(x))^2, \tag{A.8}$$

where g is a coupling constant describing the strength of the interactions. The potential appears quartic in spite of the kinetic term which is quadratic. Re-writing the Hamiltonian in terms of the ϕ and θ operators gives

$$\text{kinetic term:} \qquad \int dx \cdot \frac{\nabla\psi^\dagger\nabla\psi}{2m} = \frac{\rho_0}{2m}\int dx \cdot (\nabla\theta)^2, \tag{A.9}$$

$$\text{interactions:} \qquad g\int dx \cdot (\rho(x) - \rho_0)^2 = g\int dx \cdot \frac{1}{\pi^2}(\nabla\phi)^2 + \text{oscillating terms.} \tag{A.10}$$

---

[1]However, the bosons are bosonied in this technique as well! Here, bosonisation carries the *collectivisation* meaning, and the name has some historical flavors.

Assuming integrating over the oscillating terms brings the average to zero, one reaches

$$\hat{\mathcal{H}} = [\frac{\rho_0}{2m} \int \mathrm{d}x \cdot (\nabla\theta)^2 + g \int \mathrm{d}x \cdot \frac{1}{\pi^2}(\nabla\phi)^2]. \tag{A.11}$$

Therefore, the Hamiltonian of the 1-D interacting system is described by a series of harmonic oscillators. Since the Hamiltonian is now in form of a simple harmonic oscillator problem, all the correlation functions are commutable at both zero and finite T (see the next paragraph).

It is convenient to re-parameterise the two coefficients as $uK \propto \rho_0/2m$ and $u/K \propto g$. These two numbers $u \propto \sqrt{g}$ and $K \propto 1/\sqrt{g}$, are the sound velocity of the propagating excitations, and the dimensionless parameter K, nicknamed the *Tomonaga-Luttinger liquid* parameter, respectively. The Hamiltonian becomes

$$\hat{\mathcal{H}} = \frac{\hbar}{2\pi} \int \mathrm{d}x [\frac{uK}{\hbar^2}(\pi\Pi(x))^2 + \frac{u}{K}(\nabla\phi(x))^2]; \tag{A.12}$$

The TLL theory, depends only on the two parameters u and K, characterising the low-energy properties of any mass-less 1-D system, and depending on the type and the strength of the interactions. The bosonic representation plays the same role for 1-D that the FL theory plays for higher-dimensional systems, and 1-D quantum liquids can be described using this theory in an adequate wide range of parameters [31, 33]. Since the TLL parameter K is proportional to $1/\sqrt{g}$, it starts from infinity for no repulsion, reduces by enlarging the repulsion and ends in $K = 1$ for infitively repulsive bosons.

Correlation relations: As the quadratic Hamiltonian is driven (Relation A.11), correlation relations can be computed. One is referred to elsewhere for a complete description [7]. A remarkable universal physics of the TLL is the power-law functionality of the correlation relations controlled by the TLL parameter K. As an instance, the spin-spin correlation functions turn out to be

$$< S^z(x,0)S^z(0,0) > = C_1\frac{1}{x^2} + C_2(-1)^x\left(\frac{1}{x}\right)^{2K}, \tag{A.13}$$

$$< S^+(x,0)S^-(0,0) > = C_3\left(\frac{1}{x}\right)^{2K+\frac{1}{2K}} + C_4(-1)^x\left(\frac{1}{x}\right)^{\frac{1}{2K}}, \tag{A.14}$$

where the C_i coefficients are non-universal amplitudes. All the terms decay as a power law with exponents that are controlled by K. The same is shown for other correlation functions of the 1-D systems, e.g., the single particle, density-density and etc., see ,e.g., [7].

To close, to describe the low-energy properties of the system within this theory, it is *enough* to compute the two coefficients u and K. These coefficients can be determined numerically, using either analytic calculations or by exact solutions. Therefore, the TLL theory coupled with the numerics, provides an accurate way to compute correlations and physical properties of the 1-D system.

B More details on the magnetic structure of YbAlO$_3$

B.1 Inter-chain interactions in YbAlO$_3$

The crystal structure and single-ion anisotropy of YbAlO$_3$ were described in Chapter 3. The Yb^{3+} magnetic moments can form only configurations in which the moments lie within the ab-plane and are tilted with respect to the a-axis by the angle $\varphi = 23.5°$. The selected configuration depends on the environment, e.g., applied magnetic field (B). Figure 3.2 **(d)** represented an instance of a possible configuration. Figure B.1 **(a)** illustrates four different magnetic structures allowed through representation analysis, labelled as $AxGy$, $GxAy$, $FxCy$, and $CxFy$. Thanks to the large local saturation moment of Yb^{3+} ($\sim 3.8\mu_{\mathrm{B}}$/Yb) at low temperature (T), the dipole-dipole interaction is not negligible in inter-chain interactions. Therefore, Wu *et al.* calculated the dipole-dipole energy (E_{dip}) of each of the four $GxAy$, $AxGy$, $FxCy$ and $CxFy$ magnetic structures to be $E_{\mathrm{dip}}/k_{\mathrm{B}} = -0.67\,\mathrm{K}$, $-0.29\,\mathrm{K}$, $-0.01\,\mathrm{K}$, and $0.38\,\mathrm{K}$, respectively[1] [59]. Thus, the $AxGy$ configuration is suggested as the ground state (GS) at low enough T consistent with the experimental observation below T_{N} = 0.88 K. Figure B.1 **(b)** plots the E_{dip} field dependency of each configuration. By applying B along the a- and b-axis, the ferromagnetic (FM) $FxCy$ and $CxFy$ configurations are favoured by the so-called *Zeeman interaction* [62], to be the new GS with critical fields of $\sim 0.3\,\mathrm{T}$ and $1.0\,\mathrm{T}$, respectively. Therefore, the calculations suggests a possible quantum critical (QC) region between 0.3 - 1.1 T for $B \parallel a$, where the $AxGy$ static magnetic ordering in the ab-plane is suppressed [74].

In the absence of interactions within the ab-plane, the two $AxGy$ and $GxAy$ configurations should be degenerate; nevertheless, the intra-plane interaction lifts the degeneracy selecting the static magnetic-ordering pattern in the ab-plane [234]. Looking for the GS between the two $AxGy$ and $GxAy$ anti-ferromagnetic (AFM) structures depending on the relative tilting angle of the Ising moments φ, Figure B.1 **(c)** shows E_{dip} as a function of the φ value, calculated in [59]. The red dashed line confirms the selected GS of YbAlO$_3$ with $\varphi = 23.5°$ to be $AxGy$.

B.2 Origin of staggered fields

Special magnetic configurations can generate staggered molecular fields (B_{st}) in a system. In the case of YbAlO$_3$, Wu *et al.* explained how magnetic sub-lattices provide B_{st} at very low T [74]. Figure B.2 illustrates the magnetic sub-structures of YbAlO$_3$ in the absence of any external B. Figures B.2 **(a)**-**(b)** demonstrate Yb^{3+} moments confined in the ab-plane at $c/4\,\hat{\boldsymbol{c}}$ and $3c/4\,\hat{\boldsymbol{c}}$, respectively, with $\hat{\boldsymbol{c}}$ being the unit vector along the c-axis. For a static moment on each Yb site of $3.8\mu_{\mathrm{B}}$/Yb, the dipole-dipole interactions between the nearest neighbours, J_1, J_2, J_3, and J_4 are calculated to be $-0.058\,\mathrm{K}$, $-0.037\,\mathrm{K}$, $-0.10\,\mathrm{K}$ and $0.03\,\mathrm{K}$ in the $c/4$-plane (see Supplementary Materials of [74]). The moments at $3c/4\,\hat{\boldsymbol{c}}$ are anti-

---

[1]In this attempt, 10 near-neighbour moments (eight within distance $\sim 5.7\,\text{Å}$ in the ab-plane and two of distance $\sim 4\,\text{Å}$ along the c-axis) were considered, and the effect of the neighbours at larger distances was reported to exhibit negligible variation in the dipole-dipole energy.
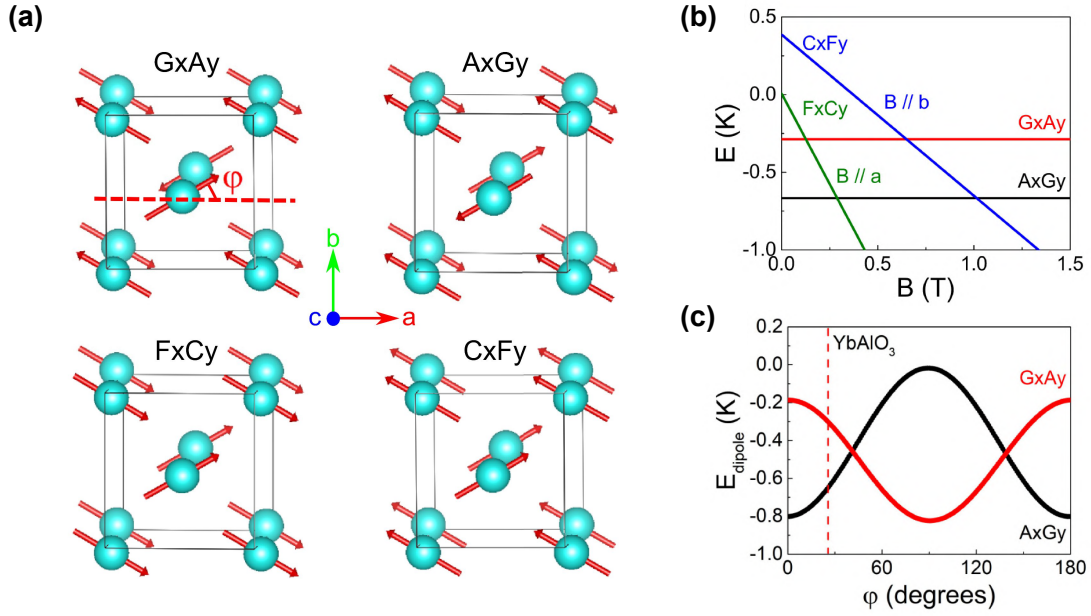
Figure B.1: Magnetic structure of YbAlO$_3$. **(a)** Four symmetrically-allowed magnetic structures in the system. Red vectors indicate the Yb^{3+} moment directions tilted by the angle of φ with respect to the a-axis. **(b)** Calculated E_{dip} of the four magnetic configurations as a function of B. For field applied along the a- and b-axes, the FM *FxCy* and *CxFy* configurations will be the new GS, with critical fields of 0.3 T and 1.0 T, respectively. **(c)** Calculated angular dependence of the E_{dip} for two *AxGy* and *GxAy* AFM structures. The red dashed line indicates the selected GS of YbAlO$_3$ with $\varphi = 23.5°$ to be *AxGy*. Figures reproduced from [59].

parallel to the ones at $c/4\ \hat{\boldsymbol{c}}$, and the interactions are of the same magnitude. In the ordered state, the molecular B produced by these interactions results in a B_{st}. This B_{st} is indicated by the red and green arrows in Figures B.2 **(a)**-**(b)**, and is quantitatively calculated to be $B_{\mathrm{st}} = -2(\sum_{i=1}^{4} J_i) \simeq 0.135J$ [74].[2] Figures B.2 **(c)**-**(d)** show two separated magnetic sub-lattices, where the Yb^{3+} moments have the same local Ising-axis in the corresponding sub-lattices. In this case, a pair of domain walls can propagate along the chain direction, behaving as free $S = 1/2$ spinons for $T > T_{\mathrm{N}}$. Finally yet important, the staggered molecular filed in the ordered state of YbAlO$_3$ in zero externally-applied magnetic field is about 0.3 T (see also Supplementary Materials of [74]).

---

[2]Extending the near neighbours to forty-eight for the long-range dipole-dipole interactions saturates B_{st} at $\sim 0.2J$ quite close to the best fit of the Density-matrix renormalisation group (DMRG) calculations $B_{\mathrm{st}} = 0.27J$ [74].
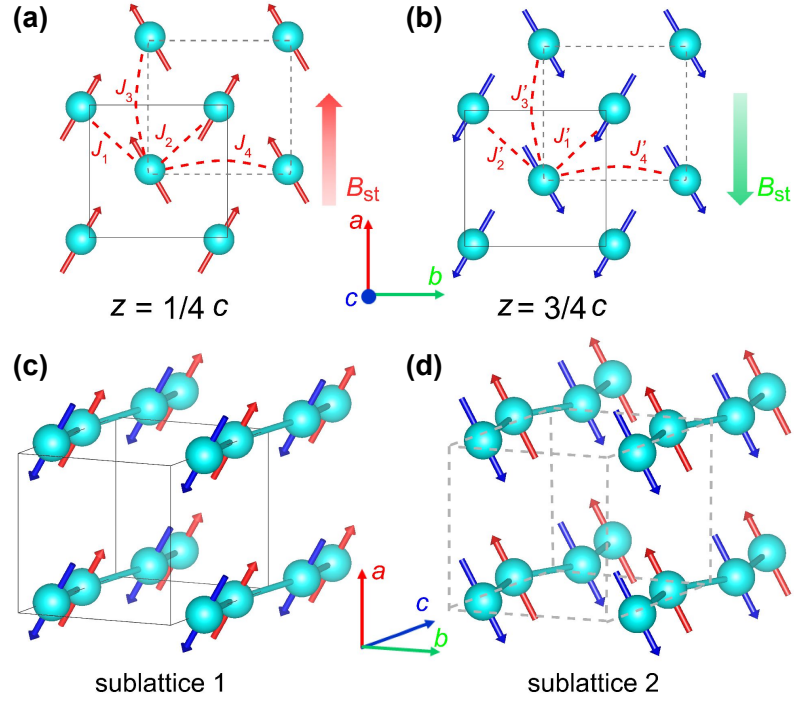
Figure B.2: Magnetic sub-lattices and staggered field B_{st} of YbAlO$_3$. **(a)**-**(b)** Yb^{3+} moment configurations in planes at **(a)** $c/4\,\hat{\boldsymbol{c}}$ and **(b)** $3c/4\,\hat{\boldsymbol{c}}$, respectively. Black solid and grey dashed lines construct the unit cell for the two magnetic sub-lattices. Red dashed lines indicate the near neighbour dipole-dipole interaction between Yb^{3+} Ising-like moments leading to a net B_{st}, with opposite directions in $c/4$- and $3c/4$-planes, as indicated by **(a)** the big red and **(b)** green arrows, respectively. **(c)**-**(d)** Two separated sub-lattices with 1-D Yb^{3+} AFM spin chains along the c-axis, where the Yb^{3+} moments have the same local Ising-axis in the magnetic sub-lattices. Figure from Supplementary Materials of [74].

APPENDIX C Cold-finger contacting technique

The demand of an improvement of the conventional clamping technique at the cold finger (CF) of a Physical Property Measurement System (PPMS) puck was examined. Here, I present a comparison of the measurement results using the typical silver-paint cover at the interface between the sample and the CF, with the technique of an indium wrapping proposed as method (iii) in Section 5.4. Figure C.1 shows the results of thermal conductivity (κ) measurements on YAlO$_3$ in the PPMS temperature (T) range with a similar measuring routine and the same set T gradient of 3 %, otherwise mentioned. As mentioned in Section 5.5, the PPMS device sets the T gradient based on the rise of T at the hot thermometer (T_H) as a result of turning the gradient heater on. In what follows, $\Delta T/T$ indicates the difference between the hot and cold points of the sample $T_\mathrm{H} - T_\mathrm{C}$ over the mean T of the sample. In an ideal case of perfect thermal coupling at the sample contact to the CF, the T gradient set by the PPMS device equals the $\Delta T/T$ value.

The main plot of Figure C.1 displays $\Delta T/T$ in percentage as a function of the mean T of the sample, and the inset shows κ as a function of T on a log-log scale. The results of the conventional CF contact, namely clamping plus covered by silver paste is depicted by red circles. In the main plot, the value of $\Delta T/T$ declines and refuse to follow the set T gradient. The observed behaviour is due the fact that the PPMS device sets the T gradient in defined by the increase of T_H for the PPMS device as mentioned above, however, reveals a lack of an appropriate thermal coupling to the cold bath (see Chapter 5). However, $\Delta T/T$ is used in measuring the thermal transport. The resolution of the data is poor below 50 K due to the too low $\Delta T/T$. Eventually, κ could be measured only down to around 10 K although the cold reservoir reached a base T of 1.8 K. In another attempt, the CF contacting technique was improved using the indium wrapping instead of the silver-paste covering of the sample at the CF, the results of which are shown in black. κ is measurable down to the lowest T. Moreover, the resolution of the data is much higher. In fact, for the same T gradients set to the PPMS program, a huge increase (even 1 order of magnitude) of $\Delta T/T$ was achieved. Finally yet important, the quality of the contact was checked with an increase of the set T gradient from 3 % to 5 %. This produces an immediate increase in $\Delta T/T$ (jump in the black curve at $\sim$10 K); nonetheless, no effects on the κ results were observed indicating reproducibility of the measured κ at this point with both $\Delta T/T$ values (see the inset). In addition, a $\Delta T/T$ of 2 % is achievable in the whole T range.

It is so important that though pure bulk indium has a superconducting phase transition at $T_\mathrm{c} \simeq 3.4$ K, no effects are observable down to the lowest measured T, which ensures the applicability of this technique in the whole aimed T range. Two essential causes are that: (i) The utilised indium wire is not pure resulting in both broadening of transition and reduction of T_c [235, 236]. For instance, antimony impurity in indium was reported to drop the superconductivity T_c onset down to 2.1 K and the offset below $\sim$1.6 K [237]. (ii) Thermal transport is a bulk property and the consequent thermal insulation is relevant as the transition to the superconductivity phase is completed.

In conclusion, in order to boost the thermal coupling to the cold reservoir and enable high resolution measurements down to the lowest T, the indium wrapping method was opted for the CF contacting technique at the PPMS puck.
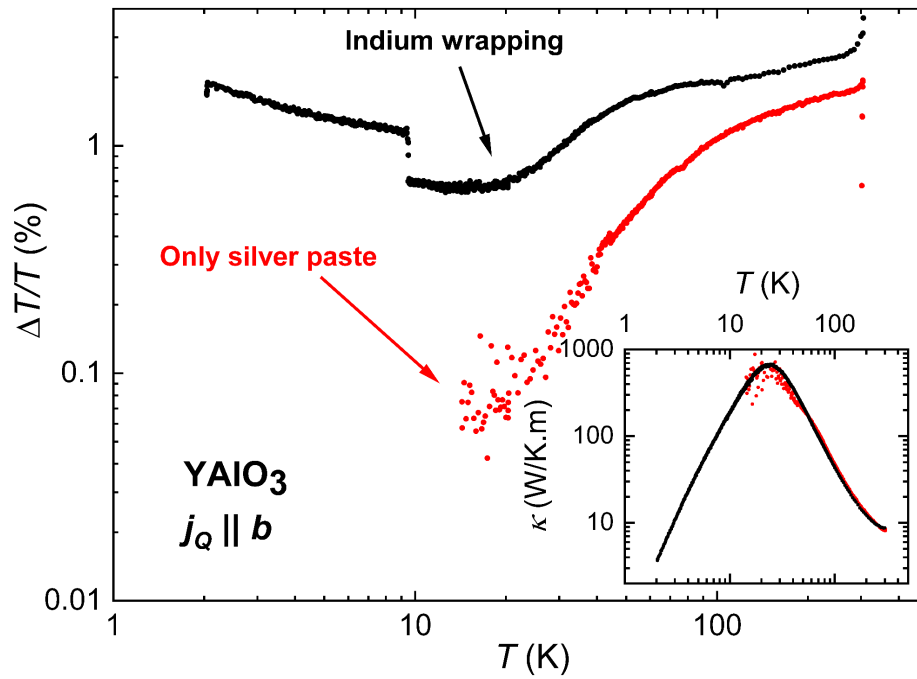
Figure C.1: Comparison of high-T κ measurement results of YAlO$_3$ with two different methods of CF contacting: Silver paint (red) and indium wrapping (black). The main plot shows $\Delta T/T$ in percentage as a function of the mid T of the sample for both contacting methods for the same set T gradient of 3%. The inset shows κ versus T on a log-log scale. The smooth behaviour of measured κ with indium wrapping upon increasing the T gradient set on the PPMS device around $10\,\text{K}$ confirms the appropriate thermal coupling. More details are provided in the text.

D New designs

In this chapter, I will present the plans of the new components designed in this work. Most of the explanations are already given in the main text once the piece is mentioned. However, here I will go through their drawings, features and installation methods. It must be noted that the pieces were mainly designed in *Autodesk Inventor Professional 2015*, and machined by me in the *Student Workshop of Max Planck Institute for Chemical Physics of Solids (MPI-CPfS)*. A Fused filament fabrication (FFF) 3-D printer[1] was sometimes used as part of a design-evaluation loop in the early design stages (attention: a 3-D-printed prototype does NOT suit for tight-fit checking purposes, due to the low accuracy level). The final version was manufactured using a Cartesian-coordinate-based computer numerical control (CNC) mill[2].

If mentioned, the piece was built at *Main Workshop* of the MPI-CPfS once I evaluated the applicability and assessed the buildability in the student workshop. In such case, either the material expenses, e.g., pure silver, or sequence requiry of super fine milling, e.g., $\varnothing 0.5\,\text{mm}$, made it desirable to get the benefit of the experience and the fancy milling devices of the main workshop.

D.1 *M* piece

In order to preserve the same contacts in transport measurements in (i) the dilution refrigerator in two different field directions ($\boldsymbol{B} \parallel \boldsymbol{j}_{\text{Q}}$ and $\boldsymbol{B} \perp \boldsymbol{j}_{\text{Q}}$) or/and (ii) the dilution fridge and the PPMS to cover temperatures (T) from a few milli-Kelvin to room temperature, a new silver M-shaped piece, shortly called *M piece* was designed and built. Figures D.1 **(a)-(b)**, show the mechanical drawings of the two parts that an *M* piece is composed of, here named as **(a)** lid and **(b)** main part. One of the M1 thread holes is spare, by the fact that silver is soft and in case of damage of the threads the relatively expensive piece can be used further. I should mention, one has to drill a through hole with an 0.8 mm mill to achieve an M1 thread hole. Figure D.1 **(c)** shows the exploded view of an *M* piece with the main part and the lid. The lid connects to the main part via an M1 screw while the lid faces the front edge of the main part and the larger face touches the specimen.

In addition to being entirely from silver and compatibility to both the high- and low-T measurement sample holders, the *M* piece has a particular symmetry, which makes it possible to measure the once-mounted sample along two perpendicular directions with respect to the external field, depending on the chosen mounting hole (see Figure D.2). The installation styles shown in Figures D.2 **(a)-(b)** on *Franz* sample holder correspond $\boldsymbol{B} \perp \boldsymbol{j}_{\text{Q}}$ and $\boldsymbol{B} \parallel \boldsymbol{j}_{\text{Q}}$, respectively. The final version of the *M* piece made of silver was milled in the main workshop of the *MPI-CPfS*.

D.2 *M*-piece-*mini-TTO* adaptor

In order to measure the sample mounted on the newly-designed *M* piece at higher T, the *mini-TTO* puck was used, as explained in Section 5.5. However, the dimensions and the

---

[1]SP 200, Saarpri.com 3D Druck Fachgeschäft
[2]DATRON neo, DATRON Dynamics, Inc

(a)

(b)

(c)
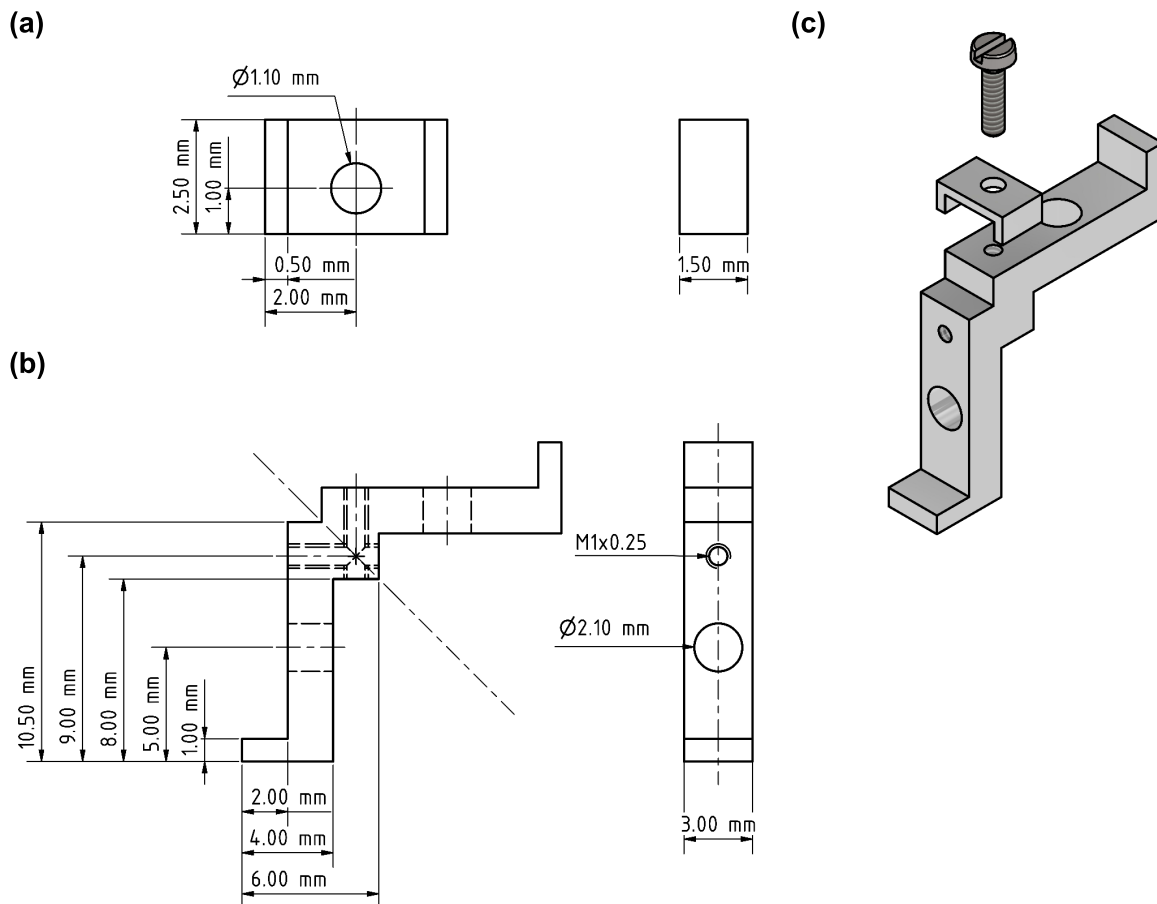
Figure D.1: Newly-designed *M* piece. **(a)**-**(b)** Drawings of the two constituting elements. **(a)** Lid for clamping the specimen on the main piece. The top view (left) shows the asymmetry. The larger side faces the front, increasing the effective clamping area touching the sample. **(b)** Main part of an *M* piece. As drawn, the small and large holes are thread and all-through, respectively. **(c)** Explosion of an *M* piece assembly. Note that the lid on **(a)** is scaled twice compared to the drawings and assembly in **(b)** and **(c)**.

required mounting screws of the cold finger of the *mini-TTO*-holder and of *Franz* are different. Considering these facts, a copper *M-piece-mini-TTO adaptor* was designed as planned in Figure D.3 **(a)**. Figure D.3 **(b)** illustrates the exploded view of the adaptor installed on the *Mini*-TTO's original cold finger (dark brown lying below the adaptor). The adaptor is screwed to the base from the bottom via an M2.5 screw as seen in Figure D.3 **(b)**[3]. Attention, connecting to the base directly needs an M3 screw. Therefore, the M2.5 screw is not touching the threads of the base at all (visible in Figure D.3 **(c)**).

Figure D.3 **(c)** bottom depicts the side-view cross-section *A-A* of the whole set assembly. The specimen is clamped underneath an *M*-piece lid one at a time (marked in red). Then, the *M* piece is installed on the adaptor via an M2 screw. The final design was self-machined at the student workshop of the MPI-CPfS. Finally yet important, the installation assembly

---

[3]If not downside tightened, the screw head will block the *M* piece touching surface.

(a)

(b)
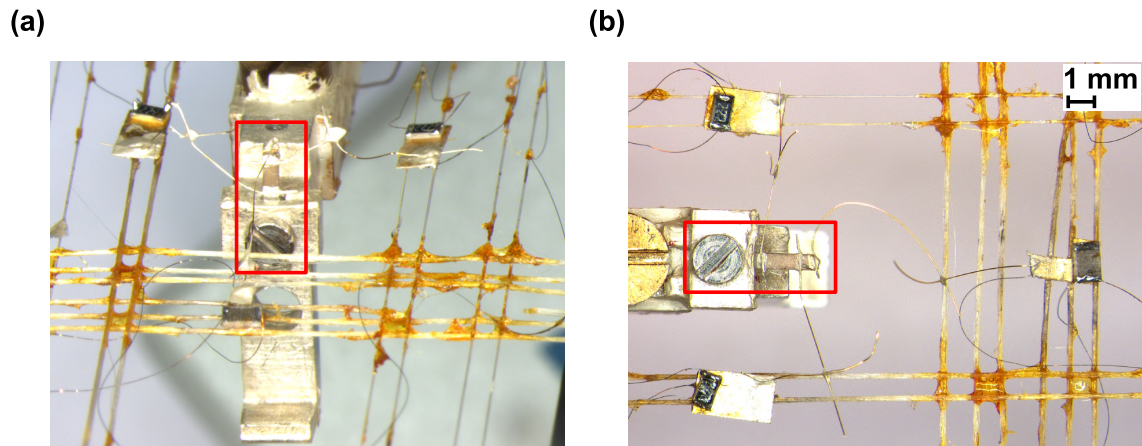
Figure D.2: Two possible mounting styles of an M piece carrying a built-in specimen marked by red boxes, on *Franz* sample holder. **(a)** $\boldsymbol{B} \perp \boldsymbol{j}_Q$ and **(b)** $\boldsymbol{B} \parallel \boldsymbol{j}_Q$ are accomplished based on the opted through hole.

(a)

(c)

(b)
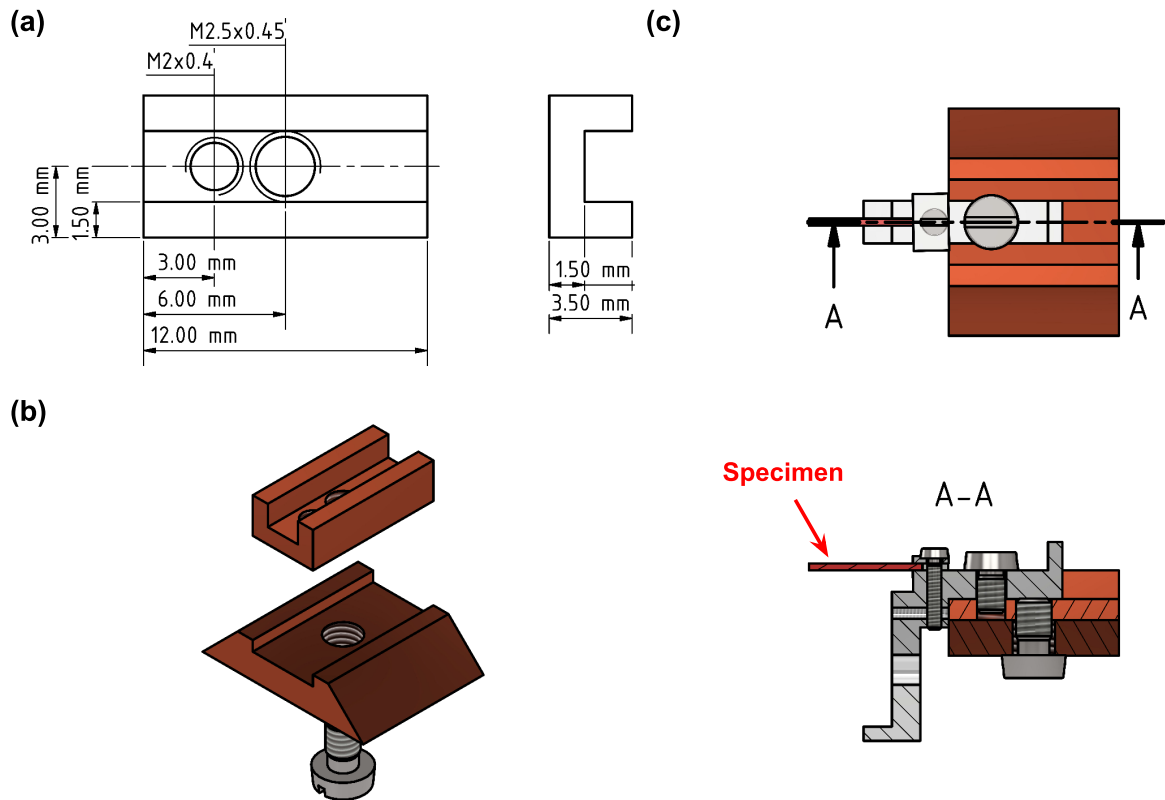
Figure D.3: *M-piece-mini-TTO* adaptor. **(a)** Mechanical drawing of the adaptor. Both holes have threads. **(b)** Explosion of the adaptor-on-base assembly. An M2.5 screw connects the adaptor to the cold finger tightened from the bottom. **(c)** Side-view cross-section of the full installation. The adaptor is first fixed on the cold finger (M2.5 screw) to host an M piece. A bar-shaped specimen is mounted on the M piece (M1 screw). Finally, the M piece is attached to the adaptor (M2 screw).

here does not show that all the surfaces were covered with silver paste in practice, as explained in Section 5.4 paragraph § **Cold-finger contact**.

D.3   New sample holder

A sample holder is a key part of an experimental set-up of thermal transport. It provides a way to mechanically fix the sample with high stability, and thermal coupling to the mixing chamber of the fridge. The currently in-use sample holder named as *Franz* in this research, was designed in about 2005 by S. Hartmann [183]. Some details regarding the *Franz* sample holder are provided in Section 5.6. More than one decade usages and frequent repairing led to brittleness of the holder, thus necessitating a replacement. One of the side projects to my doctoral work became design and preparation of a new sample holder for future thermal transport measurements in ^{3}He-^{4}He dilution refrigerators (or dil fridge for short) of the thermal transport laboratory of the *Max Planck Institute for Chemical Physics of Solids*, with a compatibility to both the Kelvinox MX 400 (K400) dil fridge of the *Franz* magnet and the Kelvinox MX 100 (K100) dil fridge of the *rotator* magnet. Here, I report the process in two sections of design and implementation.

Design: Figure 5.6 shows the *Franz* sample holder. Main considerations on the main body and components of my newly-designed sample holder included the challenges I had with the *Franz* sample holder: (i) The Vespel frame was connected to the main gold-plated copper body via screws. The Vespel frame had been broken many times over the time particularly at the screwing point, and got super fragile. (ii) Although providing a large working area is favourable, a force applied on a longer frame can produce larger torque and increase the risks of breaking. (iii) The Nylon threads used to thermally isolate the gold islands had been broken and repaired many times, especially due to soldering of the electrical components on the islands. (iv) In the design of the *Franz* holder, the Nylon threads went over the Vespel frame. If they pass deeper than the top surface of the frame, they will be in less risk of unwanted breaking, and finally (v) reduction of the heat-loss if possible.

- **Main body:** Figure D.4 displays the main body of the newly-designed sample holder. A holder compatible to both of the dil fridges requires to fit to both rods and radiation shields. Besides, the sample installed on the *M* piece must remain within the centre of the field of both magnets[4]. The dimensions of the current design satisfy the required conditions. Figure D.4 **(a)** shows the mechanical drawings. Firstly, the Vespel frame is replaced by a frame of the same material as the main body. Secondly, the length of the frame is optimised for the required working area. The only thread hole is on the cold finger where the *M* piece will be installed via an M2 screw. Several slits are added on the main body to eliminate eddy currents along with the cut at the bottom of the frame to open the big metallic loop. Moreover, special cuts zoomed in section *M* and *P* in Figure D.4 **(a)** are designed to keep the threads for 1 mm below the top surface of the main body. Figure D.4 **(b)** presents an isometric projection of the main body for more clearness of the design.

  The core constituting material is copper then coated by gold. This combination provides a rather rough piece, which exhibits good thermal connections to the fridge and a proper specific heat for fast cooling down to lowest *T*.

---

[4]According to mechanical drawings of the magnets and experimental tests done by the former PhD student of the group *Dr Marcel Naumann*.

(a)

(b)
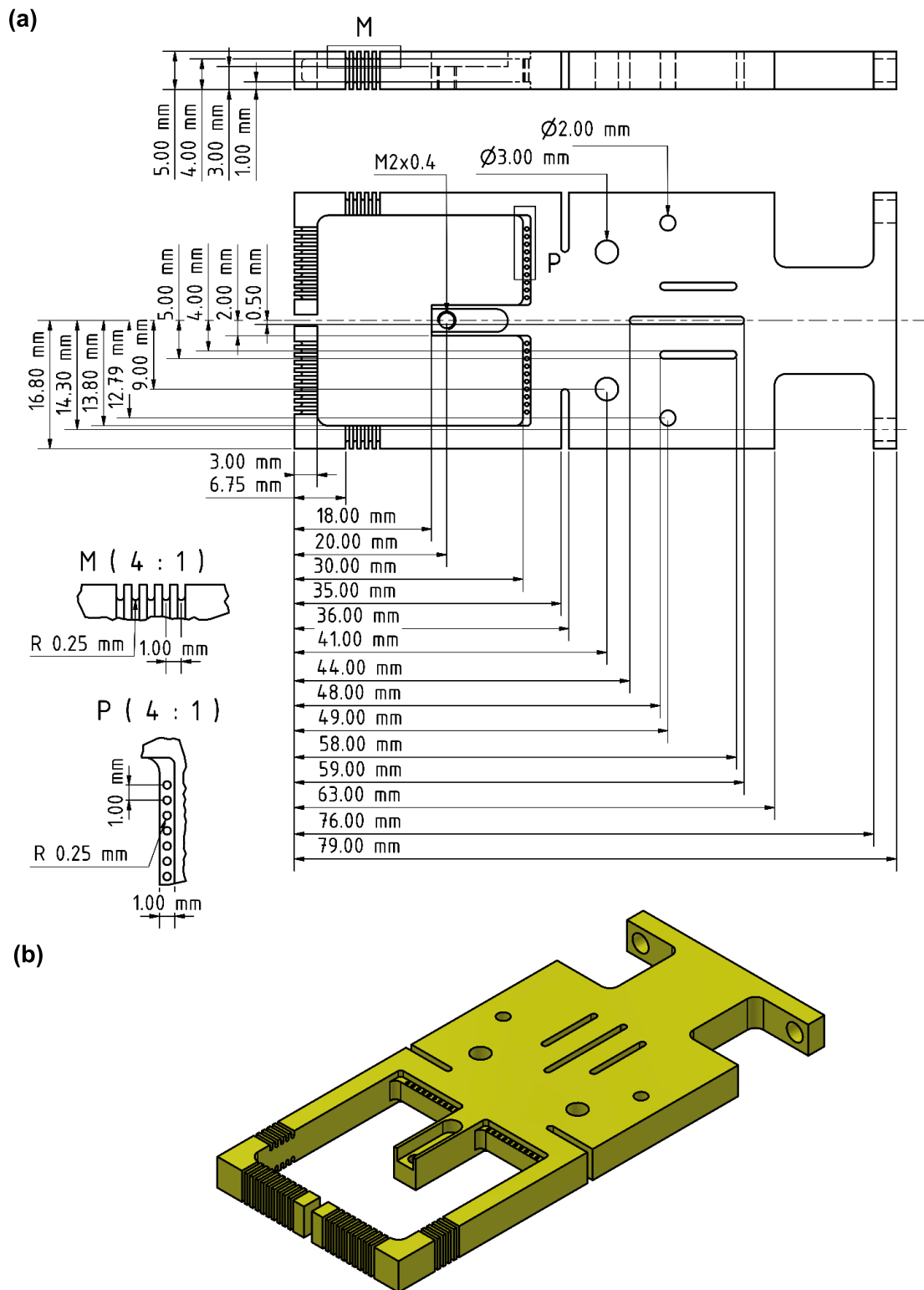
Figure D.4: Main body of the newly-designed sample holder. **(a)** Mechanical drawings, and **(b)** an isometric projection of the main body.

(a)

(b)

(c)
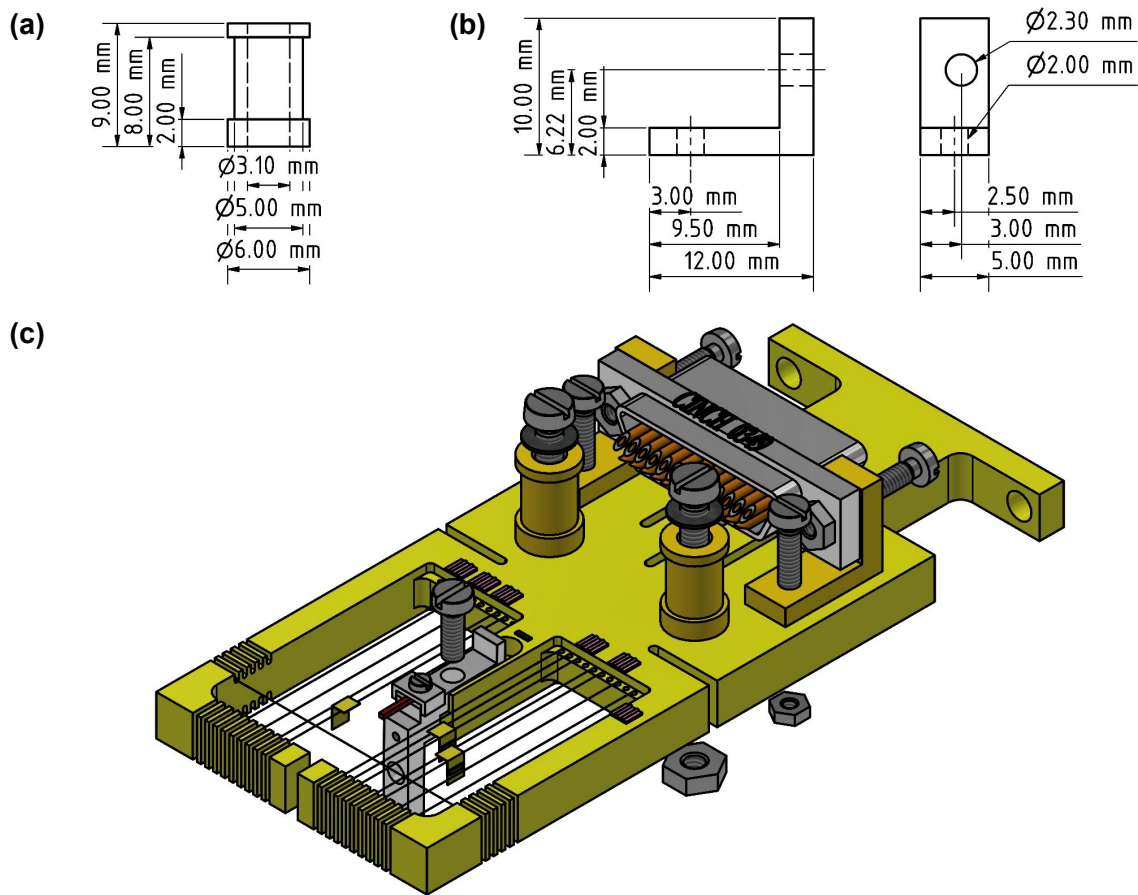
Figure D.5: Mechanical design of the new sample holder. **(a)**-**(b)** Mechanical drawings of the additional pieces of the new sample holder, **(a)** thermal-anchoring cylinder, and **(b)** an L-shaped leg for fixing the 25-pin D-sub connector on the holder's body. The shown leg is for the right hole once looking on the plane. The asymmetric location of the centre of the hole is mirrored for the left leg. **(c)** Explosion of the new sample holder assembly. Except the screwing hole of the *M* piece, all the holes on the main body are through holes (see Figure D.4).

- **Assembly of the holder:** In addition to the main body of the holder, a pair of thermal-anchoring cylinders and a pair of legs for fixing the female 25-pin D-sub connector on the holder's body were required, the mechanical drawings of which are brought in Figures D.5 **(a)**-**(b)**. Each designed leg has one non-symmetric hole to match the corresponding mounting hole of the female D-sub connector. Figure D.5 **(b)** shows the drawings of the right leg, the left one being mirror-inverted. In closing, Figure D.5 **(c)** presents the explosion of the new sample holder assembly without any electrical wiring. The electrical components and the wiring are focused later.

  In the new design, the Nylon yarns ($\varnothing 100\,\mu$m) are replaced by Kevlar threads ($\varnothing 70\,\mu$m). Despite the favourable low thermal conductivity of Nylon, it has a melting point of $\sim 250\,^{\circ}$C and does not tolerate soldering heat. In contrast, Kevlar is a durable, heat resistant sewing thread which begins decomposing at $\sim 430\,^{\circ}$C. Thus, Kevlar is not sensitive or breakable, rather ideal for the soldering heat and high stress
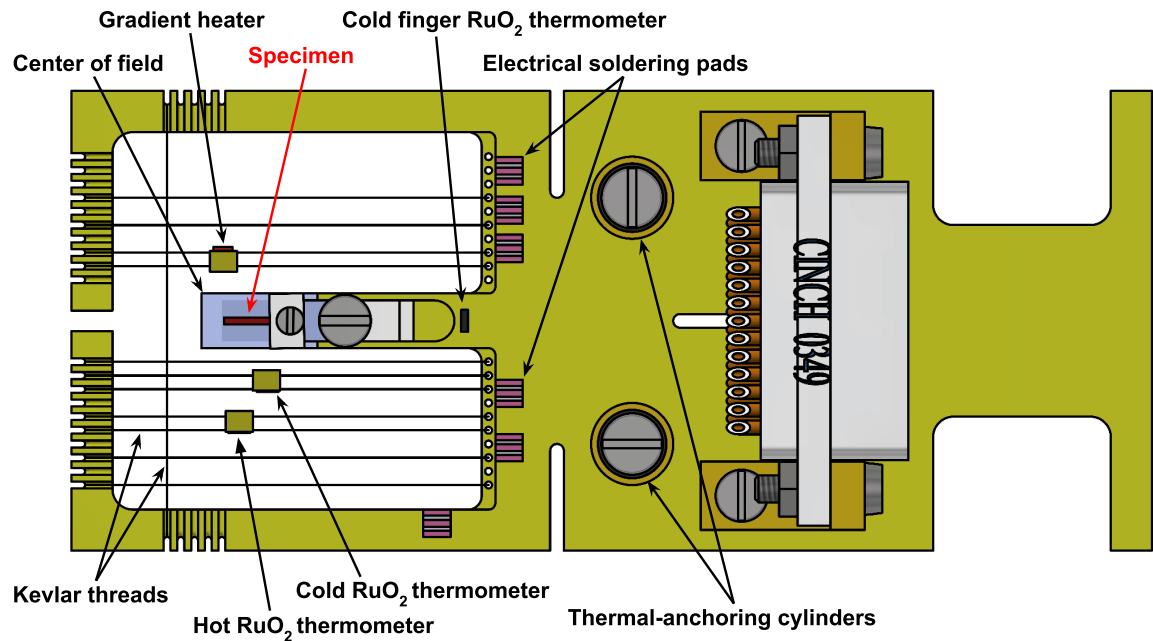
Figure D.6: Sketch of the new sample holder before wiring. The blue box indicates the centre $\pm 0.5\,\%$ of the field of the magnet, within which the sample must lie in an ideal design. The electrical components sit on the gold island, which lie on the Kevlar threads. The cylinders are to ensure a good thermal anchor to the holder's body and avoid any unwanted thermo-voltage additional to the signal.
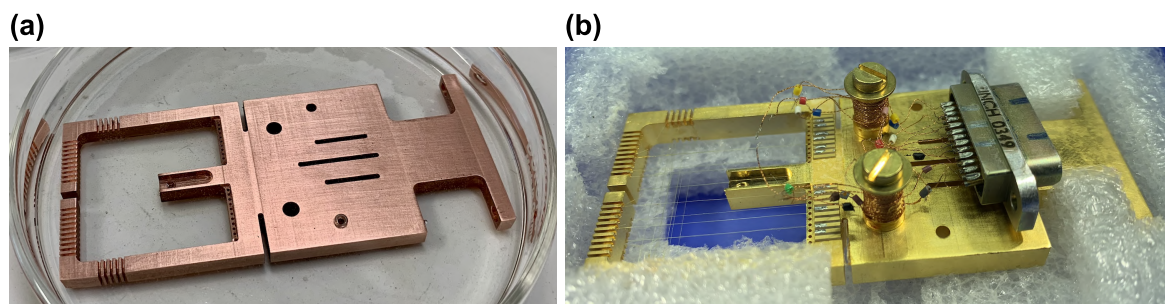
Figure D.7: Main body of the new sample holder. **(a)** The copper body was annealed, and then cleaned in sulphuric acid before gold coating. **(b)** The new sample holder with the Kevlar threads and the thermal-anchoring cylinders. Installation of the electrical components and the corresponding wiring are in progress.

situations. An advantage of Nylon, however, is its lower thermal conductivity compared to Kevlar. $\kappa_{\mathrm{Kevlar}} = 3.9 \cdot 10^{-3}\, T^{1.17}\,\mathrm{W\,m^{-1}\,K^{-1}}$ which is higher than of $\kappa_{\mathrm{Nylon}} = 2.6 \cdot 10^{-3}\, T^{1.75}\,\mathrm{W\,m^{-1}\,K^{-1}}$ in a common T range of 0.2 - 1 K.[5] This means that compared to the Nylon yarns with a similar diameter, the Kevlar threads conduct heat 1.5 times more at 1 K which amounts to 3.8 at 0.2 K. Taking the different diameters also into account, the heat sink via the Kevlar threads and the ones made of Nylon stay still in the same order of magnitude and are low enough for our purposes.

- **Electrical components and wiring:** Figure D.6 shows the plan of the new holder without wiring. The blue box indicates the joint centre $\pm 0.5\,\%$ of the field of the magnets, within which the sample must sit in an ideal design. RuO_2 thermometers will be used for thermometry, and a $10\,\mathrm{k\Omega}$ resistive chip as the gradient heater similar to the *Franz* holder. The electrical components sit on the gold islands suspended to the frame with fine Kevlar threads. All the connections between the sample and the gold islands are supposed to be made the same as before with gold wires. Considering the fact that one of the major challenges in the design is to integrate all the components in such way that heat losses are reduced, the islands are designed so that the sample, thermometers and heater are not directly facing each other. Besides, the heater can have a metallic cap of radiation shield over it or be placed in a metallic capsule rather than on a plane island. Electrical wiring from the electrical components to the terminal pads is made with $100\,\mathrm{\mu m}$ isolated wires of NbTi which are twisted. These wires can get soldered to the gold-sputtered contact stripes after electroplating Cu^{2+} ions on NbTi via an electrochemical deposition in $CuSO_4$ solution. The terminal pads with the gold-sputtered stripes, are used to change the wiring to $100\,\mathrm{\mu m}$ Cu wires and from two-point measurements to four-point ones. The twisted pairs of Cu wires go to the female D-sub connector. The cylinders are used to ensure a good thermal anchor to the holder's body and avoid any unwanted thermo-voltages additional to the measured signals.

Implementation: The designed main body and the additional pieces were milled from copper. In order to reduce the residual resistivity ratio (RRR) at lowest T, the copper was baked at up to $950\,^{\circ}\mathrm{C}$ in the furnace[6]. The annealing plan is provided in Table D.1. Figure D.7 **(a)** depicts the milled main body of the new sample holder washed in sulphuric acid after the annealing process. The piece was then gold plated for $100\,\mathrm{\mu m}$. Figure D.7**(b)** shows the gold-coated body including the terminal pads of the wiring and the Kevlar threads. The twisted pairs of 100-micron Cu wires are thermally anchored via the gold-plated cylinders. The work is in progress and the sample holder is ready for installing the RuO_2 thermometers and the heater.

Set T	Duration
$950\,^{\circ}\mathrm{C}$ (ramp)	9 h
$950\,^{\circ}\mathrm{C}$ (hold)	4 h
$850\,^{\circ}\mathrm{C}$ (ramp)	0.3 h
$850\,^{\circ}\mathrm{C}$ (hold)	8 h
RT (ramp)	7 h

Table D.1: Annealing plan of the milled copper body of the new holder.

---

[5]$\kappa_{\mathrm{Kevlar}} = 3.9 \cdot 10^{-6}\, T^{1.17}\,\mathrm{W\,m^{-1}\,K^{-1}}$ is mentioned in 'Matter and methods at low temperatures' by Frank Pobell, third edition, page 71, which does not match the original paper [238].

[6]by help of *Dr Nubia Caroca-Canales*
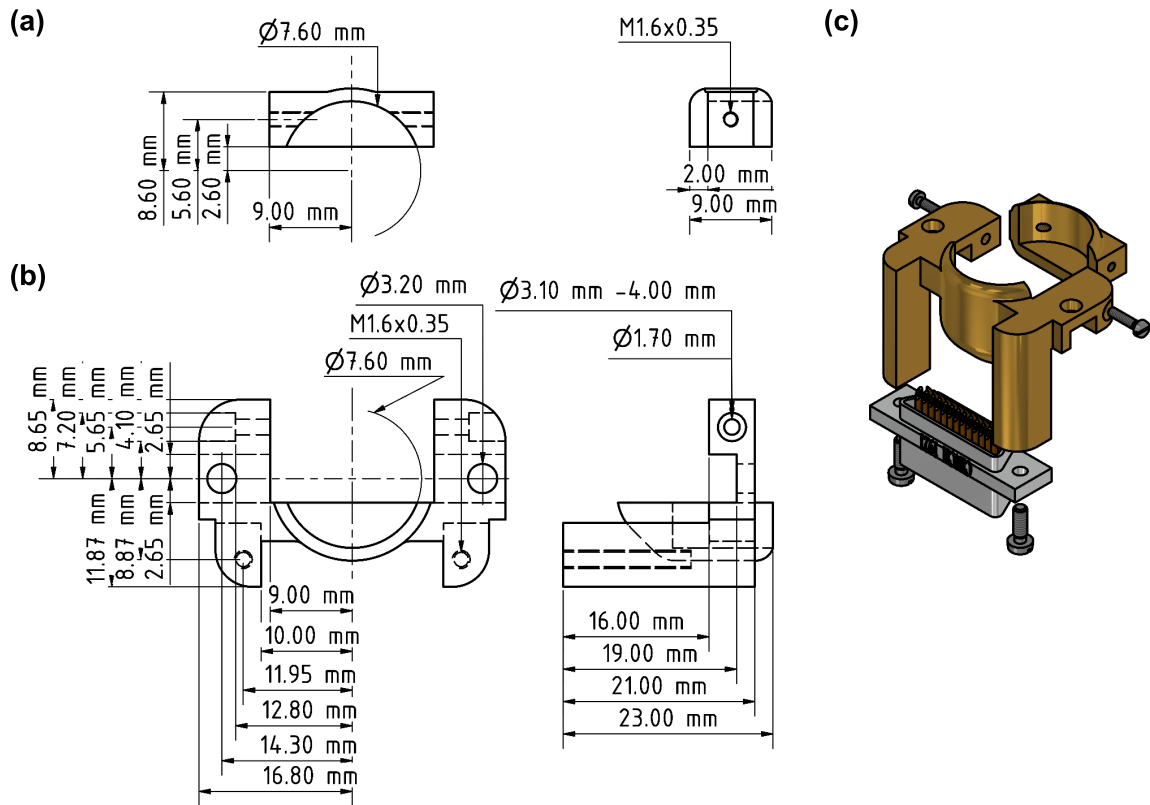
Figure D.8: D-sub connector stabiliser. The design of the stabiliser consists of two pieces, which form a ring once connected to each other. **(a)**-**(b)** Mechanical drawings of the **(a)** back and **(b)** front pieces of the ring. **(c)** Explosion of the assembly. The front piece carries the D-sub connector at a permanent position, and the back piece helps to fix the whole part to the rod of the dilution fridge.

D.4   Connector stabiliser and uniform nut

Major modifications of the experimental set-up were applied on the connection spot of the sample holder to the bottom rod of the dil-fridge in two parts: (i) A precisely designed and milled stabiliser of the D-sub connector, so that the male (on the dil fridge) and female (on sample holder) D-sub connectors are held perfectly tight, along with (ii) a uniform nut that the male and female D-sub connectors tight into each other by mounting the sample holder on the dil fridge without introducing any pressure or tension on the fine electrical wiring.

Figure D.8 shows the design of the D-sub connector stabiliser which consists of one big and one small part, named *front* and *back* in this text respectively. The front piece holds the D-sub connector of the dil fridge using two M1.6 screws, and the back piece is used to mount the whole connector stabiliser on the bottom rod of the fridge (as shown later in Figure D.9). Figures D.8 **(a)**-**(b)** show the mechanical drawings of the back and front pieces separately. The pieces make a ring once connected to each other. The two pieces get installed on the rod by connecting the front and back pieces, and tightening two M1.6 screws as shown in Figure D.8 **(c)**. The mechanical drawing of the uniform nut is shown in Figure D.9 **(a)**, and a cartoon of how the body of the sample holder is carried by the uniform nut is displayed in Figure D.9 **(b)**. The design of the uniform nut prevents any slide or unwanted movement

(a)

(b)

(c)
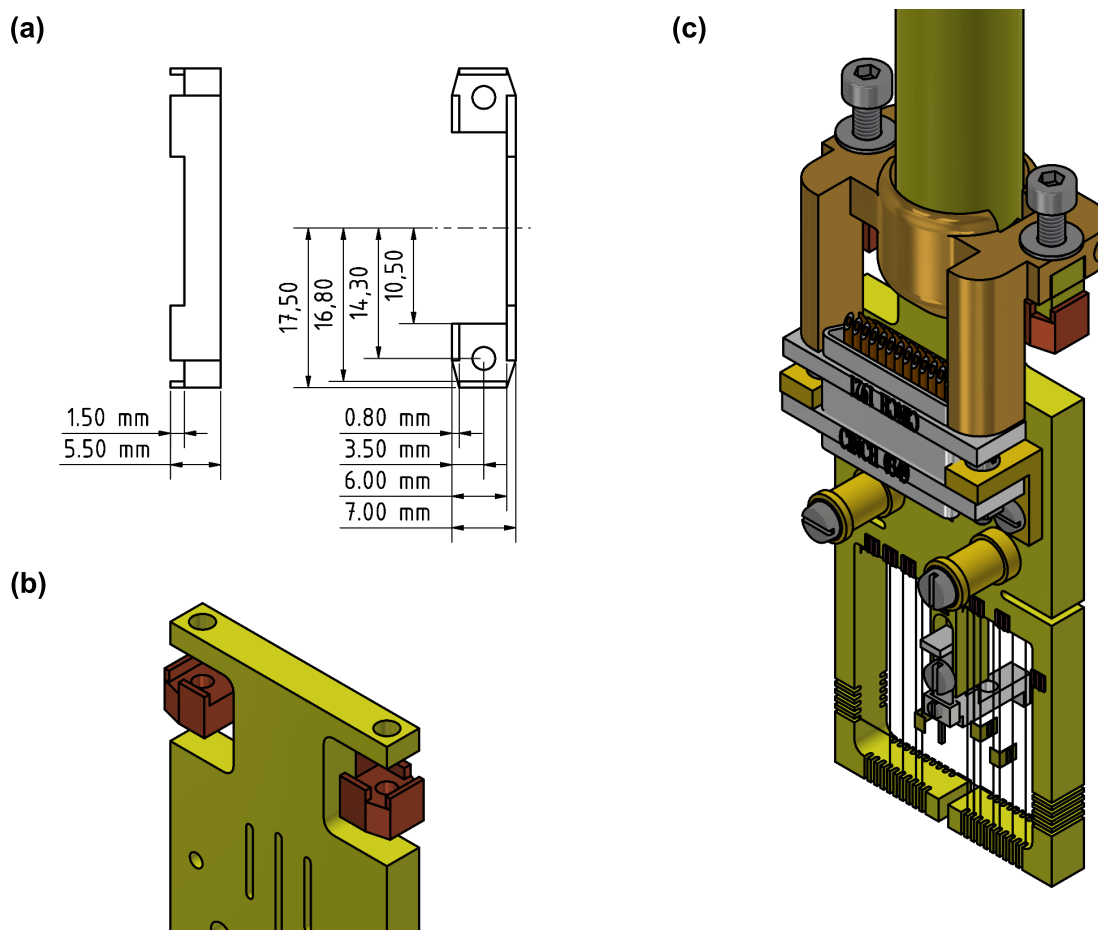
Figure D.9: Uniform nut. **(a)** Mechanical drawing of the uniform nut. **(b)** The whole body is held by the uniform nut. The design of the uniform nut prevents any slide or unwanted movement of the sample holder. **(c)** Full assembly of the new sample holder attached to the rod of the dilution fridge using a uniform nut. Male and female D-sub connectors connect into each other automatically by tightening the screws to the uniform nut, without introducing any pressure or tension on the fine electrical wiring (see Figure D.8).

of the sample holder. Figure D.9 **(c)** depicts the full assembly of the aforementioned new sample holder attached to the rod of the dil fridge using the uniform nut and the stabiliser of the 25-pin D-sub connector. The male D-sub connector installed at the dil fridge is no longer suspending on soldering points of fine 100-µm electrical wires thanks to its stabiliser. With this combination, the sample holder is mounted by tightening two screws on one big piece of nut which eliminates the risk of dropping tiny nuts over the sample. Moreover, the male and female D-sub connectors connect into each other automatically by tightening the screws on the uniform nut. Thus, the fine electrical wires and the soldering points will not undergo the risk of unwanted stress during connecting the connectors into each other. The connector stabiliser was milled on brass and the uniform nut on copper.

Bibliography

[1] M. Naumann[†] and *P. Mokhtari*[†], Z. Medvecka, F. Arnold, M. Pillaca, S. Flipo, D. Sun, H. Rosner, A. Leithe-Jasper, P. Gille, M. Baenitz and E. Hassinger. 'Fermi surface of the skutterudite $CoSb_3$: Quantum oscillations and band-structure calculations'. *Phys. Rev. B* **103**, 085133 (2021). [†]*Equal contributions.*

[2] M. Baenitz, M. M. Piva, S. Luther, J. Sichelschmidt, K. M. Ranjith, H. Dawczak-D bicki, M. O. Ajeesh, S.-J. Kim, G. Siemann, C. Bigi, P. Manuel, D. Khalyavin, D. A. Sokolov, *P. Mokhtari*, H. Zhang, H. Yasuoka, P. D. C. King, G. Vinai, V. Polewczyk, P. Torelli, J. Wosnitza, U. Burkhardt, B. Schmidt, H. Rosner, S. Wirth, H. Kühne, M. Nicklas and M. Schmidt. 'Planar triangular $S = 3/2$ magnet $gCrSe_2$: Magnetic frustration, short range correlations, and field-tuned anisotropic cycloidal magnetic order'. *Phys. Rev. B* **104**, 134410 (2021).

[3] *P. Mokhtari*, U. Stockert, S. Galeski, R. Wawrzyńczak, R. Kuechler, L. Vasylechko, S. E. Nikitin, M. Brando, O. Starykh and E. Hassinger. 'Magnetization plateaux at $1/3$ and $1/5$ M_{sat} in the spin $1/2$ chain system $YbAlO_3$'. *Unpublished* (2023).

[4] *P. Mokhtari*, G. Duan, U. Stockert, S. E. Nikitin, M. Brando, R. Yu and E. Hassinger. 'Huge enhancement of thermal conductivity within the Tomonaga-Luttinger-liquid region of $YbAlO_3$: Experimental heat transport and numerical thermal Drude weight'. *Unpublished* (2023).

[5] *P. Mokhtari*, U. Stockert and E. Hassinger. 'Experimental thermal transport studies and Callaway modelling of the electrically insulating systems $YAlO_3$ and $YbAlO_3$'. *Unpublished* (2023).

[6] S. Blundell. *Magnetism in Condensed Matter* (OUP Oxford, 2001).

[7] T. Giamarchi. *Quantum Physics in One Dimension* (Clarendon Press, 2004).

[8] I. Bose. 'Quantum magnets: a brief overview'. *arXiv:cond-mat/0107399v1* (2001).

[9] W. Heisenberg. 'Zur Theorie des Ferromagnetismus'. *Zeitschrift für Physik* **49**, 619–636 (1928).

[10] P. A. M. Dirac and R. H. Fowler. 'Quantum mechanics of many-electron systems'. *Proc. R. soc. Lond. Ser. A-Contain. Pap. Math. Phys. Character* **123**, 714–733 (1929).

[11] T. Eggel, M. A. Cazalilla and M. Oshikawa. 'Dynamical theory of superfluidity in one dimension'. *Phys. Rev. Lett.* **107**, 275302 (2011).

[12] S. C. Furuya and T. Giamarchi. 'Spontaneously magnetized Tomonaga-Luttinger liquid in frustrated quantum antiferromagnets'. *Phys. Rev. B* **89**, 205131 (2014).

[13] Weiss, Pierre and Forrer, R. 'La saturation absolue des ferromagnétiques et les lois d'approche en fonction du champ et de la température'. *Ann. Phys.* **10**, 279–372 (1929).

[14] M. Mourigal, M. Enderle, A. Klöpperpieper, J.-S. Caux, A. Stunault and H. M. Rønnow. 'Fractional spinon excitations in the quantum Heisenberg antiferromagnetic chain'. *Nat. Phys.* **9**, 435–441 (2013).

[15] N. D. Mermin and H. Wagner. 'Absence of ferromagnetism or antiferromagnetism in one- or two-dimensional isotropic Heisenberg models'. *Phys. Rev. Lett.* **17**, 1133–1136 (1966).

[16] F. D. M. Haldane. ''Fractional statistics" in arbitrary dimensions: A generalization of the Pauli principle'. *Phys. Rev. Lett.* **67**, 937–940 (1991).

[17] F. D. M. Haldane. '"Spinon gas" description of the $S = 1/2$ Heisenberg chain with inverse-square exchange: Exact spectrum and thermodynamics'. *Phys. Rev. Lett.* **66**, 1529–1532 (1991).

[18] L. Faddeev and L. Takhtajan. 'What is the spin of a spin wave?' *Phys. Lett. A* **85**, 375–377 (1981).

[19] T. Matsui. 'Fermionic spinons in antiferromagnetic Heisenberg chain'. *J. Phys. Soc. Jpn.* **63**, 256–263 (1994).

[20] B. S. Shastry and D. Sen. 'Majorana fermion representation for an antiferromagnetic spin-chain'. *Phys. Rev. B* **55**, 2988–2994 (1997).

[21] W. McRae and O. P. Sushkov. 'Magnetic moment of a spinon and thermodynamic properties of the one-dimensional Heisenberg model'. *Phys. Rev. B* **58**, 62–64 (1998).

[22] E. Shimshoni, D. Rasch, P. Jung, A. V. Sologubenko and A. Rosch. 'Large thermomagnetic effects in weakly disordered Heisenberg chains'. *Phys. Rev. B* **79**, 064406 (2009).

[23] M. Karabach, G. Müller, H. Gould and J. Tobochnik. 'Introduction to the Bethe ansatz I'. *Comput. Phys.* **11**, 36–43 (1997).

[24] M. Karbach, K. Hu and G. Müller. 'Introduction to the Bethe ansatz II'. *Comput. Phys.* **12**, 565–573 (1998).

[25] J. des Cloizeaux and J. J. Pearson. 'Spin-wave spectrum of the antiferromagnetic linear chain'. *Phys. Rev.* **128**, 2131–2135 (1962).

[26] S. Notbohm. 'Spin dynamics of quantum spin-ladders and chains'. Doctoral dissertation. University of St. Andrews, 2007.

[27] B. Willis and C. Carlile. *Experimental Neutron Scattering* (OUP Oxford, 2017).

[28] A. T. Boothroyd. *Principles of Neutron Scattering from Condensed Matter* (Oxford UP, 2020).

[29] M. Karbach, K. Hu and G. Muller. 'Introduction to the Bethe ansatz III'. *arXiv:cond-mat/0008018v1* (2000).

[30] M. Kohno. 'Dynamically dominant excitations of string solutions in the spin-1/2 antiferromagnetic Heisenberg chain in a magnetic field'. *Phys. Rev. Lett.* **102**, 037203 (2009).

[31] S.-i. Tomonaga. 'Remarks on Bloch's method of sound waves applied to many-fermion problems'. *Prog. Theor. Phys.* **5**, 544–569 (1950).

[32] T. Giamarchi. 'One-dimensional physics in the 21st century'. *Comptes Rendus Physique* **17**, 322–331 (2016).

[33] J. M. Luttinger. 'An exactly soluble model of a many-fermion system'. *J. Math. Phys.* **4**, 1154–1162 (1963).

[34] F. D. M. Haldane. ''Luttinger liquid theory' of one-dimensional quantum fluids. I. Properties of the Luttinger model and their extension to the general 1D interacting spinless Fermi gas'. *J. Phys. C: Solid State Phys.* **14**, 2585–2609 (1981).

[35] T. Giamarchi. 'Some experimental tests of Tomonaga-Luttinger liquids'. *Int. J. Mod. Phys. B* **26**, 1244004 (2012).

[36] B. Dalla Piazza, M. Mourigal, N. B. Christensen, G. J. Nilsen, P. Tregenna-Piggott, T. G. Perring, M. Enderle, D. F. McMorrow, D. A. Ivanov and H. M. Rønnow. 'Fractional excitations in the square-lattice quantum antiferromagnet'. *Nat. Phys.* **11**, 62–68 (2015).

[37] W. J. Gannon, I. A. Zaliznyak, L. S. Wu, A. E. Feiguin, A. M. Tsvelik, F. Demmel, Y. Qiu, J. R. D. Copley, M. S. Kim and M. C. Aronson. 'Spinon confinement and

a sharp longitudinal mode in Yb_2Pt_2Pb in magnetic fields'. *Nat. Commun.* **10**, 1123 (2019).

[38] A. J. Schofield. 'Non-Fermi liquids'. *Contemp. Phys.* **40**, 95–115 (1999).

[39] S. Kimura, M. Matsuda, T. Masuda, S. Hondo, K. Kaneko, N. Metoki, M. Hagiwara, T. Takeuchi, K. Okunishi, Z. He, K. Kindo, T. Taniyama and M. Itoh. 'Longitudinal spin-density wave order in a quasi-1D Ising-like quantum antiferromagnet'. *Phys. Rev. Lett.* **101**, 207201 (2008).

[40] H. v. Löhneysen, A. Rosch, M. Vojta and P. Wölfle. 'Fermi-liquid instabilities at magnetic quantum phase transitions'. *Rev. Mod. Phys.* **79**, 1015–1075 (2007).

[41] P. Coleman and A. J. Schofield. 'Quantum criticality'. *Nature* **433**, 226–229 (2005).

[42] S. Sachdev and B. Keimer. 'Quantum criticality'. *Phys. Today* **64**, 29–35 (2011).

[43] R. B. Laughlin, G. G. Lonzarich, P. Monthoux and D. Pines. 'The quantum criticality conundrum'. *Adv. Phys.* **50**, 361–365 (2001).

[44] T. Vojta. 'Disorder in quantum many-body systems'. *Annu. Rev. Condens. Matter Phys.* **10**, 233–252 (2019).

[45] S. Sachdev. *Quantum Phase Transitions* (Cambridge University Press, 2011).

[46] J. A. Hertz. 'Quantum critical phenomena'. *Phys. Rev. B* **14**, 1165–1184 (1976).

[47] Coldea R., Tennant D. A., Wheeler E. M., Wawrzynska E., Prabhakaran D., Telling M., Habicht K., Smeibidl P. and Kiefer K. 'Quantum criticality in an Ising chain: Experimental evidence for emergent E_8 symmetry'. *Science* **327**, 177–180 (2010).

[48] A. K. Bera, J. Wu, W. Yang, R. Bewley, M. Boehm, J. Xu, M. Bartkowiak, O. Prokhnenko, B. Klemke, A. T. M. N. Islam, J. M. Law, Z. Wang and B. Lake. 'Dispersions of many-body Bethe strings'. *Nat. Phys.* **16**, 625–630 (2020).

[49] R. Yu, L. Yin, N. S. Sullivan, J. S. Xia, C. Huan, A. Paduan-Filho, N. F. Oliveira Jr, S. Haas, A. Steppke, C. F. Miclea, F. Weickert, R. Movshovich, E.-D. Mun, B. L. Scott, V. S. Zapf and T. Roscilde. 'Bose glass and Mott glass of quasiparticles in a doped quantum magnet'. *Nature* **489**, 379–384 (2012).

[50] J. Wu, M. Kormos and Q. Si. 'Finite-temperature spin dynamics in a perturbed quantum critical Ising chain with an E_8 symmetry'. *Phys. Rev. Lett.* **113**, 247201 (2014).

[51] V. Zapf, M. Jaime and C. D. Batista. 'Bose-Einstein condensation in quantum magnets'. *Rev. Mod. Phys.* **86**, 563–614 (2014).

[52] E. Faizi and H. Eftekhari. 'Quantum correlations in Ising-XYZ diamond chain structure under an external magnetic field'. *Chin. Phys. Lett.* **32**, 100303 (2015).

[53] Q. Faure, S. Takayoshi, S. Petit, V. Simonet, S. Raymond, L.-P. Regnault, M. Boehm, J. S. White, M. Månsson, C. Rüegg, P. Lejay, B. Canals, T. Lorenz, S. C. Furuya, T. Giamarchi and B. Grenier. 'Topological quantum phase transition in the Ising-like antiferromagnetic spin chain $BaCo_2V_2O_8$'. *Nat. Phys.* **14**, 716–722 (2018).

[54] Z. Wang, J. Wu, W. Yang, A. K. Bera, D. Kamenskyi, A. T. M. N. Islam, S. Xu, J. M. Law, B. Lake, C. Wu and A. Loidl. 'Experimental observation of Bethe strings'. *Nature* **554**, 219–223 (2018).

[55] Y. Cui, H. Zou, N. Xi, Z. He, Y. X. Yang, L. Shu, G. H. Zhang, Z. Hu, T. Chen, R. Yu, J. Wu and W. Yu. 'Quantum criticality of the Ising-like screw chain antiferromagnet $SrCo_2V_2O_8$ in a transverse magnetic field'. *Phys. Rev. Lett.* **123**, 067203 (2019).

[56] Z. Wang, M. Schmidt, A. Loidl, J. Wu, H. Zou, W. Yang, C. Dong, Y. Kohama, K. Kindo, D. I. Gorbunov, S. Niesen, O. Breunig, J. Engelmayer and T. Lorenz.

'Quantum critical dynamics of a Heisenberg-Ising chain in a longitudinal field: Many-body strings versus fractional excitations'. *Phys. Rev. Lett.* **123**, 067202 (2019).

[57] O. Buryy, Y. Zhydachevskii, L. Vasylechko, D. Sugak, N. Martynyuk, S. Ubizskii and K. D. Becker. 'Thermal changes of the crystal structure and the influence of thermochemical annealing on the optical properties of YbAlO$_3$ crystals'. *J. Phys. Condens. Matter* **22**, 055902 (2010).

[58] M. A. Noginov, G. B. Loutts, K. Ross, T. Grandy, N. Noginova, B. D. Lucas and T. Mapp. 'Role of traps in photocoloration of Mn:YAlO$_3$'. *J. Opt. Soc. Am. B* **18**, 931–941 (2001).

[59] L. S. Wu, S. E. Nikitin, M. Brando, L. Vasylechko, G. Ehlers, M. Frontzek, A. T. Savici, G. Sala, A. D. Christianson, M. D. Lumsden and A. Podlesnyak. 'Antiferromagnetic ordering and dipolar interactions of YbAlO$_3$'. *Phys. Rev. B* **99**, 195117 (2019).

[60] G. Deng, P. Guo, W. Ren, S. Cao, H. E. Maynard-Casely, M. Avdeev and G. J. McIntyre. 'The magnetic structures and transitions of a potential multiferroic orthoferrite ErFeO$_3$'. *J. Appl. Phys.* **117**, 164105 (2015).

[61] Y.-J. Ke, X.-Q. Zhang, Y. Ma and Z.-H. Cheng. 'Anisotropic magnetic entropy change in RFeO$_3$ single crystals (R = Tb, Tm, or Y)'. *Sci. Rep.* **6**, 19775 (2016).

[62] L. S. Wu, S. E. Nikitin, M. Frontzek, A. I. Kolesnikov, G. Ehlers, M. D. Lumsden, K. A. Shaykhutdinov, E.-J. Guo, A. T. Savici, Z. Gai, A. S. Sefat and A. Podlesnyak. 'Magnetic ground state of the Ising-like antiferromagnet DyScO$_3$'. *Phys. Rev. B* **96**, 144407 (2017).

[63] Y. Tokunaga, S. Iguchi, T. Arima and Y. Tokura. 'Magnetic-field-induced ferroelectric state in DyFeO$_3$'. *Phys. Rev. Lett.* **101**, 097205 (2008).

[64] H. Schuchert, S. Hüfner and R. Faulhaber. 'Optical investigation of metamagnetic DyAlO$_3$'. *Zeitschrift für Physik A Hadrons and nuclei* **222**, 105–127 (1969).

[65] S. Hüfner, L. Holmes, F. Varsanyi and L. G. Van Uitert. 'Investigation of magnetic interactions in TbAlO$_3$ by optical spectroscopy'. *Phys. Rev.* **171**, 507–513 (1968).

[66] A. Podlesnyak, S. E. Nikitin and G. Ehlers. 'Low-energy spin dynamics in rare-earth perovskite oxides'. *J. Phys. Condens. Matter* **33**, 403001 (2021).

[67] M. Rotter. 'Using *McPhase* to calculate magnetic phase diagrams of rare earth compounds'. *J. Magn. Magn. Mater.* **272-276**, E481–E482 (2004).

[68] K. W. H. Stevens. 'Matrix elements and operator equivalents connected with the magnetic properties of rare earth ions'. *Proc. Phys. Soc. A* **65**, 209–215 (1952).

[69] M. Hutchings. 'Point-charge calculations of energy levels of magnetic ions in crystalline electric fields'. *Solid State Phys.* **16**, 227–273 (1964).

[70] M. Rotter, B. Fåk and J. A. Blanco. 'Magnetic excitations in the longitudinally amplitude modulated magnetic structure of PrNi$_2$Si$_2$'. *J. Phys.: Conf. Ser.* **325**, 012008 (2011).

[71] S. E. Nikitin. 'Competing Magnetic Interactions in $4f$-based Magnets Studied by Neutron Scattering'. Doctoral dissertation. Technische Universität Dresden, 2019.

[72] P. Radhakrishna, J. Hammann, M. Ocio, P. Pari and Y. Allain. 'Antiferromagnetic ordering in the ytterbium aluminum perovskite YbAlO$_3$'. *Solid State Commun.* **37**, 813–817 (1981).

[73] D. Ehlers, L. Vasylechko, Z. Medvecká and J. Sichelschmidt. 'Magnetic anisotropy in YbAlO$_3$ studied by electron spin resonance'. *Appl. Magn. Reson.* **53**, 1399–1405 (2022).

[74] L. S. Wu, S. E. Nikitin, Z. Wang, W. Zhu, C. D. Batista, A. M. Tsvelik, A. M. Samarakoon, D. A. Tennant, M. Brando, L. Vasylechko, M. Frontzek, A. T. Savici, G. Sala, G. Ehlers, A. D. Christianson, M. D. Lumsden and A. Podlesnyak. 'Tomonaga-Luttinger liquid behavior and spinon confinement in $YbAlO_3$'. *Nat. Commun.* **10**, 698 (2019).

[75] P. Bonville, J. A. Hodges, P. Imbert and F. Hartmann-Boutron. 'Spin-spin and spin-lattice relaxation of Yb^{3+} in $YbAlO_3$, $TmAlO_3$:Yb, and $YAlO_3$:Yb and magnetic ordering in $YbAlO_3$ measured by the Mössbauer effect'. *Phys. Rev. B* **18**, 2196–2208 (1978).

[76] P. Bonville, J. Hodges and P. Imbert. 'Yb^{3+} in $RAlO_3$ (R = Eu, Gd, Tb, Dy, Ho, Er). A ^{170}Yb Mössbauer effect study of the hyperfine parameters, magnetic ordering and relaxation'. *Journal de Physique* **41**, 1213–1223 (1980).

[77] Y. Fan and R. Yu. 'Role of the spin anisotropy of the interchain interaction in weakly coupled antiferromagnetic Heisenberg chains'. *Chin. Phys. B* **29**, 057505 (2020).

[78] Y. Fan, J. Yang, W. Yu, J. Wu and R. Yu. 'Phase diagram and quantum criticality of Heisenberg spin chains with Ising anisotropic interchain couplings'. *Phys. Rev. Res.* **2**, 013345 (2020).

[79] S. E. Nikitin, S. Nishimoto, Y. Fan, J. Wu, L. S. Wu, A. S. Sukhanov, M. Brando, N. S. Pavlovskii, J. Xu, L. Vasylechko, R. Yu and A. Podlesnyak. 'Multiple fermion scattering in the weakly coupled spin-chain compound $YbAlO_3$'. *Nat. Commun.* **12**, 3599 (2021).

[80] F. H. L. Essler, A. M. Tsvelik and G. Delfino. 'Quasi-one-dimensional spin-$\frac{1}{2}$ Heisenberg magnets in their ordered phase: Correlation functions'. *Phys. Rev. B* **56**, 11001–11013 (1997).

[81] H.-J. Mikeska and A. K. Kolezhuk. 'One-dimensional magnetism'. Ed. by U. Schollwöck, J. Richter, D. J. J. Farnell and R. F. Bishop *Quantum Magnetism* (Springer Berlin Heidelberg, 2004), pp. 1–83.

[82] B. Lake, A. Tsvelik, S. Notbohm, D. A. Tennant, T. G. Perring, M. Reehuis, C. Sekar, G. Krabbes and B. Büchner. 'Confinement of fractional quantum number particles in a condensed-matter system'. *Nat. Phys.* **6** (2010).

[83] S. E. Nikitin (private communication).

[84] P. Deen. 'Introduction to neutron scattering techniques'. *11th International Conference on Highly Frustrated Magnetism (HFM22)*, Conference lectures (Sorbonne Université, France, 20th–25th June 2022).

[85] P. Deen (private discussion, 20th June 2022).

[86] A. Zorko. 'Local probes (ESR/µSR/NMR)'. *11th International Conference on Highly Frustrated Magnetism (HFM22)*, Conference lectures (Sorbonne Université, France, 20th–25th June 2022).

[87] A. Zorko (private discussion, 20th June 2022).

[88] R. L. Aggarwal, D. J. Ripin, J. R. Ochoa and T. Y. Fan. 'Measurement of thermo-optic properties of $Y_3Al_5O_{12}$, $Lu_3Al5O12$, YAlO3, $LiYF_4$, $LiLuF_4$, BaY_2F_8, $KGd(WO_4)_2$, and $KY(WO_4)_2$ laser crystals in the 80 - 300 K temperature range'. *J. Appl. Phys.* **98**, 103514 (2005).

[89] H. Xiang, Z. Feng and Y. Zhou. 'Theoretical investigations on mechanical anisotropy and intrinsic thermal conductivity of $YbAlO_3$'. *J. Eur. Ceram. Soc.* **35**, 1549–1557 (2015).

[90] X. Zhan, Z. Li, B. Liu, J. Wang, Y. Zhou and Z. Hu. 'Theoretical prediction of elastic stiffness and minimum lattice thermal conductivity of $Y_3Al_5O_{12}$, $YAlO_3$ and $Y_4Al_2O_9$'. *J. Am. Ceram. Soc.* **95**, 1429–1434 (2012).

[91] N. Ashcroft and N. Mermin. *Solid State Physics* (Holt, Rinehart and Winston, 1976).

[92] C. Kittel. *Introduction to Solid State Physics* (Wiley, 2004).

[93] S. H. Simon. *The Oxford Solid State Basics* (Oxford University Press, 2013).

[94] R. Gross and A. Marx. *Festkörperphysik* (De Gruyter Oldenbourg, 2014).

[95] J. M. Ziman. *Principles of the Theory of Solids* (Cambridge University Press, 1972).

[96] C. Weissmantel, H. Burghardt, C. Hamann, H. Giegengack, G. Hecht and H. Hinneberg. *Grundlagen der Festkörperphysik* (Springer Berlin Heidelberg, 1979).

[97] C. Enss and S. Hunklinger. *Low-Temperature Physics* (Springer Berlin Heidelberg, 2005).

[98] F. Pobell. *Matter and Methods at Low Temperatures* (Springer Berlin Heidelberg, 2007).

[99] R. P. Tye. *Thermal Conductivity* (Academic Press, 1969).

[100] Ed. by T. M. Tritt. *Thermal Conductivity: Theory, Properties, and Applications* (Springer New York, 2004).

[101] H. Goldsmid. *Introduction to Thermoelectricity* (Springer Berlin Heidelberg, 2009).

[102] P. G. Klemens. 'Thermal conductivity and lattice vibrational modes'. *Solid State Phys.* **7**, 1–98 (1958).

[103] J. Parrott and A. Stuckes. *Thermal Conductivity of Solids* (éditeur non identifié, 1975).

[104] R. Berman. *Thermal Conduction in Solids* (OXFORD University Press, 1976).

[105] J. Singleton. *Band Theory and Electronic Properties of Solids* (Oxford University Press, 2001).

[106] N. Hlubek. 'Magnetic heat transport in one-dimensional quantum antiferromagnets'. Doctoral dissertation. Technische Universität Dresden, 2010.

[107] G. Kolland. 'Thermal conductivity of the Spin-Ice Compound $Dy_2Ti_2O_7$ and the Spin-Chain System $BaCo_2V_2O_8$'. Doctoral dissertation. Universität zu Köln, 2013.

[108] H. Pfau. 'Thermal Transport in Strongly Correlated Rare-Earth Intermetallic Compounds'. Doctoral dissertation. Technische Universität Dresden, 2015.

[109] L. Onsager. 'Reciprocal relations in irreversible processes. I.' *Phys. Rev.* **37**, 405–426 (1931).

[110] Anonymous. 'Report of the 32nd Meeting of the British Association for the Advancement of Science' (Natural History Museum Library, London, 1862), pp. 144–150.

[111] A. Einstein. 'Die Plancksche Theorie der Strahlung und die Theorie der spezifischen Wärme'. *Annalen der Physik*. 4th ser. **22**, 180–190 (1907).

[112] P. Debye. 'Zur Theorie der spezifischen Wärmen'. *Annalen der Physik*. 4th ser. **39**, 789–839 (1912).

[113] T. Feng, L. Lindsay and X. Ruan. 'Four-phonon scattering significantly reduces intrinsic thermal conductivity of solids'. *Phys. Rev. B* **96**, 161201 (2017).

[114] T. Feng and X. Ruan. 'Quantum mechanical prediction of four-phonon scattering rates and reduced thermal conductivity of solids'. *Phys. Rev. B* **93**, 045202 (2016).

[115] A. A. Maradudin and A. E. Fein. 'Scattering of neutrons by an anharmonic crystal'. *Phys. Rev.* **128**, 2589–2608 (1962).

[116] J. Callaway. 'Model for lattice thermal conductivity at low temperatures'. *Phys. Rev.* **113**, 1046–1051 (1959).

[117] D. T. Morelli, J. P. Heremans and G. A. Slack. 'Estimation of the isotope effect on the lattice thermal conductivity of group IV and group III-V semiconductors'. *Phys. Rev. B* **66**, 195304 (2002).

[118] P. G. Klemens. 'The scattering of low-frequency lattice waves by static imperfections'. *Proc. Phys. Soc. A* **68**, 1113–1128 (1955).

[119] Y. Cheng, M. Nomura, S. Volz and S. Xiong. 'Phonon-dislocation interaction and its impact on thermal conductivity'. *J. Appl. Phys.* **130**, 040902 (2021).

[120] R. O. Pohl. 'Thermal conductivity and phonon resonance scattering'. *Phys. Rev. Lett.* **8**, 481–483 (1962).

[121] S. R. Peierls. 'Zur kinetischen Theorie der Wärmeleitung in Kristallen'. *Annalen der Physik.* 5th ser. **3**, 1055–1101 (1929).

[122] J. Yang, D. T. Morelli, G. P. Meisner, W. Chen, J. S. Dyck and C. Uher. 'Influence of electron-phonon interaction on the lattice thermal conductivity of $Co_{1-x}Ni_xSb_3$'. *Phys. Rev. B* **65**, 094115 (2002).

[123] P. D. Thacher. 'Effect of boundaries and isotopes on the thermal conductivity of LiF'. *Phys. Rev.* **156**, 975–988 (1967).

[124] R. Berman, J. C. F. Brock and B. Bleaney. 'The effect of isotopes on lattice heat conduction I. Lithium fluoride'. *Proc. R. Soc. Lon. A: Math. Phys. Sci.* **289**, 46–65 (1965).

[125] T. Kawamata, H. Nagasawa, K. Naruse, M. Ohno, Y. Matsuoka, Y. Hagiya, M. Fujita, T. Sasaki and Y. Koike. 'Thermal conductivity due to spins in the frustrated two-leg spin ladder system $BiCu_2PO_6$'. *J. Phys. Soc. Jpn.* **87**, 074702 (2018).

[126] C. Hess, H. ElHaes, A. Waske, B. Büchner, C. Sekar, G. Krabbes, F. Heidrich-Meisner and W. Brenig. 'Linear temperature dependence of the magnetic heat conductivity in $CaCu_2O_3$'. *Phys. Rev. Lett.* **98**, 027201 (2007).

[127] H. Miike and K. Hirakawa. 'Evidence of the diffusive thermal conduction in a one-dimensional antiferromagnet $KCuF_3$ above T_N.' *J. Phys. Soc. Jpn.* **38**, 1279–1285 (1975).

[128] A. V. Sologubenko, E. Felder, K. Giannò, H. R. Ott, A. Vietkine and A. Revcolevschi. 'Thermal conductivity and specific heat of the linear chain cuprate Sr_2CuO_3: Evidence for thermal transport via spinons'. *Phys. Rev. B* **62**, R6108–R6111 (2000).

[129] A. V. Sologubenko, K. Giannò, H. R. Ott, A. Vietkine and A. Revcolevschi. 'Heat transport by lattice and spin excitations in the spin-chain compounds $SrCuO_2$ and Sr_2CuO_3'. *Phys. Rev. B* **64**, 054412 (2001).

[130] A. V. Sologubenko, H. R. Ott, G. Dhalenne and A. Revcolevschi. 'Universal behavior of spin-mediated energy transport in $S = 1/2$ chain cuprates: $BaCu_2Si_2O_7$ as an example'. *Europhys. Lett.* **62**, 540 (2003).

[131] B. Y. Pan, Y. Xu, J. M. Ni, S. Y. Zhou, X. C. Hong, X. Qiu and S. Y. Li. 'Unambiguous experimental verification of linear-in-temperature spinon thermal conductivity in an antiferromagnetic Heisenberg chain'. *Phys. Rev. Lett.* **129**, 167201 (2022).

[132] T. Kawamata, M. Uesaka, M. Sato, K. Naruse, K. Kudo, N. Kobayashi and Y. Koike. 'Thermal conductivity due to spinons in the one-dimensional quantum spin system $Sr_2V_3O_9$'. *J. Phys. Soc. Jpn.* **83**, 054601 (2014).

[133] A. V. Sologubenko, K. Giannó, H. R. Ott, U. Ammerahl and A. Revcolevschi. 'Thermal conductivity of the hole-doped spin ladder system $Sr_{14-x}Ca_xCu_{24}O_{41}$'. *Phys. Rev. Lett.* **84**, 2714–2717 (2000).

[134] C. Hess, C. Baumann, U. Ammerahl, B. Büchner, F. Heidrich-Meisner, W. Brenig and A. Revcolevschi. 'Magnon heat transport in $(Sr,Ca,La)_{14}Cu_{24}O_{41}$'. *Phys. Rev. B* **64**, 184305 (2001).

[135] C. Hess, H. ElHaes, B. Büchner, U. Ammerahl, M. Hücker and A. Revcolevschi. 'Magnon-hole scattering and charge order in $Sr_{14-x}Ca_xCu_{24}O_{41}$'. *Phys. Rev. Lett.* **93**, 027005 (2004).

[136] C. Hess, B. Büchner, U. Ammerahl, L. Colonescu, F. Heidrich-Meisner, W. Brenig and A. Revcolevschi. 'Magnon heat transport in doped La_2CuO_4'. *Phys. Rev. Lett.* **90**, 197002 (2003).

[137] H. Fröhlich and W. Heitler. 'Time effects in the magnetic cooling method II- The conductivity of heat'. *Proc. R. Soc. Lon. A: Math. Phys. Sci.* **155**, 640–652 (1936).

[138] B. Lüthi. 'Thermal conductivity of yttrium iron garnet'. *J. Phys. Chem. Solids* **23**, 35–38 (1962).

[139] C. Hess. 'Heat transport of cuprate-based low-dimensional quantum magnets with strong exchange coupling'. *Phys. Rep.* **811**, 1–38 (2019).

[140] C. Hess. 'Heat conduction in low-dimensional quantum magnets'. *Eur. Phys. J. Spec. Top.* **151**, 73–83 (2007).

[141] X. Zhao, Z. Zhao, X. Liu and X. Sun. 'Low-temperature heat transport of spin-gapped quantum magnets'. *Sci. China Phys. Mech. Astron.* **59** (2016).

[142] A. V. Sologubenko, T. Lorenz, H. R. Ott and A. Freimuth. 'Thermal conductivity via magnetic excitations in spin-chain materials'. *J. Low Temp. Phys.* **147**, 387–403 (2007).

[143] Y. Ando, J. Takeya, D. L. Sisson, S. G. Doettinger, I. Tanaka, R. S. Feigelson and A. Kapitulnik. 'Thermal conductivity of the spin-Peierls compound $CuGeO_3$'. *Phys. Rev. B* **58**, R2913–R2916 (1998).

[144] M. Hofmann, T. Lorenz, A. Freimuth, G. Uhrig, H. Kageyama, Y. Ueda, G. Dhalenne and A. Revcolevschi. 'Heat transport in $SrCu_2(BO_3)_2$ and $CuGeO_3$'. *Phys. B: Condens* **312-313**. The International Conference on Strongly Correlated Electron Systems, 597–599 (2002).

[145] N. Hlubek, M. Sing, S. Glawion, R. Claessen, S. van Smaalen, P. H. M. van Loosdrecht, B. Büchner and C. Hess. 'Heat conductivity of the spin-Peierls compounds TiOCl and TiOBr'. *Phys. Rev. B* **81**, 144428 (2010).

[146] B.-G. Jeon, B. Koteswararao, C. B. Park, G. J. Shu, S. C. Riggs, E. G. Moon, S. B. Chung, F. C. Chou and K. H. Kim. 'Giant suppression of phononic heat transport in a quantum magnet $BiCu_2PO_6$'. *Sci. Rep.* **6**, 36970 (2016).

[147] A. V. Sologubenko, T. Lorenz, J. A. Mydosh, A. Rosch, K. C. Shortsleeves and M. M. Turnbull. 'Field-dependent thermal transport in the Haldane chain compound NENP'. *Phys. Rev. Lett.* **100**, 137202 (2008).

[148] M. Hase, I. Terasaki, K. Uchinokura, M. Tokunaga, N. Miura and H. Obara. 'Magnetic phase diagram of the spin-Peierls cuprate $CuGeO_3$'. *Phys. Rev. B* **48**, 9616–9619 (1993).

[149] R. Hentrich, A. U. B. Wolter, X. Zotos, W. Brenig, D. Nowak, A. Isaeva, T. Doert, A. Banerjee, P. Lampen-Kelley, D. G. Mandrus, S. E. Nagler, J. Sears, Y.-J. Kim, B. Büchner and C. Hess. 'Unusual phonon heat transport in $\alpha-RuCl_3$: Strong spin-phonon scattering and field-induced spin gap'. *Phys. Rev. Lett.* **120**, 117204 (2018).

[150] R. Hentrich, X. Hong, M. Gillig, F. Caglieris, M. Čulo, M. Shahrokhvand, U. Zeitler, M. Roslova, A. Isaeva, T. Doert, L. Janssen, M. Vojta, B. Büchner and C. Hess.

'High-field thermal transport properties of the Kitaev quantum magnet $\alpha-\text{RuCl}_3$: Evidence for low-energy excitations beyond the critical field'. *Phys. Rev. B* **102**, 235155 (2020).

[151] X. Hong, M. Gillig, R. Hentrich, W. Yao, V. Kocsis, A. R. Witte, T. Schreiner, D. Baumann, N. Pérez, A. U. B. Wolter, Y. Li, B. Büchner and C. Hess. 'Strongly scattered phonon heat transport of the candidate Kitaev material $\text{Na}_2\text{Co}_2\text{TeO}_6$'. *Phys. Rev. B* **104**, 144426 (2021).

[152] F. Heidrich-Meisner, A. Honecker, D. C. Cabra and W. Brenig. 'Thermal conductivity of anisotropic and frustrated spin-$\frac{1}{2}$ chains'. *Phys. Rev. B* **66**, 140406 (2002).

[153] F. Heidrich-Meisner, A. Honecker, D. C. Cabra and W. Brenig. 'Zero-frequency transport properties of one-dimensional spin-$\frac{1}{2}$ systems'. *Phys. Rev. B* **68**, 134436 (2003).

[154] E. Shimshoni, N. Andrei and A. Rosch. 'Thermal conductivity of spin-$\frac{1}{2}$ chains'. *Phys. Rev. B* **68**, 104401 (2003).

[155] A. Klümper and K. Sakai. 'The thermal conductivity of the spin-$\frac{1}{2}$ XXZ chain at arbitrary temperature'. *J. Phys. A: Math. Gen.* **35**, 2173 (2002).

[156] K. Sakai and A. Klümper. 'Non-dissipative thermal transport in the massive regimes of the XXZ chain'. *J. Phys. A: Math. Gen.* **36**, 11617 (2003).

[157] C. Hess, C. Baumann and B. Büchner. 'Scattering processes and magnon thermal conductivity in $\text{La}_5\text{Ca}_9\text{Cu}_{24}\text{O}_{41}$'. *J. Magn. Magn. Mater.* **290-291**, 322–325 (2005).

[158] G. Mahan. *Many-Particle Physics* (Springer US, 2012).

[159] R. Kubo. 'The fluctuation-dissipation theorem'. *Rep. Prog. Phys.* **29**, 255 (1966).

[160] R. Kubo. 'Statistical-mechanical theory of irreversible processes. I. General theory and simple applications to magnetic and conduction problems'. *J. Phys. Soc. Jpn.* **12**, 570–586 (1957).

[161] X. Zotos, F. Naef and P. Prelovšek. 'Transport and conservation laws'. *Phys. Rev. B* **55**, 11029–11032 (1997).

[162] X. Zotos and P. Prelovšek. 'Evidence for ideal insulating or conducting state in a one-dimensional integrable system'. *Phys. Rev. B* **53**, 983–986 (1996).

[163] H. Castella, X. Zotos and P. Prelovšek. 'Integrability and ideal conductance at finite temperatures'. *Phys. Rev. Lett.* **74**, 972–975 (1995).

[164] X. Zotos. 'Finite temperature Drude weight of the one-dimensional spin- 1/2 Heisenberg model'. *Phys. Rev. Lett.* **82**, 1764–1767 (1999).

[165] X. Zotos. 'Ballistic transport in classical and quantum integrable systems'. *J. Low Temp. Phys.* **126**, 1185–1194 (2002).

[166] X. Zotos. 'High temperature thermal conductivity of two-leg spin-1/2 ladders'. *Phys. Rev. Lett.* **92**, 067202 (2004).

[167] J. V. Alvarez and C. Gros. 'Conductivity of quantum spin chains: A quantum Monte Carlo approach'. *Phys. Rev. B* **66**, 094403 (2002).

[168] J. V. Alvarez and C. Gros. 'Low-temperature transport in Heisenberg chains'. *Phys. Rev. Lett.* **88**, 077203 (2002).

[169] J. V. Alvarez and C. Gros. 'Anomalous thermal conductivity of frustrated Heisenberg spin chains and ladders'. *Phys. Rev. Lett.* **89**, 156603 (2002).

[170] E. Orignac, R. Chitra and R. Citro. 'Thermal transport in one-dimensional spin gap systems'. *Phys. Rev. B* **67**, 134426 (2003).

[171] P. Zavitsanos and X. Zotos. 'Ballistic magnetic thermal transport coupled to phonons'. *Phys. Rev. B* **104**, 024429 (2021).

[172] O. Buryy, Y. Zhydachevskii, L. Vasylechko, D. Sugak, N. Martynyuk, S. Ubizskii and K. D. Becker. 'Thermal changes of the crystal structure and the influence of thermo-chemical annealing on the optical properties of YbAlO$_3$ crystals'. *J. Phys.: Condens. Matter* **22**, 055902 (2010).

[173] 'DuPont Conductive Silver Compositions for General Purpose Air-Dry Applications' (DuPont, Online; visited on 09-08-2023).

[174] A. Wang, O. Ohashi, N. Yamaguchi, M. Aoki, Y. Higashi and N. Hitomi. 'Cleaning of diffusion bonding surface by argon ion bombardment treatment'. *Nucl. Instrum. Methods Phys. Res.* **206**, 219–223 (2003).

[175] 'VersaLab™: 3 Tesla, Cryogen-Free Physical Property Measurement System' (Quantum Deign Education, Online; visited on 09-08-2023).

[176] 'Physical Property Measurement System: Thermal Transport Option Unser's Manual'. 3rd ed. 1684-100 Rev. B (Quantum Design, 2002).

[177] 'Physical Property Measurement System: Hardware Manual'. 3rd ed. 1070-150, Rev. B5 (Quantum Design, 2008).

[178] 'PPMS Platform Measurement Options'. 1084-500, Rev. D0 (Quantum Design, 2002).

[179] 'Physical Property Measurement System: PPMS MultiVu Application User's Manual'. 2nd ed. 1070-110, Rev. A-1 (Quantum Design, 2004).

[180] 'Kelvinox: Dilution Refrigerators to Suit All Applications' (Oxford Instruments, Online; visited on 09-08-2023).

[181] H. London. Ed. by R. Bowers. *Proceedings of the 2nd International Conference on Low-Temperature Physics* (North-Holland, 1951).

[182] H. London, G. R. Clarke and E. Mendoza. 'Osmotic pressure of He^3 in liquid He^4, with proposals for a refrigerator to work below 1°K'. *Phys. Rev.* **128**, 1992–2005 (1962).

[183] S. Hartmann. 'Thermoelectric Transport in Correlated Electron Systems'. Doctoral dissertation. Technische Universität Dresden, 2010.

[184] Q. Li, C. Watson, R. Goodrich, D. Haase and H. Lukefahr. 'Thick-film chip resistors for use as low-temperature thermometers'. *Cryogenics* **26**, 467–470 (1986).

[185] M. Meisel, G. Stewart and E. Adams. 'Thick-film chip resistors as millikelvin temperatures'. *Cryogenics* **29**, 1168–1169 (1989).

[186] A. Briggs. 'Characterisation of some chip resistors at low-temperatures'. *Cryogenics* **31**, 932–935 (1991).

[187] W. Schoepe. 'Conduction mechanism in in granular RuO$_2$-based thick-film resistors'. *Phys. B: Condens. Matter* **165**, 299–300 (1990).

[188] M. Watanabe, M. Morishita and Y. Ootuka. 'Magnetoresistance of RuO$_2$-based resistance thermometers below 0.3 K'. *Cryogenics* **41**, 143–148 (2001).

[189] K. Uhlig. 'Magnetoresistance of thick-film chip resistors at millikelvin temperatures'. *Cryogenics* **35**, 525–528 (1995).

[190] W. Bosch, F. Mathu, H. Meijer and R. Willekers. 'Behaviour of thick film resistors (Philips type RC-01) as low temperature thermometers in magnetic fields up to 5 T'. *Cryogenics* **26**, 3–8 (1986).

[191] J. Ekin. *Experimental Techniques for Low-Temperature Measurements: Cryostat Design, Material Properties and Superconductor Critical-Current Testing* (Oxford UP, 2006).

[192] G. Ihas, L. Frederick and J. McFarland. 'Low temperature thermometry in high magnetic fields'. *J. Low Temp. Phys.* **113**, 963–968 (1998).

[193] M. Affronte, M. Campani, S. Piccinini, M. Tamborin, B. Morten, M. Prudenziati and O. Laborde. 'Low temperature electronic transport in RuO₂-based cermet resistors'. *J. Low Temp. Phys.* **109**, 461–475 (1997).

[194] M. Affronte, M. Campani, B. Morten, M. Prudenziati and O. Laborde. 'Magnetoresistance of RuO₂-based thick film resistors'. *J. Low Temp. Phys.* **112**, 355–371 (1998).

[195] R. L. White. 'Review of recent work on the magnetic and spectroscopic properties of the rare-earth orthoferrites'. *J. Appl. Phys.* **40**, 1061–1069 (1969).

[196] V. Plakhty, Y. Chernenkov and M. Bedrizova. 'Neutron diffraction study of weak antiferromagnetism in ytterbium orthoferrite'. *Solid State Commun.* **47**, 309–312 (1983).

[197] S. E. Nikitin, L. S. Wu, A. S. Sefat, K. A. Shaykhutdinov, Z. Lu, S. Meng, E. V. Pomjakushina, K. Conder, G. Ehlers, M. D. Lumsden, A. I. Kolesnikov, S. Barilo, S. A. Guretskii, D. S. Inosov and A. Podlesnyak. 'Decoupled spin dynamics in the rare-earth orthoferrite YbFeO₃: Evolution of magnetic excitations through the spin-reorientation transition'. *Phys. Rev. B* **98**, 064424 (2018).

[198] S.-W. Cheong and M. Mostovoy. 'Multiferroics: a magnetic twist for ferroelectricity'. *Nat. Mater.* **6**, 13–20 (2007).

[199] A. V. Kimel, A. Kirilyuk, A. Tsvetkov, R. V. Pisarev and T. Rasing. 'Laser-induced ultrafast spin reorientation in the antiferromagnet TmFeO₃'. *Nature* **429**, 850–853 (2004).

[200] P. Ricci, A. Casu, D. Chiriu, C. Corpino, C. Carbonaro, M. Marceddu, M. Salis and A. Anedda. 'Optical properties of pure Ytterbium Alluminium perovskites'. *Opt. Mater.* **33**. RE doped materials for optical based technologies Symposium K of the 2010 EMRS Spring Meeting, 1000–1003 (2011).

[201] C. E. Agrapidis, J. van den Brink and S. Nishimoto. 'Field-induced incommensurate ordering in Heisenberg chains coupled by Ising interaction: Model for ytterbium aluminum perovskite YbAlO₃'. *Phys. Rev. B* **99**, 224423 (2019).

[202] L. Balents. 'General introduction to magnetic frustration'. *11ᵗʰ International Conference on Highly Frustrated Magnetism (HFM22)*, Conference lectures (Sorbonne Université, France, 20th–25th June 2022).

[203] V. Martelli, F. Abud, J. L. Jiménez, E. Baggio-Saitovich, L.-D. Zhao and K. Behnia. 'Thermal diffusivity and its lower bound in orthorhombic SnSe'. *Phys. Rev. B* **104**, 035208 (2021).

[204] F. I. Chu, R. E. Taylor and A. B. Donaldson. 'Thermal diffusivity measurements at high temperatures by the radial flash method'. *J. Appl. Phys.* **51**, 336–341 (1980).

[205] S. Galeski (private communication).

[206] G. A. Slack and S. Galginaitis. 'Thermal conductivity and phonon scattering by magnetic impurities in CdTe'. *Phys. Rev.* **133**, A253–A268 (1964).

[207] A. Taheri, C. Da Silva and C. H. Amon. 'Phonon thermal transport in β-NX (X = P, As, Sb) monolayers: A first-principles study of the interplay between harmonic and anharmonic phonon properties'. *Phys. Rev. B* **99**, 235425 (2019).

[208] H. Beck, P. F. Meier and A. Thellung. 'Phonon hydrodynamics in solids'. *Physica Status Solidi (a)* **24**, 11–63 (1974).

[209] W. D. Seward, D. Lazarus and S. C. Fain. 'Thermal Conductivity of Hexagonal Close-Packed Solid Helium Four at High Densities'. *Phys. Rev.* **178**, 345–355 (1969).

[210] W. C. Thomlinson. 'Evidence for Anomalous Phonon Excitations in Solid He³'. *Phys. Rev. Lett.* **23**, 1330–1332 (1969).

[211] V. Kopylov and L. Mezhov-Deglin. 'Study of kinetic coefficients of bismuth at helium temperatures'. *Zhurnal Éksperimental'noǐ i Teoreticheskoǐ Fiziki* **65**, 720–734 (1974).

[212] Y. Machida, A. Subedi, K. Akiba, A. Miyake, M. Tokunaga, Y. Akahama, K. Izawa and K. Behnia. 'Observation of Poiseuille flow of phonons in black phosphorus'. *Science Advances* **4**, eaat3374 (2018).

[213] C. Hess and B. Büchner. 'Thermal conductivity of doped La_2CuO_4 as an example for heat transport by optical phonons in complex materials'. *Eur. Phys. J. B* **38**, 37–41 (2004).

[214] M. N. Wybourne and B. J. Kiff. 'Acoustic-optical phonon scattering observed in the thermal conductivity of polydiacetylene single crystals'. *J. Phys. C: Solid State Phys.* **18**, 309 (1985).

[215] M. N. Wybourne, B. J. Kiff and D. N. Batchelder. 'Anomalous Thermal Conduction in Polydiacetylene Single Crystals'. *Phys. Rev. Lett.* **53**, 580–583 (1984).

[216] M. Yamashita, N. Nakata, Y. Kasahara, T. Sasaki, N. Yoneyama, N. Kobayashi, S. Fujimoto, T. Shibauchi and Y. Matsuda. 'Thermal-transport measurements in a quantum spin-liquid state of the frustrated triangular magnet κ-(BEDT-TTF)$_2$Cu$_2$(CN)$_3$'. *Nat. Phys.* **5**, 44–47 (2009).

[217] G. Chen. 'Distinguishing thermodynamics and spectroscopy for octupolar U(1) spin liquid of Ce-pyrochlores'. *arXiv:2304.01892v1* (2023).

[218] G. Laurence. 'Low-temperature thermal conductivity of $CdCl_2$ and $FeCl_2$ and critical magnetic scattering of phonons in $FeCl_2$'. *Phys. Lett. A* **34**, 308–309 (1971).

[219] G. Laurence and D. Petitgrand. 'Thermal Conductivity and Magnon-Phonon Resonant Interaction in Antiferromagnetic $FeCl_2$'. *Phys. Rev. B* **8**, 2130–2138 (1973).

[220] M. Gillig, X. Hong, P. Sakrikar, G. Bastien, A. U. B. Wolter, L. Heinze, S. Nishimoto, B. Büchner and C. Hess. 'Thermal transport of the frustrated spin-chain mineral linarite: Magnetic heat transport and strong spin-phonon scattering'. *Phys. Rev. B* **104**, 235129 (2021).

[221] M. S. B. Hoque, Y. R. Koh, J. L. Braun, A. Mamun, Z. Liu, K. Huynh, M. E. Liao, K. Hussain, Z. Cheng, E. R. Hoglund, D. H. Olson, J. A. Tomko, K. Aryana, R. Galib, J. T. Gaskins, M. M. M. Elahi, Z. C. Leseman, J. M. Howe, T. Luo, S. Graham, M. S. Goorsky, A. Khan and P. E. Hopkins. 'High in-plane thermal conductivity of aluminum nitride thin films'. *ACS Nano* **15**, 9588–9599 (2021).

[222] S. Zherlitsyn, S. Yasin, J. Wosnitza, A. A. Zvyagin, A. V. Andreev and V. Tsurkan. 'Spin-lattice effects in selected antiferromagnetic materials (Review Article)'. *Low Temp. Phys.* **40**, 123–133 (2014).

[223] R. Küchler, R. Wawrzyńczak, H. Dawczak-Dębicki, J. Gooth and S. Galeski. 'New applications for the world's smallest high-precision capacitance dilatometer and its stress-implementing counterpart'. *Rev. Sci. Instrum.* **94**. 045108 (2023).

[224] O. Starykh (private communication).

[225] N. Blanc, J. Trinh, L. Dong, X. Bai, A. A. Aczel, M. Mourigal, L. Balents, T. Siegrist and A. Ramirez. 'Quantum criticality among entangled spin chains'. *Nat. Phys.* **14**, 273–276 (2018).

[226] A. W. Sandvik. 'Computational studies of quantum spin systems'. *AIP Conf. Proc.* **1297**, 135–338 (2010).

[227] R. Yu (private communication).

[228] U. Schollwöck. 'The density-matrix renormalization group in the age of matrix product states'. *Ann. Phys.* **326**. Special Issue, 96–192 (2011).

[229] G. Vidal. 'Classical simulation of infinite-size quantum lattice systems in one spatial dimension'. *Phys. Rev. Lett.* **98**, 070201 (2007).

[230] A. Klümper. 'The spin-1/2 Heisenberg chain: thermodynamics, quantum criticality and spin-Peierls exponents'. *Eur. Phys. J. B* **5**, 677–685 (1998).

[231] A. Klümper and D. C. Johnston. 'Thermodynamics of the spin-1/2 antiferromagnetic uniform Heisenberg chain'. *Phys. Rev. Lett.* **84**, 4701–4704 (2000).

[232] T. Giamarchi. 'Deconstructing the electron'. *Physics* **2**, 78 (2009).

[233] F. D. M. Haldane. 'Effective harmonic-fluid approach to low-energy properties of one-dimensional quantum fluids'. *Phys. Rev. Lett.* **47**, 1840–1843 (1981).

[234] Kappatsch, A., Quezel-Ambrunaz, S. and Sivardière, J. 'Structures et propriétés magnétiques des orthocobaltites de terres rares TCoO$_3$'. *Journal de Physique* **31**, 369–376 (1970).

[235] G. Chanin, E. A. Lynton and B. Serin. 'Impurity effects on the superconductive critical temperature of Indium and Aluminum'. *Phys. Rev.* **114**, 719–724 (1959).

[236] E. A. Lynton and D. McLachlan. 'Boundary scattering effects on the superconducting transition temperature of Indium'. *Phys. Rev.* **126**, 40–42 (1962).

[237] H. E. Bömmel, A. J. Darnell, W. F. Libby and B. R. Tittmann. 'Indium Antimonide: Superconductivity of the Metallic Form'. *Science* **139**, 1301–1302 (1963).

[238] G. Ventura, M. Barucci, E. Gottardi and I. Peroni. 'Low temperature thermal conductivity of Kevlar'. *Cryogenics* **40**, 489–491 (2000).

Acknowledgement